XMCD investigation at $M_{4,5}$ edges of the rare earth elements in high-performance permanent magnet

Von der Fakultät Mathematik und Physik der Universität Stuttgart zur

Erlangung der Würde eines Doktors der Naturwissenschaften (Dr. rer. net.)

genehmigte Abhandlung

Vorgelegt von

Sapana Tripathi

Aus Indore, India

Hauptberichter: PD Dr. Eberhard Goering

Mitberichter: Prof. Dr. Jörg Wrachtrup

Tag der mündlichen Prüfung: 22. März 2018

Max-Planck-Institut für Intelligente Systeme, Stuttgart

2018

To my Parents and beloved Husband

मेरे माता-पिता और प्रिय पति के लिए

Acknowledgements

I still remember the day, when I applied for Ph.D. studies in Prof. Gisela Schütz department of Modern magnetic systems and then followed by an interview with Prof. Schütz and "Mr. Goering". It is their trust that gave me this opportunity and adventure.

Firstly, I would like to thank my main supervisor ***"Mr.Goering"*** *for teaching me enormous things: how to do research, how to define and answer scientific questions. I am also thankful to him for all the patience, freedom and enormous support throughout my Ph.D. and for his jargon "****Don't be afraid****". Many thanks to* ***Prof. Gisela Schütz****, without whom my Ph.D. would not start in Max Planck Institute. Thank you for always being positive, encouraging and inspiring, giving lots of generous help. Many thanks to* ***Prof. Dr. Jörg Wrachtrup for accepting my various questions.***

I must thank ***Prof. Frank de Groot*** *whose expertise in simulations and modeling helped me a lot. Thank you for teaching me, revising my thesis and for strong support in learning new software during my visit to Utrecht University, Netherlands. I would like to thank* ***Mario Delgado Jamie*** *and* ***Heba Alnajjar*** *for their help during my visit to Utrecht University and their valuable discussion during my Ph.D. time.*

I would like to thank, ***Thomas Tietze,*** *for kindness and support during the initial times in MPI. Thank you for all the care during my Ph.D. I owe many thanks to my colleagues* ***Chen and Kwanghyo Son*** *for all the help during tedious beam-time measurements at ANKA, KIT and various discussion related to work and general life during my Ph.D. I would like to thank* ***Matthias Schmidt*** *for sharing an office with me and to an angel* ***Monika Kötz*** *for solving all the administration related .problems for me. I would also like to thank Mrs.* ***Dorothee Klink*** *for taking care of my visa and residence permit during my time in Germany. Special thanks to the WERA beamline scientist at ANKA synchrotron* ***Stefan Schuppler****,* ***Peter Nagel,*** *and* ***Michael Merz*** *for the help and support during beam times at beamline. Thanks to the x-ray diffraction groups* ***Dr. A. Leineweber*** *and* ***Dr. R. Dinnebier*** *for helping in phase analysis. Special love and thanks to my nice friend* ***Linda*** *for sharing food with me and for the outdoor activities fun. Thanks to* ***Kahraman*** *and* ***Umut*** *for being my agony aunt.*

It has been a great experience in a dynamic and interdisciplinary research environment at MPI. I am also grateful to all the institutions providing funding for research work: RELEAMAG project, DFG, BMBF, BOSCH, Max Planck Institute. Thanks to Aalen University collaborators

*and **Bernd Ludescher** for providing samples. "I am grateful to KARA and to the Karlsruhe Nano Micro Facility (KNMF) for the provision of beamtime".*

*I would like to thank many of my Indian friends for their caring and wonderful time together, especially, **Aditi Singh**, **Sutapa Roy**, **Rachana Acharya**, **Jagriti Pal and Renuka Tayade.** Many thanks to my friend **Renuka Tayade** for listening to my thesis shaping ideas, suggesting things and all the care she put forth. Also, many thanks to **Roopa Shinde** for her enormous support and motivation during all the struggling time.*

*Finally, I would like to thank my Husband and my parents, my brother and my whole family. I have been away from home to study for more than 8 years. Their care, support, and understanding always accompany me; without them, I can never make it. Special thanks to my Husband, **Sagar Jain** for his endless love and support. While writing the acknowledgment, I realized that it could never be completed. Thanks for all the love and care that I received, all the great people I met in the last years. I am sincerely grateful to all of them.*

From a loquacious physicist

Sapana Tripathi

Contents

1. Zusammenfassung 4

2. Scientific background 9

2.1. Introduction: Rare-earth permanent magnets 9

2.2. Ferromagnetism and x-ray absorption spectra (XAS) 11

2.2.1. Magnetic moment of a single ion 12

2.2.2. Exchange interaction 13

2.2.3. Interaction of x-rays with the matter: X-ray absorption spectra (XAS) 15

2.2.4. Dipole selection rules 16

2.2.5. X-ray magnetic circular dichroism (XMCD): principle 18

2.2.6. Detection method 20

2.3. Experimental aspects of XMCD measurements 22

2.3.1. WERA beamline 24

2.3.2. XMCD set up at WERA beamline 26

2.3.3. XMCD data acquisition and evaluation 27

2.4. Theoretical aspects of XMCD measurements 30

2.4.1. Term symbols 31

2.4.2. Calculation of matrix elements 32

2.4.3. Calculation of spectra (XAS) with atomic multiplets 32

2.4.4. Calculation of x-ray magnetic dichroism spectra (XMCD) 33

2.5. CTM4XAS-Software for simulations 34

3. Atomic multiplet Theory simulations for full lanthanide series 38

3.1. Introduction 38

3.2. Lanthanides (4*f*) magnetic moments (Hund's rule) 38

3.3. Previous studies of XAS and XMCD at $M_{4,5}$ edges in 4*f* elements 40

3.4. Atomic Multiplet theory simulations for the full lanthanide series 43

3.4.1. Software details 43

3.4.2. Simulations details and parameters 44

3.4.3. An example: simulated XAS and XMCD spectra of Ytterbium (Yb^{3+}) 46

3.4.4. Simulation results for full lanthanide series 48

3.5. XMCD sum rule analysis for 4*f* (rare earth elements) 52

3.5.1. Orbital moment (L_z) 54

3.5.2. Effective spin magnetic moment (S_z+3*T_z) 56

3.5.3. Estimation of the deviation in XMCD spin sum rule 58

3.5.4. Estimation of spin magnetic moment by elimination of magnetic dipole term 61

3.6. Analysis procedure of the experimental spectra 66

3.7. Discussion 70

4. X-ray absorption (XAS) and x-ray magnetic circular dichroism (XMCD) investigation of $CeFe_{11}Ti$ magnets 72

4.1. Introduction 72

4.2. Studies on Ce-Fe compounds 74

4.3. Structural Investigations 76

4.3.1. Inductive coupled plasma spectroscopy (ICP –OES) and SEM microscopy: 76

4.3.2. X-ray diffraction investigation (XRD) 77

4.4. Magnetic investigation-SQUID magnetometry 79

4.5. Spectroscopic XAS and XMCD investigations 81

4.5.1. XAS and XMCD spectra of Iron and Titanium $L_{2,3}$ edges: 81

4.5.2. XAS and XMCD spectra of Cerium $M_{4,5}$ edges: Line shape analysis 83

4.6. Theoretical modeling 90

4.6.1. Crystal field multiplet model 90

4.6.2. Charge transfer multiplet model (CTM) 93

4.7. Discussion 96

5. XMCD Investigation on Rare Earth Garnets 98

5.1. Introduction - Rare earth Garnets (RIGs) 98

5.2. Magnetization and Compensation temperature (T_c) of rare earth garnets 100

5.3. Reported XMCD studies at $M_{4,5}$ edges on the rare earth garnets 102

5.4. Structural investigations 103

5.5. Magnetic investigation - SQUID results 105

5.6. Spectroscopic investigation-XAS and XMCD results 110

5.6.1. XAS and XMCD –Fe $L_{2,3}$ edges: 110

5.6.2. XAS and XMCD –rare earth elements –$M_{4,5}$ edges and sum rule analysis 115

5.6.3. Comparison of SQUID results with sum rule analysis results 119

5.7. Discussion 121

6. XAS and XMCD investigations at Nd $M_{4,5}$ edge in Nd-based permanent magnets 123

6.1. Introduction 123

6.2. Reported XAS and XMCD studies at Nd edges (*L*, *M*) in Nd-based magnets . 125

6.3. Specimen details 126

6.3.1. Fe/Nd multilayer 127

6.3.2. $Fe_{14}Nd_2B$ single phase 130

6.3.3. $Fe_{14}Nd_2B$ textured thin film (340nm) 132

6.3.4. $Fe_{14}(Nd, Dy)_2B$ hard magnet 136

6.4. Spectroscopy results: XAS and XMCD investigation 139

6.4.1. XAS and XMCD spectra of iron $L_{2,3}$ edges 140

6.4.2. XAS and XMCD spectra of Neodymium $M_{4,5}$ edges: Line shape analysis 144

6.4.3. Explanation for reduction in neodymium magnetic moment 150

6.5. Discussion 156

7. Reference 158

8. CURRICULUM VITAE 171

9. Erklärung 172

1. Zusammenfassung

Ziel dieser Arbeit ist die Untersuchung in wie weit man mit Hilfe des magnetischen Röntgendichroismuses (XMCD) neue Erkenntnisse an den $M_{4,5}$ Kanten der Seltenerdmetalle gewinnen kann. Die XMCD-Technik ist abgeleitet von der Röntgenabsorptionsspektroskopie (XAS) und erlaubt, mittels zirkular polarisierter Röntgenstrahlung, elementspezifisch die magnetischen Eigenschaften des Materials zu messen und quantitativ magnetische Bahn- und Spinmomente durch die Zirkularpolarisation und Anwendung der Summenregeln zu trennen. Die XMCD-Summenregeln gelten besonderes gut für die schweren 3*d* Übergangsmetalle und wurden bisher noch nicht für die $M_{4,5}$-Kanten der Seltenerdmetalle angewandt. Zum ersten Mal werden hier systematische Untersuchen an den $M_{4,5}$ Kanten von Seltenerdmetallen an verschiedenen Systemen durchgeführt. Einerseits werden $CeFe_{11}Ti$ basierende Granate mit intermetallischen Phasen aus den Seltenerdmetallen Samarium, Dysprosium und Gadolinium und andererseits Permanentmagnete wie $Fe_{14}Nd_2B$, welche eine elektronische Anregung von $3d^{10}4f^n \rightarrow 3d^9 4f^{n+1}$ aufweisen, untersucht. Im Bereich der Röntgendichroismusuntersuchungen wird durch das lokale Verhalten der 4*f* Wellenfunktion der Seltenerdmetalle angenommen, dass sich die spektrale Form dieser nicht ändert. Die Auswertung der Summenregeln ermöglicht es, quantitative Aussagen über das Bahn- und Spinmoment zu treffen. Die Anwendbarkeit der Summenregeln auf die $M_{4,5}$ Kanten für Seltenerdmetalle ist ein großes Diskussionsthema, da es hier zu einer Vermischung der $3d_{3/2}$ und $3d_{5/2}$ Zustände kommt und ein zusätzlicher Beitrag durch die Spin-Bahn-Kopplung im magnetischen Dipolterm (T_Z) induziert wird.

Unter diesen Voraussetzungen wird in diese Arbeit die Änderung der Spektralform, die quantitative Abschätzung der magnetischen Momente (Spin und Bahn) unter Verwendung der Summenregeln und deren temperaturabhängige Änderung an verschieden magnetischen Materialien untersucht. Die Ergebnisse sind wie folgt gegliedert:

1. Zum Vergleich der experimentellen Ergebnisse mit der Theorie der gesamten Seltenerdmetallserie (von La^{3+} bis Yb^{3+}) wurden Simulationen mit Hilfe der atomic multiplet Theorie durchgeführt. An den simulierten Spektren wurde die Anwendbarkeit der XAS und XMCD Bahn- und Spin-Summenregeln untersucht. Basierend auf den Simulationsergebnissen wurden Korrekturmethoden der Summenregeln entwickelt und an den experimentellen Spektren überprüft. Für die Seltenerdmetalle (ausgenommen Cer) kann das Linienprofil der

XMCD und XAS Spektren der $M_{4,5}$ Kanten durch die Konfiguration des Grundzustandes erklärt werden.

2. Für die $CeFe_{11}Ti$ intermetallischen Phasen konnte die Veränderung des Linienspektrums der XAS und XMCD an den Ce-$M_{4,5}$ Kanten mit einem 10-15% Beitrag des J=5/2 Zustands zum Grundzustand (J=5/2) erklärt werden. Die Summenregeln zeigen einen schwachen Ferromagnetismus an den Cer Seltenerdmetallplätzen. Es wurde gezeigt, dass Eisen und Cer nur schwach miteinander gekoppelt sind. Das magnetische Moment von Cer scheint unterhalb von Raumtemperatur aufgrund der Wechselwirkung mit dem Kristallgitter eigefroren zu sein. Diese Kopplung ist stärker als die Austauschwechselwirkung zwischen den Eisen 3*d*-Elektronen und den Cer 4*f*-Elektronen, weshalb es nicht einmal bei tiefen Temperaturen zu einer magnetischen Ordnung der Cer-Momente kommt.

3. Die ferrimagnetischen Seltenerdmetall-Granate zeigen eine Kompensationstemperatur bei der die komplette Magnetisierung null ist. Durch die schwache Kopplung der Seltenerdmetallionen zeigt die Magnetisierung des Seltenerdmetalluntergitters eine andere Temperaturabhängigkeit, welche dazu führt, dass sich das magnetische Moment mit sinkender Temperatur erhöht. Für tiefe Temperaturen konnte gezeigt werden, dass die Summenregeln geeignet sind, das Verhalten unterhalb der Kompensationstemperatur zu beschreiben. In den Granaten wurde ein reduziertes magnetisches Moment für Dysprosium, Gadolinium und Samarium im Vergleich zur Hund‘schen Regel und theoretischen Untersuchungen beobachtet, welches durch ein Verkanten der magnetischen Momente verursacht wird.

4. An texturierten $Fe_{14}Nd_2B$ Filmen, Fe/Nd Multischichtsystemen, $Fe_{14}Nd_2B$ Einzelphasen und $Fe_{14}(Nd,Dy)_2B$ Permanentmagneten wurden Röntgendichroismusmessungen durchgeführt. Obwohl die 4*f* Neodym-Elektronen lokalisiert sind, werden die magnetischen Eigenschaften sowie die Ausrichtung der Spins der 4*f* Elektronen von Nd stark von der Kristallstruktur und den Korngrenzen beeinflusst. Dies führt in gesinterten Nd Magneten zu einer drastischen Verkleinerung des magnetischen Moments (verglichen zur Hund’schen Regel und theoretischen Arbeiten). Weiterhin kann das verkleinerte magnetische Moment des Nd durch die Oberflächenempfindlichkeit bei der Messung der Gesamtelektronenausbeute verursacht sein.

5. Die Änderungen des Bahn- und Spin-Moments wurde für die Seltenerdmetalle, wie Nd, Sm und Dy in den Granaten und den Neodym-basierten Proben mit Hilfe der Änderungen in der XAS und XMCD Spektralform beobachtet. Obwohl die 4*f*-Wellenfunktion der Seltenerdmetalle lokalisiert ist, wird diese von der Umgebung des Festkörpers beeinflusst, was zu einer Änderung in den Spektren an den $M_{4,5}$-Kanten führt.

In dieser Arbeit wurde systematisch der Einfluss der lokalen Umgebung auf das XAS und XMCD Spektrum und die Spin zu Bahn Verhältnis der Seltenerdmetalle an verschiedenen Probensystemen, wie dünnen Schichten, gesinterten Magneten, Viellagensystemen und Pulvern in Abhängigkeit der Temperatur untersucht.

Summary-English

The purpose of the present thesis is to explore the potential of the x-ray magnetic circular dichroism (XMCD) on gaining new insight at $M_{4,5}$ edges of rare earth (RE) elements. The XMCD technique is derived from the x-ray absorption spectroscopy (XAS), allows probing element specific magnetic properties and to separate in a quantitative way orbital and spin magnetic moments, using circular polarization in combination with entitled sum rules. The XMCD sum rules work distinctively for the heavy 3*d* transition metals, it could not be used so far for the RE $M_{4,5}$ edges. For the first time, the systematic investigations are presented associated to $M_{4,5}$ edges of rare earth elements into the $CeFe_{11}Ti$ based intermetallic, rare earth (samarium, dysprosium, and gadolinium) garnets and rare earth permanent magnets such as $Fe_{14}Nd_2B$ magnets corresponding to the electronic excitation of the $3d^{10}4f^{n} \rightarrow 3d^{9}4f^{n+1}$. Prior to in the field of RE $M_{4,5}$ edges XMCD investigation, it is considered that the spectral shape of the rare earth elements does not change. This is due to the localized behavior of the 4*f* wave functions in rare earth elements. To this point also the applicability of the spin sum rule for the $M_{4,5}$ edges of the rare earth elements is in general not relevant and still a wide topic of discussion. This is due to the mixing of the $3d_{3/2}$ and $3d_{5/2}$ initial state excitations as well the strong contribution from the spin-orbit coupling induced magnetic dipole term (T_Z), which could not merely remove by angular dependent measurements, as it is the case for the 3*d* TM.

Considering the studies in thesis, It will cover the observation of the change in spectral shape, quantitative estimation of the magnetic moments (spin and orbital) using XMCD sum rules and their ratio as a function of variation in temperature in different magnetic materials. The results are presented as follows:

1. The atomic multiplet theory simulations are performed to compare the experimental results with a theory for the full rare earth series (from La^{3+} to Yb^{3+}). For a successful understanding of the experimental spectra simulations have been performed. The applicability of the XAS and XMCD orbital and spin sum rules is investigated for the simulated spectra. Based on the simulation results, sum rule correction methods have been found and confirmed for the experimental spectra. XMCD and XAS experimental spectra of all the rare earth elements (except cerium) at the $M_{4,5}$ edges can be explained by a well-defined ground state configuration.

2. In $CeFe_{11}Ti$ intermetallic, the XAS and XMCD experimental spectra line shape variations at the Ce-$M_{4,5}$ edge can be explained by the admixture of the 10-15 % contribution of the J=7/2 state in the J=5/2 pure ground state configuration of the cerium $M_{4,5}$ edge. The XMCD sum rule analysis shows a very weak ferromagnetism at the rare earth (Ce) site. It has been observed that the cerium and iron are not very well coupled with each other. The Ce magnetic moment appears to freeze below room temperature in the disordered state due to the crystal structure or the interaction with the lattice. This interaction is stronger than the exchange coupling between iron 3*d* and the cerium 4*f* electrons. Therefore, even at the low temperature, no magnetic ordering in the cerium magnetic moment is taking place.
3. The rare earth garnet ferrimagnets are known to exhibit the compensation temperature where the total magnetization of the specimen is zero. Due to the relatively weak coupling of the RE ions, the RE sub-lattice magnetization has a different temperature dependence, resulting in an increase in the magnetic moment down to lower temperatures. At low temperatures, the applicability of the XMCD orbital and spin sum rule for the rare earth elements on the experimental spectra measured below the compensation temperature is confirmed. A reduced magnetic moment has been observed at the rare earth elements site such as at dysprosium, gadolinium, and samarium in the garnets compared to the Hund's rule and theoretical investigations due to canting of the magnetic moments.
4. XMCD investigations have been performed on neodymium-based specimens such as $Fe_{14}Nd_2B$ textured thick film, Fe/Nd multilayer, and $Fe_{14}Nd_2B$ single phase along with the $Fe_{14}(Nd, Dy)_2B$ permanent magnets. Although the 4*f* neodymium electrons are localized, the crystalline environment of the solid and the grain boundary phase is noticeably affecting the magnetic properties and the orientation of the spin alignment of the neodymium 4*f* electrons. Which is causing a severe reduction in the magnetic moment (compared to Hund's rule and theoretical investigation) of the Nd in the sintered magnets. The reduction in the magnetic moment of the neodymium compared to the bulk investigation is also explained by the surface sensitivity of the total electron yield measurements.
5. The change in the orbital to spin ratio has been observed for all the rare earth elements such as Nd, Sm, and Dy in the garnets and the neodymium-based specimens due to change in the XAS and XMCD spectral shape. Although rare earth elements 4*f* wave functions are localized, in influence with the environment of the solid in different systems is noticeably affecting the spectral shape at the $M_{4,5}$ edges in the rare earth systems.

In this thesis, the systematic investigation of influence of the local environment on the XAS and XMCD spectral shape and the spin to the orbital ratio of the rare earth elements have been

shown in the different types of systems in the thin film, sintered magnets, multilayer and powder form as a function of temperature.

2. Scientific background

2.1. Introduction: Rare-earth permanent magnets

Permanent magnets are the vital components in a variety of electronic devices and electromechanical applications. However, their presence is usually hidden in subassemblies. The history of the use of permanent magnets in the electrical components dates back to a period of 100 years. However, due to dramatic improvements in the properties and abundant availability of permanent magnets their applications has been rapidly growing. Applications in sound production systems, watches, weighing systems, automotive ignitions, starters, microwave ovens, small motors, actuators for computer peripheral devices, telephones, in particle accelerators, industries, defense and also in nuclear magnetic resonance (NMR) imaging [1]. The first permanent magnets introduced are steel magnets using 30% cobalt in 1917 by Kotaro Honda[1]. They exhibit a coercivity of 520 Oe and energy product of 1MGOe. Later in 1931, Tokuhichi Mishima introduced the magnets based on iron, nickel, and aluminum named “Alni”[1]. After 30 years of the long development, “Alnico” magnets came into the picture, where the cobalt was added in Alni magnets up to 40%. In these magnets, the coercivity is increased up to 1900 Oe and energy product 9.5 MGOe was achieved [1]. However, most of the Alnico alloys contain a large amount of the expensive metal cobalt and they possess relatively lower energy density due to their lower coercivity. Subsequently, in 1960’s the new cobalt free cheaper magnets named “ferrites” were introduced and these magnets show relatively better coercivity (~5KOe) [1]. The ferrites are oxides of generic formula $MFe_{12}O_{19}$, where the metal M is barium, strontium or mixture. They have one great advantage as the raw materials are economical and abundant. This is an added advantage over all other permanent magnet types, which explains their enormous competitive success. Despite all the positive points for their applications, the major disadvantage of ferrites is the undesirable mechanical properties. The sintered ferrites were hard and very brittle and they had the lower energy product (less than 5MGOe) compare to Alnico[1].

The modern and still growing family of hard magnetic alloys are samarium cobalt and the neodymium-iron-boron magnets with the highest coercivity (>50 KOe) and energy product (>35MGOe) [1, 2]. A large number of such binary and ternary alloys either ferrimagnetic or

ferromagnetic. In and around 1970´s, the variety of phases has been synthesized exhibiting different stoichiometry and a variety of crystal structures. In many cases, their magnetic properties came out as a high technical importance and these compounds are manufactured on an industrial scale. The rare earth (RE) magnets that are extensively studied for more than 20 years are the $RE_2M_{14}B$ magnets where RE=Nd, Ce, Sm, and M=Fe.

The unique magnetic properties of the RE series from lanthanum to lutetium (also yttrium) result from the unfilled 4*f* shells. The 4*f* orbitals are rather dense and well localized on the atom and there are both large spin and orbital contributions to the magnetic moment. The large orbital moment and the asymmetric charge distribution of the rare earth elements lead to the uniaxial anisotropy, which is crucial for the permanent magnets development. The magnetic interactions between the localized 4*f* electrons are weak and the exhibit the lower Curie temperature. By combining the 4*f* rare earth elements with 3*d* transition elements of higher Curie temperature and magnetization possibly can combine the advantages of both and can create high-performance permanent magnet[3]. These rare earth-transition metal-based permanent magnets are not simply the intermetallic compounds they are multiphase, multicomponent and non-equilibrium metallurgical systems. Their magnetization curve behavior is controlled by the submicroscopic details of the microstructure. It is well known that the intergranular structure between the grains plays a significant role determining the magnetic properties, thus a detailed understanding of the microstructures and grain boundaries have been performed using microscopic investigations in the past years [4-7]. It has been discovered that this intergranular phase plays an important role in coercivity enhancement. There are several micromagnetic modeling has been also performed in order to understand the magnetization reversal, hysteresis effects and to understand the effect of microstructure on the coercive field of the sintered magnets [8-10].

Apart from a large number of investigations on rare earth permanent magnets, there is still lack of element-specific studies at the neodymium (at $M_{4,5}$ edges) site in these multifarious permanent magnets. Due to the difficult extraction process of the rare earth elements from their ores, the availability of these rare earth elements is less compared to their market demand. As a result, continuous research has been going on to develop the rare earth lean or rare earth free permanent magnets. In order to replace rare earth elements, the better understanding of rare earth elements in these permanent magnets at the elements specific level is necessary.

Therefore, the main objective of this thesis is to perform the x-ray absorption (XAS) and x-ray magnetic circular dichroism (XMCD) spectroscopic investigation at rare earth $M_{4,5}$ edges in order to develop the understanding of these rare earth elements present inside these high-performance permanent magnets.

The rare earth $M_{4,5}$ edges corresponding to the electronic excitation of the $3d^{10}4f^{n} \rightarrow 3d^{9}4f^{n+1}$. Prior to in the field of RE $M_{4,5}$ edges XMCD investigation, it is considered that the spectral shape of the rare earth elements does not change. This is due to the localized behavior of the 4*f* wave functions in rare earth elements. To this point also the applicability of the spin sum rule for the $M_{4,5}$ edges of the rare earth elements is in general not relevant and still a wide topic of discussion. This is due to the mixing of the $3d_{3/2}$ and $3d_{5/2}$ initial state excitations as well the strong contribution from the spin-orbit coupling induced magnetic dipole term (T_Z), which could not merely remove by angular dependent measurements, as it is the case for the 3*d* TM.

Considering this, the studies in this thesis will cover the observation of the change in spectral shape, magnetic moments (spin and orbital) and their ratio as a function of variation in temperature and magnetic field in different magnetic materials. Such as rare earth garnets, neodymium-based soft and hard magnets, cerium-based magnets. XMCD techniques that allow the quantitative estimation of the orbital and spin magnetic moment from the XMCD sum rule analysis. Hence this study will pave a route for understanding the fundamental properties of rare earth elements especially in case of neodymium.

2.2. Ferromagnetism and x-ray absorption spectra (XAS)

X-ray magnetic circular dichroism (XMCD) is a magneto-optical effect. The magneto-optical effect arises due to the influence of the magnetic properties of a system on its spectroscopic and optical properties[11]. The polarization vector of light rotates in reflection or transmission through the magnetic matter. The magneto-optical Kerr effect is commonly known as (MOKE) in conventional magnetization measurements with linearly polarized laser light. The basic principle of MOKE is the different absorption of left and right circularly polarized light. The Kerr signal is a direct measure of the magnetization of the magnetic specimen. In MOKE the optical transitions are always within the valence band region with very low energy electrons of few electron volts. The information obtained is influenced by both initial and final state densities. Similar magneto-optical effects have been also tried to discover in the x-ray regime. However, the lack of an appropriate x-ray source is the reason for unsuccessful attempts. In

1975, Erskine and Stern, by their calculations predicted the presence of a magneto-optical effect in x-ray absorption of circularly polarized light, i.e. XMCD, at the $M_{2,3}$ edges of ferromagnetic Nickle [12]. In 1987, Schütz and coworker with the availability of synchrotron radiation sources provided x-rays with tunable energy and polarization. Thus, finally successfully performed XMCD measurements in hard x-ray regime at the iron *K* edge[13]. The transitions occur via some selection rules in well-defined initial and final states. Thus, methods based on x-ray absorption of XMCD provides shell-selective magnetic information. Therefore, XMCD has proven very useful for the understanding of complex magnetic structures, where it is possible to probe contribution of constituents on an individual level.

2.2.1. Magnetic moment of a single ion

The fundamental entity in magnetism is a magnetic moment. In classical electrodynamics we consider it as a current loop carrying current "*I*" around an elementary loop of area "*ds*", so the magnetic moment is given by following equation

$$d\mu = I\, ds \text{……..equation (2.1)}$$

Here, the magnetic moment (μ) has unit Am^2 [14].The source of the magnetic moment of an atom is due to the spin and orbital motion of the valence electrons.

According to the Bohr model, Bohr magneton (μ_B) is the elementary magnetic moment and is defined as the magnetic moment of the electron, performing circular orbit around the nucleus of the atom with the orbital angular momentum of $|l| = h/2\pi$ or $\hbar$. An electron with the ħ orbital angular momentum produces the magnetic moment which is given by [14]

$$\mu_B = \frac{e}{2 \times m_e} \times \hbar = 9.274078.10^{-24}\,Am^2 \text{.....equation (2.2)}$$

Where *e*=charge of the electron, $\hbar$=plank's constant and m_e=mass of the electron. The magnitude of the orbital angular momentum is given by the orbital angular quantum number *l* and orbital magnetic moment(μ_l) is defined as[15]

$$\mu_l = \sqrt{l(l+1)}\,\mu_B \text{.....equation (2.3)}$$

The orbital magnetic moment vector is defined as [15]

$$\boldsymbol{\mu_l} = -g_l \mu_B \frac{\boldsymbol{l}}{\hbar} \text{.....equation (2.4)}$$

The electron also possesses spin and it is associated with the spin angular momentum. The magnitude of the spin angular momentum is given by the spin quantum number "s". The spin angular momentum μ_s is defined as [15]

$$\mu_s = \sqrt{s(s+1)}\mu_B \text{.....equation (2.5)}$$

The spin magnetic moment vector $\boldsymbol{\mu_s}$ is defined as [15]

$$\boldsymbol{\mu_s} = -g_s\mu_B \frac{\boldsymbol{s}}{\hbar} \text{.....equation (2.6)}$$

Equation (5) and (6) defines the g factor. It was introduced by Landé in order to characterize the ratio of the magnetic moment (in μ_B) and the total angular momentum (in a unit of $\hbar$).It is the dimensionless quantity and the numerical value of a spin (g_s)=2.0023 and orbital (g_l)=1[15]. There is a magnetic interaction present between the orbital and spin angular momentum of the electrons defined as spin-orbit coupling (SOC). This interaction depends on whether two moments are coupled parallel or antiparallel to each other's[15]. In one electron systems, the individual angular momentum *l* and *s* combine to lead the total angular momentum *j*. In case of multi-electron systems, similar coupling takes place between the angular momentum of the different electrons in the same atom.

The total angular momentum of the filled shells is equal to zero, therefore the electron with the unfilled shells are considered. These angular momenta are coupled by the electric and magnetic interaction between the electrons in the atom[15].The coupling mechanism can be described by two different ways- *LS* coupling(Russell-Saunders coupling) and *JJ* coupling[15]. In case of heavy atoms like rare earth elements where the spin and orbital coupling is strong, the coupling mechanism described by the *JJ* coupling.

2.2.2. Exchange interaction

In all the ferromagnetic materials the magnetic moment lies along a single direction on application of magnetic field but even on the removal of the magnetic field still, some magnetism is present. There exist different types of magnetic interaction which can be important in allowing the magnetic moments in a solid to communicate with each other and potentially to produce long-range order. Therefore, the ordering of the ferromagnetic materials is explained by the quantum mechanical concept. It is based on the Pauli Exclusion Principle and the Coulomb repulsion. Exchange interactions are nothing more than electrostatic interactions, arising because charges of the same sign cost energy, when they are close together and save energy when they are apart [14].

Consider a simple model in which just two electrons are at positions $\boldsymbol{r_1}$ and $\boldsymbol{r_2}$, represents by the wave functions ψ_a $(\mathbf{r_1})$ and ψ_b $(\mathbf{r_2})$ respectively. The total wave function should be antisymmetric and should be unchanged under particle exchange. The total wave function contains the spatial and spin part. For electrons, the overall wavefunction must be antisymmetric so the spin part of the wave function must either be an antisymmetric singlet state χs (S=0) in the case of asymmetric spatial state or asymmetric triplet state χ_T (S = 1) in the case of an antisymmetric spatial state. Therefore, we can write the wave function for the singlet case χs and the triplet case χ_T as[14].

$$\psi_s = \frac{1}{\sqrt{2}}\left(\psi b(r_1)\psi a(r_2) + \psi a(r_1)\psi b(r_2)\right)\chi_s \text{.....equation(2.7)}$$

$$\psi_T = \frac{1}{\sqrt{2}}\left(\psi b(r_1)\psi a(r_2) - \psi a(r_1)\psi b(r_2)\right)\chi_T \text{.....equation(2.8)}$$

The Coulomb repulsion is reduced in the triplet state. The electron-electron interaction is minimized which results in parallel orientation of the electron and causes a non-vanishing spin. The resulting orientation dependent energy is defined by the effective operator knows as Heisenberg Hamiltonian[14]

$$\mathrm{H} = \sum_{i,j} J_{ij} \cdot S_i \cdot S_j \text{.....equation(2.9)}$$

Where $\mathbf{J_{ij}}$ is exchanged constant between the i^{th} and j^{th} spin. The sign of the J determines the relative orientation of the spin[14]

1. If J>0 than triplet state (**S**=1 and antisymmetric state) is favored. The orientation of the spin will be parallel and system will have the ferromagnetic contribution.
2. If J<0 than singlet state (**S**=0 and symmetric state) is favored. The orientation of the spin will be antiparallel and system will have the antiferromagnetic contribution.

Inside a solid the ordering of spin via exchange interaction has 3 possible ways:

1. Direct exchange: The interaction proceeds directly, without an intermediate. In general, the direct exchange cannot be an important mechanism in controlling the magnetic properties because there is insufficient direct overlap between neighboring magnetic orbitals[14].
2. Indirect exchange interaction:

In metals, the exchange interaction between magnetic ions can be mediated by the conduction electrons. A localized magnetic moment spin-polarizes the conduction electrons and this polarization in turn couples to a neighboring localized magnetic moment a distance away. The exchange interaction is thus indirect because it does not involve direct coupling between magnetic moments. It is known as the RKKY interaction (or also as itinerant exchange). The name RKKY is used because of the initial letters of the surnames of the discoverers of the effect, Ruderman, Kittel, Kasuya, and Yosida[14].

3. Superexchange interaction:

Inside some ionic solids, including some oxides and fluorides, have magnetic ground states. For example, MnO and MnF_2 are both anti-ferromagnets, It is rather surprising because there is no direct overlap between the electrons on Mn^{2+} ions in each system. The exchange interaction is normally very short-ranged so that the long-ranged interaction that is operating in this case in some sense 'super'. Therefore, the exchange mechanism which is operative here is in fact known as superexchange. It can be defined as an indirect exchange interaction between non-neighboring magnetic ions which is mediated by a non-magnetic ion which is placed in between the magnetic ions[14].

In rare earth metals, this conduction electron or RKKY interaction is responsible for the ferromagnetic ordering. In other ferromagnetic metals such as Fe, Ni, and Co also have conduction electrons which are responsible for the ferromagnetism.

2.2.3. Interaction of x-rays with the matter: X-ray absorption spectra (XAS)

Consider a thin film sheet of thickness *dz* and a beam of electromagnetic radiation (x-ray) intensity I_0 transverse through the thin film at a depth z from the surface than the x-ray absorption intensity is attenuated upon transmission through a sample with linear absorption coefficient μ_x, according to [16]

$$I(z) = I_0 e^{-\mu_x(E)z} \quad \text{.....equation(2.10)}$$

When x-ray incident on any matter, like any other electromagnetic radiation they attenuated. The reason of attenuation is that, either they get absorbed or scattered through the matter. In soft x-ray regime the absorption related phenomenon is dominating over scattering processes or other processes like Compton scattering and inelastic scattering the absorption coefficient μ(E) will be in good approximation equal to the attenuation coefficient [16].

Due to absorption process x-rays of intensity I=c ε_0 | E^2|, incident on the matter, up to certain length decays exponentially. Each substance has a characteristics length λ_x which leads to an intensity attenuation by a factor of 1/e. The quantity $\mu_x = 1/\lambda_x$ with the dimension of length^{-1} is called *Linear X-ray absorption coefficient.* The absorption coefficient is related to the absorption cross section $\sigma(E) = \mu(E)/n$ via "n" the density of atoms [16]. X-ray interacts with the charged particle such as electrons, the electric field of EM wave makes them oscillate. The electronic transitions are driven by the electric field of EM wave. The time-dependent field induces a transition between initial and final state and at the certain energy sharp rise in absorption is observed. The sharp rise is called *absorption edge*. The energy of absorption edges is determined by the binding energy of a core level. The edge identifies the transition from the ground state to the lost empty state. For example *M* edge related to 3*d, L* edge is 2*p* and *K* is to 1*s* [17].

2.2.4. Dipole selection rules

When a photon in the X-ray regime with energy E = $\hbar\omega$ is absorbed, an electron in a core-shell of energy Ei is excited from its initial state $|i_i>$ to a final state $<f_i|$ with energy $E_f = E_i + E$ and density of the final states ρ (E_f). The absorption cross-section is given by the transition probability T_{if} and the photon flux I_{ph}, The *Fermi golden rule* gives the transition probability per unit time T_{if} , which is stated by equation written below[16]

$$T_{if} = 2\pi/\hbar \left| < \varnothing_f \left| H_{int} \right| \varnothing_i > \right|^2 \delta_{Ef\text{-}Ei\text{-}\hbar\omega} \text{.....equation(2.11)}$$

Where $\mathbf{H_{in}}$ is the interaction operator and the delta function takes care of energy conservation. The squared matrix element gives the transition rate. The transition operator or interaction Hamiltonian describe the one-photon transition such as x-ray absorption. Here, interaction operator reflecting a time-dependent perturbation of the Hamiltonian $\mathbf{H_0}$ of the atom. The Hamiltonian of an electron with charge "e" and mass "m" in an electromagnetic field described by the vector potential **A** (**r**, t) and the scalar potential $\varnothing$ (**r**, t).

$$\mathbf{H} = \mathbf{H_0} + \mathbf{H_{int}}$$

$$H = \frac{1}{2m}\left(\frac{\hbar}{i}\nabla - \frac{e}{c}\mathrm{A}(r,t)\right)2 + \varphi(r,t) \text{.....equation(2.12)}$$

$$H = H_0 - \frac{e}{2mc}\mathrm{A}(r,t).\frac{\hbar}{i}\nabla + \frac{e^2}{2mc^2}.\mathrm{A}(r,t) \text{.....equation(2.13)}$$

Within the Coulomb gauge ($\nabla \cdot \mathbf{A} = 0$). Expressing the vector potential of the incoming photons by plane waves with amplitude A_0, wave vector **k**, frequency ω, and polarization vector ε, the interaction operator H_{int} becomes[16]

$$H_{\text{int}} = -\frac{e}{2imc} A_0 \varepsilon e^{-i(k.r-\omega t)} * \nabla \text{.....equation(2.14)}$$

The EM wave electric field has exponential dependence. Therefore, using Taylor expansion we get

$$A_0 \varepsilon e i(k.r - \omega t) = A_0 \varepsilon e^{-i\omega t}\left(1 - ik.r - \frac{1}{2}(ik.r)^2 \ldots\right) \text{.....equation(2.15)}$$

In the dipole approximation, the expansion is truncated after the first term. This corresponds to the electric dipole (E1) transitions. The dipole approximation assumes that the size of absorbing atomic shell is small relative to x-ray wavelength <<<I/k. Therefore, the electric field that drives the electronic transition is constant over atomic volume[16]. Considering $(\mathbf{k.r})^n$ means considering higher order transitions. The transition probability is equal to matrix element square, Hence the electric quadrupole transitions are smaller by a factor of 2×10^{-3}, can be neglected. We are interested in Photon energy range ≤1000 eV corresponding wavelength > 1.2 nm and transition from 2p core shell of radius 0.01nm <<1/k-0.2nm. Hence, it is reasonable to use dipole approximation [16]. So the Fermi golden rule can be written as[16]

$$T_{if} = 2\pi / \hbar \left| < \varnothing_f \left| \varepsilon.r \right| \varnothing_i > \right|^2 \delta_{Ef-Ei-\hbar\omega}, \text{.....equation(2.16)}$$

Fermi golden rule is a very general expression and uses the initial and final wave functions. These wave functions are generally not known but in practice, one must make approximations to calculate the x-ray absorption cross-sections. The most often used assumption for XAS is single electron approximation. Here, we assume that the other electrons do not participate in the x-ray induced transition process [16].

The matrix element can be written as M and the delta function implies the density of empty states "ρ". So the X-ray absorption resonance intensity in dipole approximation is given by [17]

$$I_{\text{XAS}} = M^2 \rho \text{……..equation (2.17)}$$

The x-ray absorption rule determines that dipole matrix elements M is nonzero if L of final state differs by 1 from the initial state (ΔL=±1, s→p, p→s or d) and spin are conserved (ΔS=0). The quadrupole transition implies final states differ by 2(or 0) from the initial state (ΔL=±2, s→d,

p→f or p→p). It is observed that the quadrupole transitions are hundred times weaker than the dipole transitions so can be neglected in most of the cases[17].

(i) for electric dipole (E1) transitions

$$\Delta j = 0, \pm 1,\ \Delta s = 0,\ \Delta l = \pm 1,\ \Delta m = \begin{cases} +1 \text{ left circular polarized} \\ 0 \text{ linear polarized} \\ -1 \text{ Right cirular polarized} \end{cases} \quad \text{.....equation(2.18 a)}$$

(ii) for electric quadrupole (E2) transitions

$$\Delta j = 0, \pm 1, \pm 2,\ \Delta s = 0,\ \Delta l = 0, \pm 2,\ \ \Delta m = 0, \pm 1, \pm 2 \text{.....equation (2.18 b)}$$

However, if $l(|i\rangle) = 0$ then $l(\langle f|) = 0$ is not allowed for E_2 transitions.

In principle, the absorption coefficient will be characterized by the transition matrix element and the initial core states have an atomic character with well-defined quantum numbers. The strong localization of the core-shell makes the absorption spectroscopy element specific and sensitive to the valance shell properties within the atomic volume[16].

2.2.5. X-ray magnetic circular dichroism (XMCD): principle

The x-ray absorption spectrum sometimes depends on the polarization of the light. A phenomenon in which inside a magnetized specimen different absorption takes place in the left and right circularly polarized light. This difference in absorption is known as “XMCD effect”. XMCD is a direct consequence of the dependence of the absorption cross section on the magnetic state.

The absorption coefficients of the specimen have magnetization **M** is measured when the sample is irradiated with the left and right circularly polarized light. The absorption coefficient of the sample has been measured at parallel and antiparallel to the orientation of the magnetization **M** direction and the polarization **P**. The relation is given as [11, 16]

$$\Delta\mu(E) = \mu^{+}(E) - \mu^{-}(E) = P.M \approx |P||M|.cos(P,M) \text{.....equation (2.19)}$$

The element and orbital selectivity in XMCD are due to the dipole selection rules in the x-ray absorption process. Figure 2.1 shows the one-electron picture and the conservation of the angular momentum during the electron excitation process from the core to valence shell. From the core-shell with the non-zero orbital angular momentum, when an electron is excited during the absorption process then the core hole which is created is subject to spin-orbit coupling. Due

to this the preference in orbital polarization which is induced by the circularly polarized light also induces the preferential alignment of the spin moment. This effect is presented in Figure 2.1 for the cerium $M_{4,5}$ edge. In the lower part, the spin-orbit states are written in form of basis $|l,m_l\rangle\langle s,m_s|$ with their respective Clebsh-Gordon coefficients. In the upper part, the 4*f* levels are presented by the 14 possible combinations. The relevant conclusion regarding the orbital and spin polarization can be drawn from the sum over all the possible transitions. The lines that are connected to 3*d* to 4*f* states in Figure 2.1, represents the transitions allowed by the dipole selections rules for the left circularly polarized light. The transition probabilities also can be calculated by the Wigner's 3*J* symbols[19] presented in the lower part of Figure 2.1.

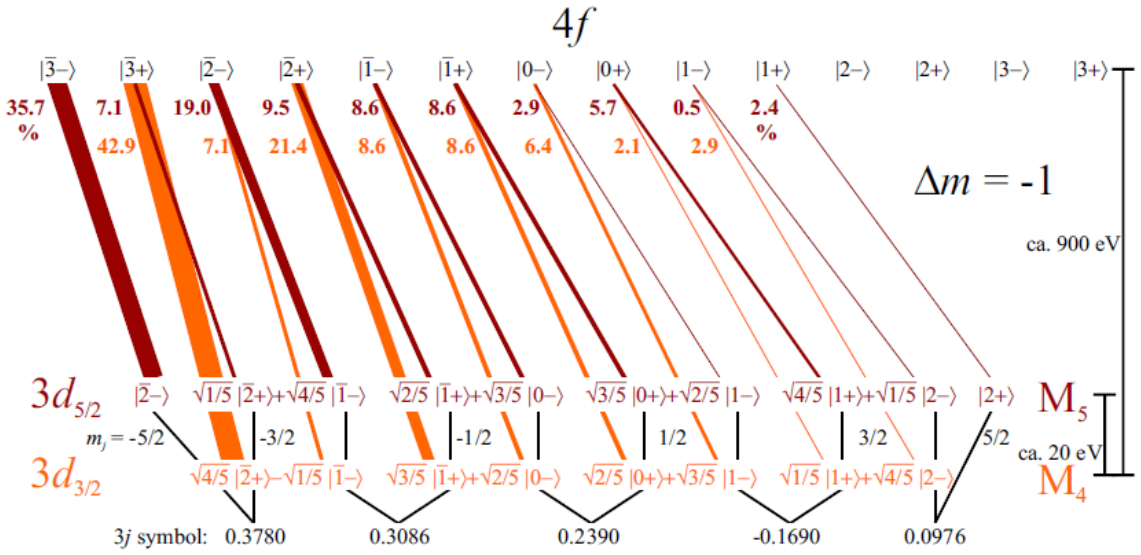

Figure 2.1 one-electron transition probabilities from the spin-orbit split 3*d* core shell to the 4*f* valence shell (Ce $M_{4,5}$ edges) in a $|l,m_l\rangle\langle s,m_s|$ basis for left circularly polarized light ($m_l = -1$). The states are given in a shortened notation (m_l, m_s). For $ms = \pm 1/2$ only the sign is given and m_l denotes a negative value. The transition probabilities for each edge are given in percent and are also reflected by the width of the lines connecting the states. Furthermore, the numeric values of the 3*j* symbols that are needed for the calculation of the transition strengths are given in the lower part. The picture for right circularly polarized light ($m_l = +1$) can be constructed by reversing the signs of all *m* quantum numbers. The figure is reproduced from the reference [18]

The schematic representation of the XMCD measurements is presented in Figure 2.2. With this principle, the quantitative estimation of the quantities which are interesting are the expectation values for the *z* component of the orbital ($\langle L_z \rangle$) and the spin magnetic momentum ($\langle S_z \rangle$) operators respectively. In addition, the qualitative understanding of the mechanism behind the XMCD effect, the considerations have been developed in order to connect the integrated

XMCD and XAS signal to the expectation values of the orbital $<L_z>$ and spin $<S_z>$ moment and can be done by the XMCD sum rule analysis proposed by the Thole and Carra [20, 21] for the 4*f* electrons. The sum rule analysis will be discussed in detail in chapter 3.

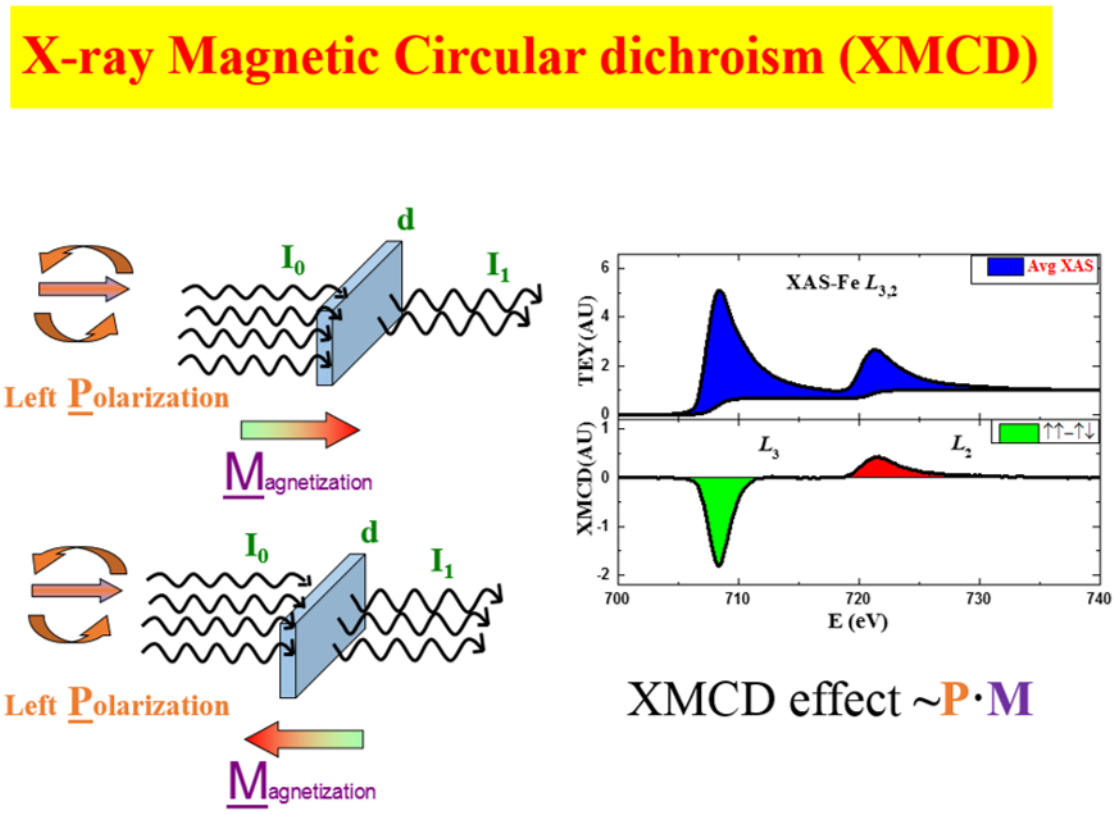

Figure 2.2 basic principle of the XMCD effect. The absorption coefficient is different for the parallel and antiparallel orientation of **P** and **M**, The figure is reproduced from reference[22].

2.2.6. Detection method

XMCD is essentially a measurement of relative absorption coefficients. There are various possibilities to measure the X-ray absorption coefficients. Depending on the measuring conditions and especially the samples themselves. All of the methods used for conventional XAS in principle can be applied as shown in Figure 2.2. Experimentally, the three most important modes are the transmission, fluorescence, and electron yield[23] (Refer figure 2.3).

I Transmission mode (TMY):

A direct measurement of the absorption cross-section is through the detection of the photon flux before and after the sample. Such kinds of transmission experiments are probably the most

reliable but they are rarely possible especially in the soft x-ray regime due to the strong absorption. Hardly, any sample is transparent to a sufficient extent in the x-ray regime. A major advantage of such transmission experiments is that they are not sensitive to the surface only, but probe the entire sample. The beam intensity before the sample (I_0) is often measured using the electron yield or photocurrent from a partially transmitting metal grid. The intensity of the sample (I) can be measured using a second grid, a solid metal plate, or a Si photodiode[23]. Chen and coworkers have done careful transmission measurements of the XMCD of thin metal foils to check the accuracy of the sum rules[24].

II Total electron yield mode (TEY)

In a quantitative analysis of the total electron yield (TEY), it has been shown that the TEY will be proportional to the absorption coefficient if the absorption length of the incoming photons is much larger than the average escape depth of the photoelectrons. This proportionality has been tested and confirmed in various examples. When measuring at grazing incidence, saturation effects have to be taken into account in the analysis of the spectra[23]. The probing depth of secondary electrons is around 20Å, which makes the detection via TEY surface sensitive. One possibility to record TEY is by using a channel. Another possibility is to record the sample drain current with the help of an electrometer in the range of picoampere. This method is chosen in the experimental setup for measurements at WERA beamline (ANKA, Synchrotron radiation source, Karlsruhe Institute of Technology, Germany).In this situation, the sample must be highly electrically insulated which requests low-level DC measurements. For measurements in applied magnetic fields, the proper escape of the secondary electrons may be guaranteed by an extraction grid close to the sample[23]. Thus, it is possible to measure element-specific hysteresis loops by TEY detection [25].

III Fluorescence mode

In most of the experiments, secondary effects are exploited to determine the absorption coefficient. The excited states decay via x-ray fluorescence and the Auger effect. In both cases, the probability of emission (X-ray or electron) will be directly proportional to the absorption probability under certain conditions. Thus, detecting the fluorescence photons or the Auger electrons yields the absorption coefficient. Besides TEY detection, fluorescence yield (FY) detection is another method of choice for the investigation of nontransparent samples. FY detection is used, for example, for absorption measurements at the ID12 beamline at the ESRF (European Synchrotron Radiation Facility). In comparison to Auger electrons, fluorescence

photons are not sensitive to an external magnetic field when they escape from a sample. Furthermore, fluorescence detection has the advantage that it is also applicable to insulating materials [23]. Due to the larger escape depth of the fluorescence photons, in general, the probing depth is much larger than in TEY. Thus, by FY bulk properties of the sample can be investigated. If dilute samples or thin films are investigated, the FY signal will be directly proportional to the absorption coefficient. For concentrated bulk samples, the FY signal can exhibit a strong nonlinearity. These self-absorption effects result from the attenuation of the penetrating and escaping X-ray radiation while propagating through the sample. It has been shown that these self-absorption effects in FY can fully be corrected. FY decreases with decreasing atomic number and Auger transitions are the dominant decay channel. Therefore, TEY detection is, in general, applied more commonly for absorption measurements of the lighter elements in the soft x-ray regime whereas FY is used for elements with a larger atomic number in the hard X-ray regime[23].

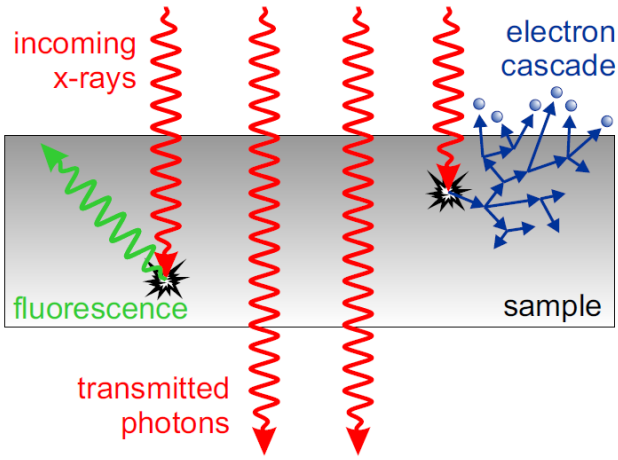

Figure 2.3 Schematic representation of the three detection modes for absorption coefficients μ_x(E) that are labeled i.e. transmission, electron and fluorescence yield. X-ray photons that penetrate a sample are either absorbed or transmitted. The reduced number of transmitted photons is a measure of the amount of absorption, as well as the numbers of photons and electrons that are created as a consequence of absorption events. The figure is reproduced from the reference [18].

2.3. Experimental aspects of XMCD measurements

In order to measure XMCD on the transition metal, $L_{2,3}$ edges or rare earth elements at $M_{4,5}$ edges with the soft x-rays, the energy range of 400 eV to 1400 eV is required. It is necessary that the energy of the x-ray is tunable and exhibit the high degree of the circular polarization. These requirements are only fulfilled by the modern synchrotron light sources. A synchrotron

is circular particle accelerator in a combination with the storage ring. The schematic layout is shown in Figure 2.4. A hot cathode produces electrons which are accelerated by the microtones to almost the speed of light and then injected into the synchrotron. Here are the electrons are again accelerated to their terminal energy, usually in the GeV range and from the synchrotron, the electrons are injected into the storage ring.

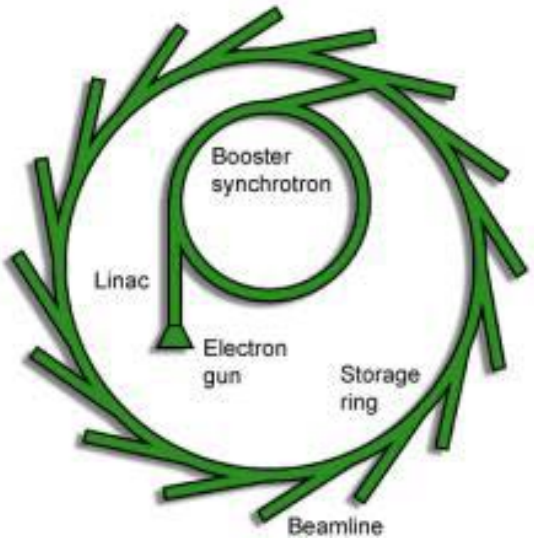

Figure 2.4 Schematic layout of the synchrotron light source. Figure reproduced from reference[26].

At a certain position, undulators, wigglers, and bending magnets are installed. Bending magnets are necessary to keep the electrons in a circular orbit in the storage ring. Accelerated electrons emit radiations and the bending magnet/undulator locations are the spots where the synchrotron radiation is produced. If an electron moves almost with the speed of light, nearly all the radiation is emitted along the trajectory of movement –tangential to its orbit in the storage ring. The bending magnet shown in the right Figure 2.5 is a dipole magnet bending the electrons orbit to the center of the storage ring. This lateral acceleration leads to the production of the synchrotron radiation. Wigglers and undulators (left Figure 2.5) are the opposite of the bending magnet, magnetic devices which were designed to produce the synchrotron radiation with much higher brightness. The difference between the wiggler and the undulators are generally given by its emitted radiation. The magnets used in wigglers are stronger than the bending magnets, deflecting the electrons from its original orbit.

The sensitive XAS and XMCD experiments, which is part of the present thesis work is performed at ANKA synchrotron radiation source in Karlsruhe Institute of Technology, Karlsruhe, Germany.

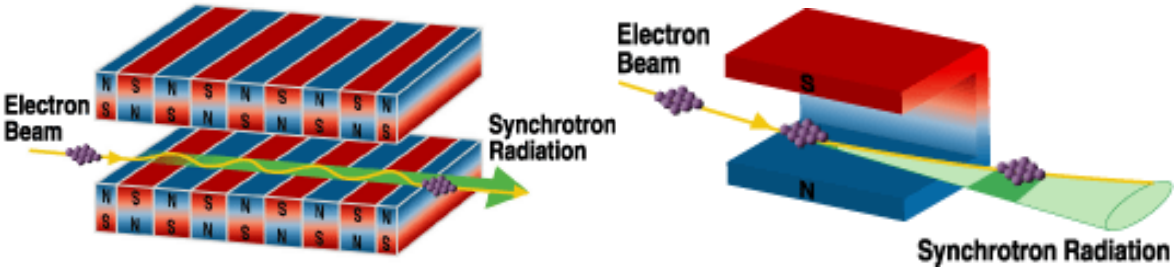

Figure 2.5 planar undulator (left) deflects the electrons from the original orbit and bending magnet (right) used to keep electrons in circular orbit in the storage ring. Figure reproduced from reference (spring 8 synchroton website).

2.3.1. WERA beamline

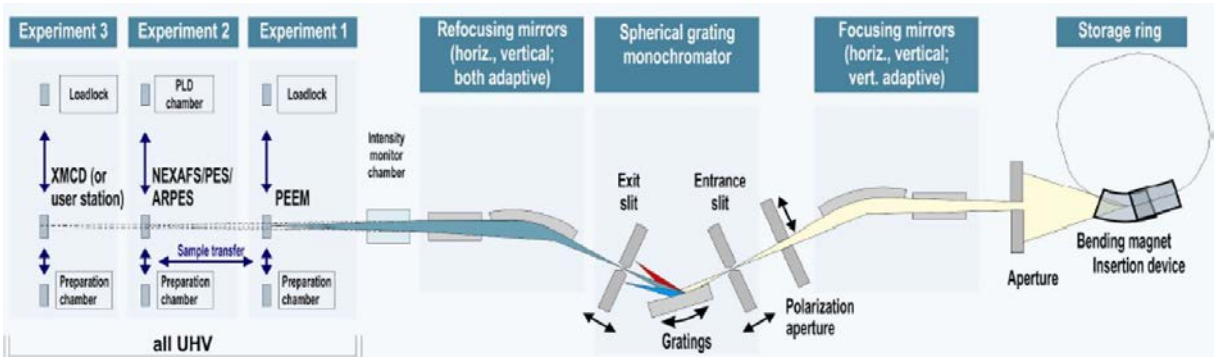

Figure 2.6 overview of the WERA beamline, with the experimental end-station at the left-hand side. Figure reproduced from reference[28]. The monochromators, the apertures, and the mirrors refine the beam before it reaches the end-stations. The XMCD end station in the end at the left-hand side is owned by the Max Planck Institute for the Intelligent systems, (MPI-IS), Stuttgart, Germany. The blue arrows stand for the UHV sample transfers- many combinations between the experiments and methods and also with sample preparation are possible without breaking the vacuum.

The synchrotron radiations obtained from the bending magnets or the insertion devices are still polychromatic. In order to extract the circularly polarized soft x-rays, the synchrotron beam has to pass a number of optical elements, the entitled “beamlines”. The schematic setup for the WERA beam line[27] inn ANKA presented in Figure 2.6. The most important components are the polarization aperture in order to set the polarization and monochromator grating to tune the beam energy. A typical bending magnet of the WERA beamline has a magnetic field of 1.5 T. The synchrotron radiations emitted from the bending magnets cover the energy range of

approximately 100 eV to 1400 eV. It is giving access to the transition metals $L_{2,3}$ edges, Oxygen *K*-edge and rare earth metals $M_{4,5}$ edges. This beamline is specially designed for the soft x-ray experiments of energy range 100eV to 1400 eV.

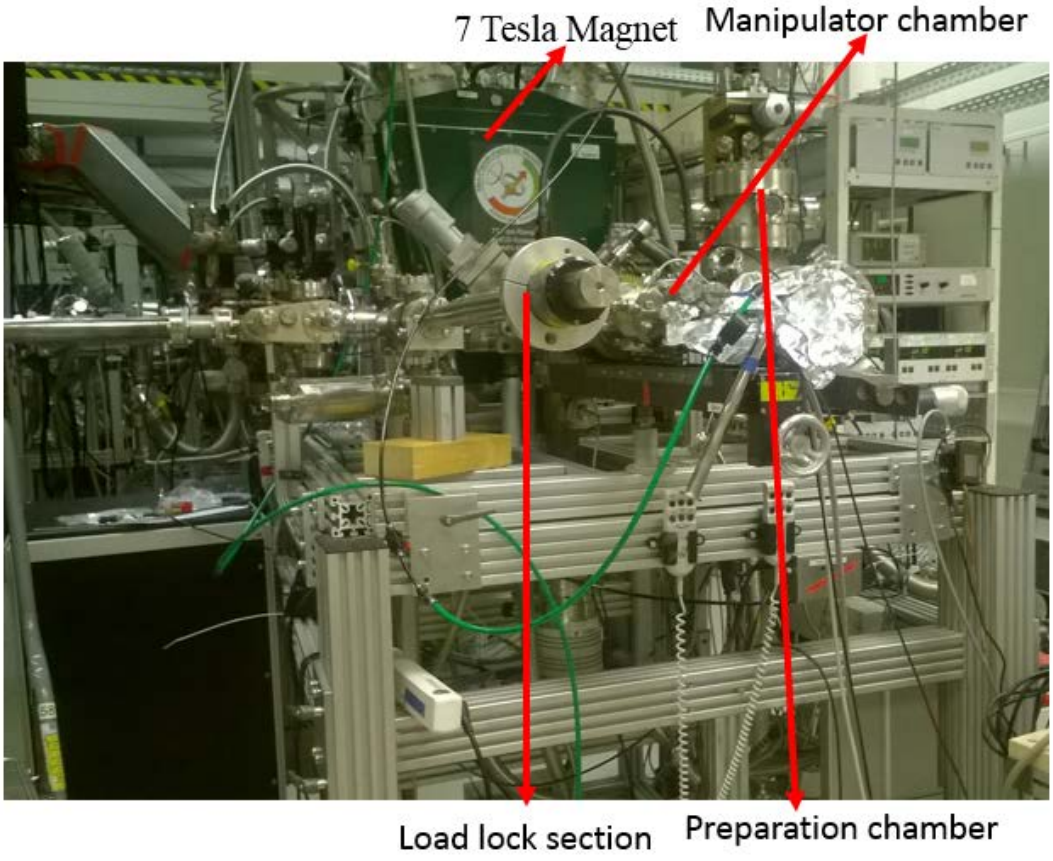

Figure 2.7 A 7 Tesla magnetic field fast switching XMCD set-up, designed and constructed in the Schütz department, Max Planck Institute for intelligent systems and the important sections are labeled.

The beamline is equipped with the different experimental arrangements [27].

I A photoemission electron microscope (PEEM) with the lateral resolution of the <100 nm.

II An electron energy analyzer in order to perform the photoemission spectroscopy (PES), angle-resolved photoemission (ARPES) and resonant photoemission (resPES). The energy resolution is <2 nm.

III The main chamber with the total electron yield (TEY) and total fluorescence yield (FY) measurements facility in order to perform near edge x-ray absorption spectra (NEXAS).

IV An XMCD end station equipped with a 7Tesla fast switching superconducting magnet system. This end station is provided by the Professor Gisela Schütz group from the Max Planck Institute for the intelligent systems.

The degree of polarization is typically 80-85% without significant beam intensity loss. A spherical grating monochromator with the three different gratings is used to obtain the monochromatic synchrotron light in the respective energy range. The typical energy resolution is $\Delta E/E=2\cdot10^{-4}$. Beamline and the experimental stations are kept under the ultra-high vacuum (UHV) conditions with a typical base pressure of the 10^{-10} mbar.

2.3.2. XMCD set up at WERA beamline

The XMCD measurements have been performed with our own self-designed ultra-high vacuum XMCD chamber (refer Figure 2.7). The system is equipped with the fast switching 7 Tesla magnet system. The measurements of all the specimens have been performed with this setup. The chamber consists of four different sections.

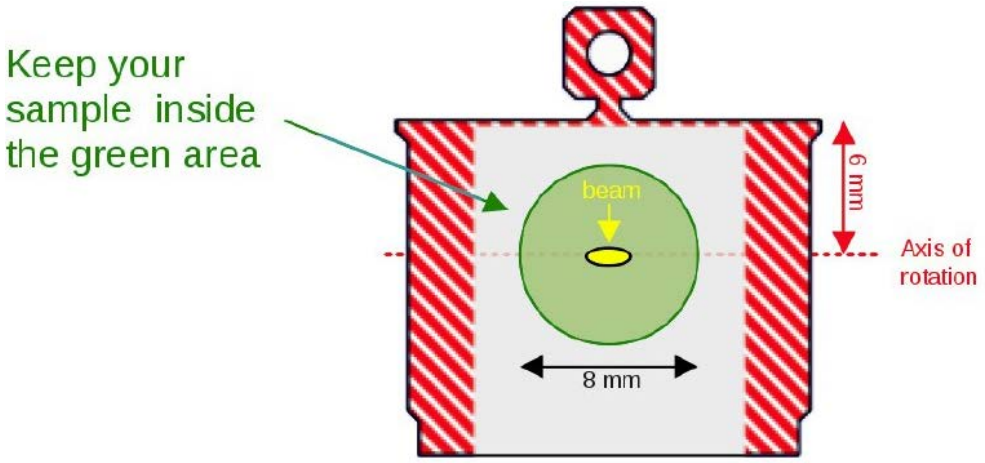

Figure 2.8 sample plate example for the XMCD chamber. The areas where white and red strips are no go area and the sample should be mounted in the green region. The figure is reproduced from reference.

I **I_0 section**- This section comes along with the gold mesh in order to probe the incoming beam intensity and a mirror prism for the sample or beam adjustment. The pressure of this section is usually $3\cdot10^{-10}$ mbar.

II **Fast load lock section**- this system provides the ultra-high vacuum sample transfer system with sample six stands. The sample can be quickly transferred from the transfer chamber

to the manipulator and the preparation chamber. The sample transfer and removal does not take more than 30-45 minutes. All the steps can be performed without disturbing the vacuum.

III **Manipulator section**-In this section sample is mounted for the measurements. The manipulator contains a cryostat for the liquid helium (10K) and nitrogen (80K) cooling also. It has also sample heater to perform the measurements above the room temperature (up to 350 K). It is equipped with the three measurement modes – total electron yield (TEY), total transmission yield (TMY) and total fluorescence yield (TFY). The samples can be rotated at azimuthal (0-360^{o}) and polar angles (0-90^{o}). The base pressure of this section is usually $3\cdot10^{-10}$ mbar.

IV **Preparation section**- The *in-situ* sample preparation can be performed in this section. The base pressure of this section is usually $1\cdot10^{-10}$ mbar.

Sample preparation for measurements- In general for measurements at the WERA beamline, the sample is mounted on a sample holder or plate (size-15·15 mm^2 refer Figure 2.8) of a nonmagnetic material (stainless steel, molybdenum, and tantalum) using a vacuum safe glue (for sintered magnet or bulk specimen) or silver paste (for thin films). The sample should be mounted in the green region shown in Figure 2.8.

2.3.3. XMCD data acquisition and evaluation

The basic principle of the XMCD measurements already discussed in the previous sections. The XMCD effect depends on the relative orientation of the polarization of the incoming beam and the magnetization. The measurement procedure has been optimized to the technical situation at the synchrotron. Instead of switching the helicity, one usually reverse the magnetic field. The main advantage of this way of measurement is that the energy shift due to switching helicity can be avoided. This energy shift can include a first derivative structure in their XMCD spectrum, which can be misinterpreted as XMCD effect. Another reason is that due to fast switching 7 Tesla magnet allows us a fast reversal of the magnetic field. The XMCD data acquisition and analysis can be performed in the following ways.

I **Fast continuous mode**- An important issue for the data acquisition is to find an appropriate compromise between maximum speed and the loss of resolution of the fine structure of the absorption spectra. For measuring TEY and I_0 current commercial Keithley 6517A multi-meters with a time constant of about 1 second was used. Above a certain monochromator speed,

only discharge of input capacitance is measured and spectral structure cannot be resolved anymore. Therefore, the monochromator speed has been optimized with the NiO reference system, measuring the respective transition metal $L_{2,3}$ edge. Another important factor is the integrated intensity of the spectra because it is used to determine the magnetic spin and orbital moment, as described previously in section 2.5. For higher monochromator speed, the integrated XAS value can drops within in the peak energy range. Therefore, the calibration for the WERA beamline was performed measuring the Ni L_3 edge of NiO single crystal at different monochromator speeds 0.1eV/s to 2eV/s.

II **Offset correction for XMCD spectra measured with TEY**- A major problem occurs when acquiring the XMCD spectra in the TEY mode the "offset". In particular, offset is reflected as a constant shift of the XMCD on the y-axis. Usually, the XMCD effects disappear due to this offset in the off-edge regions. The origin of the offset signal is a different trajectory of electrons in a magnetic field pointing in the +B and –B magnetic field directions. The photoelectrons move on spiral orbit and some of them may be refracted back to the sample surface reducing the TEY current. The electron orbit is not necessarily same for the opposite applied a magnetic field, this the TEY signal becomes not only energy dependent but also field dependent. As demonstrated in the results of this thesis, magnetic field of 6.5 Tesla is applied. Several spectra exhibit the offset. The offset correction is shown in Figure 2.9 (a). The XMCD signal is shifted downwards slightly on the y-axis. The offset correction is very crucial in order to apply the XMCD sum rule because the spectra need to be integrated. If the XMCD spectrum is shifted then it will introduce the additional slope in the integrated XMCD spectrum. Figure 2.9 (b) shows the comparison of two integrated XMCD signals[29].

The offset corrections cannot performed by just subtracting the shift in the y-direction. This will lead false XMCD signal and will provide an incorrect magnetic moment for the sum rule analysis. A proper correction of the XMCD signal has to be performed in the following ways. The measured XMCD signal is given by in form of intensity of the spectra as follow-

$$I_{XMCD}(E, \mathbf{B}) = I_{\uparrow\uparrow}(E)\cdot k_{\uparrow\uparrow}(\mathbf{B}) - I_{\uparrow\downarrow}(E)\, k_{\uparrow\downarrow}(\mathbf{B}) \quad \text{.....equation (2.20)}$$

Where, $I_{\uparrow\uparrow}$ and $I_{\uparrow\downarrow}$ are the I_0 normalized TEY current for parallel and antiparallel alignment of magnetization and polarization respectively. The $k_{\uparrow\uparrow}(\mathbf{B})$ and $k_{\uparrow\downarrow}(\mathbf{B})$ are the constants depending on the applied magnetic field. They display the proportionality of the TEY signal and the absorption signal.

On the other hand, the absorption spectrum is given by the

$$I_{XAS}(E) = \frac{I_{\uparrow\uparrow}(E) + I_{\uparrow\downarrow}(E)}{2} \text{.....equation (2.21)}$$

The true XMCD signal is -

$$XMCD = I_{\uparrow\uparrow}(E) - I_{\uparrow\downarrow}(E) \text{.....equation (2.22)}$$

Using equation (20) and (21), one can isolate the $I_{\uparrow\uparrow}$ (E) and $I_{\uparrow\downarrow}$(E).

$$I_{\uparrow\uparrow}(E) = I_{XAS}(E) + \frac{XMCD}{2} \text{.....equation (2.23)}$$

$$I_{\uparrow\downarrow}(E) = I_{XAS}(E) - \frac{XMCD}{2} \text{.....equation (2.24)}$$

Substituting the $I_{\uparrow\uparrow}$(E) and $I_{\uparrow\downarrow}$(E) in equation (19), the expression will be

$$I_{XMCD}(E, \mathbf{B}) = I_{XAS}(E) \cdot (k_{\uparrow\uparrow}(\mathbf{B}) - k_{\uparrow\downarrow}(\mathbf{B})) + XMCD \cdot \left(\frac{k_{\uparrow\uparrow}(\mathbf{B}) + k_{\uparrow\downarrow}(\mathbf{B})}{2} \right) \text{.....equation (2.25)}$$

If the field dependent constants $k_{\uparrow\uparrow}$ (**B**) and $k_{\uparrow\downarrow}$ (**B**) are equal then there will be no offset observed in the measured XMCD signal. If they are different then the fraction of I_{XAS} will be added to the measurements. The correction of the XMCD signal is given by following equation

$$XMCD = I_{XMCD}(E) + c \cdot I_{XAS}(E) \text{.....equation (2.26)}$$

The parameter c is chose in such way that the XMCD signal disappears the off-edge. The corresponding absorption I_{XAS} (E) signal must be I_0 normalized only. If the signal is very noisy then for the accuracy it can be corrected via the XMCD integrated signal.

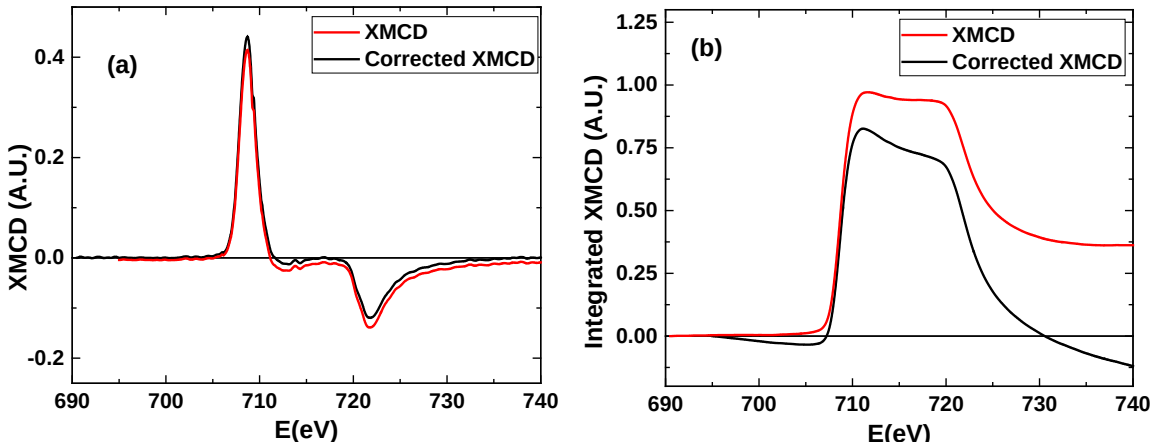

Figure 2.9 (a) Comparison of an XMCD spectrum with offset and after offset correction. (b) Comparison of the integral of XMCD spectra before correction (red) with the integral of offset corrected (black).

There are not only influence from the offset that is present in the experimental spectra but due to the incident beam influence background is also present in the spectra at the pre-edge and the post-edge region. The background subtraction and the complete analysis of the spectra with sum rule analysis will be discussed in detail in chapter 3.

2.4. Theoretical aspects of XMCD measurements

Atomic multiplet theory: Atomic multiplet theory is the description of the atomic structure of the quantum mechanics. The basic starting point for a large part of the analysis of core-level spectra is atomic multiplet theory [30, 31]. Atomic multiplet theory describes the correlated electronic states in partially-filled atomic shells. It is the general theory in use for the calculation of core excitation spectra of atoms. The problem is to find the best way to treat the x-ray absorption process with the combination of extended valence states in the following section, some aspects of atomic multiplet theory that are important for the analysis of x-ray absorption spectra are briefly introduced. A successful analysis method has been developed based on a ligand-field multiplet model. It offers large sensitivity to the valence and the symmetry of the element studied [32].

The atomic Hamiltonian is given by the Schrödinger equation for an N-electron atom. The Schrödinger equation consists of the kinetic energy of the N electrons ($P^2/2m$) the electrostatic interaction of the N electrons with the nucleus of charge $+Z$ ($\sum_N -Ze^2/r_i$), the electron−electron

repulsion ($H_{ee} = \sum_{pairs} e^2/r_{ij}$), and the spin−orbit coupling of each electron ($H_{ls} = \sum_N \zeta(r_i)\, l_i \cdot s_i$). The overall Hamiltonian is

$$H = \sum_N \frac{P_i^2}{2m} + \sum_N \frac{-Ze^2}{r_i} + \sum_{pairs} \frac{-e^2}{r_{ij}} + \sum_N \zeta(r_i) l_i . s_i \quad \text{.....equation(2.27)}$$

The kinetic energy and the interaction with the nucleus are the same for all electrons in a certain atomic configuration, for example, $3d^5$ in the case of Mn^{II}. They define the average energy of a certain state (H_{av}). This leaves the electron−electron repulsion and the spin−orbit coupling as the important interactions. The basic difficulty when solving the Schrödinger equation is that H_{ee} is too large to be treated as a perturbation. This problem has been solved with the *central field approximation*, in which the spherical average of the electron−electron interaction is separated from the non-spherical part.

The spherical average $<H_{ee}>$ is added to H_{av} to form the average energy of a configuration. In the modified electron−electron Hamiltonian the spherical average has been subtracted.

$$H_{ee}^{'} = H_{ee} - \left\langle H_{ee} \right\rangle = \sum_{pairs} \frac{-e^2}{r_{ij}} - \left(\sum_{pairs} \frac{-e^2}{r_{ij}} \right) \quad \text{.....equation(2.28)}$$

This leaves the two interactions H_{ee} and H_{ls} to determine the energies of the various electronic symmetry configurations within the atomic configuration[32].

2.4.1. Term symbols

Electronic symmetry configurations are indicated with their orbital moment *L*, spin moment *S*, and total moment *J*. Together, these three quantum numbers indicate a certain state and determine its specific energy. If the spin−orbit coupling is neglected, all configurations with the same *L* and *S* moments have the same energy. A specific configuration is indicated with a so-called term symbol $^{2S+1}L_J$. A term symbol gives all three quantum numbers and as such determines the symmetry and energy of a certain configuration. A single 1s electron has an orbital moment $L = 0$, a spin moment $S = 1/2$, and a total moment $J = 1/2$. This is written with a term symbol as $^2S_{1/2}$[32].

2.4.2. Calculation of matrix elements

The next task is to calculate the matrix elements of these states with the Hamiltonian H_{ATOM}. As discussed in the previous section, H_{ATOM} consists of the effective electron−electron interaction H'_{ee} and the spin−orbit coupling H_{ls}

$$H_{\mathrm{atom}} = \sum_{N} \zeta(r_i) l_i . s_i + \left(\sum_{pairs} \frac{-e^2}{r_{ij}} \right) \text{.....equation(2.29)}$$

The electron−electron interaction commutes with L^2, S^2, L_z, and S_z, which implies that all off-diagonal elements are zero. A simple example is a 1*s*-2*s* configuration consisting of ^{1}S and ^{3}S term symbols. The respective energies can be shown as following:

$$\left\langle {}^1S \left| \frac{e^2}{r_{12}} \right| {}^1S \right\rangle = F^0(1s2s) + G^0(1s2s) \text{.....equation(2.30)}$$

$$\left\langle {}^3S \left| \frac{e^2}{r_{12}} \right| {}^3S \right\rangle = F^0(1s2s) - G^0(1s2s) \text{.....equation(2.31)}$$

F^0 and G^0 are the Slater−Condon parameters for, respectively, the direct Coulomb repulsion and the Coulomb exchange interaction. The main result can be stated as "The singlet and the triplet state are split by the exchange interaction". This energy difference is $2G^0$ (1*s*2*s*). An analogous result is found for a 1*s*2*p* state for which the singlet and triplet states are split by $2/3G^0$ (1*s*2*p*). The 2/3 prefactor is determined by the degeneracy of the 2*p* state. The general formulation of the matrix elements of two-electron wave functions can be written as

$$\left\langle {}^{2S+1}L_J \left| \frac{e^2}{r_{12}} \right| {}^{2S+1}L_J \right\rangle = \sum_k f_k F^k + \sum_k g_k G^k \text{.....equation(2.32)}$$

To obtain this result, the radial parts F^k and G^k have been separated using the Wigner-Eckardt theorem and Hamiltonian $1/r_{12}$ has been expanded in a series[30]. The angular parts f_k and g_k can be calculated using angular momentum coupling[32].

2.4.3. Calculation of spectra (XAS) with atomic multiplets

Firstly, I will start with the description to introduce the of closed-shell systems. The 2*p* X-ray absorption process excites a 2*p* core electron into the empty 3*d* shell, and the transition can be described as $2p^6 3d^0 \rightarrow 2p^5 3d^1$. The ground state has $^1S_0$ symmetry, and it is found that the term symbols of the final state are $^1P_1$, $^1D_2$, $^1F_3$, $^3P_{012}$, $^3D_{123}$, and $^3F_{234}$. The energies of the final

states are affected by the 2p3d Slater−Condon parameters, the 2*p* spin−orbit coupling, and the 3*d* spin−orbit coupling. The X-ray absorption transition matrix elements to be calculated as

$$I_{XAS} = \left\langle 3d^0 \left| p \right| 2p^5 3d^1 \right\rangle^2 \text{.....equation(2.33)}$$

The symmetry aspects are

$$I_{XAS} = \left\langle \left[{}^1S_0 \right] \left| \left[{}^1P_1 \right] \right| \left[{}^{1,3}PDF \right] \right\rangle^2 \text{.....equation(2.34)}$$

The symmetry of the dipole transition is given as $^1P_1$, according to the dipole selection rules, which state that $\Delta J = +1, 0, -1$. Within *LS* coupling, also $\Delta S = 0$ and $\Delta L = 1$. The dipole selection rule reduces the number of final states that can be reached from the ground state. The *J* value in the ground state is zero. In this case, the dipole selection rule proclaims that the *J* value in the final state must be 1; thus, only the three-term symbols $^1P_1$, $^3P_1$, and $^3D_1$ can obtain finite intensity. The problem of calculating the 2*p* absorption spectrum is reduced to solving the 3 × 3 energy matrix of the final states with $J = 1$. As discussed above, the atomic energy matrix consists of terms related to the two-electron Slater integrals and the 2*p* and 3*d* spin−orbit couplings.

Atomic multiplet theory is able to accurately describe the 3*d* and 4*d* x-ray absorption spectra of the rare earth metals[33]. In the case of the 3*d* metal ions, atomic multiplet theory cannot simulate the x-ray absorption spectra accurately because the effects of the neighbors on the 3*d* states are too large. It turns out that it is necessary to include both the symmetry effects and the configuration-interaction effects of the neighbors explicitly. Ligand-field multiplet theory takes care of all symmetry effects, while charge-transfer multiplet theory allows the use of more than one configuration [34].

2.4.4. Calculation of x-ray magnetic dichroism spectra (XMCD)

X-ray magnetic circular dichroism (XMCD) is an important phenomenon in both x-ray absorption and x-ray emission. The magnetic structure of a system is studied by making use of circular or linear polarized x-rays. The magnetic circular dichroism (MCD) effect in x-ray absorption is defined as the difference in absorption between left- and right-polarized x-rays. A non-zero MCD effect is observed only in magnetic systems (the natural dichroism effects are neglected).

The MCD effect in x-ray absorption has been measured for the first time by Schütz and co-workers[13]. They showed that the absorption cross-section is different for left- and right-polarized x-rays. The difference between the left- and right-polarized x-rays was shown to be proportional to the spin-polarized density of states. Using the proportionality between x-ray absorption (I_{XAS}) and the density of state (ρ) as the starting point, one obtains:

$$I_{MCD} = \frac{I_{XAS}^{L} - I_{XAS}^{R}}{I_{XAS}^{L} + I_{XAS}^{R}} = P_e \frac{\rho_+ - \rho_-}{\rho_+ + \rho_-} \quad \text{.....equation(2.35)}$$

Where I^{L} denotes left- polarized x-rays and I^{R} denotes right-polarized x-rays. ρ_+ and ρ_- relate to, respectively, spin-up and spin-down density of states. The proportionality factor P_e is the Fano factor.

The original paper used the iron K edge as an example and did find a small effect, in other words, did find a Fano factor of approximately 0.01. It was later shown that this small MCD effect was particular to the use of a 1*s* core level and was related to the absence of a core hole spin−orbit coupling [34]. An important development in the use of XMCD was the development of sum rules by Thole and co-workers [20, 35]. It was shown that the integral of the XMCD signal could be related to the ground-state expectation value of the orbital moment $\langle L_Z \rangle$. A second sum rule was postulated relating the weighted integration of the L_3 edge plus the L_2 edge to an effective spin moment. Many papers deal with the validity, derivation, and experimental complications of the sum rules.

2.5. CTM4XAS-Software for simulations

In core-level spectroscopy of strongly correlated systems such as rare-earth systems and transition metal compounds, the single electron picture often breaks down, therefore single electron excitation is mainly divided into the charge transfer effect and intra-atomic multiplet coupling effects. These two important aspects of charge transfer and multiplet effects are generally taken into account for the software used for simulations of x-ray absorption spectra for the $M_{4,5}$ edges of the rare-earth and transition metal systems. The recognition that the x-ray absorption spectra of transition metal and rare earth systems were dominated by atomic effects was first made in the sixties for the $M_{4,5}$ edges and $N_{4,5}$ edges of the rare earth [36]. Within this background, Theo Thole developed his multiplet code and in 1985; he calculated all rare earth $M_{4,5}$ edge with atomic multiplet theory[37]. They have added the crystal field effects using the group theory from the Butler program and performed the simulations for the transition elements

L edges[38]. Later systematic studies of the transition metal *L* edges were performed with de Groot *et al* [39] and by van der Laan[40]. The combination of Theo Thole's crystal field multiplet calculations with charge transfer effects was programmed by Theo Thole and Ogasawara[41] in 1991 for mixed valence rare earth ions. Groot *et al*[42] use the charge transfer multiplet model as developed by Theo Thole and with contributions by Ogasawara as the basis for the CTM4XAS calculations [42] and developed CTM4XAS as a tool to simulate the *L* edges of transition metal systems. The latest version of CTM4XAS is 5.5 where it allowed us the simulation for rare earth elements $M_{4,5}$ edges also and it also provides the window for the crystal field calculations and charge transfer calculations.

The window of the CTM4XAS5.5 version software has been presented below in the Figure 2.10. The discription of the software is following:

- The top part of the screen, shown enlarged in the Figure 2.10, is used to generate the atomic parameters or to perform atomic multiplet calculations. On the top line, one has to provide the element that has to be calculated, including its oxidation state also. This defines the number of occupied *d* electrons in the ground state. It allows you to control the 2 electron integrals atomic parameters like slater integrals and spin-orbit coupling (SOC).

- The bottom panel in the Figure 2.10 shows symmetry-options for the crystal field calculations and the calculations can be performed for the cubic symmetry (C_4), tetragonal symmetry (D_{4h}) and octahedral symmetry (O_h). The advantage is that all the calculations can be performed in the C_4 symmetry, however, the choice of the higher symmetry limits the parameters choice. If all the crystal field parameters are zero then the symmetry is the spherical and negative value of 10*Dq* yield the tetrahedral symmetry. The values of 10Dq, Ds and Dt are given in eV.

- A molecular (exchange) field can also be included in meV to break the spin symmetry. Without the exchange field, XMCD spectrum cannot be generated. The exchange field direction is constrained to the z-axis.

- If one would like to perform more complex calculations this is possible with the range of charge transfer multiplet models that are also available in the middle right panel Figure 2.10. With the charge transfer tick mark, one activates the charge transfer parameters. This is the charge transfer parameter, which gives the energy difference between the (centers of the) $3d^N$ and $3d^{N+1}L$ configurations. The U_{dd} parameter defines the Hubbard U value and the U_{pd}

parameter the core hole potential. The right column of parameters define the hopping terms that are defined for the four different symmetries in D_{4h} symmetry, respectively B1, A1, B2 and E symmetry, related to the $x^2 - y^2$, z^2, xy and xz/yz orbitals respectively.

- In Figure 2.10 right part of the CTM4XAS interface only takes care of the plotting options. The files that are calculated appear in the main plotting box. In order to match with the experimental broadening in the spectra, Gaussian and Lorentzian broadening can be modified. Two separate Lorentzian broadenings can be included with the provided energy separating the two regions.

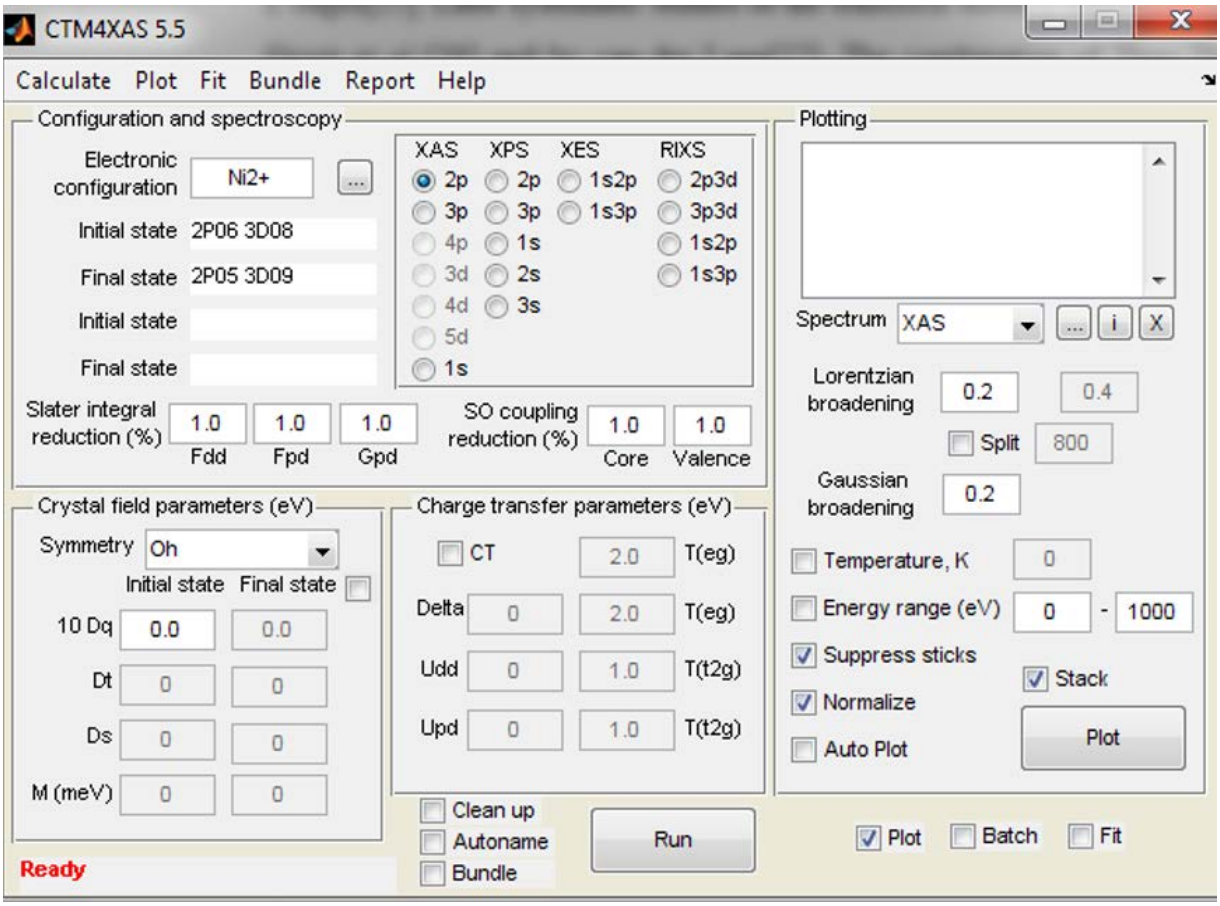

Figure 2.10. CTM4XAS5.5 program is based on a parameter-based panel. The panel is divided into four sections, respectively, the configuration and the atomic calculations at the top, the crystal field parameters (middle, left), and the charge transfer parameters (middle, right) and the plotting options (bottom). Enlarged sections of the panel are shown below.

Till 2010, there was no general approach was available that includes the charge transfer and the multiplet effects within the ab-initio codes like the density functional theory and the wave

function based codes. The methods that are developed by the Maurits W. Haverkort also follow the same procedures but Quanty is the advanced version of the CTM4XAS software and much more user-friendly. The CTM4XAS software has been used for the crystal field calculations and charge transfer calculations in chapter 4 as the Quanty is new software for us, therefore some calculations have been performed with the CTM4XAS software. In chapter 3 for the atomic multiplet theory simulations for full lanthanide series Quanty has been considered, therefore further detail discussion on Quanty is in chapter 3. The results produced by the Quanty and the CTM4XAS are analogous therefore in some cases results can be compared.

3. Atomic multiplet Theory simulations for full lanthanide series

3.1. Introduction

In this chapter, we present the atomic multiplet theory simulations of x-ray absorption spectra (XAS) and x-ray magnetic circular dichroism (XMCD) spectra of trivalent rare earth ions. The calculation covers the ground state spectra (at T=0 kelvin) of the full 4*f* rare earth element series from cerium (Ce) to ytterbium (Yb). The expectation values of the orbital and the spin angular momentum operator are the most fundamental quantities explaining the magnetic properties of the materials. These characteristics also have been estimated via atomic multiplet simulation theory. Spectral features are also explained and 4*f* sum rule has been applied to the integrated XAS and XMCD spectra. In this chapter, the emphasis has been given on the dichroism spectra and the applicability of the XMCD sum rules for the rare earth elements. Additionally, the role of the magnetic dipole term (T_Z) in the spin magnetic moment sum rule is also illustrated.

3.2. Lanthanides (4*f*) magnetic moments (Hund's rule)

Lanthanides (4*f*) includes 14 elements from Lanthanum (La) to Lutetium (Lu) and positioned in the *f*-block of period six in the periodic table. The lanthanides are also known as "rare earth metals" or "rare earth". In fact, they are not especially rare, except for Promethium (Pm) which has a very short half-life and is produced artificially but occurs naturally in trace amounts of Uranium (U) ores. In terms of magnetism, the rare earth elements are known to have large orbital angular momentum (*L*) even inside the solids because of the localized behavior of the *f*-orbitals. The combination of angular momentum quantum numbers (*L*, *S*, and *J*) which are found to minimize the energy can be estimated using Hund's rules (as mentioned in chapter1). Hund's rule leads to the prediction of the ground state but does not give any information about excited states or how close they are to the ground state. The application of the Hund's rule for 4*f* elements is shown in Figure 3.1 and Table 3.1. The spin (*S*) value increases and reach a maximum limit. The *L* and *J* have maxima roughly at the quarter and three-quarter positions, although for *J* there is an asymmetry between these maxima which reflects the differing rules for being in a shell which is less than or more than half-filled. According to Hund's rule, the ground state for rare earth elements is the *LS* multiplet with the largest total spin *S* and the largest total orbital moment *L* allowed.

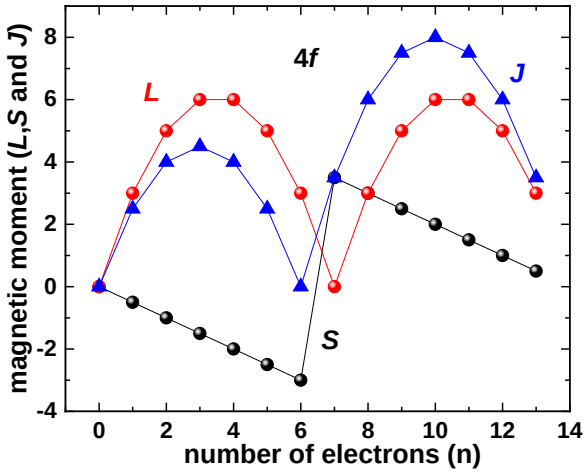

Figure 3.1 magnetic moment (*S*, *L*, and *J* for 4*f* ions) versus a number of electrons (n). According to Hund's rules for each ion the predicted values of *S*, *L* and *J* are plotted here for the full lanthanide series.

Table 3.1 Magnetic ground state for 4*f* ions using Hund's rule. For each ion, the shell configuration and the predicted values of *S*, *L* and *J* for the ground state are listed. This table is taken from the reference [14].

Ion	Shell	S	m_s	L $=m_l$	J	Term
Ce^{3+}	$4f^1$	$\frac{1}{2}$	1	3	$\frac{5}{2}$	$^2F_{5/2}$
Pr^{3+}	$4f^2$	1	2	5	4	$^3H_4$
Nd^{3+}	$4f^3$	$\frac{3}{2}$	3	6	$\frac{9}{2}$	$^4I_{9/2}$
Pm^{3+}	$4f^4$	2	4	6	4	$^5I_4$
Sm^{3+}	$4f^5$	$\frac{5}{2}$	5	5	$\frac{5}{2}$	$^6I_{5/2}$
Gd^{3+}	$4f^7$	$\frac{7}{2}$	7	0	$\frac{7}{2}$	$^8S_{7/2}$
Tb^{3+}	$4f^8$	3	6	3	3	$^7F_6$
Dy^{3+}	$4f^9$	$\frac{5}{2}$	5	5	$\frac{15}{2}$	$^6H_{15/2}$
Ho^{3+}	$4f^{10}$	2	4	6	8	$^5I_8$
Er^{3+}	$4f^{11}$	$\frac{3}{2}$	3	6	$\frac{15}{2}$	$^4I_{15/2}$
Yb^{3+}	$4f^{13}$	$\frac{1}{2}$	1	3	$\frac{7}{2}$	$^2F_{7/2}$

When n≤6, J takes the lowest value $|L\text{-}S|$ so that the *L* and *S* couple antiparallel to each other. If the negative *z* component is considered parallel to the magnetic field direction, in a case, when n≤5, since *L* is larger than *S*, the average value of the *L*z is negative and the value of *S*z is positive. Hence the occupied one electron states are mainly of up-spin and negative *L*z (or vice versa). When n=7 (Gd^{3+}), *L*=0 and *S*=7/2, so that in the initial state, *S*z is 7/2 because all spin one-electron orbitals are half occupied. When n≥8, both *L*, and *S* are parallel to each other

so that $J = L+S$. In the initial state, J_z takes $-J$ and hence the average values of L_z and S_z are both negative, so as the vacant one electron states are mainly of up-spin and positive l_z.

For the further investigation on rare earth elements, atomic multiplet theory simulations have been performed for all the trivalent rare earth elements, which will be discussed in the next sections and results of the simulations are compared with the Hund's rule ground state results.

3.3. Previous studies of XAS and XMCD at $M_{4,5}$ edges in 4*f* elements

The availability of synchrotron sources in 1980's allowed higher quality data of x-ray absorption spectra for the element-specific studies. In the process of understanding the experimental spectra of rare earth elements, theoretical models have been developed. Moreover, the atomic model approach has been quiet successful in explaining the experimental 3*d* XAS and XMCD spectra of rare earth elements and the localized systems also have been illustrated in many other studies in the past [37, 43-45].

The earliest reports of rare earth $M_{4,5}$ x-ray absorption spectra were in 1931 [46]. In progress, Schütz *et al.* in 1980´s pioneered XMCD work in the hard x-ray range [13, 47]. However, around the same time Thole [5], Van der Laan [9], Sawatzky and coworkers [10] investigated x-ray magnetic linear dichroism (XMLD) and have shown a strong interest in the $M_{4,5}$ edges of rare-earths materials. Remarkably, the work by Bonnelle, Karnatak and Sugar already contain a calculated spectrum. On the theoretical side, the studies of Gunnarsson and Schönhammer and Thole [37], Van der Laan [48] and Sawatzky established two working directions, that largely improved the understanding of the measured spectra i.e. (1) The Gunnarsson and Schönhammer (GS) theory and (2) The application of full multiplet calculations. The GS theory was introduced in 1983 [49, 50]. It allowed addressing the signatures of the *f*-level occupation in the spectra and clarified the issue of the Cerium valence.

In 1985, Thole *et al.* published experimental and calculated $M_{4,5}$ spectra for the complete rare-earth series including different ground-state valences [37]. The calculations were performed in full multiplet theory. While this approach had already been applied before [51, 52], the work by Thole *et al.* significantly led to the acceptance of full multiplet theory as the ideal tool to describe such x-ray absorption spectra. The excellent agreement between calculated $f^{n} \rightarrow f^{n+1}$ spectra and experimental data was shown for the whole rare earth series. This is certainly owed to the completeness of the study, as well as to the fact that the representation of the calculated spectra resembles experimental ones instead of being just as a bar diagrams [53]. The individual

transition lines are broadened under the assumption of line shapes widths. The agreement of this approach with experimental data once again reflects the local character of the 4*f* shell. Thole *et al.* introduced the well-established concepts of atomic physics to their computer code on the basis of a program written by R. Cowan to calculate atomic spectra [54]. Since the initial publication, the Thole-code has extensively been used to interpret experimental data and for further calculations [55]. Infarct, XMLD was predicted on this basis [21]. A comprehensive account of this effect for the whole rare earth series was given by Goedkoop *et al.* in 1988 [33], following the essence of the 1985 publication. The extended understanding of XAS involving partially filled inner shells that were generated through the study by Thole *et al.* was carried on in succeeding theoretical works, especially regarding the XMCD sum rules [20, 35]. Moreover, Thole *et al*.[20] and Carra *et al*.[35] have provided the theoretical description of the XMCD experiments by deriving the sum rules [13, 24] Chen *et al* in 1990, performed XMCD measurements in the soft x-ray region for investigation of the $L_{2,3}$ edges of nickel [56] and $L_{2,3}$ edges of iron and cobalt [24]. In the same year, two theoretical works were published by Jo *et al*. and Imada *et al*. that covers XMCD at the Ce $M_{4,5}$ edges [57, 58]. The analysis of the spectra with this model has been successfully used to study the ground state effects, such as the relative population of the spin-orbit coupled ground state in case of cerium [59] and the determination of the occurrence of the different valances [18].

The description of the hybridization effects or the charge transfer effects has been also successfully studied for cerium[18]. For the first time, the expectation values of the spin and the orbital angular momentum operator of the trivalent rare earth ions was presented in 1996 [60]. Atomic multiplet theory simulations explained the effect of 3*d*-4*f* exchange interaction in the rare earth [61]. A deviation from the spin sum rule, which relates the integrated intensity of x-ray magnetic circular dichroism spectra to the expectation values of the spin angular momentum operator is quantitatively estimated for the full rare earth series[60]. It has been explained that the interplay of 3*d*-4*f* exchange interaction, 3*d* spin-orbit interaction and the 4*f* electronic configuration in the ground state is the reason of the deviation of the sum rules with the expected 4*f* ground state properties and generate mixing in $3d_{3/2}$ and $3d_{5/2}$ state problem in the final state of the $M_{4,5}$ edges. The correction factor for the effective spin magnetic moments, which consists of the weighted sum of the spin and the magnetic dipole term (T_Z) contribution, have been presented. For cerium, the overestimation of the spin magnetic moment using sum rules approximately amounts to a factor of 1.6. This factor was used by Tolinski *et al.* to correct their spin sum rule results[62]. However, the spin sum rule additionally requires assumptions about the magnetic dipole term T_Z in order to yield the pure spin moment. This quantity was

experimentally addressed by Okane *et al*[63]. However, the study did not consider the weight transfer between the two edges in their analysis. Hence, this effect is intermixed to their quantification of T_Z. Except for cerium, no representative XMCD sum rule investigations have been presented till now for the other rare earth elements.

Our primary purpose for this research work is to perform the atomic multiplet simulations for full rare earth series to generate XAS and XMCD spectra at $M_{4,5}$ edges and to confirm the applicability of the XMCD spin sum rule for the theoretical and experimental investigation on rare earth ions spectra by eliminating the mixing problem in the final state of the $M_{4,5}$ edges. The spin sum rule [35, 60] shows that S_z is strongly influenced by magnetic dipole term (T_z). As the magnetic dipole term in the 4*f* series is dominated by the 4*f* spin-orbit coupling, therefore always aligned parallel to the spin, the magnitude of the T_Z cannot be determined experimentally, as suggested by Stöhr and König [64] for the 3*d* series, where the orbital moment is almost quenched therefore the related T_Z part is small. Hence, the purpose of this work is to estimate the T_Z by theory and test the applicability of the T_Z value correction to the experimental results.

The different ways for estimation of T_Z term can lead us to different values of the spin moment (S_z). The assumption of the crystallographic negligible T_Z ($\langle T_Z \rangle = 0$) term is worthy in case of $L_{2,3}$ edges for cubic crystals. However, as mentioned above, it is inappropriate in case of $M_{4,5}$ edges due to the asymmetry of the 4*f* shell charge cloud modified by the external magnetic field. Therefore, It is also important to eliminate the contribution of the magnetic dipole term T_Z in order to estimate precise spin magnetic moments.

In the field of XMCD investigation due to the localized behavior of the 4f wave functions in rare earth elements, it is always considered that the spectral shape of the rare earth elements does not change. For example, as a function of the temperature or the magnetization state of the sample. Considering this, our studies will cover the observation of the change in spectral shape, magnetic moments (spin and orbital) and their ratio as a function of variation in temperature and magnetic field in different magnetic materials. Such as rare earth garnets, neodymium-based soft and hard magnets.

For a successful understanding of the experimental spectra, the theoretical aspects also need to learn, as a consequence, we have performed the atomic multiple theory simulations to compare the experimental results with a theory for the full rare earth series and first the applicability of

the XAS and XMCD sum rules is confirmed for the simulated spectra. This chapter will cover individual multiplet theory simulation aspects.

3.4. Atomic Multiplet theory simulations for the full lanthanide series

In this chapter, we will use the recent "**Quanty**" software for the simulations of the ground state XAS and XMCD spectra at $M_{4,5}$ edges of the trivalent lanthanides ions (Lanthanum to Ytterbium). The atomic multiplet theory simulation information, parameters, software details and an example of the simulated spectra are presented in this section.

3.4.1. Software details

Quanty is a script language which allows the users to program quantum mechanical problems in second quantization. It can be used in any problems related to such as x-ray spectroscopy, quantum mechanics. Where it uses Hartree-Fock approximation or the Local density approximation (LDA^{++}) schemes (self-consistent field, configuration interaction, coupled cluster, restricted active space). The main purpose of the software Quanty is that the user can focus on the model and its physical or chemical meaning and Quanty will take care of the mathematics involved related to atomic physics and quantum mechanics. Quanty is still in its initial stages, but growing fast among the users. The code developed from the need to calculate core level spectroscopy (x-ray absorption, resonant diffraction, x-ray resonant scattering) of correlated transition metals and rare earth compounds. So, these areas are the well documented. But many more examples in different fields are added [65-67].

The code is written and maintained by Maurits W. Haverkort and coworkers and can be used and available for Windows, Linux, and Mac. Quanty is able to run parallel jobs using all cores on a single node [65-67]. After registration, you can download the code from the download area. The current version is text-based. Quanty is based on Lua, providing a flexible script language. It can be edit in the notepad and can be run on laptops or on any computers. There is no need to know the "Lua" to run Quanty, but can be used as all extensions Lua provides [65-67]. Quanty is a much more advanced version of the Cowan's program [42]. The advantage using Quanty over CTM4XAS software[42] is that it has amendable raw files. The possibilities of the errors are less compared to CTM4XAS where the format is complicated.

CTM4XAS is very well developed for the transition elements and mostly for the $L_{2,3}$ edges simulations. The large calculations like crystal field calculations for the 4*f* atoms in the vicinity to half filling atoms like neodymium, dysprosium and other lanthanides are not possible in CTM4XAS software. These calculations could be performed comfortably and much faster in Quanty than CTM4XAS. Quanty not only provides the spectra for all possible *J* states but also provides the expectation values of spin ($<S_{x,\,y,\,z}>$), orbital ($<L_{x,\,y,\,z}>$) and magnetic dipole moment ($<T_{x,\,y,\,z}>$) in all possible orientations. It also allows us to calculate *T*z with a variation of the crystal field which we cannot perform in CTM4XAS. An example of Lua file image is shown in Figure 3.2.

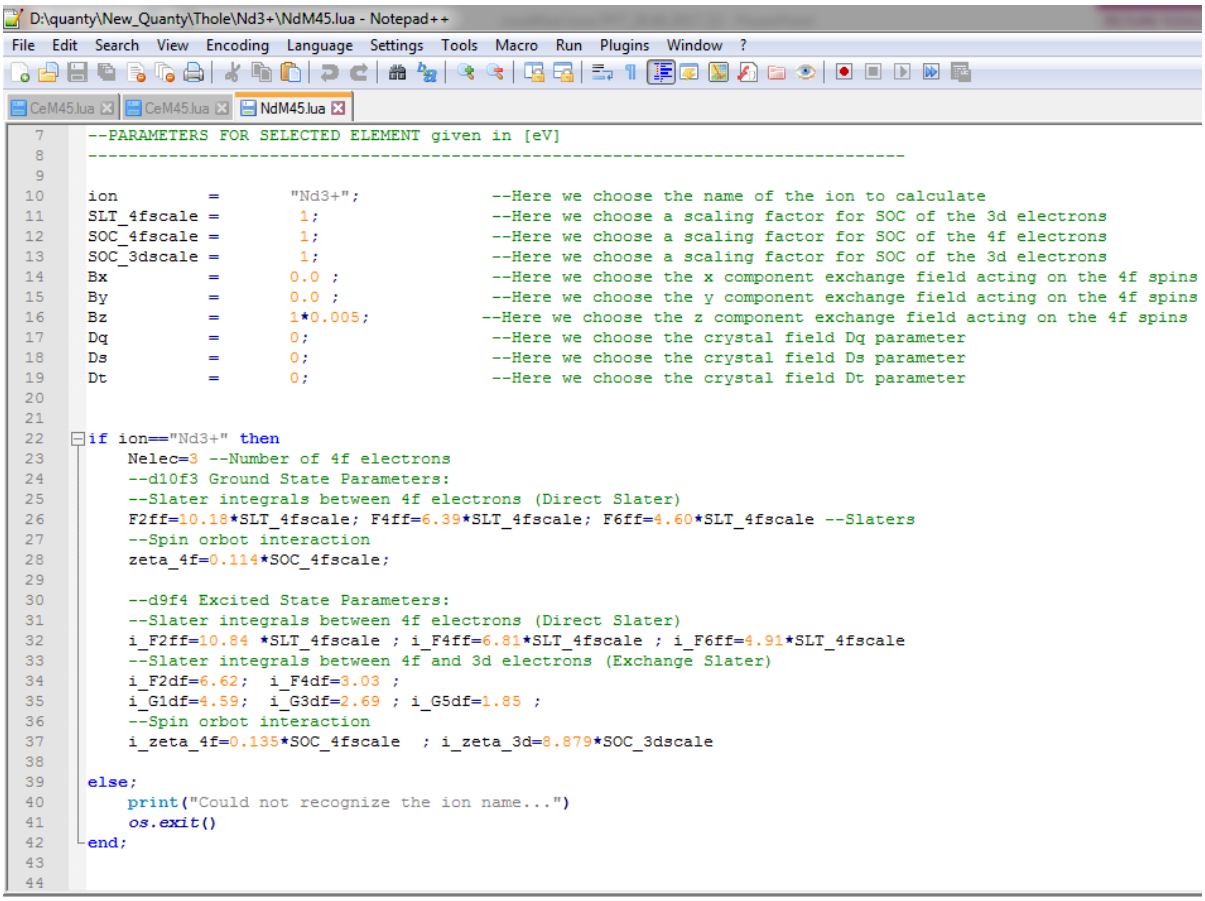

Figure 3.2 example of coding in Quanty software for neodymium XAS and XMCD spectra simulations.

3.4.2. Simulations details and parameters

Table 3.2 initial and final state electrostatics and exchange parameters for the atomic multiplet simulations. The slater integral reduced to 80% of HF values. All the simulation parameters used in this thesis is from reference [37].

In the atomic picture of the $3d \rightarrow 4f$ absorption process includes the electronic excitation of the $3d^{10}4f^{n} \rightarrow 3d^{9}4f^{n+1}$.The final state of the configuration contains the two-open shell and the overlapping of the core and the valance shell creates multiplet structures which are complicated

	$3d^{10}4f^{n}$					$3d^{9}4f^{n+1}$									
	n	F^2_f	F^4_f	F^6_f	ξ_f	F^2_f	F^4_f	F^6_f	F^2_{fd}	F^4_{fd}	G^1_{fd}	G^3_{fd}	G^5_{fd}	ξ_d	ξ_d
La^{3+}	0								5.65	2.53	3.78	2.21	1.52	6.80	0.092
Ce^{3+}	1				0.087	10.10	6.35	4.57	5.99	2.71	4.06	2.37	1.64	7.45	0.107
Pr^{3+}	2	9.78	6.14	4.41	0.103	10.48	6.59	4.74	6.31	2.87	4.33	2.53	1.75	8.14	0.124
Nd^{3+}	3	10.18	6.39	4.60	0.114	10.84	6.81	4.91	6.62	3.03	4.59	2.69	1.85	8.88	0.135
Pm^{3+}	4	10.56	6.63	4.77	0.136	11.18	7.03	5.07	6.92	3.19	4.84	2.83	1.96	9.67	0.160
Sm^{3+}	5	10.92	6.85	4.93	0.155	11.51	7.24	5.21	7.21	3.34	5.09	2.98	2.06	10.51	0.180
Eu^{3+}	6	11.27	7.07	5.09	0.175	11.84	7.44	5.36	7.50	3.48	5.33	3.12	2.16	11.41	0.202
Gd^{3+}	7	11.60	7.28	5.24	0.197	12.46	7.64	5.50	7.77	3.63	5.56	3.26	2.25	12.36	0.226
Tb^{3+}	8	11.93	7.49	5.39	0.221	12.47	7.84	5.64	8.04	3.77	5.79	3.40	3.35	13.37	0.251
Dy^{3+}	9	12.25	7.69	5.53	0.246	12.77	8.03	5.78	8.31	3.91	6.02	3.53	2.44	14.44	0.278
Ho^{3+}	10	12.57	7.88	5.67	0.273	13.07	8.21	5.91	8.57	4.04	6.24	3.66	2.53	15.57	0.307
Er^{3+}	11	12.87	8.08	5.81	0.302	13.37	8.40	6.04	8.83	4.18	6.46	3.79	2.62	16.78	0.338
Tm^{3+}	12	13.18	8.26	5.94	0.333				9.09	4.31	6.68	3.92	2.71	18.05	0.371
Yb^{3+}	13				0.366									19.39	

and contains several thousand of levels. The strongest final state multiplet interaction is the spin-orbit coupling (SOC) for the 3*d* hole, which splits the ground state into 2 energy levels, which are named as $3d_{3/2}$ (M_4 edge) and $3d_{5/2}$ (M_5 edge) respectively. The transition to the n-p continuum states are also allowed but have much smaller cross-sections compared to the 4*f* resonance and lie into higher photon energies. The theory of the multiplet spectra is quite evolved and it is difficult to give a rough outline to the spectrum simulation procedure (discussed in Cowan book) [19]. The atomic multiplet simulations of XAS and MCD spectra for the ground states of the trivalent rare earth elements have been performed for full lanthanide series (lanthanum to ytterbium) using Quanty software. The simulations parameter values were obtained by the Cowan's Hartree Fock (HF) program with the relativistic corrections. The simulation parameters are similar as presented in paper [37] and shown in Table 3.2. The electrostatic and exchange parameters were scaled down to 80% of their HF values [37]. An ion is assumed to be placed in a reasonable magnetic field. Symmetry breaking of the spin and orbital moment in the initial state is determined by the electrostatic interaction between the 4*f* electrons, their spin-orbit interaction, and the magnetic field. In the final state of the absorption

process, there are some additional interactions such as the electrostatic interaction between the core hole and the 4*f* electrons, and the spin-orbit interaction of the core hole. The aim of this work is to simulate the MCD spectra for the rare earth elements, study the basic features of the MCD spectra and check the applicability of the spin sum rule for full lanthanides series. An example of the simulated spectra is presented below in the following section.

3.4.3. An example: simulated XAS and XMCD spectra of Ytterbium (Yb^{3+})

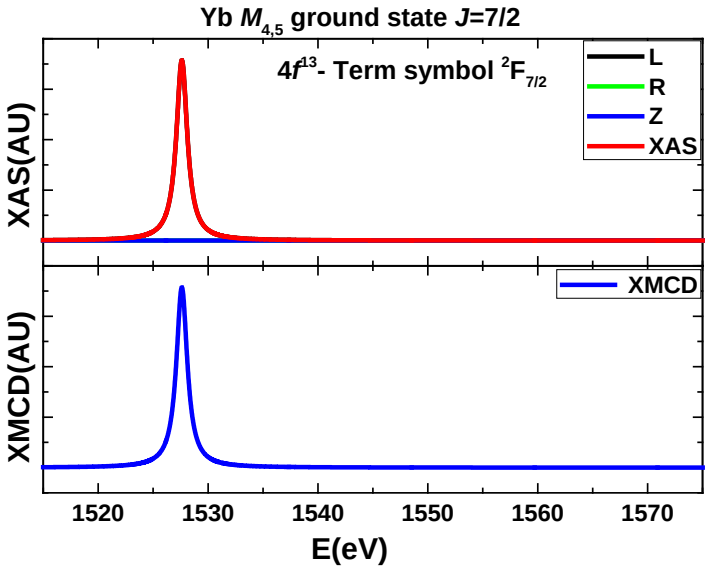

Figure 3.3 simulated XAS (red curve) and XMCD (blue curve) spectra for the Yb^{3+} ion. The spectra labeled as XAS have been represented in three different colors. The black color is for left polarized spectra representing (J=+1 state), the green color is for right polarized spectra representing (J=-1 state) and the blue color is for left polarized spectra representing (J=+1 state). The red color spectra are the sum of L, R and Z polarized spectra denoting the theoretical dipole excitation spectrum from the Hund's rule ground state of the configuration $3d^{10}4f^{13}\rightarrow 3d^{9}4f^{14}$. The only possible transition in case of Yb^{3+} is -7/2 →-5/2 therefore 1 peak is visible.

Here, we will start with the overview of the nonmagnetic $3d\rightarrow 4f$ x-ray absorption spectra of ytterbium (Yb^{3+}) and will explain the XMCD effect on the basis of the most simple case. Ytterbium has 13 electrons present in *f* shell. The spin (*S*) and orbital (*L*) moment Yb^{3+}, according to Hund's rule will be ½ and 3 respectively. The ground state for Yb^{3+} ion will be $^2F_{7/2}$. Figure 3.3 shows the very simple absorption spectrum of Yb^{3+} ion which consists of J=-1. The only possible transition which is allowed by the selection rules is $3d^{10}4f^{13}\,(^2F_{7/2}) \rightarrow 3d^{9}4f^{14}\,(^2D_{5/2})$. The spectral shape is in good agreement with the reported results [33]. In presence of magnetic field, both the initial ($^2F_{7/2}$) and final ($^2D_{5/2}$) states are split into the Zeeman levels with the energy of $-g\mu_B HM$, as shown in Figure 3.4. The dots below the energy

levels diagram in Figure 3.4 shows the relative amplitudes which are given by the square of 3-*j* symbols. If all the m_j states (Zeeman states) are equally populated than all the three groups (left polarized, right polarized and linearly polarized) will exhibit equal contribution and then all the three components will appear same. No effect of the magnetic field will be present in it because the magnetic field splitting is smaller than 1 eV than experimental line width. In Figure 3.4, at T=0 Kelvin only M=-7/2 level is occupied. Therefore, the ΔM=1 transition is indicated by the arrow. Since the shape of the spectra is dependent on the size and the orientation with respect to the polarization of the ionic moment. Hence the MCD spectra can be used to obtain the magnetic moment related information [33].

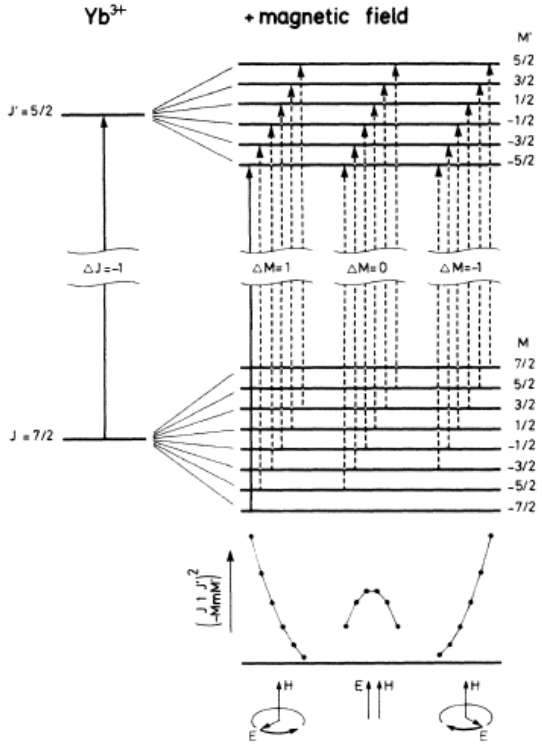

Figure 3.4 energy level diagram of the $3d^{10}4f^{13}\rightarrow 3d^{9}4f^{14}$ transition of the Yb^{3+} with (right) and without (left) a magnetic field. The transitions allowed by the dipole selection rules are indicated by arrows. The relative intensities are given by dots[33]. At T=0 Kelvin the only possible transition in case of Yb^{3+} is indicated by the solid arrow (-7/2 →-5/2) [33].

If there is no ferromagnetic ordering present in the magnetic moment then the spectrum will be a superposition of the spectra of the individual ions. It can lead to pure paramagnetic and very small XMCD effect[33].

3.4.4. Simulation results for full lanthanide series

All the simulated spectra are presented in Figure 3.5 (a) to (n). For each element in Figure 3.5 (a) to (n) on the top panel, we show the absorption for the left (L) circularity polarized light (J=+1), right (R) circularity polarized light (J=-1) and linearly (Z) polarized light (J=0) parallel to the z-axis. In case of all rare earth elements, the spin-orbit interaction of the core hole is strong, the XAS spectra divide into two parts, which corresponds to $3d_{3/2}$ -higher energy (M_4) and $3d_{5/2}$ -lower energy (M_5). Figure 3.5 (a) and (b) shows the calculated spectra of the rare earth ions (La^{3+} and Eu^{3+}), which exhibit J=0 ground state and the spectral shapes are conventional as reported previously [37, 68]. For J=0 (La^{3+} and Eu^{3+}), there is no difference in left, right and linearly polarized spectra where ΔJ=1 is the only possible transition Figure 3.5 (a) and (b). For the La^{3+} weight of the $3d_{3/2}\rightarrow 4f_{5/2}$ excitation is 24 states and for $3d_{5/2}\rightarrow 4f_{7/2}$ excitation is 48 states. The figures of Eu and La are presented individually in Figure 3.5 (a) and (b) from other rare ions.

Figure 3.5 (c) to (n) shows the calculated spectra for all trivalent rare earth ions with non-zero J ground state ($J\neq 0$). The black color spectra show left (J=+1) polarized spectra, green is right (J=-1) polarized spectra, blue is linearly (J=0) polarized spectra and red are XAS spectra (sum of left, right and zero polarized spectra). In the lower panel XMCD (left-right) spectra have been presented. The total multiplet structure is complex and there are thousands of energy levels for RE elements series in the vicinity of half filling. The dipole selection rule reduces the final states which can be reached during excitation form the initial or the ground state, even this does produce the complicated shape of the spectra. The number of final states, which can be reached via dipole selection rule is increased from 3 for La^{3+} to 53 Ce^{3+} and 200 for Pr^{3+} to 1077 for Gd^{3+}. In late heavy rare earth elements, the number of holes is again reduced than it falls to 4 for Tm^{3+} to 1 for Yb^{3+}. Ytterbium (Yb^{3+}) presents the simplest case among all the rare earth elements. It has only one hole in the initial state and $3d_{5/2}\rightarrow 4f_{7/2}$ excitation provides fill the final 4f shell, which is spherically symmetric. Therefore, only a single peak is visible at each resonance (as presented in section 3.4.3). In Gd^{3+} (f^7 ion), the splitting between the J component is small as L=0 (orbital singlet state) ground state[37].

In other elements with non-zero J and L has a clear difference in the x-ray absorption spectra at the left, right and zero polarization. The shape of the multiplet has a dependence on the total number of the f electrons in the outer most orbit. The multiplet effects lead to the significant structure in RE elements as a number of holes increases which are visible in calculated spectra

Figure3.5 (c) to (n). The intensity of the M_4 absorption spectra is comparable with the M_5 edge absorption spectra for the light rare earth elements (refer Figure3.5 red curves Ce, Pr, Nd, Sm etc.) but decreasing in the case of the heavy rare earth (refer Figure3.5 red curves Dy, Ho, Tb etc.). As it is already mentioned in the above section 3.4.1, Quanty provides the expectation values of the spin ($<S_z>$), orbital ($<L_z>$) and magnetic dipole term ($<T_z>$) in the valence state. All the expectation values have been presented in Table 3.3 with the ground state energies of the respective trivalent rare earth ions. The results are in good agreement with the previously reported results [60]. In order to compare the expectation values of spin ($<S_z>$), and orbital ($<L_z>$) angular momentum, the XMCD sum rules have been applied on the integrated spectra of the ground states of full lanthanide series. Further details regarding sum rule analysis are presented in the next section and the results of the expectation values will be also discussed in details.

Table 3.3 Quanty provides the expectation values of the spin ($<S_Z>$), orbital ($<L_Z>$) and magnetic dipole term ($<T_Z>$) for the ground state. All the expectation values have been presented with the ground state energies of the respective trivalent rare earth ions.

Elements	Number of holes (n_h)	Ground state Energy (eV)	$<L_Z>$	$<S_Z>$	$Jz=<L_Z>+<S_Z>$	$<T_Z>$
La^{3+}	14	0	0	0	0	0
Ce^{3+}	13	-0.1758	2.861	-0.361	2.5	-0.569
Pr^{3+}	12	-1.3653	4.776	-0.776	4	-0.669
Nd^{3+}	11	-3.2241	5.711	-1.211	4.5	-0.376
Pm^{3+}	10	-4.8115	5.595	-1.595	4	0.032
Sm^{3+}	9	-6.0208	4.305	-1.805	2.5	0.386
Eu^{3+}	8	-7.9225	0.652	-0.652	0	0.159
Gd^{3+}	7	-10.779	-0.034	-3.465	-3.5	0.010
Tb^{3+}	6	-8.3361	-3.056	-2.943	-6	0.243
Dy^{3+}	5	-6.9284	-5.082	-2.417	-7.5	0.128
Ho^{3+}	4	-6.0947	-6.083	-1.916	-8	-0.136
Er^{3+}	3	-4.5189	-6.032	-1.467	-7.5	-0.312
Tm^{3+}	2	-2.2458	-5.009	-0.990	-6	-0.407
Yb^{3+}	1	-0.5515	-3	-0.5	-3.5	-0.333

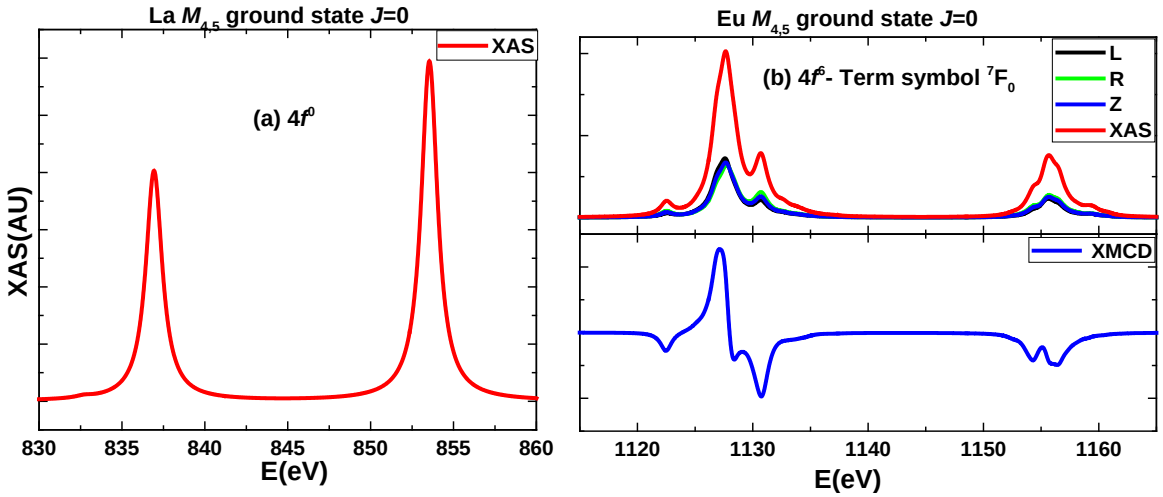

Figure 3.5 Atomic multiplet theory calculations of XAS and MCD $M_{4,5}$ edge spectra for rare earth ions.(a) La^{3+} and (b) Eu^{3+} exhibit J=0 ground state.

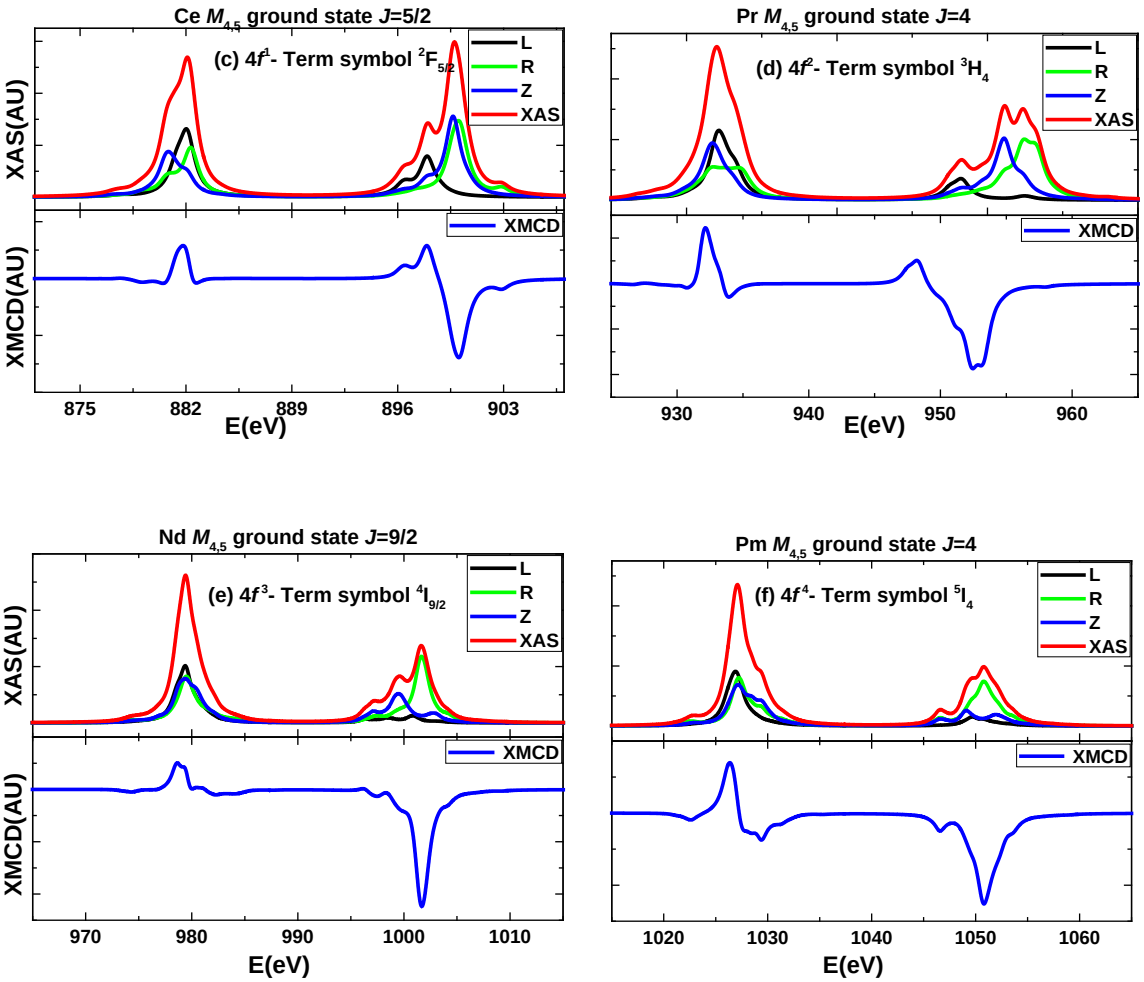

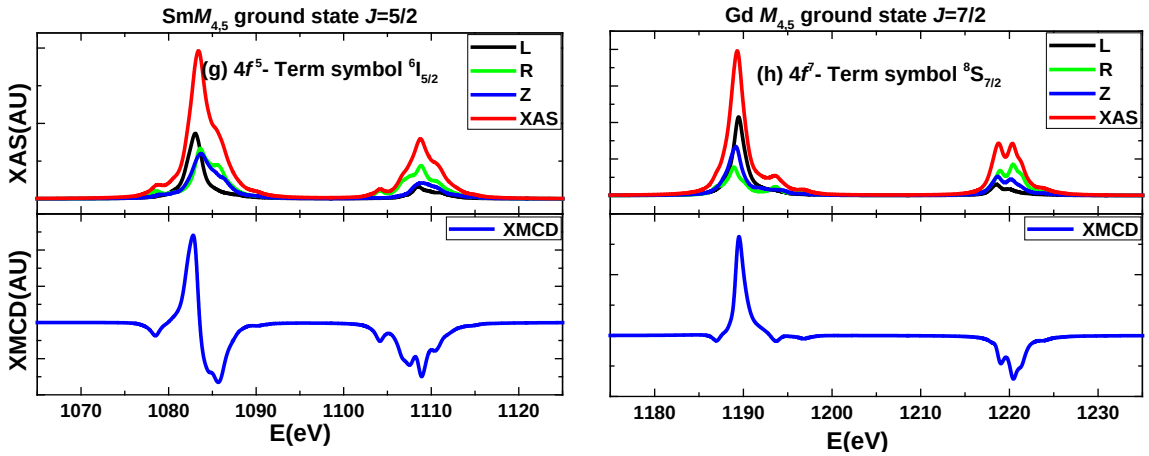

Figure 3.5 Atomic multiplet theory calculations of XAS and MCD $M_{4,5}$ edge spectra of the trivalent rare earth ions (from c to h) exhibit non-zero J ground state configuration. The spectra labeled as XAS have been represented in three different colors. The black color is for left polarized spectra representing the J=+1 state, the green color is for right polarized spectra representing J=-1 state and the blue color is for linearly polarized spectra representing J=0 state. The red color spectra are sum of left (L), right (R) and linearly (Z) polarized spectra denoting the theoretical dipole excitation spectrum from the Hund's rule ground state of the configuration $4f^n$ to the $d^9 4f^{n+1}$ level [37].

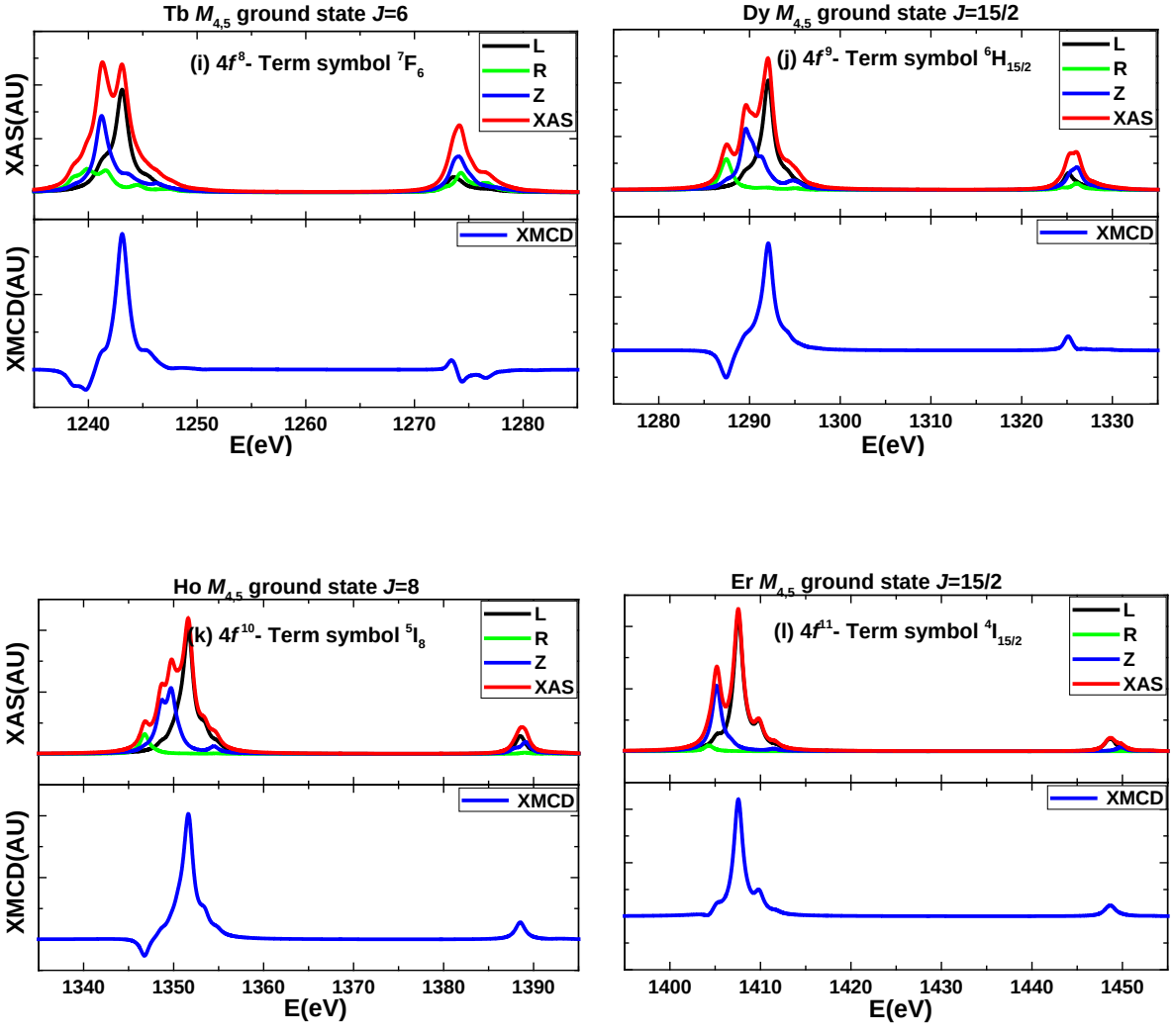

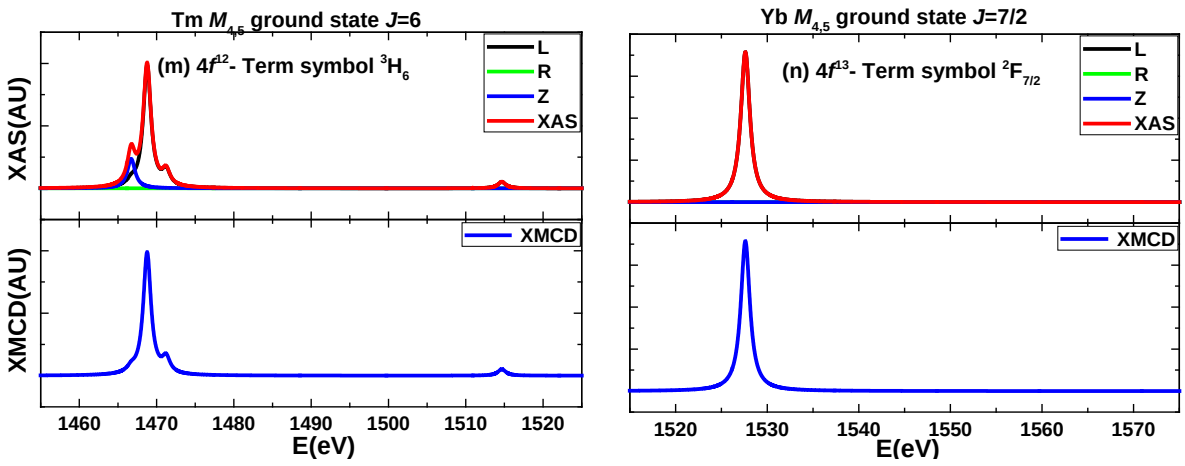

Figure 3.5 Atomic multiplet theory calculations of XAS and MCD $M_{4,5}$ edge spectra of the trivalent rare earth ions (from i to n) exhibit non-zero J ground state configuration. The spectra labeled as XAS have been represented in three different colors. The black color is for left polarized spectra representing the J=+1 state, the green color is for right polarized spectra representing J=-1 state and the blue color is for linearly polarized spectra representing J=0 state. The red color spectra are sum of left (L), right (R) and linearly (Z) polarized spectra denoting the theoretical dipole excitation spectrum from the Hund's rule ground state of the configuration $4f^n$ to the $d^9 4f^{n+1}$ level [37].

3.5. XMCD sum rule analysis for 4*f* (rare earth elements)

The basic properties of magnetism are strongly depended on the spin and the orbital magnetic components of the magnetization. These moments are determined by the interplay of the hybridization, SOC, crystal field, Coulomb, and exchange interaction. The rare earth elements are characterized by the strong SOC interaction and a degree of localization of the 4*f* electrons which gives a variety of magnetic properties, for example, large orbital moment (as mentioned in section 3.2 by Hund's rule). There are sum rules proposed for XAS and XMCD spectroscopy which relates the expectation values of the spin (<S_z>) [35], orbital (<L_z>) [20] and magnetic dipole term (<T_z>) in the valence state [69]. The expressions is developed by Thole and Carra are given here:

$$\frac{a}{n_h}\langle L_z\rangle = \frac{-\int_{j-+j+}\left(\mu^+(E)-\mu^-(E)\right)\cdot dE}{\int_{j-+j+}\left(\mu^+(E)+\mu^-(E)+\mu^0(E)\right)\cdot dE} \quad \text{.....equation (3.1)}$$

$$c\cdot\langle S_z\rangle + d\cdot\langle T_z\rangle = -n_h\cdot\frac{\left[\int_{M_5}\mu^+(E)-\mu^-(E)\cdot dE - b\cdot\int_{M_4}\mu^+(E)-\mu^-(E)\cdot dE\right]}{\int_{M_4+M_5}\left(\mu^+(E)+\mu^-(E)+\mu^0(E)\right)dE} \quad \text{.....equation (3.2)}$$

Here $<L_Z>$, $<S_Z>$ and $<T_Z>$ are the expectation values of the spin operator, orbital operator, and the magnetic dipole operator, projection along the *z* (photon beam) direction. The values for the pre-factors *a–d* are shown in Table 3.4 [70].and j_+ and j_- spin-orbit split states respectively. The l_f and l_i are the orbital angular momentum quantum numbers of the final and initial states, which are connected to each other by the dipole selection rule $l_f=l_i\pm1$ in Table 3.4 [70] The magnetic dipole term $<T_Z>$ is related to the quadrupole moment of the spin density distribution [70, 71]. The number of unoccupied final states (n_h) in the valence shell which contains *n* electrons is given by $(4l+2-n)$. The μ^+ and μ^- represent the measured helicity or magnetization absorption dependent coefficients and the difference between them is a measure of XMCD effect [20, 70]. In experimental spectra, we measure the left and right polarized spectra only therefore we use $\mu^+ + \mu^{-+} + \mu^0 = 3/2$ $(\mu^+ + \mu^-)$ approximation. Spin and orbital moments are related to the integrated areas of the x-ray magnetic circular dichroism and the isotropic x-ray absorption spectra by the integral sum rules.

Table 3.4 sum-rule related prefactors (*a*,*b*,*c* and *d*).initial ($\boldsymbol{l}_i$) and final ($\boldsymbol{l}_f$) state of the system [70].

l_i	l_f	*a*	*b*	*c*	*d*
s:0	*p*:1	1	–	–	–
p:1	*d*:2	½	2	2/3	7/3
d:2	*f*:3	1/3	3/2	2/3	2

The quantitative estimation of the $<S_z>$, $<L_z>$ and $<T_z>$ can be performed by these sum rules in order to get the magnetic moment values in Bohr magneton per atom. The main purpose here is an effective application of these spin and orbital sum rule on the integrated intensity of XA and XMCD spectra. In upcoming sections, orbital and spin sum rules will be discussed separately. The results of the sum rule analysis will be compared with the spin and orbital magnetic moments values of the Hund's rule, Quanty expectation values of spin and orbital angular momentum (mentioned in section 3.4.4), results reported by vanderlaan *et* al [48] and expectation values of spin and orbital angular momentum generated by atomic multiplet theory simulations results by Takeo *et* al [61].

3.5.1. Orbital moment (L_z)

Substituting the coefficient *a* value from the Table 3.4 in equation 3.1, one can give the corresponding sum rule expression for the orbital moment (refer equation 3.3). As consequence for $3d \rightarrow 4f$ transition, the orbital magnetic moment sum rule is as follows.

$$\frac{a}{n_h}\langle L_z\rangle = \frac{-\int_{j-+j+}\left(\mu^+(E)-\mu^-(E)\right)\cdot dE}{\int_{j-+j+}\left(\mu^+(E)+\mu^-(E)+\mu^0(E)\right)\cdot dE}$$

$$\frac{1}{3\cdot n_h}\langle L_z\rangle = \frac{-\int_{M_4+M_5}\left(\overbrace{\mu^+(E)-\mu^-(E)}^{XMCD}\right)\cdot dE}{\int_{M_4+M_5}\left(\underbrace{\mu^+(E)+\mu^-(E)+\mu^0(E)}_{XAS}\right)\cdot dE} \quad \text{.....equation (3.3)}$$

Figure 3.6 shows the orbital magnetic moment values for all the rare earth elements estimated by the XMCD orbital sum rule analysis (in blue color -circle +solid line) and all the values are listed in (Table 3.6 at the end of the section 3.5). The sum rule analysis results of the orbital magnetic moment is compared with the orbital magnetic moments values of the Hund's rule (in magenta color -circle +solid line), Quanty expectation values of orbital angular momentum (mentioned in section 3.4.4) (in red color -circle + solid line), results reported by Vanderlaan (in olive color -circle +solid line) [48] and expectation values of spin and orbital angular momentum generated by atomic multiplet theory simulations results by Takeo *et* al (in black color -circle +solid line) [61].

In the simulations, the magnetic field along z-direction (B_z) is applied to generate the XMCD effect. In order to compare the results with Takeo's results [61] the sign for the orbital moment has been changed accordingly in the graph to compare the results. The orbital moment (L_z) sum rule analysis results are in good agreements with the Takeo's results, Vanderlaan results and the real expectation values generated by Quanty. It confirms the applicability of the XMCD orbital sum rule for the rare earth elements. The sum rule analysis results are following the trend of the Hund's rule results. For $n \leq 5$ less than half field shells orbital contribution is larger than the spin contribution so the antiparallel coupling of their moment results in positive value for

the orbital moment, therefore, neodymium (n=3) exhibit highest orbital moment and shows maxima value in the curve. For *n*=7 half field shells (gadolinium), the orbital moment is zero and the curve shows the minima. For $n > 7$ more than half field shells due to the parallel coupling orbital and spin both have the same sign, positive or negative depends on the direction of the magnetic field. For completely field shell *n*=14, the orbital moment again turns into zero. The heavy rare earth elements results are in good agreement with the real expectation values and the sum rule analysis due to the parallel coupling of the *L* and *S* and is defined by the single Slater determinant. In case of light rare earth element, the average over all the possible states will end up into the smaller orbital moment due to the antiparallel coupling of the *L* and *S* [48].

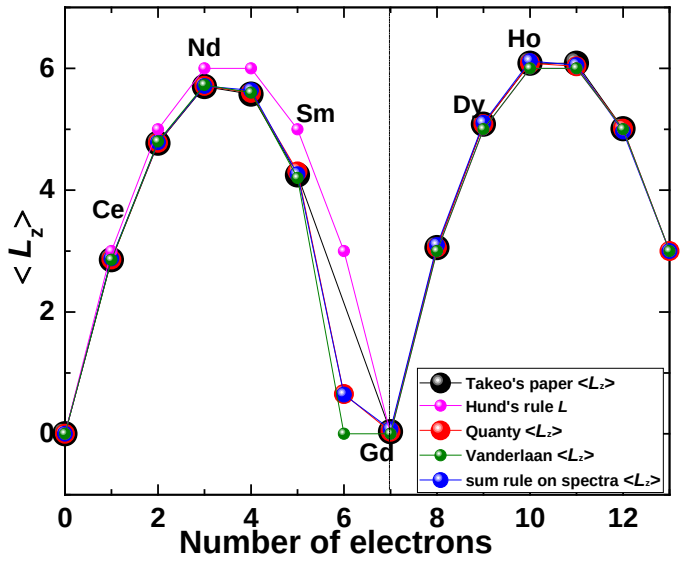

Figure 3.6 orbital magnetic moment values for all the rare earth elements estimated by the XMCD orbital sum rule analysis shown in blue color (circle+ solid line). The sum rule analysis results of the orbital magnetic moment is compared with the expectation values of spin and orbital angular momentum generated by atomic multiplet theory simulations results by Takeo *et al* (black color-circle+ solid line)l[61], orbital magnetic moments values of the Hund's rule (magenta color -circle+ solid line), Quanty expectation values of orbital angular momentum (red color-circle+ solid line) (refer section 3.4.4), results reported by Vanderlaan (green color-circle+ solid line) [48].

3.5.2. Effective spin magnetic moment (S_z+3*T_z)

Substituting the coefficients (*b*, *c*, and *d*) values from the Table 3.4 in equation 3.2, we can give the corresponding sum rule expression for the spin moment (equation 3.4). As consequence of $3d \rightarrow 4f$ transition, the spin magnetic moment sum rule is as follows.

$$c\cdot\langle S_z\rangle + d\cdot\langle T_z\rangle = -n_h\cdot\frac{\left[\int_{M_5}\mu^+(E)-\mu^-(E)\cdot dE - b\cdot\int_{M_4}\mu^+(E)-\mu^-(E)\cdot dE\right]}{\int_{M_4+M_5}\left(\mu^+(E)+\mu^-(E)+\mu^0(E)\right)dE}$$

$$\frac{2}{3}\cdot\langle S_z\rangle + 2\cdot\langle T_z\rangle = -n_h\cdot\frac{\left[\int_{M_5}\mu^+(E)-\mu^-(E)\cdot dE - \frac{3}{2}\cdot\int_{M_4}\mu^+(E)-\mu^-(E)\cdot dE\right]}{\int_{M_4+M_5}\left(\mu^+(E)+\mu^-(E)+\mu^0(E)\right)dE}$$

$$\langle S_z\rangle + 2\cdot\frac{3}{2}\cdot\langle T_z\rangle = -\frac{3}{2}\cdot n_h\cdot\frac{\left[\int_{M_5}\mu^+(E)-\mu^-(E)\cdot dE - \frac{3}{2}\cdot\int_{M_4}\mu^+(E)-\mu^-(E)\cdot dE\right]}{\int_{M_4+M_5}\left(\mu^+(E)+\mu^-(E)+\mu^0(E)\right)dE}$$

$$\langle S_z\rangle = -\frac{3}{2}\cdot n_h\cdot\frac{\left[\int_{M_5}\mu^+(E)-\mu^-(E)\cdot dE - \frac{3}{2}\cdot\int_{M_4}\mu^+(E)-\mu^-(E)\cdot dE\right]}{\int_{M_4+M_5}\left(\mu^+(E)+\mu^-(E)+\mu^0(E)\right)dE} - 3\cdot\langle T_z\rangle \quad \text{.....equation(3.4)}$$

The left part $\langle S_Z\rangle + 3\langle T_Z\rangle$ is called the *effective XMCD spin* (S_{eff}) and the $\langle S_Z\rangle_{pure}$.is the pure spin contribution after subtraction of the magnetic dipole term T_Z. Figure 3.7 (a) shows the spin magnetic moment values for all the rare earth elements estimated by the XMCD spin sum rule analysis (in blue color -circle +solid line). The sum rule analysis results of the spin magnetic moment are compared with the Quanty real expectation values of spin angular momentum $\langle S_z\rangle$ (refer section 3.4.4). The sum rule estimation does not fit very well with the real expectation values and light rare earth deviated much stronger than the heavy rare earth elements. This deviation clearly shows that the accuracy of the spin sum rule is not good especially in case of light rare earth elements. In order to estimate the spin magnetic moment, corrections need to be done.

In 1996, Teramura and Takeo Jo *et al* have explained the origin of the deviation from the spin sum rule by the similar multiplet calculations [60, 61]. Due to the 4*f*-3*d* interaction, the 3*d* XAS and XMCD spectra $M_5(M_4)$ region do not correspond to the pure $3d_{5/2}$ ($3d_{3/2}$) constituents.

Unless the spin-orbit coupling constant ζ_d is infinite. In this case, the spin sum rule will completely satisfy. The results for the extent of mixing provided by the Takeo Jo *et al* are presented in Figure 3.7 (b). The Figure 3.7 (b) is reproduced from the values presented in the Takeo Jo paper [61]. Where they have provided the relative extent of mixing of the $3d_{5/2}$ and $3d_{3/2}$ states in both XAS and XMCD spectra. The magnitude of the mixing for the XAS spectra is18% for cerium (n=1) and decrease as the number of electrons increases. It reaches the 5% for the samarium (n=5). For the gadolinium is almost negligible at the order of 0.1%. For most of the heavy rare earth elements also it is in the order of 0.1%. It is almost negligible compared to the light rare earth elements.

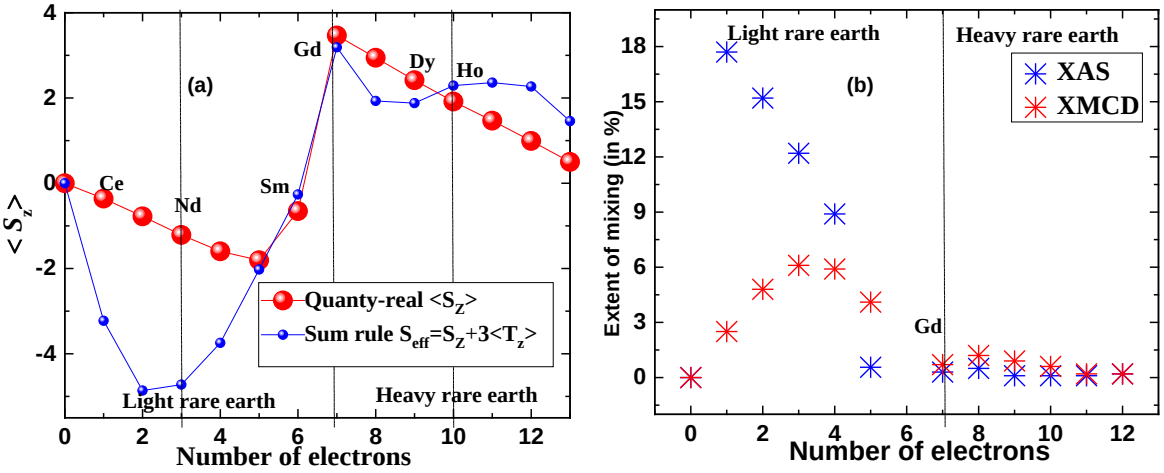

Figure 3.7 (a) spin magnetic moment values for all the rare earth elements estimated by the XMCD spin sum rule analysis shown in blue color (circle + solid line). The sum rule analysis results of the spin magnetic moment are compared with the quanty generated real expectation values of spin (red color-circle + solid line) (b) extent of mixing in $3d_{5/2}$ -$3d_{3/2}$ components for all the rare earth elements are presented. Mixing in XAS and XMCD spectra are presented in blue and red scatters respectively. The extent of mixing for XAS and XMCD have been estimated by making spin-orbit coupling constant ζ_d is infinite in reference [61]. As our results are analogous to the Takeo Jo *et* al results, the graph is reproduced from the values presented in the reference [61].

As the 3*d* spin-orbit coupling becomes larger the mixing is also reduced this is the reason that for heavy rare earth the mixing is very small. In XMCD spectra the mixing is highest in case of neodymium (7%) [60]. The difference in the extent of mixing in XAS and XMCD spectra and it cannot be alone explained by the 4*f*-3*d* interaction and spin-orbit splitting. The large extent of mixing in case of neodymium in XMCD is explained by the spin-flip process, as in the heavy rare earth more than half *f* shell is already filled, therefore spin-flip process is forbidden. It is large in case of less than half filled orbitals [60, 61]. Our simulation results are analogous to

Takeo et al results [60], the mixing contribution is also expected to be the same with the error bar of ±0.1 and therefore we did not perform these calculations to check the extent of mixing.

It is confirmed on the application of the spin sum rule on XAS and XMCD spectra that the spin magnetic moment will have strong deviation due to $3d_{5/2}$ -$3d_{3/2}$ mixing and spin-flip process, especially in the case of light rare earth elements. In order to solve this mixing problem in spectra we need to find out the deviation in the spin sum rule (where the integrated intensity of the XAS and XMCD spectra used) compared to the effective spin $\langle S_Z \rangle + 3 \langle T_Z \rangle$ and the real expectation values (S_Z and T_Z) quantitatively. This discussion will be done in the further section.

3.5.3. Estimation of the deviation in XMCD spin sum rule

As far from the above discussion we need to find out the deviation in the spin sum rule (where the integrated intensity of the XAS and XMCD spectra used) compared to the real expectation values (S_Z and T_Z) quantitatively. The atomic multiplet theory simulations not only provide the XAS and XMCD spectra but also provides the real expectation values for the $\langle S_z \rangle$, $\langle L_z \rangle$ and $\langle T_z \rangle$ along the z component in the presence of B_z magnetic field (refer Table 3.3). The relation between integrated XAS and XMCD intensity with the expectation values is as follows

$$\frac{2}{3 \cdot n_h} \cdot \langle S_z \rangle + \frac{2}{n_h} \cdot \langle T_z \rangle = -\cdot \frac{\left[\int_{M_5} \text{XMCD} - \frac{3}{2} \cdot \int_{M_4} \text{XMCD} \right]}{\int_{M_4+M_5} \text{XAS}} \quad \text{.....equation (3.5)}$$

Where n_h is the number of holes for the rare earth elements in the 4*f* shell and T_Z denotes the expectation value of the magnetic dipole operator (or quadrupole spin distribution). Then the $\langle S_z \rangle$ sum rule can be expressed in form of X_I and X_E, Where $X_I = X_E$. The relative integrated XAS and XMCD intensity is defined as X_I and the expectation value part is defined by X_E.

$$X_I = -\cdot \frac{\left[\int_{M_5} \text{XMCD} - \frac{3}{2} \cdot \int_{M_4} \text{XMCD} \right]}{\int_{M_4+M_5} \text{XAS}} \quad \text{.....equation (3.6)}$$

$$X_E = \frac{2}{3 \cdot n_h} \cdot \langle S_z \rangle + \frac{2}{n_h} \cdot \langle T_z \rangle \quad \text{.....equation (3.7)}$$

$$X_{\mathrm{I}} = X_{\mathrm{E}} \quad \text{and} \quad \frac{X_{\mathrm{I}}}{X_{\mathrm{E}}} = \mathbf{1}$$

By defining these equations, the right part (equation 3.6) and the left (equation 3.7) of the spin sum rule equation should be equal to unity (In the case, if both sides are same) [60]. In the spin sum rule formula; the deviation from X_I/X_E =1 represents the extent of non-applicability of the sum rule.

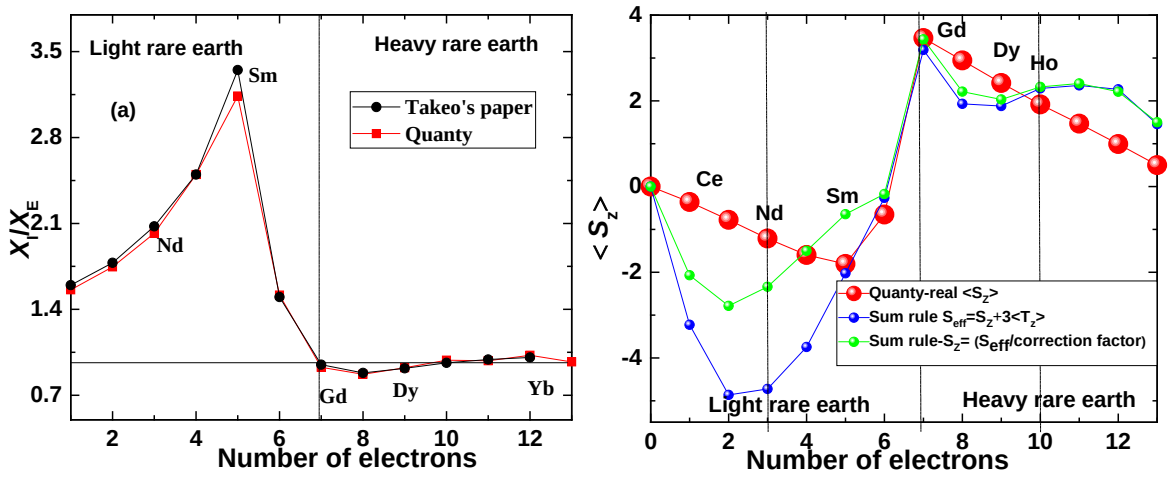

Figure 3.8 (a) calculated the ratio of the left-hand side of the XMCD spin sum rule formula (X_I) to the right-hand side (X_E) from Ce^{3+} to Yb^{3+} to check the applicability of the spin sum rule. The X_I/X_E results estimated from Quanty (red color-circle +solid line) are compared with the Takeo's reported results (Black color-circle +solid line) [60, 61]. (b) Estimation of the spin magnetic moment after using the correction factor (green color-circle +solid line). The results are compared with the quanty generated real expectation values of spin (red color-circle + solid line).

Figure 3.8 (a) and Table 3.5 shows the results of the ratio of X_I to X_E for all the rare earth elements. The X_I/X_E results are in agreement with the Takeo's reported results [60, 61]. From Figure 3.8 (a) it can be concluded that the deviation from the spin sum rule is 60 % in the case of cerium and increases with the increasing number of 4*f* electrons in light rare earth elements. For the elements which have more than half filled shells deviation are less than 10 %. The deviation is sharply changing in between Sm^{3+} and Gd^{3+}. As the spin-orbit coupling between the M_4 and M_5 edges increase for the heavy rare earth elements, then the $3d_{5/2}$ -$3d_{3/2}$ mixing becomes smaller and the sum rule analysis results are in nice agreement with the simple estimates. The multiplet theory simulation results clearly show that the deviation in the spin sum rule for light rare earth elements and X_I /X_E ratio also provides the correction factors for

eliminating the $3d_{5/2}$ -$3d_{3/2}$ mixing problem. We have used this correction factor in spin sum rule in order to eliminate the mixing and the results after correction are presented in Figure 3.8 (b).

Table 3.5 Calculated ratio of the left-hand side of the XMCD spin sum rule formula (X_I) to the right-hand side (X_E) from Ce^{3+} to Yb^{3+} in order to check the applicability of the spin sum rule. The ratio X_I/X_E shows the deviation from the sum rule, so the number can be used as a correction factor for the spin sum rule.

Elements	Number of holes (n_h)	X_I	X_E	Ratio (X_I /X_E) (Correction factor)
Ce^{3+}	13	-0.165	-0.106	1.558
Pr^{3+}	12	-0.270	-0.154	1.745
Nd^{3+}	11	-0.286	-0.141	2.019
Pm^{3+}	10	-0.249	-0.099	2.497
Sm^{3+}	9	-0.149	-0.047	3.137
Eu^{3+}	8	-0.022	-0.014	1.516
Gd^{3+}	7	-0.303	-0.327	0.927
Tb^{3+}	6	-0.214	-0.246	0.871
Dy^{3+}	5	-0.250	-0.271	0.923
Ho^{3+}	4	-0.381	-0.387	0.985
Er^{3+}	3	-0.524	-0.534	0.981
Tm^{3+}	2	-0.756	0.738	1.025
Yb^{3+}	1	-0.971	-0.999	0.971

After correcting the spin magnetic moment using the correction factor the deviation is less compared to previously reported results (refer section 3.5.2 S_{eff}) but still the real expectation values and sum rule analysis results are different. The spin sum rule does not have contribution alone from the $3d_{5/2}$ -$3d_{3/2}$ mixing, it is also influenced by the magnetic dipole term (T_Z) (refer equation 3.2 and 3.4) which can be defined as the quadrupole spin distribution. As rare earth elements exhibit strong spin-orbit coupling, the contribution of the T_Z term cannot be neglected [70]. The influence of the magnetic dipole term will be discussed in the upcoming section with the purpose to estimate the pure spin contribution from spin sum rule.

3.5.4. Estimation of spin magnetic moment by elimination of magnetic dipole term

(i) Magnetic dipole term

The magnetic dipole term (T_Z) is not discussed previously in magnetism until the XMCD sum spin rules have been introduced [24, 35]. It can be described as a quadrupolar spin distribution result of the non-cubic symmetry of the surrounding charge density. A schematic diagram is presented in Figure 3.9 explaining the contribution of T_Z term in terms of influence of environment in solid. Figure 3.9 shows an absorber atom (light gray center) in non-cubic symmetry environment exhibit a fourfold symmetry. If this environment is now uni-axially pressed from the top by internal or external force (indicated by the vertical arrows on the left side), the charge distributions will be changed (refer Figure 3.9 right). The atoms on the left and right side along the horizontal axis will diverge from the central atom. Thus, the charge density on the upper and lower side of the central atom is higher, and reduced at the left and right side. The total charge distribution at the central atom is predominantly regarded as by a radially dependent monopolar charge distribution without symmetry breaking and with the symmetry breaking additional contribution will appear [70] .

Each electron provides spin and on the application of magnetic field spin will aligned itself along the direction of the external magnetic field in the fully attainable saturation condition. In principle, the magnetic dipole term can be described in terms of quadrupolar spin distribution. The change in quadrupolar charge distribution is clear reflection of change in the magnetic dipole moment (T_Z). The magnetic dipole operator mathematically can be defined as $\boldsymbol{T}=\boldsymbol{S}-3\mathbf{r}(\mathbf{r}\cdot\boldsymbol{S})$. The z component of $\boldsymbol{T}$ is defined as $\boldsymbol{Tz}=\boldsymbol{Sz}-3z(x*\boldsymbol{Sx}+y*\boldsymbol{Sy}+z*\boldsymbol{Sz})/r^2$ [70]. If the sample is in saturation and measured at high magnetic field aligned along the direction of the beam, provides an isotropic spin related XMCD spectra. Along the x-y direction measurement the projection of the *T*z component is the half of the value measure along the z direction and will carry the opposite sign (corresponding to the charge distribution). The different orientation along all the directions provides the fully cancelled magnetic dipole moment along the *z*-direction in a case where a uniaxial force will introduce a magnetic dipole term. On the other hand, it can be possible that this type of uniaxial symmetry breaking can be applied by the spin itself under the influence of the external field, in this case the spin –orbit coupling plays major role and alter the charge distribution and will introduce the nonzero magnetic dipole term. The elements where the spin orbit coupling is strong i.e. rare earth elements in that case on changing the direction of the magnetic field will rotate the T_Z along with it. The effective spin moment

(S_{eff}) always includes the spin orbit induced dipole term contribution (refer equation 3.2 and 3.4). This is the case in our rare earth systems, therefore the contribution of the magnetic dipole term (T_Z) needs to be eliminated. There are some simulation results published by the Teramura and Takeo *et al* [60]. They have performed estimation of the T_Z values for full lanthanide (La^{3+} to Yb^{3+}) series using atomic multiplet theory simulations but no application of spin sum rules have been verified for the experimental and theoretical spectra.

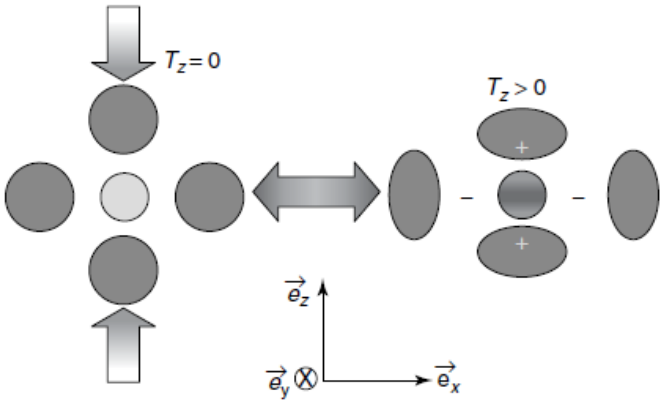

Figure 3.9 schematic diagram of the spin and the charge distribution providing nonzero magnetic dipole term contribution (T_Z) in spin sum rule. The figure is reproduced from the reference [70].

(ii) Magnetic dipole moment for rare earth elements

As we have explained the importance of the magnetic dipole term in case of rare earth elements, now we need to estimate the quadrupole charge distribution for the rare earth elements and the influence of the charge distribution on the magnetic dipole term will be examined. The total negative charge distribution of the 4*f* shell can be defined as [71]:

$$Q = \int n_{4f}(r) \cdot dV$$

However, this distribution is isotropic and does not influence the magnetic anisotropy. To introduce the anisotropy we defined the angle between the 4*f* symmetry axis and the 4*f* charge so that the $n_{4f}(r) = n_{4f}(r,\theta)$. The quadrupole moment is given by following equation [71].

$$Q_2 = \int n_{4f}(r)\left(3\cos^2\theta - 1\right) r^2 \cdot dV \quad \text{.....equation (3.8)}$$

This quadrupole moment is responsible for the crystal field interactions [71]. The sign of the Q decides the shape of the electronic charge distribution. If the value of Q is greater than zero then the shape will be prolate, Q is less than zero then the shape will be oblate or Q=0 it means

it is spherically symmetric [71]. The quadrupole moments are the specific properties of the Hund's rule rare earth ions due to the asymmetric charge distribution.

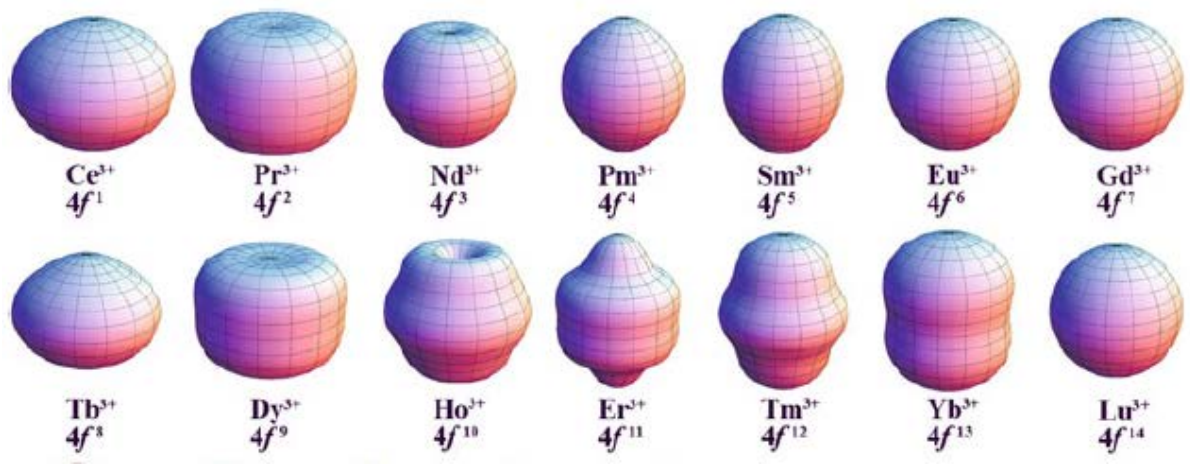

Figure 3.10 charge distribution of the trivalent rare earth ion. Ce^{3+}, Pr^{3+}, Nd^{3+},Tb^{3+}, Dy^{3+}, and Ho^{3+} are oblate ions (axially pressed); Pm^{3+}, Sm^{3+}, Er^{3+}, Tm^{3+}, and Yb^{3+} are prolate ions (axially elongated); Eu^{3+}, Gd^{3+}, and Lu^{3+} are isotropic ion (spherical).The figure is reproduced from reference [72].

From the quadrupole charge distribution definition signifies that Ce^{3+}, Pr^{3+}, Nd^{3+}, Dy^{3+}, Ho^{3+} are oblate ions, while Pm^{3+}, Sm^{3+}, Er^{3+}, Tm^{3+}, Yb^{3+} are prolate ions. Gd^{3+} and Lu^{3+} are isotropic ions since the orbital moment is zero (refer Figure 3.10). The change in the magnetic dipole term in our simulations can be completely explained by the quadrupole moment Q_2 (equation 8). We have performed the atomic multiplet theory simulation using Quanty, which provides the expectation values for the magnetic dipole term (refer Table 3.3).

Figure 3.11 (a) shows the magnetic dipole term estimated by Quanty and the results are compared with the Teramura and Takeo *et al* results [60] and Vanderlaan results [48]. Our results are in good agreement with the results reported by the Takeo *et al*. The results explained by Vanderlaan *et al* [48] are pure Hund's rule values. Therefore the values are larger than the atomic multiplet theory simulation results.

The magnetic dipole moment values estimated by the simulations (refer Table 3.3) are used late on in the spin sum rule in order to eliminate the contribution of the magnetic dipole term. The S_Z estimation (refer Figure 3.11 (b). orange color -solid line + circle) from the spin sum rule analysis is in good agreement now with the real expectation values (refer Figure 3.11 (b) red color -solid line+circle) provided by quanty. Figure 3.12 shows the curves overlapped with the possible corrections as mentioned above and all the values are presented in Table 3.6 (at the end of the section 3.5). These results show that by incorporating all the possible correction one

can estimate the spin magnetic moment using the spin sum rule on theoretical and experimental spectra.

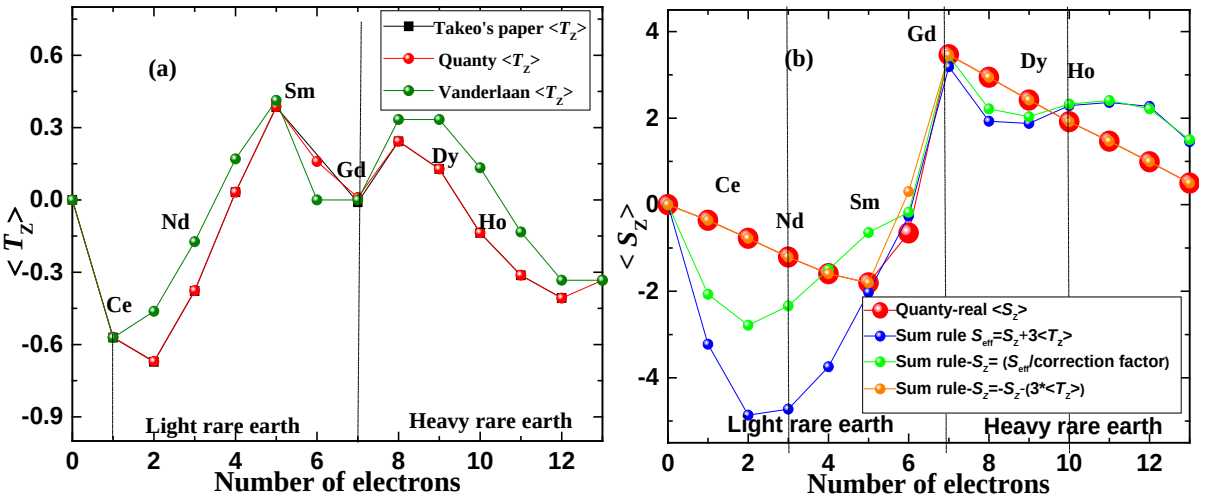

Figure 3.11 (a) estimation of the expectation values magnetic dipole term via Quanty software (circle + solid line- red color) and the results are compared with the Takeo's paper results (circle + solid line- black color)[60] (The light rare earth elements have different sign in Takeo's paper due to different sign convention for *L* and *S* than our results. In order to compare with our results sign has been changed) and from Vander laan paper (circle + solid line- olive color) [48]. All the values plotted here are presented in Table 3.6. (b) Spin magnetic moment corrected from the necessary correction and shown in order as presented in previous sections 3.5.2. 3.5.3 and 3.5.4.

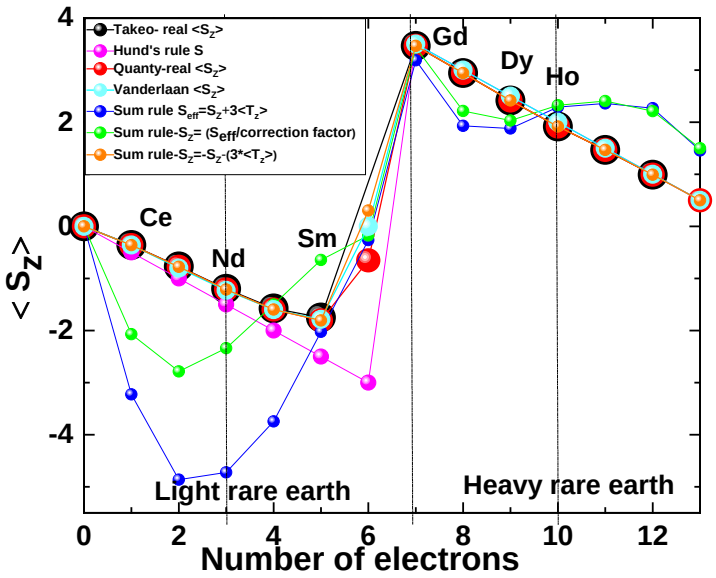

Figure 3.12 spin magnetic moment values estimated from the spin sum rule is compared with the previously reported (Takeo et al [60] and Vanderlaan [48]) results and the expectation values estimated from Quanty.

Table 3.6 atomic multiplet theory simulations provide the XAS and XMCD spectra and the expectation values of the spin (S_Z), orbital (L_Z) and the magnetic dipole term (T_Z). The XMCD orbital and spin sum rules have been applied to full rare earth series spectra and the results are presented in the table. Column (3) shows the orbital angular momentum (Lz). Column (4) Sz+3Tz effective spin (S_{eff}). Column (5) the S_{eff} has been corrected from the correction factor (X_I/X_E) to eliminate the mixing problem. Column (6) spin moment values are estimated by eliminating the magnetic dipole term (T_Z).

Elements	Number of holes (n_h)	Sum rule analysis $\langle L_z \rangle$	Sum rule analysis $S_{eff}=\langle S_z \rangle+3\cdot\langle T_z \rangle$	S_Z= S_{eff}/Correction factor	$S_Z=S-3\cdot T_Z$
Ce^{3+}	13	2.878	-3.226	-2.069	-0.361
Pr^{3+}	12	4.785	-4.862	-2.785	-0.776
Nd^{3+}	11	5.709	-4.761	-2.339	-1.211
Pm^{3+}	10	5.639	-3.745	-1.499	-1.595
Sm^{3+}	9	4.261	-2.023	-0.644	-1.805
Eu^{3+}	8	0.645	-0.264	-0.174	-0.652
Gd^{3+}	7	-0.073	-3.188	-3.435	-3.465
Tb^{3+}	6	-3.098	-1.928	-2.214	-2.943
Dy^{3+}	5	-5.105	-1.877	-2.032	-2.417
Ho^{3+}	4	-6.118	-2.291	-2.325	-1.916
Er^{3+}	3	-6.052	-2.359	-2.405	-1.467
Tm^{3+}	2	-4.963	-2.269	-2.213	-0.990
Yb^{3+}	1	-2.999	-1.456	-1.499	-0.5

Figure 3.12 shows the spin magnetic moment results in the following order-

1. Takeo *et al* [60] results (refer Figure 3.12 black color -solid line+circle)
2. Hund's rule (refer Figure 3.12 magenta color -solid line+circle)
3. Quanty real expectation values (refer Figure 3.12 red color -solid line+circle)
4. Vanderlaan [48] results (refer Figure 3.12 cyan color -solid line+circle)
5. The effective spin values (refer Figure 3.12 blue color -solid line+circle)
6. The spin (S_z) after correcting the mixing problem via using correction factor (refer Figure 3.12 green color -solid line+circle).
7. Spin S_z estimation (refer Figure 3.12. orange color -solid line+circle) after eliminating the magnetic dipole term contribution.

The complete sum rule analysis results (orbital L_Z and spin S_Z angular momentum) of the simulated spectra of the full rare earth series ground state configurations are presented in table 3.6. The sum rule analysis results are also presented in Bohr magneton/atom (in red).

Table 3.7 shows the orbital moment, spin moment, their sum and ratio for all rare earth elements. Spin moment corrected to all necessary corrections. The values in red show the magnetic moment in Bohr magneton /atom.

Elements	Number of holes (n_h)	L_z	S_z (m_S=μ_B/atom)	L_z+S_z (m_L +m_S =μ_B/atom)	L_z/S_z (m_L/m_S)
Ce^{3+}	13	2.88	-0.36(-0.72)	2.48(2.16)	-7.88(-4)
Pr^{3+}	12	4.79	-0.78(-1.56)	4.01(3.23)	-6.17(-3.07)
Nd^{3+}	11	5.71	-1.21(-2.42)	4.49(3.29)	-4.72(-2.36)
Pm^{3+}	10	5.64	-1.59(-3.18)	4.04(2.46)	-3.54(-1.77)
Sm^{3+}	9	4.26	-1.81(-3.62)	2.46(0.64)	-2.36(-1.18)
Eu^{3+}	8	0.65	-0.65 (-1.3)	-0.01(-0.65)	-0.99(-0.5)
Gd^{3+}	7	-0.07	-3.47(-6.94)	-3.54(-7.01)	0.02(0.01)
Tb^{3+}	6	-3.10	-2.94(-5.88)	-6.04(-8.98)	1.05(0.53)
Dy^{3+}	5	-5.11	-2.42(-4.84)	-7.52(-9.95)	2.11(1.06)
Ho^{3+}	4	-6.12	-1.92(-3.84)	-8.03(-9.96)	3.19(1.59)
Er^{3+}	3	-6.05	-1.47(-2.94)	-7.52(-8.99)	4.13(2.06)
Tm^{3+}	2	-4.96	-0.99(-1.98)	-5.95(-6.94)	5.01(2.51)
Yb^{3+}	1	-2.99	-0.5(-1)	-3.49(-3.99)	5.99(2.99)

3.6. Analysis procedure of the experimental spectra

The process of XMCD data analysis and the application of the XMCD sum rules for the rare earth $M_{4,5}$ edge is presented in this section. To obtain the spin-averaged XAS and the XMCD, the absorption is measured as a function of the photon energy for parallel and antiparallel orientation of the photon spin (polarization) in total electron yield mode. The analysis of the spectra is shown here using the absorption at the neodymium $M_{4,5}$ edges of the rare earth-based ferromagnet $FeNd_{14}B$ textured thin film as an example. The analysis of the XMCD spectra can be done using spin sum rule. The underlying principles are explained as follows.

1. The measured raw absorption spectra are normalized to the incoming photon flux. The remaining linear background is fitted by a linear function in the pre-edge region and this linear function is removed by subtraction (Figure 3.13 (a) and (b)).

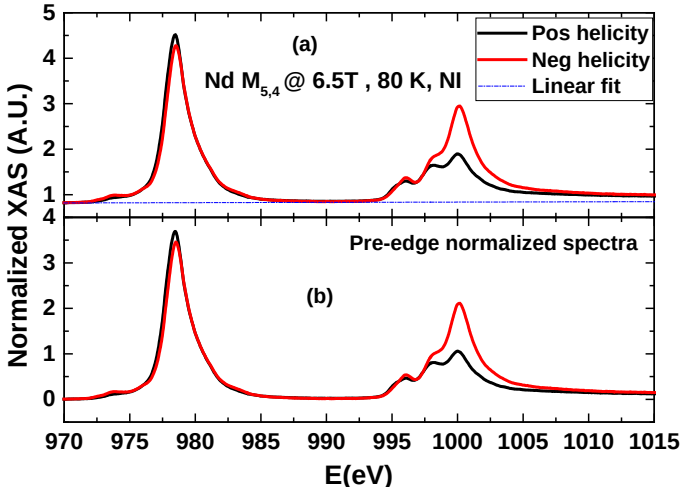

Figure 3.13 (a) the linear fitting (blue dots) at pre-edge region of the Nd $M_{4,5}$ XAS spectra. (b) The Nd $M_{4,5}$ XAS pre-edge normalized spectra

2. Thus, one obtains a pair of absorption spectra $\mu^{+}(E)$ and $\mu^{-}(E)$ for parallel and antiparallel orientation of photon spin and sample magnetization, respectively. The isotropic XAS, often also called the "white line", is then given by

$$\mu\ (E) = \mu^{+}(E) + \mu^{-}(E) + \mu^{0}(E) \text{ or } \mu\ (E) = \frac{3}{2}\left(\mu^{+}(E) + \mu^{-}(E)\right) \text{.....equation (3.9)}$$

Relation for the XMCD according to the definition presented above

$$\Delta\mu\ (E) = \mu^{+}(E) - \mu^{-}(E) \text{.....equation (3.10)}$$

3. The spectra contain contributions of the dipole transitions $3d \rightarrow 4f$ (resonance-like peaks), $2p \rightarrow s$ and to the continuum (step-like increase).

4. The continuum is approximated by a two-step function (Figure 3.14 (a) black dash-dot curve) [24].

5. Finally, the spectra are normalized to unity, to obtain the absorption and the magnetic information on a per-atom basis. When measured at grazing incidence or by Fluorescence Yield (FY) the spectra are corrected for saturation effects [73, 74]

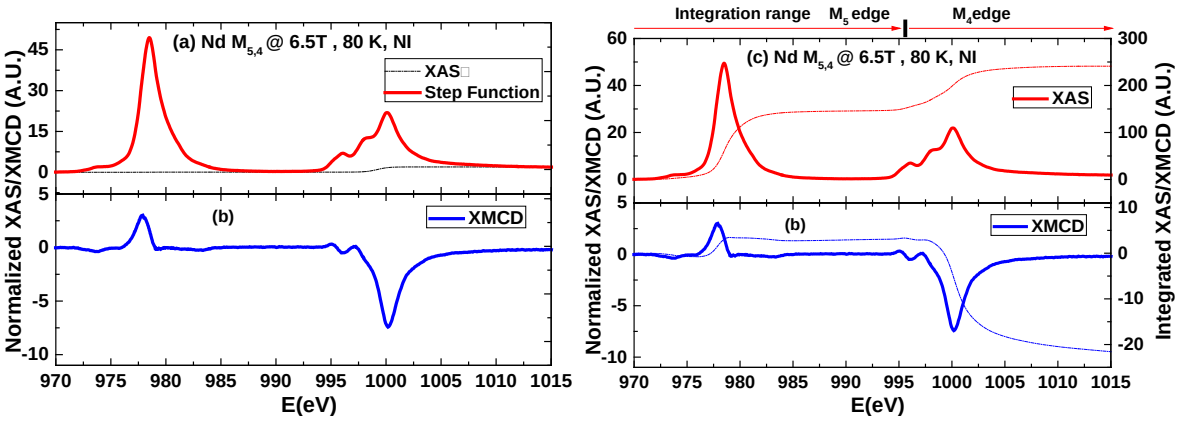

Figure 3.14 post edge normalized XAS spectra (a) and XMCD spectra (b) the contribution of the continuum-step function (black color- short dot-dashed line) of the respective XAS spectra. (a) Illustration of the application of the sum rules. The XAS and XMCD spectra of Nd $M_{4,5}$ edge ($Fe_{14}Nd_2B$ textured thin film specimen) is shown as an example. (c) Normalized isotropic XAS (solid line-red color) together with the integration (short dot-dashed line-blue color) and (d) XMCD (solid line blue) and integrals needed for the sum rule analysis (dashed lines). The integration ranges are marked at the top of the graph.

6. For the application of the sum rules to determine spin and orbital moments, the normalized XAS and XMCD spectra have to be integrated into the range of the considered edges (figure 3.14 (c) and (d)). Therefore, the continuum contribution has to be subtracted from the isotropic spectrum.

7. For experimental spectra at $M_{4,5}$ edges, the XMCD orbital (equation 3.3) and spin sum rules (equation 3.4) are presented here. Defining a number of holes n_h=14-n_{4f} and the integrated areas of the XAS and XMCD are defined as follows:

$$\text{IntXAS} = \int_{M_i} \left(\frac{1}{2}\left(\mu^+ + \mu^-\right) - \mu_{step} \right) dE \text{ and } \text{IntM}_i = \int_{M_i} \Delta\mu(E)dE \text{ where } i = 4,5 \text{.....equation (3.11)}$$

8. The example for pre edge normalization of XAS spectra is shown in Figure 3.13 (a). The upper panel shows the XAS (Figure 3.14 (a) solid red color line), the step-function (Figure 3.14 (a) dot dashed black color line) and the integral over the XAS (after step function subtraction Figure 3.14 (c)). The lower panel shows the XMCD (Figure 3 14 (b) solid blue color line) and the two integrals of it as they enter into the sum rules of equations 3.3 and 3.4 (Figure 3.14 (c) and (d) dot-dashed lines in red and blue). Note that the respective scale for the integrals is given on the right-hand side.

9. If the initial state level is not spin-orbit split, for example at K edges, the XMCD will yield only information about the orbital moment. In the orbital sum rule, the integrals are taken only over the single edge *j* with the areas IntXAS of the XAS and $IntM_i$ of XMCD at the respective edges named. By substituting the values of integrated XAS and XMCD spectra in the equation for a spin (equations 3.4) and orbital (equations 3.3) sum rule the one can obtain the projection of the orbital (L_Z) and effective spin S_{eff} (S_Z+3T_Z) along the z-direction.

10. At 300 Kelvin, neodymium provides the projected spin moment of S_{eff} =-2.25±0.2 and orbital magnetic moment of L_Z (m_L) = 2.47±0.02. The orbital to spin moment ratio (L_Z/S_Z) is -1.09±0.2 and their sum (L_Z+S_Z) is 0.22±0.01.

11. During the XMCD simulations above (section 3.6), it was suggested that the spin sum rule of equation 3.4 is invalid for rare earth $M_{4,5}$ XMCD spectra and cannot be used to deduce the spin contribution to the 4*f* moment, while the orbital sum rule of Eq. equation 3.3 is still applicable. The reason for the non-applicability of the spin sum rule is explained in detail (section 3.5). For neodymium, the correction factor is 2.019 (X_I/X_E ratio- section 3.6.3) and after correction, the effective spin moment S_{eff} is S_Z+3T_Z =-1.114±0.2.
S_{eff} (S_Z+3T_Z) =-2.25±0.2, correction factor =2.02 (Table 3.6 and 3.7), S_Z =-2.25/2.02=-1.114±0.2.

12. On the other hand, in the case of the magnetism of 4*f* electrons which possess more or less a localized nature, the magnitude of magnetic dipole term $<T_Z>$, which cannot be experimentally determined, is expected to be comparable to that of $<S_Z>$. One drawback here is that $<T_Z>$ can be only estimated via theory. The Quanty simulations results provide the expectation value for the $<T_Z>$ also, but this is applicable when magnetic moment is in saturation condition. Therefore, eliminating the $<T_Z>$ is a problematic part form the experimental data.

13. One can eliminate $<T_Z>$ (For Nd^{3+}=-0.376) without knowing its real value by just knowing the reduction between the experimental effective spin magnetic moment value (from experiment S_{eff}=-2.25±0.2) and the effective spin moment from the simulated spectra (from theory S_{eff}=-4.761 refer Table 3.6).
Reduction= -4.761/-2.25 =2.10,
$S_z= (S_Z+3T_Z)_{exp} –((3*T_Z)/reduction)$ = -1.114±0.2-(3*(-0.376))/2.10 = -0.58

The spin magnetic moment came out to be S_Z =-0.58±0.2.

14. The magnetization M of the sample is obtained from the spin magnetic moment m_S (in Bohr magneton), the orbital magnetic moment m_L (in Bohr magneton), and the atom density *n*.

$$M = n(m_S + m_L) = -n(2 \cdot \langle S_Z \rangle + \langle L_Z \rangle)\mu_B \quad \text{.....equation(3.12)}$$

15. From equation 7.4 one can estimate the orbital and spin magnetic moment in Bohr magneton/atom. The results are as follows: m_L = 2.47±0.02, m_S = -1.15±0.02, m_L+m_S = 1.32±0.02 and m_L/m_S = -2.14±0.02.

16. One can notice from the T_Z dependencies of the estimated magnetic moments that the assumption of T_Z= 0 brings about a serious overestimation or underestimation of *ms* (depends on the sign of T_Z), resulting in the resulting reduced total magnetic moment (m_L+m_S) and the ratio (m_L/m_S). After incorporating the necessary corrections one can obtain the orbital to spin ratio comparable to the Hund's rule (section 3.2-Table 3.1).

3.7. Discussion

The atomic multiplet theory simulations have been performed for full lanthanide series using Quanty software by the parameters provided in the previously reported results [37]. The sum rule analysis of the simulated spectra shows the deviation in the spin sum rule for rare earth elements. The meticulous study on the deviation from the spin sum rule (S_Z) in case of trivalent rare earth elements (from cerium to ytterbium) at $M_{4,5}$ edges is performed in order to make the spin sum rule useful for the application. To estimate the deviation left (X_I) and right (X_E) part of the spin sum rule is compared to unity. The deviation from the unity exhibit the deviation in the spin sum rule. It has been observed that for less than half filled shell the deviation is larger and increases from 60% (cerium) to the 230% (samarium), while for the half-filled *f* shell (gadolinium) and more than half-filled *f* shells (dysprosium, terbium, and holmium) it is less than 10%. These results show that the corrections must be made in order to apply the spin sum rule especially for the light rare earth elements (less than half filled *f* shells). The reason for the deviation can be explained by the 3*d*-4*f* exchange interaction, the electronic charge distribution of the electrons in ground state configuration. This mixing phenomenon is strongly influenced by the electron distribution among the orbitals in *f* shell. It has been also observed that the spin sum rule has also a strong influence from the magnetic dipole term T_Z (quadrupole spin

distribution), therefore in order to estimate the pure spin contribution of the term T_Z also need to eliminate. Briefly, our investigation explains that the spin sum rule can be applied for the $M_{4,5}$ edges if all the necessary correction have been incorporated systematically.

4. X-ray absorption (XAS) and x-ray magnetic circular dichroism (XMCD) investigation of $CeFe_{11}Ti$ magnets

4.1. Introduction

Many interesting physical properties of cerium compounds derived from the localized 4*f* shell with an electron occupancy close to unity are discussed in this chapter. Ce $M_{4,5}$ XAS and XMCD provide direct and local access to the 4*f* states and its electronic and magnetic properties. As mentioned in chapter 3 in section 3.3 the earliest reports of rare earth $M_{4,5}$ x-ray absorption spectra were dated back to 1931 [46]. The investigation of first Ce $M_{4,5}$ spectra with monochromatized bremsstrahlung was reported in 1970 [75]. Following the progress, in 1983, Gunnarsson and Schönhammer (GS) proposed the GS theory [25, 26]. It allowed addressing the signatures of the *f*-level occupation in the spectra and clarified the issue of the Ce valence In the framework of the GS theory, contributions from different 4*f* occupancies are expected in the Ce $M_{4,5}$ spectra of mixed-valent Ce compounds. Assuming that the 4*f*-4*f* Coulomb interaction reduces configurations with more than two 4*f* electrons in the ground state, contributions from the $3d^{10}4f^0 \rightarrow 3d^9 4f^1$, $3d^{10}4f^1 \rightarrow 3d^9 4f^2$ and $3d^{10}4f^2 \rightarrow 3d^9 4f^3$ transitions can appear in the spectrum[18]. Fuggle et al demonstrated the application of GS theory to Ce $M_{4,5}$ XAS. He successfully identified and quantified the contributions from the $f^0 \rightarrow f^1$ and $f^1 \rightarrow f^2$ transitions to the spectrum [76]. Shortly after their publication, the interpretation of Fuggle *et al.* was reassured in similar studies by Kaindl *et al* [77] and is accepted for the Ce $M_{4,5}$ spectra investigation addressing the issue of valence for different Cerium compounds [18, 37, 78-81].
As a progress in the computational investigation, Thole *et al.* introduced the well-established concepts of atomic physics to their computer code on the basis of a program written by Cowan to calculate atomic spectra [54]. Since the initial publication, Thole-code has extensively used to interpret experimental data and for further calculations [55]. The Ce $M_{4,5}$ spectra of materials that can be described in the atomic limit of a single localized 4*f* electron are well represented by full multiplet calculations considering only the Hund's rule ground state.[18] In 2008, Hansmann *et al.* showed that a combination of temperature-dependent x-ray natural linear dichroism (XNLD) measurements and full multiplet calculations under consideration of the crystal field allows quantitative clarification of the ground state and the crystal field scheme of Cerium compounds [82]. This had been a long-standing issue, especially in cases where the crystal field mixes the states in the $J = 5/2$ multiplet.
In the original model calculations by Gunnarsson and Schönhammer, only the relative weights of the $f^0 \rightarrow f^1$ and $f^1 \rightarrow f^2$ contributions to Ce $M_{4,5}$ XAS were analyzed [25, 26]. It can be

calculated in full multiplet theory and can be used to study crystal field effects for systems with small hybridization [83] (refer thesis by Christian Michael Praetorius [18] see section 6.1.1). The systematic studies of experimental spectra for different degrees of hybridization that are known were performed by Kaindl [52, 77], Van der Laan [79], Schillé [80] and Finazzi *et al* [81].

In these investigations, Van der Laan [8] for the first time attempt to explain hybridization induced line shape changes. They argued that local character of the atomic 4*f* level to band-like character with a finite width. This shows, if the bandwidth approaches the 3*d* shell spin-orbit splitting, *J* is not a good quantum number anymore and the *J* = 5/2 and *J* = 7/2 states are mixed[18]. In summary, Van der Laan *et al*[79] underline the importance of an interference term, which causes the mixed spectra to differ from simple weighted sums of the pure *J* = 5/2 and *J* = 7/2 spectra. Such calculations were first published in 1988 by Jo and Kotani[84]. Schillé *et al* [80]. They published XAS and XMCD spectra of three different Cerium compounds with varying degree of hybridization: CeCuSi, $CeRh_3B_2$ and $CeFe_2$[80]. The data are of higher quality than in the previous works and confirm the observed line shape changes. Apparently, these authors tried to simulate their spectra with full multiplet calculations referring to the study of Van der Laan *et al*[79].

Okane *et al* [63] simulate their data by simple weighted sums of pure *J* = 5/2 and *J* = 7/2 spectra without an interference term. They simply generated pure *J* = 5/2 and *J* = 7/2 spectra and mixed and tried different ratios. Furthermore, they did not consider that the presence of a crystal field influences the Ce $M_{4,5}$ spectral shape (see section 6.1.2). Finazzi *et al* [81] have explained the Cerium line shape variation and reduction in the magnetic moment by charge transfer effects. However, experimental studies that quantitatively include the crystal field in the analysis of Ce $M_{4,5}$ XMCD are not known.

In this direction, the present thesis addresses the issue of *J* = 7/2 admixture to the ground state, effects of crystal field in the shape of XMCD spectra and the charge transfer effects are also discussed for Ce $M_{4,5}$ XAS in section 4.6 (b).

In the following chapter, a review of the current state of research is given as well as a summary of the procedures that were developed in the present work to evaluate and simulate Ce $M_{4,5}$ XAS and XMCD spectra. These considerations provide a thoughtful background to produce theoretical and experimental results. Such results are presented and discussed in this chapter.

4.2. Studies on Ce-Fe compounds

Alloys and intermetallic compounds obtained by combining rare-earth (RE) metals with 3*d* metals have attracted tremendous interest due to their application in electronics. Their application became possible as a result of their hard magnetic properties [2]. In general, the sub-lattice is responsible for high values of magnetization and magnetic ordering temperature, while the 4*f* sub-lattice provides the magnetic anisotropy. The discovery of Nd-Fe-B type of compounds initiated a search for other novel materials and in this direction, the magnetic properties of iron-rich rare-earth intermetallic compounds with uniaxial crystal structures have been extensively studied[85].

In this respect, the ternary alloys of composition $REFe_{11}M$ (RE=rare earth, M =titanium , molybdenum) are of the great interest in research because they exhibit strong uniaxial anisotropy with reasonably high Curie temperature (T_c=487K) and magnetic moment is 15 Bohr magneton/formula unit (~1 Tesla), which can be suitable for application as permanent magnet [86]. Hence, the magnetic properties of the pseudo-binary compounds with formula REFeM (M=Ti, Cr, V, Al) mostly fulfilled requirements for the technological applications [86, 87].

The controlled annealing of alloys crystallizes them in tetragonal phase with $ThMn_{12}$ type structure with the rare earth (RE) elements such as cerium(Ce), yttrium(Y), praseodymium (Pr) and neodymium[88]. The crystal structure obtained from the neutron diffraction experiment is shown in Figure 4.1. The titanium (Ti) sites are exclusively located in the 8i site of the structure while the 8j and 8f positions are taken by the iron (Fe) and the 2a position by cerium. The position of cerium, iron, and titanium is shown in Figure 4.1. [86].These materials are known for their nitriding and hydriding properties, which can increase curie temperature (T_c) up to 700K, saturation magnetization (M_S=22 Bohr magneton/formula unit) and influence the magnetic anisotropy[89]. The hard magnetic properties of Nd-$Fe_{12-x}Mo_x$ melt spun ribbons are also studied. It is found that the nitriding improves the coercivity by 0.4kOe, while by changing the quenching rates (*v*s=10, 12.5, 15, 17.5,30 m/s) and 6kOe increase in coercivity (H_c) observed[90]. Cerium is the abundant available and it is cheapest among all the other rare earth elements i.e. neodymium, praseodymium and dysprosium elements. This makes its use economically viable in magnetic materials.

The investigation on melt-spun ribbons of the composition $CeFe_{10.5}Mo_{1.5}$ exhibits coercivity of (H_c)= 0.6KOe with maximum energy product $(BH)_{max}$=0.121 MGOe [91]. However, cerium exhibits transitional valency and has a tendency to give up the 4*f* electron resulting in Ce^{4+}

valency[92]. This itinerant nature of cerium lowers the Curie temperature (T_c) and saturation magnetization (M_s), therefore the partial substitution of cobalt (Co) is an effective way to deal with this problem[93].As cobalt has a smaller ionic diameter than Fe, the substitution of cobalt results in lattice contraction. Recently $Fe_{11-x}Co_xTiCe$ compound has been studied and observed the anisotropy constant of K_1=2.25 MJ/m^3 and a saturation polarization of J_s=1.27 Tesla were observed at 473 Kelvin (200°C)[94]. The $Fe_{11-x}TiCe$ alloys have been successfully prepared [95] by melt spinning with enhanced T_c= 963 Kelvin (690°C) on introducing Cobalt[93].

Pseudo-binary alloys are heavily investigated for magnetic and structural properties. [76][9-11] However, still there is a lack of spectroscopic investigations for understanding the contribution of cerium and iron to the magnetic behavior of the Ce-Fe-Ti compounds. The first neutron diffraction investigation showed that the total magnetic moment of cerium is -0.5 Bohr magneton (μ_B) but they were unable to isolate the separate contribution obtained from 4*f* and 5*d* electrons [96]. The effect of hydrogen (H_2) absorption on the cerium electronic state in the $CeFe_{11}Ti$ compound has been examined by XAS and XMCD spectroscopic investigations [97]. The neutron diffraction [96] and XMCD results [97] confirm the strong correlation between the structural and magnetic changes associated with the modification of the hybridization between the iron -3*d* and cerium-5*d* bands, the 4*f* localized electrons do not contribute considerably [97]. The x-ray magnetic circular dichroism experiments at the $M_{4,5}$ absorption edges of cerium in the intermetallic compounds CeCuSi, $CeRh_3B_2$, and $CeFe_2$ show that 4*f* orbital contribution is significantly higher than the one predicted from spin-resolved band-structure calculations and confirms the extreme sensitivity of the orbital contribution to the degree of localization of the 4*f* electrons[80]. For the Cerium $M_{4,5}$ absorption edges in Ce_xFe_{1-x}(x=0.19 or 0.27) amorphous alloys and Ce (10Å)/Fe (30Å) multilayers x-ray magnetic circular dichroism results described that the dichroism signal in these systems is very sensitive to the degree of hybridization of the *4f* electrons with the valence band[81]. The ground state of cerium in the more strongly hybridized system results in a mixing of atomic *J*=5/2 and *J*=7/2 states[98]. The Ce/Fe multilayer specimen investigation gives evidence of hybridization of cerium-4*f* electrons with valence band [81].The investigation on cerium-doped yttrium iron garnet ($Y_3Fe_5O_{12}$) thin films also have been performed. The results show that the cerium doping activates the selective charge transfer from cerium to iron tetrahedral sites. This causes the changes in electronic and magnetic properties of the parent compound and reduces the exchange coupling between the Cerium and Iron magnetic moments[99].

In this work, as the part of the rare earth, lean magnetic materials we investigated $CeFe_{11}Ti$ single phase specimen. [100]. The main objective of this work is to develop a microscopic

understanding of the cerium-based intermetallic compound and to discern the magnetic contribution of cerium and iron, further investigations related to the magnetic and structural properties have been performed using characterization techniques like superconducting quantum interference device (SQUID) magnetometer (Quantum design-MPMS3) and x-ray diffraction (XRD) and scanning electron microscopy (SEM) respectively.

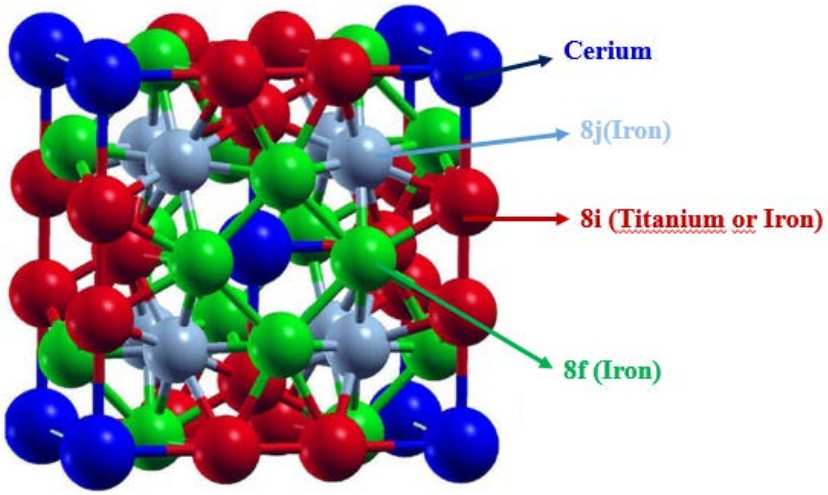

Figure 4.1 a conventional unit cell model of the $ThMn_{12}$. Large dark blue spheres represent rare earth atoms, cerium. The three different Wyckoff positions 8i (Ti, Fe), 8j (Fe) and 8f (Fe) occupied by transition metal atoms are represented by medium spheres in red, light blue and green. Reproduced from the reference[101].

4.3. Structural Investigations

4.3.1. Inductive coupled plasma spectroscopy (ICP –OES) and SEM microscopy:

We have prepared three $CeFe_{11}Ti$ specimens by conventional solid state sintering process [94]. In order to precisely compare the total sample magnetization with the element specific XMCD results, the chemical compositions of the sintered magnets have been analyzed by inductive coupled plasma spectroscopy (ICP-OES) (Spectro-Ciros). The stoichiometry turned out to be $Ce_{1.2}Fe_{12}Ti$, $Ce_{1.36}Fe_{11.8}Ti$ and $Ce_{1.6}Fe_{11.5}Ti$ for the three received specimens respectively. The ICP-OES spectroscopic analysis shows that there is the only negligible presence of impurities like Si at **0.005** %, Mg at **0.001** % and Cu at **0.007** %.

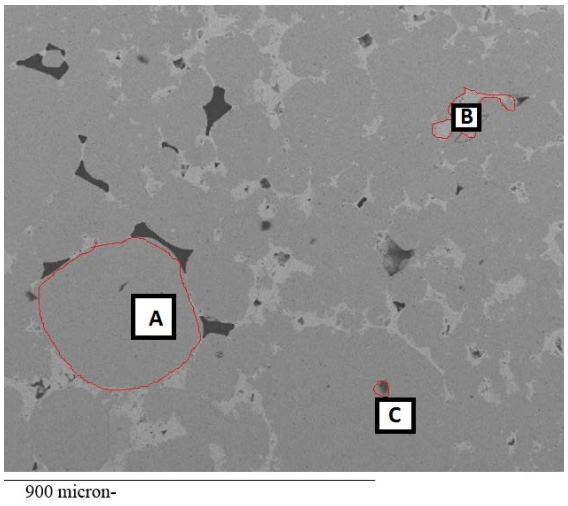

Figure 4.2 scanning electron microscopy (SEM) images of- $Ce_{1.2}Fe_{12}Ti$. Where A is hard magnetic-phase ($CeFe_{11}Ti$), B is Ti carbonitride, C is $CeFe_{2,}$ and Fe_2Ti[100].

The scanning electron microscope images of $Ce_{1.2}Fe_{12}Ti$ is shown in Figure 4.2. Line scans at different positions on the sample have been performed for elemental analysis (Position A, B, and C). The larger grains of hard magnetic-phase ($CeFe_{11}Ti$) are labeled as A in Figure 4.2) and the smaller grains labeled B and C in Figure 4.2 represents Ti carbonitride and $CeFe_{2,}$ Fe_2Ti[100]. The spectroscopic analysis shows the presence of **82.5±5**% iron, **8.3±2**% cerium and **8.1±2** % titanium. As all the line scan results are analogous to each other, therefore only one scan with error bars has been presented here. It has been found that all three different investigated samples exhibit hard magnetic phase A ($CeFe_{11}Ti$) as the major phase. The co-existence of multiple binary phases B- Ti carbonitride, soft magnetic phase C-$CeFe_{2,}$ and Fe_2Ti (Figure 4.2) respectively in the vicinity of the stoichiometry have been identified[100]. The $CeFe_2$ and Fe_2Ti give the same contrast in Figure 4.2.

The hard magnetic phase $CeFe_{11}Ti$ and $(Fe,Ti)_{17}Ce_2$ is found to be **75-80** % and $CeFe_2$ is **15-20**% with remaining fractions of oxide. (Figure 4.2 A-hard magnetic-phase $CeFe_{11}Ti$, B- Ti carbonitride, C-$CeFe_2$ and Fe_2Ti)[100].

4.3.2. X-ray diffraction investigation (XRD)

The x-ray powder diffraction patterns recorded using Co-Kα radiation (1.78896 Å) on the $Ce_{1.2}Fe_{12}Ti$ $Ce_{1.36}Fe_{11.8}Ti$ and $Ce_{1.6}Fe_{11.5}Ti$ specimens are shown in Figure 4.3., in black ($Ce_{1.2}Fe_{12}Ti$), red ($Ce_{1.36}Fe_{11.8}Ti$) and blue ($Ce_{1.6}Fe_{11.5}Ti$). The different $CeFe_{11}Ti$ alloy

samples are grinded in an agate mortar in fine powder form. Later the powder is suspended in isopropanol and sedimented onto (510)-cut silicon wafers. Diffraction patterns were recorded on an analytical/ X'Pert Multi-purpose diffractometer (MPD) working in ɵ-ɵ geometry equipped with a cobalt tube as an x-ray source, a graphite monochromator and X'Celerator detector in the diffracted beam.

Table 4.1 phase analysis results of $Ce_{1.2}Fe_{12}Ti$, $Ce_{1.36}Fe_{11.8}Ti$ and $Ce_{1.6}Fe_{11.5}Ti$ specimens presented in weight % and saturation magnetization (M_S) in T per Fe atom and μ_B/ (F.U.).

Specimen	$CeFe_{11}Ti$ (wt. %)	$CeFe_2$ (wt. %)	M_S ($\frac{\mu_B}{\text{Fe atom}}$.)
$Ce_{1.2}Fe_{12}Ti$	98.5±2	1.5±0.2	1.54±0.1
$Ce_{1.36}Fe_{11.8}Ti$	88±2	12±1	1.46±0.1
$Ce_{1.6}Fe_{11.5}Ti$	83±2	17±1	1.41±0.1

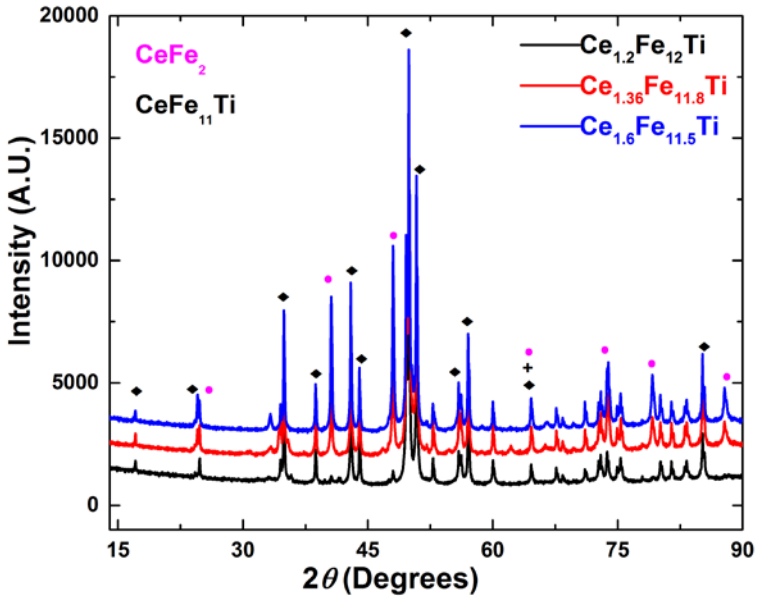

Figure 4.3 x-ray diffraction spectra of $Ce_{1.2}Fe_{12}Ti$ (black) $Ce_{1.36}Fe_{11.8}Ti$ (Red) and $Ce_{1.6}Fe_{11.5}Ti$ (Blue) specimens. The peaks correspond to $CeFe_{11}Ti$ and $CeFe_2$ phase are indicated by black and magenta dots respectively.

The diffraction data were evaluated using the TOPAS software (Bruker) by means of multi-phase Rietveld refinement without considering effects of micro-absorption. The possible occurrence of tetragonal $ThMn_{12}$-type $CeFe_{11}Ti$ phase with *I*4/*mmm* symmetry, cubic $CeFe_2$ laves phase with $Fd\bar{3}m$ symmetry, CeO_2 with $Fm\bar{3}m$ symmetry and Ce_2O_3 with $P\bar{3}m1$ symmetry has been considered. The x-ray diffraction peaks correspond to $CeFe_{11}Ti$ and $CeFe_2$

phase is indicated by black and magenta dots in Figure 4.3. The unit cell parameters like atomic distances for the analysis are referred from the database[102]. The refinement results provide the relative amount of the main phases in weight percent and the results are summarized in Table 4.1. All the specimens confirmed the presence of the desired $ThMn_{12}$ type of phase, with tetragonal structure. In the diffraction patterns of Ce-Fe-Ti alloys, the $CeFe_{11}Ti$ phase is seen predominant and a minor fraction of the $CeFe_2$ phase was detected. Additionally, very tiny reflections related to CeO_2 or Ce_2O_3 were found which are not considered in this study. The quantitative phase analysis from x-ray diffraction Rietveld refinement confirmed that $Ce_{1.2}Fe_{12}Ti$ specimen has the highest content (98.5%) of desired magnetic phase $CeFe_{11}Ti$ relative to the other specimens (Refer Figure 4.3 and Table 4.1). For the x-ray magnetic circular dichroism investigation, only the $Ce_{1.2}Fe_{12}Ti$ specimen with the highest content is considered.

4.4. Magnetic investigation-SQUID magnetometry

Figure 4.4 (a) shows the magnetization curves for the three different isotropic specimens of the stoichiometry, $Ce_{1.2}Fe_{12}Ti$ $Ce_{1.36}Fe_{11.8}Ti$, and $Ce_{1.6}Fe_{11.5}Ti$ obtained at room temperature. All the three specimens are ferromagnetically ordered at room temperature. The hysteresis (magnetization vs magnetic field) behavior is found similar for all, while all the three samples are saturated at about 2 Tesla (20KOe) and show significant compositional dependence. At the highest field of 6.5 Tesla and 300 Kelvin, the maximum magnetization of 18 Bohr magneton/formula unit: J ($\mu_0 M_s$) =1 Tesla (at 80 Kelvin is 21.7 Bohr magneton /formula unit: J ($\mu_0 M_s$) =1.2 Tesla) (refer Figure 4.4 (b)) is recorded for $Ce_{1.2}Fe_{12}Ti$. The results are similar to the experimental results reported in the literature [86, 103]. Figure 4.4 (b) shows the magnetization curves for the $Ce_{1.2}Fe_{12}Ti$ specimen at two different temperatures (300 Kelvin and 80 Kelvin). We observed 17 % increase in magnetization at low temperature. The recorded remanence is the 0.3% of the saturation magnetization and the coercivity is merely 6 Oersted at 300 Kelvin. The total magnetization of specimens decreases with the increase in $CeFe_2$ content in $Ce_{1.36}Fe_{11.8}Ti$ and $Ce_{1.6}Fe_{11.5}Ti$ specimen. The formation of $CeFe_2$ phase causes 10% reduction in total magnetization of the specimen which is in good agreement to the x-ray diffraction phase ratios presented in Table 4.2. The specimen $Ce_{1.2}Fe_{12}Ti$ with the maximum content of $CeFe_{11}Ti$ phase shows the highest magnetization compared to the other two specimens. Therefore, from the x-ray diffraction and magnetic investigation results we consider the $Ce_{1.2}Fe_{12}Ti$ specimen only for x-ray magnetic circular dichroism study.

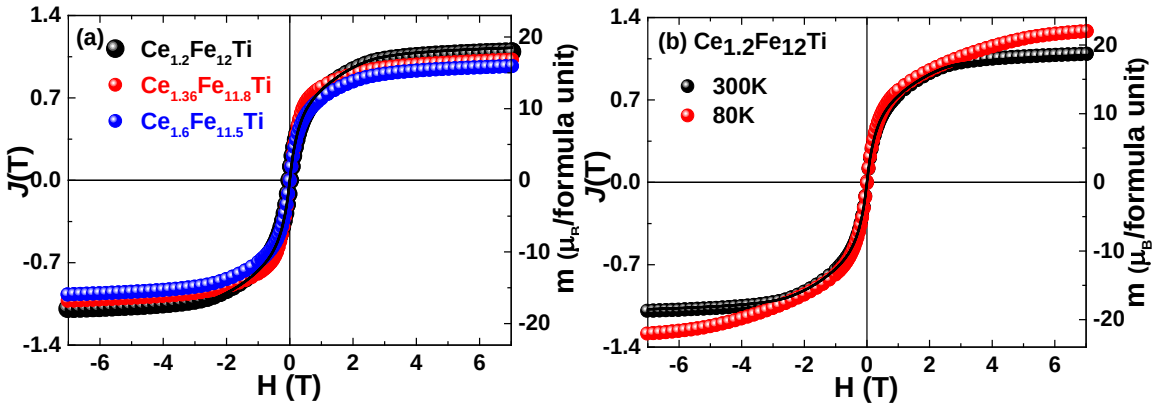

Figure 4.4 (a) SQUID Hysteresis loops of $Ce_{1.2}Fe_{12}Ti$ (black) $Ce_{1.36}Fe_{11.8}Ti$ (red) and $Ce_{1.6}Fe_{11.5}Ti$ (blue) specimens measured with magnetic field 6.5 Tesla (out of plane) at room temperature. (b) Comparison of hysteresis loops of specimen $Ce_{1.2}Fe_{12}Ti$ measured at 300 Kelvin (black) and 80 Kelvin (red).

Figure 4.5 represents the temperature dependence of magnetization ($J=\mu_0 M_s$) at a magnetic field of 0.1 Tesla. The compound exhibits ferromagnetic behavior with an estimated Curie temperature (T_c) ~490 Kelvin for the $CeFe_{11}Ti$ phase[86] and 231 K for the $CeFe_2$ phase, which is in good agreement with the earlier reported results[104].

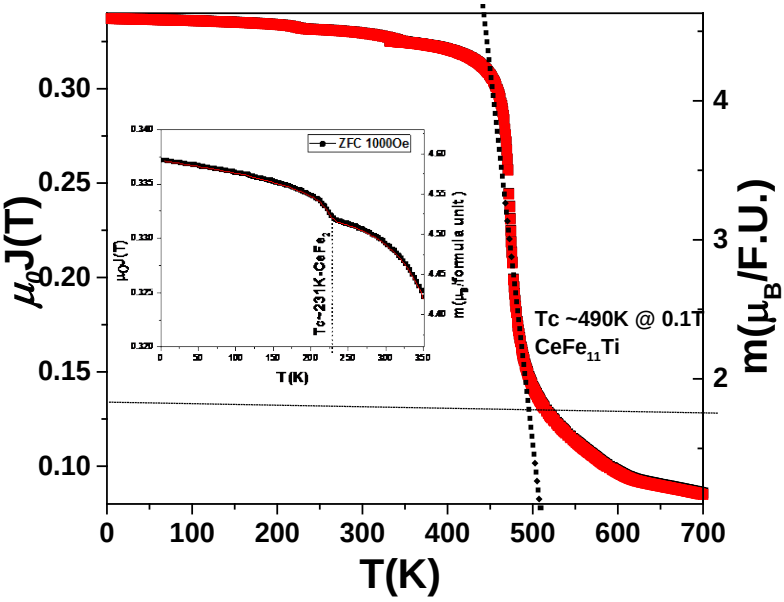

Figure 4.5 Magnetization ($M=\mu_0 J$) vs Temperature curve (temperature range-5 Kelvin to 700 Kelvin) of the $Ce_{1.2}Fe_{12}Ti$ specimen along the plane perpendicular (out of plane) at 0.1 Tesla magnetic field in SQUID.

4.5. Spectroscopic XAS and XMCD investigations

4.5.1. XAS and XMCD spectra of Iron and Titanium $L_{2,3}$ edges:

In order to discern the influence of each element in the alloy and to reveal the presence or absence of orbital magnetic moment in iron, XMCD measurements (see chapter 2 experimental techniques) have been performed *in-situ* at Fe $L_{2,3}$, Ti $L_{2,3}$ and Ce $M_{4,5}$ edges (at 300K and 80K) in the presence of 6.5 Tesla magnetic field .The surface of the specimen has been cleaned via scrapping *in-situ* to remove the oxidized surface layers. The XAS (measured at positive and negative helicity) and XMCD (difference of positive and negative helicity XAS spectra) spectra of the Ti $L_{2,3}$ edges are shown in Figure 4.6 (b). No significant XMCD signal has been observed at the Ti *L*-edges.

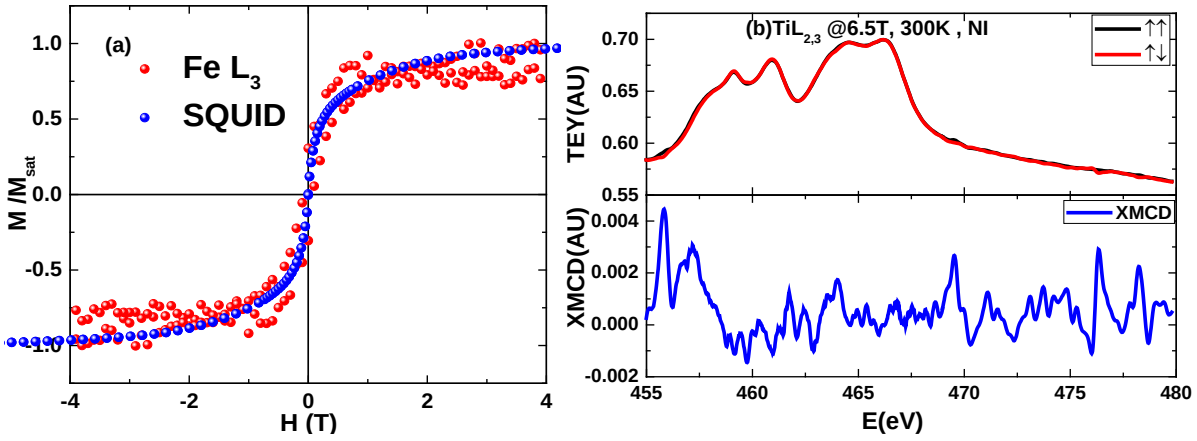

Figure 4.6 (a) XMCD element specific magnetization curves of the Fe L_3 edge (red) with SQUID hysteresis loops of $Ce_{1.2}Fe_{12}Ti$ (blue) specimen recorded at room temperature. (b) Ti $L_{2,3}$ edge XAS (measured at left and right circular polarization) and XMCD spectra (difference of left and right circular polarized XAS spectra) recorded at the 6.5 Tesla magnetic field and 300 Kelvin.

The XMCD to XAS white line intensity ratio of an element at given site is proportional to the average magnetic moment in that site [25]. Thus, the element specific hysteresis curves have been recorded by measuring the peak height of the cerium M_4, M_5 and Fe L_3 absorption edges as a function of the applied magnetic field on specimen $Ce_{1.2}Fe_{12}Ti$. The magnetic field dependence of the XMCD peak at the Fe L_3 edge of the $Ce_{1.2}Fe_{12}Ti$ specimen at 300 Kelvin along with the SQUID results are shown in Figure 4.6 (a) (normalized to unity magnetization curves). The Fe L_3 edge magnetization curve is analogous to the SQUID hysteresis and exhibits the same coercivity (8Oersted) and remanence (0.5%). There is no magnetic hysteresis behavior

observed at the Titanium $L_{2,3}$ edges (refer Figure 4.6 (b)) and at the M_4 and M_5 edge of the cerium atom (see Figure 4.8 (a) and (b)) due to a very small XMCD effect.

Figure 4.7(a) and (b) show the XAS and XMCD spectra of Fe $L_{2,3}$ edges at 300 and 80 Kelvin respectively. The corresponding sum rule analysis results are presented in Table 4.2. The 3*d* number of holes used for sum rule analysis is 3.38 for pure metallic iron[24] and 3.4 for the rare earth-transition metal magnet which is similar to pure metallic configuration[105]. The shape of XAS and XMCD spectra of Fe $L_{2,3}$ edges is analogous to the typical metallic iron configuration [24] and there are no signs of oxidation[106].

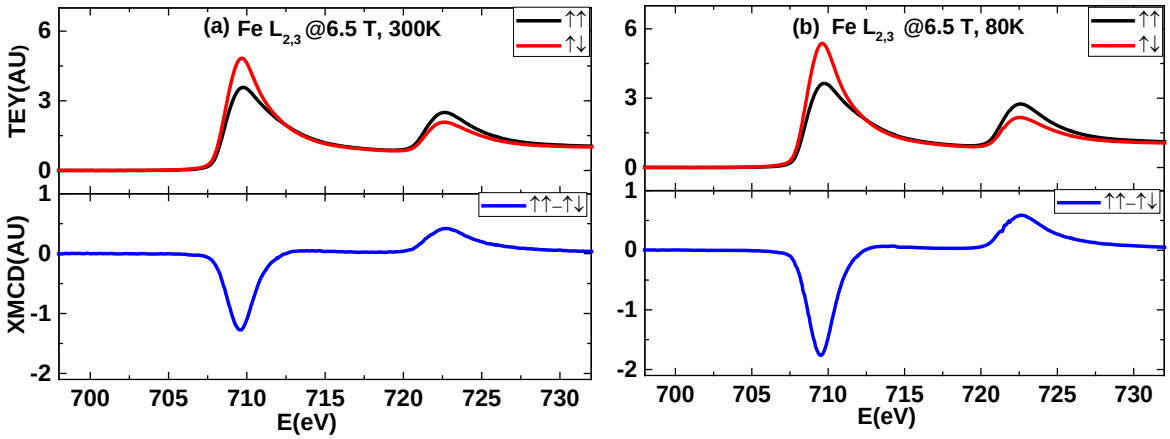

Figure 4.7 (a) Edge normalized XAS (measured at left and right circular polarization) and XMCD (difference of both left and right circular polarized XAS spectra) spectra at the Fe $L_{2,3}$ edges of the $Ce_{1.2}Fe_{12}Ti$ specimen (at 6.5T magnetic field) recorded at 300 Kelvin (left) and (b) 80 Kelvin (right).

Table 4.2 The results of the projected magnetic moment values (spin (m_S), orbital (m_L), total magnetic moment (m_S+m_L) and the ratio of the orbital and spin moment (m_S/m_L)) estimated from the XMCD sum rules analysis of $Ce_{1.2}Fe_{12}Ti$ specimen at the Fe $L_{2,3}$ edges and a comparison with the literature values[24].

Temperature (K)	**Orbital (m_L) (μ_B / atom)**	**Spin (m_S) (μ_B / atom)**	**Total (m_L+m_S) (μ_B / atom)**	**Ratio (m_L/m_S)**
300	0.06±0.01	1.37±0.2	1.43±0.2	0.04±0.01
80	0.07±0.01	1.70±0.2	1.77±0.2	0.04±0.01
Literature [24] pure Fe metal	0.085±0.01	1.98±0.2	2.07±0.2	0.043±0.01

At 300 Kelvin, iron provides the projected spin moment of m_S =1.37±0.2 Bohr magneton/atom and an orbital magnetic moment of m_L = 0.06±0.01 Bohr magneton/atom. The orbital to spin moment ratio (m_L/m_S) is 0.04±0.01 and their sum (m_L+m_S) is 1.43±0.2 Bohr magneton/atom (refer Table 4.2). In our case, the iron XAS and XMCD spectra are similar to pure metallic spectra. Therefore, our XMCD sum rule analysis results can be compared with pure metallic iron. The spin magnetic moment of iron at 300K is smaller to that of the pure iron as reported previously by Chen et al [24]. At low temperature (80 Kelvin), the iron magnetic moment is increased and it is relatively close to the literature value of 2 Bohr magneton/atom[24]. At 80 Kelvin, the projected spin moment is m_S =1.70±0.2 Bohr magneton/atom and the orbital magnetic moment of m_L = 0.07±0.01 Bohr magneton/atom. The orbital to spin moment ratio at room temperature (m_L/m_S) is 0.04±0.01 and their sum (m_L+m_S) is 1.77±0.2 Bohr magneton/atom. At low temperature, there is 17 % increase in the total magnetic moment as compared to the value at room temperature which is well consistent with the SQUID results.

4.5.2. XAS and XMCD spectra of Cerium $M_{4,5}$ edges: Line shape analysis

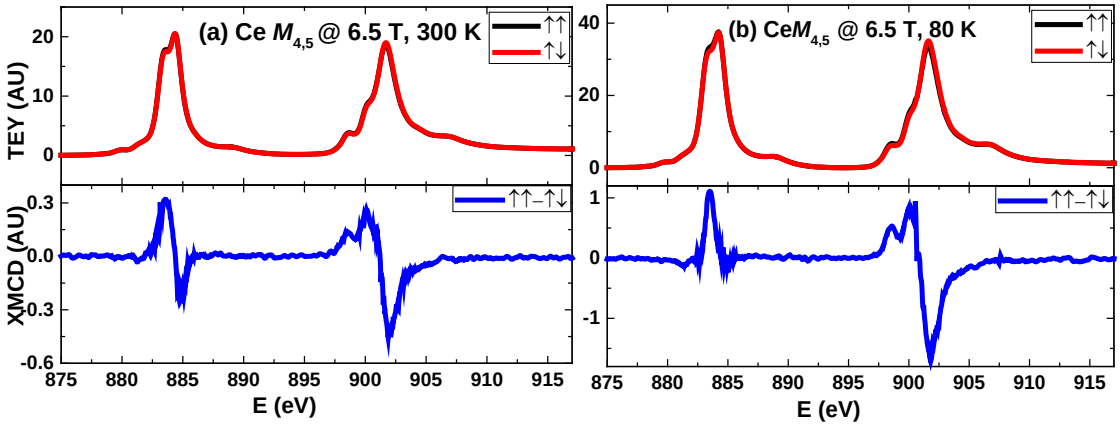

Figure 4.8 (a) Edge normalized XAS (measured at positive and negative helicity) and XMCD (difference of positive and negative helicity XAS spectra) spectra at of Ce $M_{4,5}$ edge of $Ce_{1.2}Fe_{12}Ti$ specimen (at the 6.5T magnetic field) recorded at room temperature (left) and (b) at 80K (right).

Figure 4.8(a) and (b) show the XAS and XMCD spectra of Ce $M_{4,\ 5}$ edges ($3d^{10}4f^{\ n}\rightarrow 3d^{9}4f^{\ n+1}$ transition) at 300 and 80 Kelvin respectively (in the presence of 6.5 T magnetic field). The line shape of the XAS spectrum is in good agreement with the earlier reported Ce^{3+} experimental results [37, 79]. In order to compare with the experimental spectra,

the cerium XAS and XMCD spectra at the $M_{4,5}$ edges have been simulated by atomic multiplet theory calculations (Further details presented in chapter 3). The starting point for the full multiplet calculations at Ce $M_{4,5}$ XAS spectrum is the pure Hund's rule atomic ground state J =5/2 ($^4F_{5/2}$) with a single 4f electron (see Figure 4.9 (b)).

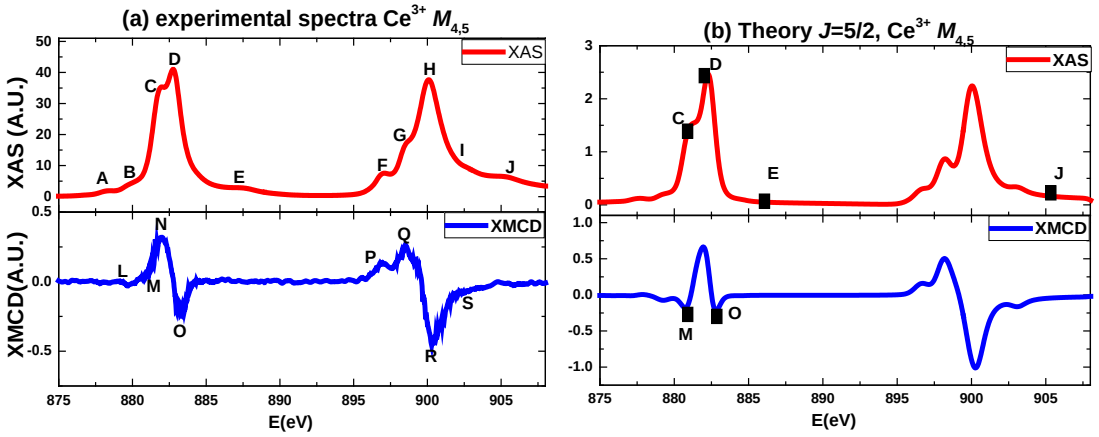

Figure 4.9 (a) Representative edge normalized Ce $M_{4,5}$ XAS and XMCD experimental spectra measured at 300K in presence of 6.5 T magnetic field, discrete subfeatures are alphabetically labelled. The contribution from transitions $3d^{10}4f^1 \rightarrow 3d^9 4f^2$ is labelled[18]. (b) Ground state J=5/2 spectra simulated by atomic multiplet theory calculations (Figure 3.5 (c)). The features, which are different in Figure 9 (a) and Figure 9 (b) are represented by the black box in pure ground state spectra.

For comparison of the experimental spectra with the theoretical spectra (Figure 4.9 (b)), the distinct features in the substructure of the XAS and XMCD experimental spectra (Figure 4.9 (a)) are alphabetically labelled from A-K and L-S respectively for imminent reference.

There are prominent differences visible in the peak positions C, D, E and J in both spectra (Figure 4.9 (a) and (b)).

1. The satellite peaks E and J are not present in theoretical XAS Figure 4.9 (b) (J=5/2)
2. The ratios of the peak height at C and D in the experimental XAS spectrum- (Figure 4.9a) is different than the theoretical XAS spectrum J=5/2 (Figure 4.9(b)) ground state.
3. The peak M is not visible in the experimental spectrum and the negative peak O in the experimental XMCD (Figure 4.9 (a)) spectra is large compared to the J=5/2 XMCD spectrum (Figure 4.9 (b)).

It signifies that the Ce $M_{4,5}$ edges XAS and XMCD experimental spectra are not pure Hund's rule ground state and the simulated XAS and XMCD spectra of pure ground state J=5/2 XAS and XMCD spectra cannot completely explain all the features in Figure 4.9(a).

The cerium compound does not give an XAS spectrum corresponding to pure $3d^9 4f^1$ and $3d^9 4f^0$ ground state configurations [18, 37, 63]. Our experimental spectrum results show similar behavior, where satellites peaks E and J are visible at both M_4 and M_5 edges of the experimental XAS spectra (Figure 4.9(a)). These satellite peaks originated from the $4f^0$ configuration which is referred as "f^0 satellite"[63]. These peaks appear generally at the higher energy side of the leading XAS peak[37]. It is considered that, as the f^0 satellite peak becomes stronger, the cerium 4*f* electrons decrease from 1 which indicates that the Ce 4*f* electrons become more delocalized. The separation of the $4f^0$ and $4f^1$ multiplets for the experimental spectra is ~ 5eV [37, 76]. In figure 9(a) the energy difference between $4f^1$ peak (D) and $4f^0$ satellite peak (E) is ~ 4.7eV and the difference between H and J is ~ 5.19eV which confirms that the peaks (E and J) visible in experimental XAS spectra (Figure 9(a)) are originate from the $4f^0$ contribution. On the other hand, the line shape of the Ce $M_{4,5}$ XMCD spectra is understood as multiplet structures which are arising mostly form the $4f^1$ configuration, since the $4f^0$ does not contribute to the magnetism.

Hund´s rule is used to estimate the ground state. According to Hund´s rule cerium has 1 electron in the *f* shell so the *L* and *S* will be 3 and ½. The parallel and antiparallel combination of *L* and *S* could provide us two different *J* states (5/2 and 7/2). The ground state is *J*= 5/2 and the next parallel coupled spin-orbit state of higher energy is *J*=7/2. The presence of negative peak M and O in the XMCD signal (Figure 4.9(a) bottom panel) and the difference in the ratios of the peak heights at C and D in XAS experimental spectrum (Figure 4.9(a) top panel) at the M_5 edge can be interpreted in terms of a contribution from the *J*=7/2 state in the ground state spectrum *J*=5/2 due to hybridization between the 4*f* level and the conduction states [63, 79, 81]. It has been discussed in the introduction (section 4.1) in detail. To explain this, we simulate the XAS and XMCD spectra for the spin-orbit coupled *J* states for cerium $4f^1$ configuration via the CTM4XAS software and by an admixture of *J*=5/2 and 7/2 states.

4.5.2.1 Admixture of Ce spin orbit coupled state

In order to clarify this issue in the $CeFe_{11}Ti$ specimen, the Ce$M_{4,5}$ XAS and XMCD spectra for *J* = 5/2 and *J* =7/2 (Figure 4.10 (a), (b)) were simulated. The results obtained from Quanty and CTM4XAS software's are analogous. Therefore, we have used the CTM4XAS program for simulations, based on Hartree-Fock calculations[107] to determine the atomic initial-state and final-state wave functions and energies. The well-known estimates in atomic multiplet theory

[37] the slater integrals $\boldsymbol{F_k}$ and $\boldsymbol{G_k}$ which are empirically scaled values are used here. The values used were all reduced to 80% of the free Ce^{3+}ion Hartree-Fock values[37].

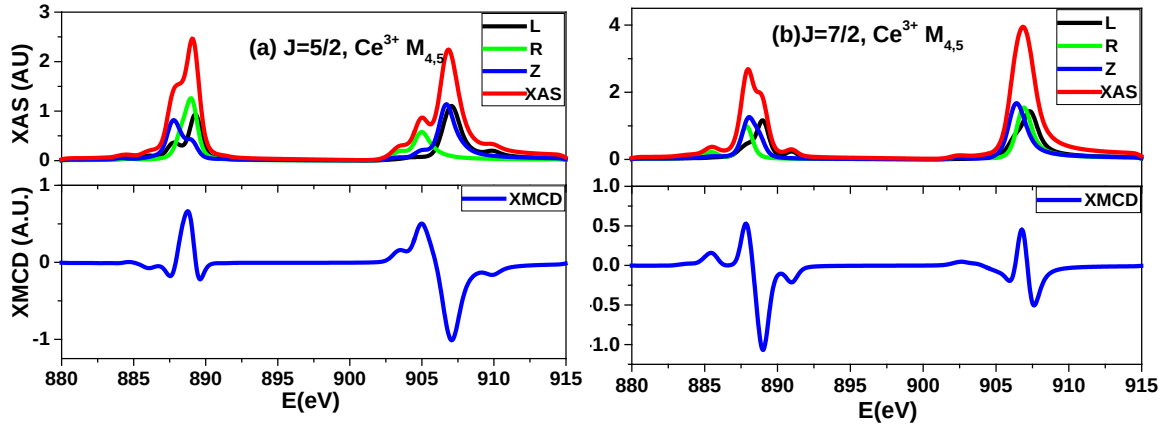

Figure 4.10 simulated Ce $M_{4,5}$ XAS and XMCD spectra (a) for Hund's rule ground state J=5/2 and (b) the next higher energy spin-orbit parallel coupled state J=7/2. The decomposition of the spectra into the contributions from the three possible values of ΔJ =0 (zero polarized-Z blue color), ΔJ =+1(left polarized-L black color) and ΔJ =-1(right polarized-R green color) of both states (J=5/2 and 7/2) is shown.

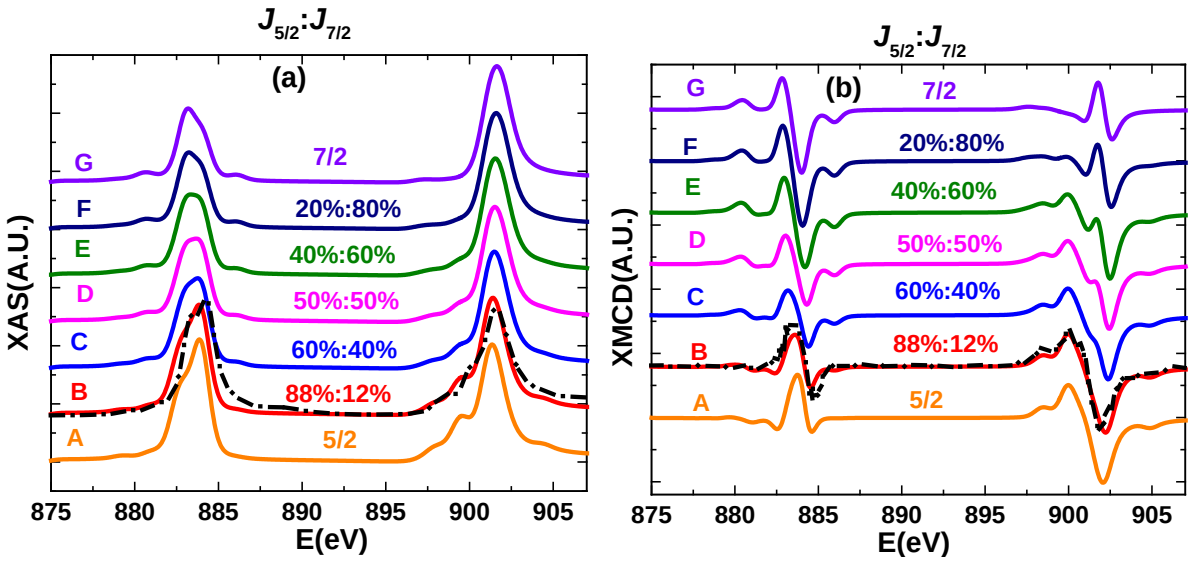

Figure 4.11 calculated isotropic Ce $M_{4,5}$ $f^1 \rightarrow f^2$ XAS: Left figure (a) XAS and (b) XMCD (right figure) spectra. The spectra (B-F) are incoherent sum of pure spectra J=5/2 and 7/2states. (A) J=5/2 pure ground state (A) 5/2=88% and 7/2=12% (overlay black dash- dot curve is an experimental spectrum measured at 300K showing well resemblance with the spectrum),(C) 5/2=60%and 7/2=40%,(D) 5/2=50%and 7/2=50%,(E) 5/2=40% and 7/2=60%,(F) 5/2=20% and 7/2=80% and (G) J=7/2 state.

The simulated spectra are fitting very well with experimental spectra using these values. The relevant slater integral parameters for the ground state (Xe) $3d^{10}4f^1$ are F^2_{ff}= F^4_{ff} = F^6_{ff} =0 and

for the excited state are i_F^2_{ff}=12.628, i_F^4_{ff} =7.940, i_F^6_{ff} =5.717, i_F^2_{df}=7.486, i_F^4_{df}=3.384, i_G^1_{df}=5.073, i_G^3_{df}=2.986, i_G^5_{df}=2.048[107]. The spin-orbit interaction parameter for ground state is Z_{4f}=0.087 and for the excited state are i_Z_{4f}=0.087 and i_Z_{3d}=7.446[81, 107]. All spectra were convoluted with a 0.3 eV Gaussian. In order to achieve a magnetized sample a virtual 25 meV exchange field have also been applied to break the spin symmetry. The M_5 (M_4) edge was convoluted with a 0.2 eV (0.4 eV) FWHM Lorentzian. We showed the decomposition of the spectra into the contributions from the three possible values of ΔJ =0 (zero polarized-Z blue color), ΔJ =+1(left polarized-L black color) and ΔJ =-1(right polarized-R green color) of both states (J=5/2 and 7/2) [68]. The resultant simulated XAS (=left +right +zero) and XMCD (=left-right) spectra for J=5/2 (see Figure 4.10 (a)) and J=7/2 (see Figure 4.10 (b)) states resemble well with the previously reported results [81, 98].

Table 4.3 the Values of orbital moment ($m_{L)}$, spin moment ($m_{S)}$, total magnetic moment (m_L+m_S), and the ratio (m_L/m_S) of magnetic moment of simulated XAS and XMCD spectra of J=5/2, J=7/2 states and their ratio (88%:12%) in units of Bohr magneton (μ_B)/atom presented here. The values have been estimated from the XMCD sum-rule analysis by incorporating all the necessary corrections (presented in chapter 2).

***J* state**	**Orbital (m_L) (μ_B / atom)**	**Spin (m_S) (μ_B / atom)**	**Total (m_L+m_S) (μ_B / atom)**	**Ratio (m_L/m_S)**
J=5/2	2.86±0.2	-0.75±0.1	2.11±0.2	-3.82±0.2
J=7/2	-2.97±0.2	-1.00±0.1	-3.98±0.2	2.97±0.2
Ratio-5/2:7/2(88%:12%)	2.16±0.2	-0.78±0.1	1.38±0.2	-2.77±0.2

The both J =5/2 and J=7/2 spectra have been incoherently added up by changing the relative contributions to reproduce the experimental spectral shape as shown in Figure 4.11(a) , (b). The XAS and XMCD line shape (see Figure 4.11 (a) , (b)) significantly varies with increasing J=7/2 ratio in the ground state. As the weight of the J=7/2 increases in ground state, the M_4 XAS peak becomes stronger relative to M_5. The multiplet structure is smeared out at M_4 edge to some extent.

The most noticeable qualitative changes that are introduced to the XMCD line shape by admixture of J=7/2 are visible at M_5 edge. The small negative feature at M_5 edge (at L and M see Figure 4.9(a)) is gradually reduced and replaced by a positive feature. On contrary the negative peak at M_5 edge on higher energy side (at O see Figure 4.9(a)) is transformed into a

further negative feature. The M_5 multiplet is consistent with our experimental results till the 12% admixture of J=7/2 (see Figure 4.11(a) and (b) spectrum B), It allowed us the estimation that the weight of J=7/2 is not larger than 10-15 %. In summary, introducing 7/2 character to the simulated Cerium $M_{4,5}$ edge ground state J=5/2 spectrum explains clearly the line shape variations in the experimental spectrum.

The sum rule analysis[20, 35] has been performed on the theoretical XAS and XMCD integrated spectra of J=5/2, J=7/2 state, and their ratio by using the correction factor and eliminating the magnetic dipole term-T_Z (chapter 3 section 3.4). Table 4.3 summarizes the values of m_L, m_S, sum (m_L+m_S) and their ratio (m_L/m_S) of cerium 4*f* electrons of the Ce^{3+} ion at the edges $M_{4,5}$ at 0 Kelvin. There is only 1 electron present in the 4*f* shell of cerium, therefore the number of holes (n_h) used here is13[63]. The correction factor for the cerium is 1.56 (chapter 3 section 3.3)[60]. The expectation value of the magnetic dipole moment used for J=5/2 and 7/2 states are -0.569[60] and -0.333 respectively (Note- spectra generated by Quanty software also presented in chapter 3 J=5/2 spectra from Quanty and CTM4XAS are analogous. The Quanty software is important and needs to mention several times because we are using expectation value of the magnetic dipole term in order to apply sum rules. CTM4XAS does not provide the expectation values). It should be noted that the correction terms of the pure ground state have been used. As the 7/2 contribution is 10-15%, we neglect the possible error for the possibility of the different correction factors and magnetic dipole term (T_Z).

4.5.2.2 Sum rule analysis results of experimental Ce $M_{4,5}$ edge XMCD spectra

One can estimate the orbital and spin magnetic moment in Bohr magneton/atom of cerium 4*f* electrons by applying XMCD spin and orbital sum rules (see chapter 3 equation 3.1 and 3.3) on experimental XAS and XMCD spectra[20, 35]. There is only 1 electron present in the 4*f* shell of cerium, therefore the number of holes (n_h) used here are 13[63]. The contribution of f0 is very small therefore it is neglected here (refer section 4.5.2).

At room temperature, the XMCD sum rule analysis of cerium spectra provides the projected effective spin of $S_z + 3T_z$ (S_{eff}) =-0.043±0.01 and orbital magnetic moment of m_L (L_z) =0.02±0.01 Bohr magneton/atom. At low temperature (80K), the XMCD spectrum is 3 times larger than the room temperature (300K) spectrum and the projected orbital m_L (L_z) =0.07±0.01 Bohr magneton/atom and effective spin is $S_z + 3T_z$ (S_{eff}) =-0.11±0.01 are respectively (see table

4). The increase at a lower temperature in cerium magnetic moment shows that cerium and iron are not very well coupled with each other.

The atomic multiplet theory simulations results showed in chapter 3 that the deviation in the spin sum rule is 60 % in the case of cerium[60] and increases with the increasing number of 4*f* electrons in light rare earth elements, therefore the spin sum rule cannot be used directly to estimate the magnetic moment value of spin (S_Z) for cerium $M_{4,5}$ edges. The magnetic dipole term T_Z is also comparable to the spin moment and affects the experimental spin magnetic moment. We have perceived a method with which we can estimate spin magnetic moment by using a correction factor to avoid the mixing problem and eliminating the T_Z term by theoretical estimation (the method is also shown in section-3.7). The complete process of correcting the effective spin value is explained stepwise in chapter 3 and the corresponding sum rule analysis results (in Bohr magneton/atom) are presented in Table 4.4

Table 4.4 the results of the projected magnetic moment values (spin (m_S), orbital (m_L), total magnetic moment (m_S+m_L) and the ratio of the orbital and spin moment (m_S/m_L)) estimated from the XMCD sum rules analysis of $Ce_{1.2}Fe_{12}Ti$ specimen at Ce $M_{4,5}$ edges. The results are compared with the sum rule analysis results of the theoretical simulated spectra (XMCD sum rules have been applied to the spectrum generated by the ratio of the 88% of the *J*=5/2 state and 12 % of the *J*=5/2 state) and Hund's rule.

T (Temperature) (K)	**Orbital (m_L) (μ_B / atom)**	**Spin (m_S) (μ_B / atom)**	**Total (m_L+m_S) (μ_B / atom)**	**Ratio (-m_L/m_S)**
300	0.02±0.01	-0.01±0.002	0.01±0.002	2.23±0.2
80	0.07±0.01	-0.03.±0.002	0.05±0.01	2.84±0.2
Ratio 5/2:7/2 (88%:12%)	2.16±0.2	-0.78±0.1	1.38±0.2	2.77±0.2
Hund's rule	3	1	2	3

At 300K, the maximum magnetization of 18 Bohr magneton/formula unit (1.2 T) is recorded for $Ce_{1.2}Fe_{12}Ti$ and at 80K is 21.7 Bohr magneton/formula unit (1.4 T) (section 4.3). At room temperature, the total magnetic moment from the element specific results is 17.15 Bohr magneton/formula unit ($Ce_{1.2}Fe_{12}Ti$ =0.011*1.2+12*1.43) and is 21.2 Bohr magneton/formula unit ($Ce_{1.2}Fe_{12}Ti$ =0.045*1.2+12*1.77) for 80 Kelvin. The total magnetic moment evaluated from the sum rule analysis by the elimination of T_z and by correcting the mixing problem is in

good agreement with the SQUID magnetization result. On the other hand, the total magnetic moments for cerium is even negligible compared to the theoretical simulation results of ratio 5/2:7/2 (88%:12%) (Refer table 4) and the Hund's rule moments (m_S = -1 Bohr magneton/atom and m_L=3 Bohr magneton/ atom). The estimation of iron and cerium magnetic moment by XMCD and comparing with the SQUID investigation, it is observed that the contribution of the cerium must be small as it is estimated by incorporating all the possible corrections.

The line shape variations of the XAS and XMCD spectra can be completely explained by introducing the contribution of J=7/2 state to the pure ground state J=5/2 (refer figure 4.10). However, the sum rule analysis results show very small magnetic moment at the cerium site. There is 34% reduction of the total magnetic moment of cerium pure ground state J=5/2 observed on mixing 7/2 state to the pure ground J=5/2 state spectrum. In experimental spectra, the XMCD effect at cerium $M_{4,5}$ edge is only 1% and compared to ground state results the magnetic moment is completely negligible. What is causing such a strong reduction in the magnetic moment of cerium ?. As the reduction in cerium magnetic moment cannot be explained by the admixture of 5/2 and 7/2 state, this creates a need for searching an alternative model.

4.6. Theoretical modeling

When we leave the atomic picture and consider the cerium atom in the certain compound, the 4*f* electron cloud could be affected by the crystalline environment even if it is well localized[63]. The crystal field[108, 109] and charge transfer[81] both can mix the J=7/2 states in ground state and can reduce the magnetic moment. The inclusion of the crystal field and the charge transfer effects in pure atomic simulations of XAS and XMCD spectra at Cerium $M_{4,5}$ edges could play important role in explaining the reduction in XMCD effect and the magnetic moment of cerium atom. For the further explanation, we have used the crystal field multiplet model and charge transfer multiplet model in the following chapters.

4.6.1. Crystal field multiplet model

The presence of crystal field can influence the spectral shape [18, 82]. Full multiplet calculation under consideration of the crystal field allows the quantitative clarification of the ground state. The spherical symmetry of a cerium ion is usually lifted when it is embedded into a solid crystal. As a consequence, the 4*f* electron has to adapt to the symmetry of the environment, which leads

to the formation of a new ground state. The Hund's rule ground state of the 4*f* electron in a Ce^{3+} ion is characterized by $J = 5/2$. The six-fold degeneracy of the $J=5/2$ states is lifted by the crystal field [14]. The determination of the crystal filed scheme is the basic part of the description of the cerium compounds because the new ground state affects the electronic and magnetic properties of the material. In most of the cerium compounds, energy splitting is not larger than $\Delta E=20\ldots200$ meV [18, 108]. The CTM4XAS program [107, 110] has been used for crystal field multiple calculations. The simulation parameters like Slater integrals, spin-orbit parameters are same as mentioned in section 4.5.2.1. For the simplification, the cubic symmetry (C_4) has been considered for the simulations in CTM4XAS software[107].

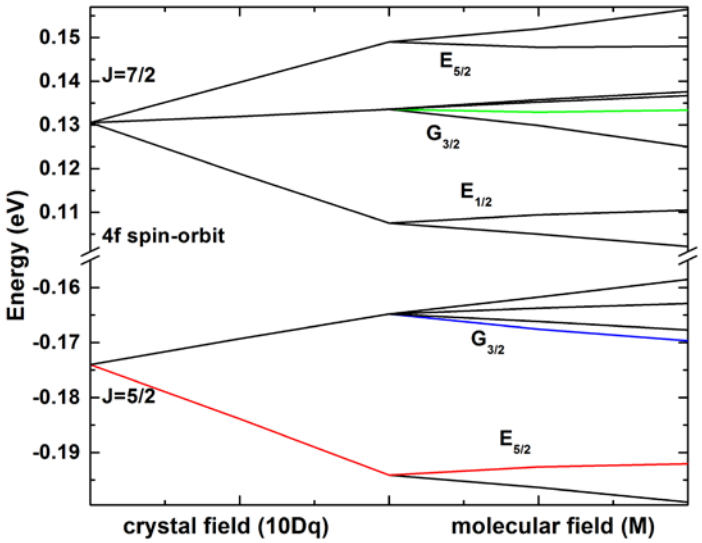

Figure 4.12 the crystal field splitting energy levels of a Ce^{3+} ion. The graph is based on the actual energies that come from the ORA-file. On the left: only the atomic 4*f* spin-orbit coupling, splitting the $4f^1$ states into $J=5/2$ and $J=7/2$. The crystal field splits $J=5/2$ into 2-dimensional E_2 and 4-dimensional G states and the crystal field splits $J=7/2$ into 2-dimensional E_1, 4-dimensional G, and 2-dimensional E_2 states. The molecular field splits the 2-dimensional states in two and the 4-dimensional states in four.

Figure 4.12 shows the crystal field splitting energy levels of a Ce^{3+} ion. The graph is based on the actual energies that originate from the ORA-file (output file in CTM4XAS, which lists the energy levels for the determined diagonalized states). In Figure 4.12, on the left-hand side-only the atomic 4*f* spin-orbit coupling, splitting the $4f^1$ states into $J=5/2$ and $J=7/2$ is presented which is the most dominant energy splitting of energy 0.305 eV. The crystal field and the molecular field splits the energy levels into 2-dimensional ($E_{1/2}$ and $E_{5/2}$) and the 4-dimensional states ($G_{3/2}$). The energies of the $4f^1$ ground state are as follows -

(i) The 6 J=5/2 states at negative energies split by crystal field into a group of 2-dimensional $E_{5/2}$ (-0.19 eV) states and a group of 4- dimensional $G_{3/2}$ (-0.16 eV) states, further split by exchange field.

(ii) The 8 J=7/2 states at negative energies split by crystal field into a group of 2 dimensional $E_{1/2}$ (0.10 eV) states, a group of 4 dimensional $G_{3/2}$ (0.13 eV) states and a group of 2 dimensional $E_{5/2}$ (0.15 eV) states and further split by exchange field.

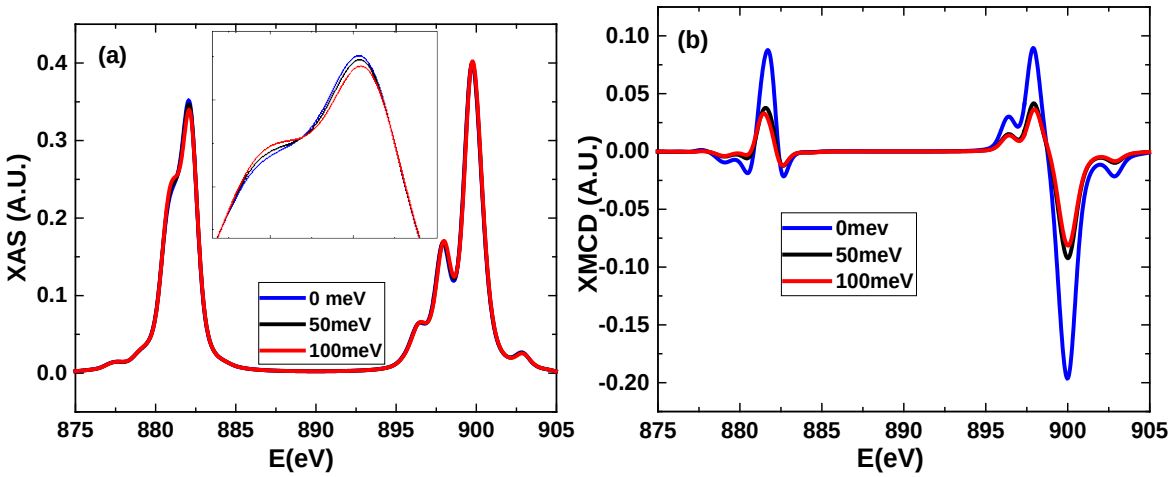

Figure 4.13 simulations of (a)XAS and (b)XMCD spectra of cubic crystal field effects for Ce^{3+} ion via CTM4XAS sodtware. The variations in the spectra with increasing 10Dq parameter from 0 meV (no crystal field) to 1eV are shown. In figure (a) region between 800 eV to 883 eV is presented at proper resolution to observe change at M_5 edge.

In Figure 4.13 (a) and (b) calculations of XAS and XMCD spectra with increasing crystal field strength ($10D_q$) in cubic symmetry are shown for the Ce^{3+} atom. The broadening has been adjusted according to the experiment. The crystalline field barely changes the line shape of the XAS and XMCD spectra even on the application of 100 meV, only change in the XAS and XMCD signal intensity is observed (see Figure 4.13 (a) and (b)). The main trend observed from the isolated atom ($10D_q$ =0 no crystal filed) to the crystal field influenced one with the 10Dq=100meV is a reduction of the peak at 882.16 eV, while at 880.7 eV it increases at M_4 edge. In absence of crystal field, the XMCD effect at M_4 edge is 50% and the XMCD signal is dramatically reduced from about 50% ($10D_q$=0) to 19% ($10D_q$=100meV) in the presence of crystal field. For large values of the crystal field i.e. 1 eV (too large for 4*f* systems), the changes in XAS and XMCD spectral shape are observed. As the 1 eV crystal field energy is too large, results of the 1eV crystal field are not presented here. From the crystal field model, it is clear

that the even small amount of crystal field is influencing the XMCD effect without changing the line shape.

In summary, there is a significant change in XMCD effect was observed on varying crystal field from 0 eV to 100 meV. Even in the presence of small crystal field in cerium one modifies the ground state spectra for Cerium and effectively lowers the MCD, by keeping the same line shape. There is still 19% XMCD effect present in presence of practical 50meV crystal field. In our experimental spectra, XMCD effect is only 1%, it shows that only crystal field is not responsible for the reduction in cerium magnetic moment. Therefore, another model needs to be examined for the further reduction in the Ce 4*f* magnetic moment. As it is mentioned earlier in section 4.5.2.2 that in case of cerium there could be two possible reasons for the reduction in magnetic moment crystal field[18, 108, 111] and charge transfer effects[81]. The crystal field cannot be large (generally lower than 50 meV) so if one needs additional reduction of the XMCD effect it is expected to be charge transfer effects.

4.6.2. Charge transfer multiplet model (CTM)

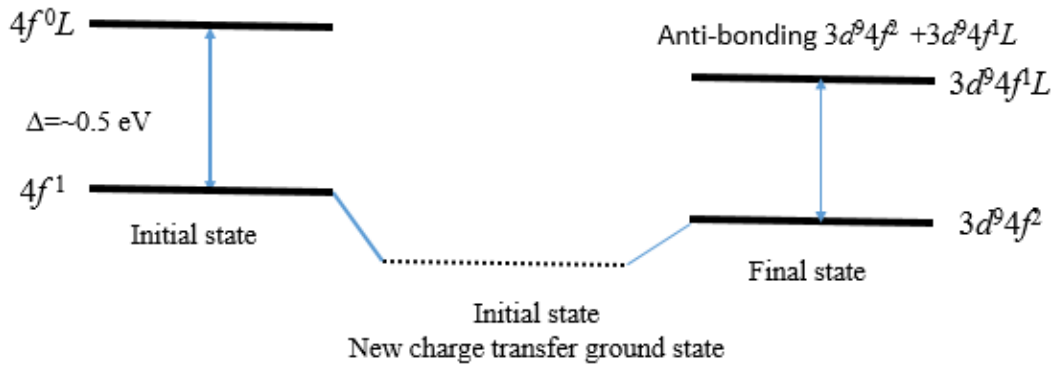

Figure 4.14 schematic representation of the cerium 4*f* charge transfer ground state. The charge transfer calculations for Ce^{3+} $M_{4,5}$ edge mixes the $4f^1$+$4f^0L$ in initial state and $3d^9 4f^2$+$3d^9 4f^1 L$ in final state. There is an anti-bonding combination in the final state, and that is the f^0 satellite peak. Hybridization energy used was 0.5 eV.

The cerium has a transitional valence and iterant nature which strongly depends on the environment [15]. When ligand to metal charge transfer effects are included, two configuration model is used to describe the ground state and the excited state. The charge transfer calculations were performed following the previous report of Frank et al[81]. In this model, the ground state wavefunction becomes the linear combination of the 2 possible states combinations. The

schematic representation of the charge transfer effect is presented in Figure 4.14. In the case of cerium, model mixes $4f^1$ with $4f^0L$ in the ground state and $3d^9 4f^2$ with $3d^9 4f^1 L$ in the final state (refer Figure 4.14). The ground and final state mixing are controlled by the energy separations and the hybridization. The charge-transfer energy delta, Δ is defined as the energy difference between the lowest states of the $4f^1$and the $L4f^0$ configurations. If the hybridization is set equal to zero, both configurations do not mix and the eigenstates will be equal to the $4f^1$. By turning on the hybridization it can be observed that the energy of the lowest configuration is even further lowered. If the hybridization shows increase then the $L4f^0$ contribution to the spectra will also increase. It has been shown that the charge transfer can lead to new type of ground state as it is very well known in the case of CeO_2[112-114] and for cerium-based specimens also i.e. CeCuSi and Ce/Fe multilayer[81].

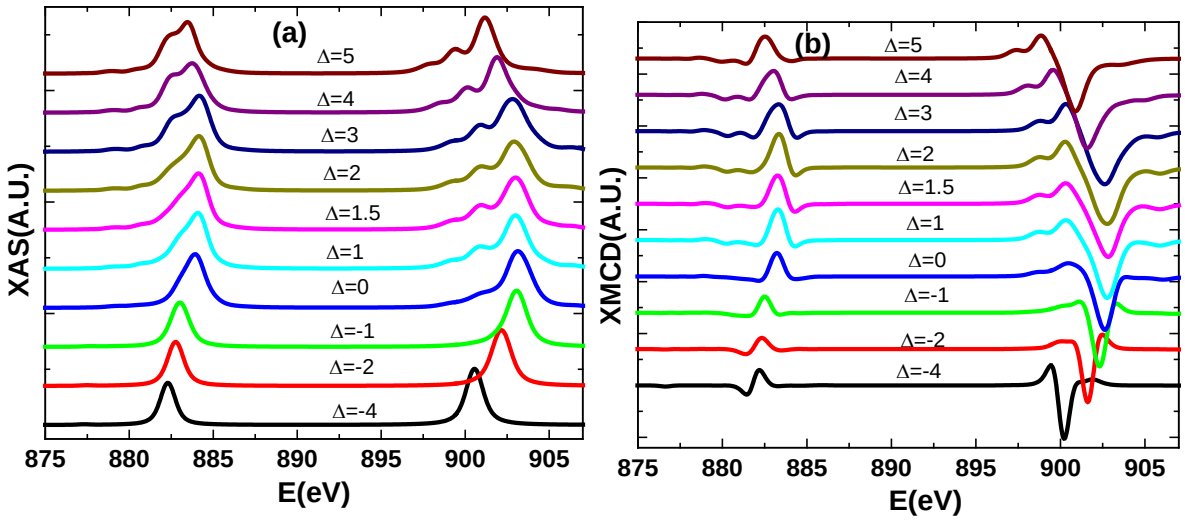

Figure 4.15 series of XAS (a) and XMCD (b) simulated by charge transfer multiplet calculations for Ce^{3+} $M_{4,5}$ edges. The ground state is mixture of $4f^1$+$4f^0L$ initial state and $3d^9 4f^2$+$3d^9 4f^1 L$ final state. Hybridization energy used was 0.5 eV and exchange field of 25 meV. Their crystal field energy is turned off here.

In this model for calculations, spin-orbit coupling and slater integral parameters are same as in the ground state as mentioned in the above calculations for spin-orbit coupled states (section 4.5.2.1) and crystal field model (section 4.6.1). The hybridization energy used was 0.5 eV[81]. The CTM calculation was performed at first without adding any crystal field. By the variation of charge transfer energy (Δ=-5 to +5) XAS and XMCD spectra have been simulated and are shown in the Figure 4.15 (a) and (b). The Δ=+5 essentially has pure ground state character (98% = configuration $4f^1$) and Δ=-5 has $4f^0$ configuration. If we decrease the value from +5 to -5 than an admixture of two states occurs and at Δ=0 is 50% mixture of both configuration. The

experimental XAS and XMCD line shapes are qualitatively well described by Δ=1.5 eV energy spectrum (refer Figure 4.15). The CTM model states that at Δ=1.5 eV experimental spectrum is an admixture of 5.3% of $4f^0$ and 94.7% of $4f^1$ states.

As presented in the crystal field calculations (section 4.6.1), the small crystal field deteriorates the XMCD effect from 50% to 19% in case of cerium. We also applied the crystal field from 10meV to 100 meV in charge transfer calculation to the spectrum of Δ=1.5 eV which is analogous to our experimental results. By the variation of crystal field (10meV to 100meV) series of XAS and XMCD spectra have been simulated and are shown in the Figure 4.16 (a), (b). It is consistent with the previous results that even in the presence of small crystal field in rare earth one modifies the ground state and effectively lowers the MCD (from 47% to 17%), by keeping the same line shape.

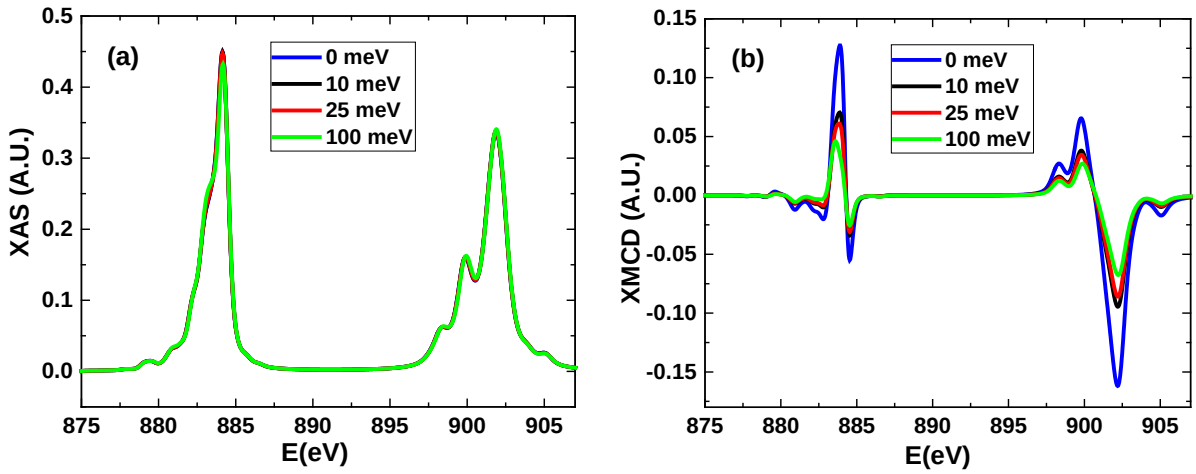

Figure 4.16 (a) XAS and (b) XMCD spectra for Ce f^0+f^1 simulated using parameters- Ef^1, Gf^1=+1.5, X-mix =0.5ev, $10D_q$=00 meV, 10meV, 25meV and 100meV, Exchange Field = 25 meV

The reduction in cerium magnetic moment via charge transfer multiplet model is still not comparable with the experimental results. The charge transfer multiplet model also can not completely explain our experimental results. All the models proposed can give the good explanation about the line shape of the XAS and XMCD spectra but cannot explain the strong reduction in the magnetic moment. Therefore, from the experimental results, it can be concluded that the cerium and iron are not very well coupled with each other (see in section 4.5.2 cerium XMCD results). The magnetic moment of cerium are frozen and not saturated.

4.7. Discussion

In this work, we investigated the magnetic properties of $CeFe_{11}Ti$ phase. As the part of the rare earth, lean magnetic materials project[34], the main objective of this work is to develop a microscopic understanding of the Cerium based intermetallic and to discern the magnetic contribution of Cerium and Iron. Further investigations related to the magnetic and structural properties have been performed using characterization techniques like superconducting quantum interference device (SQUID) magnetometer (Quantum design-MPMS3), x-ray diffraction (XRD) and scanning electron microscopy (SEM). From the microscopic images along with hard magnetic phase $CeFe_{11}Ti$, existence of multiple binary phases Ti carbonitride, soft magnetic phase $CeFe_2$, and Fe_2Ti in the vicinity of the stoichiometry have been identified in the specimen. From x-ray diffraction investigation occurrence of tetragonal $ThMn_{12}$-type $CeFe_{11}Ti$ phase with $I4/mmm$ symmetry, cubic $CeFe_2$ Laves phase with $Fd\bar{3}m$ symmetry observed (Section 4.3.2 table 1). The quantitative estimation shows the $Ce_{1.2}Fe_{12}Ti$ specimen has the 98.5% presence of main magnetic $CeFe_{11}Ti$ phase and exhibit the magnetization of 18 Bohr magneton/formula unit at room temperature (21 Bohr magneton/formula unit at 80 kelvin temperature) (Section 4.4).

In order to discern the contribution in the magnetization of each element in the alloy, XMCD measurements (see chapter 2 experimental techniques) have been performed *in-situ* at Fe $L_{2,3}$, Ti $L_{2,3}$ and Ce $M_{4,5}$ edges (at 300K and 80K) in the presence of 6.5 Tesla magnetic field no significant XMCD signal has been observed at Ti *L*-edge. The shape of XAS and XMCD spectra of Fe $L_{2,3}$ edges is analogous to the typical metallic Fe^{3+} configuration. But slightly reduced (31%) magnetic moment has been observed than pure metallic magnetic moment. The difference in line shape of experimental XAS and XMCD spectra of trivalent Ce $M_{4,5}$ edges from the simulated ground state (J=5/2) spectra of the Ce $M_{4,5}$ edges has been observed. At cerium edge very weak ferromagnetism has been observed due to the presence of only 1% XMCD effect at cerium $M_{4,5}$ edges. In order to understand the line shape and the reduced magnetic moment several models have been proposed i.e. Admixture of J=7/2 state in the ground state J=5/2 spectra (section 4.5.2), crystal field multiplet model (section 4.6.a) and charge transfer multiplet model (section 4.6.b).

Those variations in the XAS line shape can be explained by the idea of the increase in the ratio of J=7/2 state compare to that of the J=5/2 states in the ground state spectra. It turned out that the weight of J=7/2 is not larger than 10-15 % (section 4.5.1 Fig 11a and b). The crystal field multiplet model explains that there is a significant change in XMCD effect observed on varying

crystal field from 0 eV to 100 meV (section 4.6.a Fig 13a and b). Even in the presence of small crystal field in cerium one modifies the ground state spectra for cerium and effectively lowers the MCD, by keeping the same line shape. According to charge transfer multiplet model, the experimental XAS and XMCD line shapes of cerium are qualitatively well described by charge transfer energy Δ=1.5 eV energy (section 4.6.b Fig 14a and b) spectrum. The CTM model states that at Δ= 1.5 eV experimental spectrum is an admixture of 5.3 % of $4f^0$ and 94.7% of $4f^1$ state without applying any crystal field. The reduction in cerium magnetic moment via charge transfer multiplet model is still not comparable with the experimental results. The charge transfer multiplet model also can not completely explain our experimental results. All the models proposed can give the good explanation about the line shape of the XAS and XMCD spectra but cannot explain the strong reduction in the magnetic moment.

Therefore, from the experimental results it can be concluded that the cerium and iron are not very well coupled with each other (see in section 4.4.2 Cerium XMCD results) and the magnetic moment at the cerium edge in $Ce_{1.2}Fe_{12}Ti$ specimen are not saturated. Cerium magnetic moment appears to freeze at room temperature in the disordered state due to the strong interaction with the lattice. The interaction is much stronger than the exchange coupling between iron 3*d* and the cerium 4*f* electrons. Therefore even at the low temperature no ordering in the cerium magnetic moment is taking place.

5. XMCD Investigation on Rare Earth Garnets

5.1. Introduction - Rare earth Garnets (RIGs)

As magnetic insulators, rare-earth iron garnets ($R_3Fe_5O_{12}$) or RIG are an important class of materials, which are promising candidates for technological applications such as magnetic recording devices with giant magnetostriction [115], spin seebeck insulators for thermoelectric generation[116], microwave devices based on current-induced spin torque resonance[117], and faraday rotators in optical telecommunications [118, 119]. These systems are very well identified to have two different types of iron ion contributions, experiencing a tetrahedral (T_d) and octahedral (O_h) coordination environment (Figure 5.1). The general chemical formula for the rare earth garnets is $A_3B_2C_3O_{12}$. Where "A" represents the ions on dodecahedral, "B" octahedral and "C" on tetrahedral coordinated sub lattices. Each oxygen ion is surrounded by either A, B or C-sites. The schematic of sub lattices represented in Figure 5.1. The unit cell is cubic and consists of 160 atoms, 24 A, 16 B, 24 C and 96 O-sites and belongs to the space group of O_h –Ia3d [120]. A detailed description of the crystal structure is given in the reference[119] and presented in Figure 5.1.

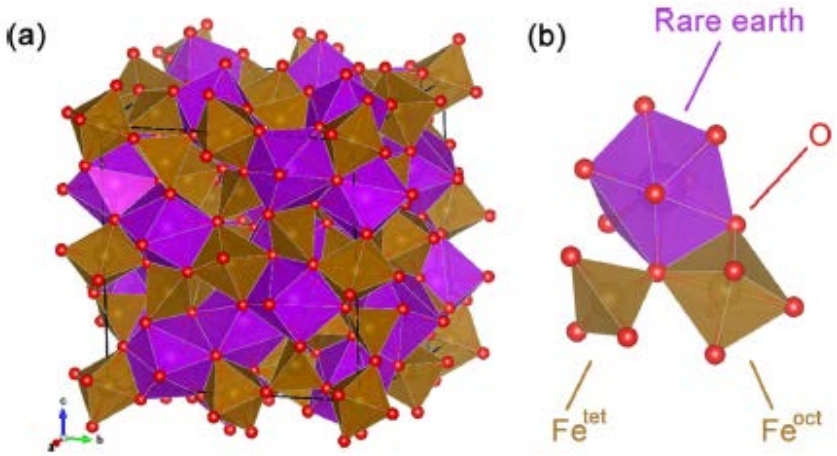

Figure 5.1 crystal structure of rare earth iron garnets. (a) Cubic unit cell. (b) Local environment experienced by Fe and R ions from their neighboring oxygen ions. The Figure is reproduced from reference[119].

Rare-earth iron garnets(RIGs) are described to possess magnetic moments of iron that are partially cancelling each other and have different magnitudes, which make the RIGs ferrimagnetic in nature [118, 121]. In the garnet structure the magnetic properties are directly affected by the type of ions which occupy a certain sub-lattice. The strongest interaction is present between the octahedral and the tetrahedral iron sites and the lattices couple with each

other antiferromagnetically. Oxygen ions are responsible for this kind of interaction between Fe^{3+} ions.

In order to understand the complex behavior of the ferrimagnetism, rare earth garnets is the standard example to consider [14, 16, 122]. These ferrimagnetic materials exhibit the compensation points and the compensation point was first predicted by Neel's theory of ferrimagnetism in 1948 [123]. The magnetic behavior of the rare earth (Gd-Lu) iron garnets was first time experimentally reported by Pauthenet *et al.* [124]. Pauthenet determined the first compensation point in gadolinium iron garnet (GdIG), which is the simplest among all the garnets. For a long time the compensation point was not considered as a point of phase transition, even though several inconsistencies were found around it [125]. The classical theory of the isotropic ferrimagnetics [126] in external fields was the first to recognize a phase transition of second order at T_{comp} and connect it with the development of canted magnetic structures in an external magnetic field. The magnetic structure in all rare earth garnets are collinear, with a domination of rare earth sub-lattice in the region of $T<T_{comp}$, and a domination of iron sub lattice for $T>T_{comp}$. Specific canted magnetic structures observed in the vicinity of the T_{comp}. Which are investigated in the gadolinium garnet using magneto optical methods. The temperature dependence of the magnetization $M(T)$ in rare earth garnets has been often measured [124]. Since 1958, it has been used for the determination of the molecular field coefficients and the exchange integrals. Several reviews on these results have been published [127, 128]. Around 1963, the detail investigation of the dependence of magnetization on temperature was studied by Geller *et al.* for all the rare earth elements (including light rare earth elements)[129, 130]. In this research work no compensation temperature was observed for light rare earth elements[129].

The $Y_3Fe_5O_{12}$ is one of the most studied rare earth garnet [119, 121, 131]. It is observed that the magnetization as a function of temperature shows a compensation point i.e. a temperature at which the spontaneous magnetization reaches almost zero [121, 132]. At this compensation temperature (T_{comp}), the total iron sub lattice magnetization becomes equal to the inverse sub lattice magnetization of the RE^{3+} ions and due to antiparallel coupling the spontaneous magnetization of the garnet reaches to zero. The weakest interaction exists between the dodecahedral (RE^{3+}) and the octahedral sites (Fe). Thus, the magnetic moments of the dodecahedral rare earth ions align parallel with the ones at the iron octahedral sites and antiparallel to the tetrahedral Fe ions. [119, 121]. The magnetic state of rare earth iron garnet is a function of the external magnetic field, temperature, pressure and composition. Due to the relative weak coupling of the RE ions, the RE sub-lattice magnetization has a different

temperature dependence, resulting in an increase in the magnetic moment of the rare earth elements to lower temperatures [119, 121].

It is important to precisely determine such sub-lattice magnetizations and the magnetic moments of the individual elements [119]. The higher contribution from the magnetic moment of rare earth elements to the total magnetization in these garnets rise to lower temperatures. For our investigation, these garnets are interesting as a reference specimen, where we can confirm the applicability of the XMCD orbital and spin sum rule for the rare earth elements on the experimental spectra measured below the compensation temperature. Due to the non-applicability of the spin sum rule for $M_{4,5}$ edges, no quantitative XMCD studies on rare earth elements of garnets at $M_{4,5}$ edge reported until present. Most of the investigations has been performed at $L_{2,3}$ edges of rare earth elements [133]. Some studies have been performed on Gd^{3+} [134] and Ho^{3+}[135] at $M_{4,5}$ edges however no sum rule analysis have been performed. Gadolinium (Gd^{+}) ion has a spherically symmetric electron distribution, negligible orbital moment and no contribution from the magnetic dipole term. In this chapter, the applicability of the spin sum rule for rare earth elements Sm^{3+}, Gd^{3+} and Dy^{3+} is confirmed.

5.2. Magnetization and Compensation temperature (T_c) of rare earth garnets

The magnetization of iron garnets can be written as sum of

$$M_s(T) = M_a(T) + M_d(T) + M_c(T) \quad \text{.....equation (5.1)}$$

Where T = temperature; M_a, M_d and M_c are the magnetizations of the octahedral, tetrahedral and dodecahedral sub lattices respectively and the $M_c(T) = M_c(0)B_j(T)$, $B_j(T)$ is Brillouin function , which depends on the temperature [121, 136]. Here, the M_c (0) $= 3Ng_cJ_c\mu_B$. Where J= effective angular momentum and g=gyromagnetic factor of the rare earth ions in the crystal [121].

The magnetization vector M_a is antiparallel to M_d, while M_c is parallel to M_d for light rare earth ions (R= cerium, neodymium, samarium), as long as L is larger than S and parallel to the heavy rare earth ions (R= dysprosium, gadolinium). In general, the direction of magnetization is considered with respect to the direction of magnetic field. In this case, if M_s is parallel to M_d then we used the positive sign and if M_s is antiparallel to M_d then we used the negative sign. [136]. For the trivalent light rare earth elements lighter than Gd^{3+}, the 4*f* spin and orbital moments are antiparallel ($J=L-S$). There is influence of lattice interaction on the orbital moment. Such contribution occurs in most of the light rare earth elements. The Sm^{3+} is exception in this case. The rare earth ions where $L>2S$ are expected that it contribute additively to the iron system

[121]. The magnetic moment (m), compensation temperature (T_{comp}) and the curie temperatures (T_C) of the garnets are presented in the table 5.1. The magnetic moment of the rare earth elements in Bohr magneton/formula unit estimated by the magnetization versus temperature curves at the lower temperatures.

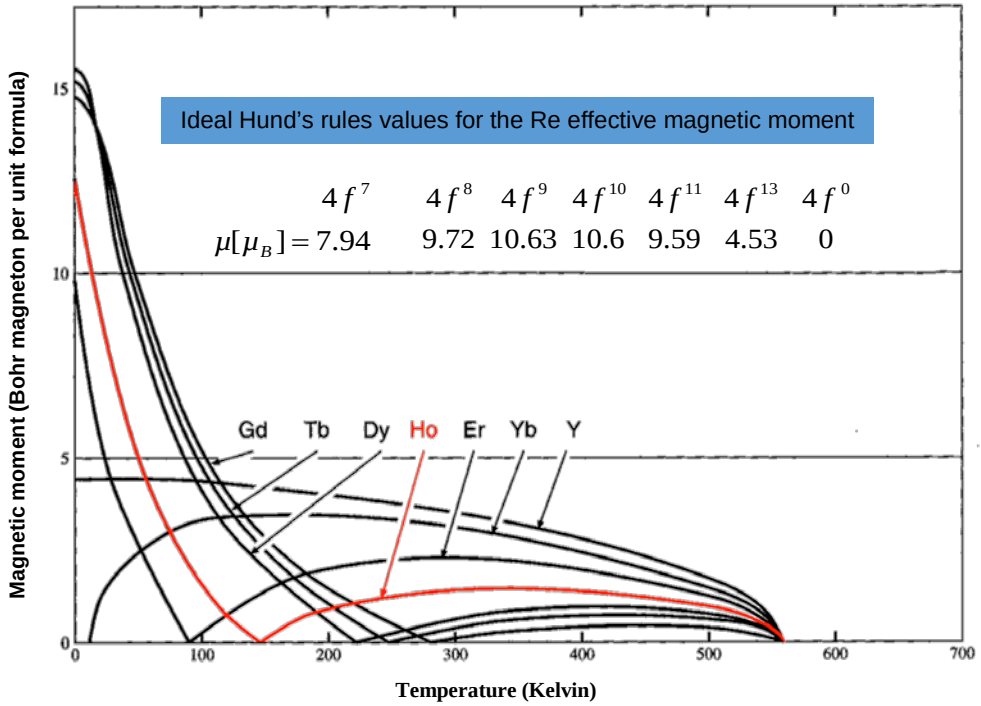

Figure 5.2 temperature dependence of the rare earth garnets $Re_3Fe_5O_{12}$ (R=Gd, Tb, Ho, Er, Yb, Y). The spontaneous magnetization is reaching zero twice as shown in figure. At the low temperatures, when the magnetic moment of Fe^{3+} T_d and O_h sites are completely compensating each other and magnetic moment is zero. Then it is called as compensation temperature (T_{comp}). At higher temperature when the total magnetic moment vanishes due to disordered magnetic moment it is known as Curie temperature (T_c). The curve is reproduced from Kittel's book[122]. The magnetic moment values shown in the box are taken from the Hund's rule values shown in chapter 3[14].

At compensation temperature (T_{comp}), the value of M (T_{comp}) =0 (refer Figure 5.2) in Gd^{3+} and heavy rare earth elements. In this thesis, the low temperature measurements (below the compensation temperatures) are predominantly interesting and we will reproduce the magnetization vs temperature (M vs T) curves for the Gd^{3+}, Sm^{3+} and Dy^{3+}. However, discussion about the Curie temperature [121] is out of the scope of this thesis. The exchange interaction between the rare earth ion and the iron is smaller compared to the Fe^{3+}-Fe^{3+}. If one need to perform the estimation of the magnetic moment of rare earth ions than the magnetization of the Yttrium garnet ($Y_3Fe_5O_{12}$) can be subtracted from the rare earth garnet $R_3Fe_5O_{12}$[138].

This can provide a good estimation about the rare earth magnetic moments contribution at the low temperature and can be compared with element specific results. Here, we systematically investigated the magnetic moment of the rare earth elements using XMCD sum rule analysis (in Bohr magneton per rare earth ion) and compared with the magnetization results obtained from SQUID magnetometer.

Table 5.1 curie temperature, Compensation temperature and magnetic moment of the rare earth garnets ($R_3Fe_5O_{12}$)[137]. At the lower temperatures, the magnetic moment of the rare earth elements in Bohr magneton/formula unit estimated by the magnetization versus temperature curves[137].

Garnets	Curie temperature (T_c) in Kelvin	Compensation temperature (T_{comp}) in Kelvin	Magnetic moment (m) μ_B/F.U.
Nd	567	-	7.16 (at 100K)
Sm	578	-	5.43
Eu	566	-	2.78
Gd	564	286	16.0
Tb	568	246	18.2
Dy	563	226	16.9
Ho	567	137	15.2
Er	556	83	10.2
Tm	549	-	1.2
Yb	548	0	-
Lu	549	-	5.07
Y	559	-	5.01

5.3. Reported XMCD studies at $M_{4,5}$ edges on the rare earth garnets

In order to understand the behavior of iron and rare earth elements in rare earth garnets, element specific studies have been performed in the hard x-ray range at iron *K*-edge[139] and at the $L_{2,3}$ edge of the rare earth elements also in $Ho_3Fe_5O_{12}$ [140] and $Dy_3Fe_5O_{12}$[141]. Some investigations were also performed in soft x-ray range at rare earth $M_{4,5}$ edge[142]. The first time angular dependent investigations have been performed at the M_5 edge in the $Tb_3Fe_5O_{12}$[143].

Using the x-ray magnetic circular dichroism the quantitative investigation of sub-lattice magnetization of iron and rare earth elements was performed. The basis of this work is to overcome the lack of the data in the XMCD study at the rare earth $M_{4,5}$ edges on rare earth garnets. There are reports of element specific studies at the rare earth's $M_{4,5}$ edges except gadolinium and holmium garnets. This is due to the non-applicability of the XMCD spin sum rule. In order to understand the magnetic behavior of the rare earth elements and their coupling with iron sub lattice three different garnets have been considered i.e. $Dy_3Fe_5O_{12}$, $Gd_3Fe_5O_{12}$ and $Sm_3Fe_5O_{12}$. We performed the XAS and XMCD studies on the iron at $L_{2,3}$ edges and the rare earth elements at $M_{4,5}$ edges on three garnets specifically, $Dy_3Fe_5O_{12}$, $Gd_3Fe_5O_{12}$ and $Sm_3Fe_5O_{12}$ present in powder-form and the estimation of the individual orbital and spin moment was done using XMCD spin and orbital sum rules by applying all the necessary corrections [20, 21, 35]. The complete analysis procedure at rare earth's $M_{4,5}$ edges for the experimental spectra is described in detail in chapter 3. Samarium is a light rare earth element where the *f* orbitals are less than half-filled, gadolinium where the *f* orbitals are half-filled and the dysprosium where the *f* orbitals are more than half filled. Due to parallel (Gd, Dy) and antiparallel (Sm) coupling between spin and orbital moment the overall coupling with the iron sub-lattice is also different.

By discussing the coupling between iron and rare earth elements, confirming the applicability of the spin sum rule and learning in detail about the XMCD sum rules for the $M_{4,5}$ edges, will also develops the better understanding in the case of complex rare earth elements based permanent magnets. Therefore, the rare earth garnets can be good reference samples. The further structural and the element specific XMCD investigations will be discussed in the next sections.

5.4. Structural investigations

In order to confirm the phase analysis of the rare earth garnets powder x-ray diffraction measurements are performed using cobalt-K_α radiation (1.78896 Å). Figure 5.3 shows the x-ray diffraction pattern for (a) samarium, (b) dysprosium and (c) gadolinium garnets. The measurement and analysis procedure via Rietveld refinement is performed in similar manner as discussed in the chapter 4 section 4.3.2. For analysis the possible occurrence of the $Sm_3Fe_5O_{12}$, $Dy_3Fe_5O_{12}$ and $Gd_3Fe_5O_{12}$ phase is considered, the lattice parameters for samarium, dysprosium and gadolinium garnets are observed as mentioned in reference [144]. Most of the reflections arise from the expected phases (labelled as red squares). In order to precisely

compare the total sample magnetization with the element specific XMCD results, the chemical compositions of the sintered magnets is analyzed by inductive coupled plasma spectroscopy (ICP-OES) (Spectro- Ciros).

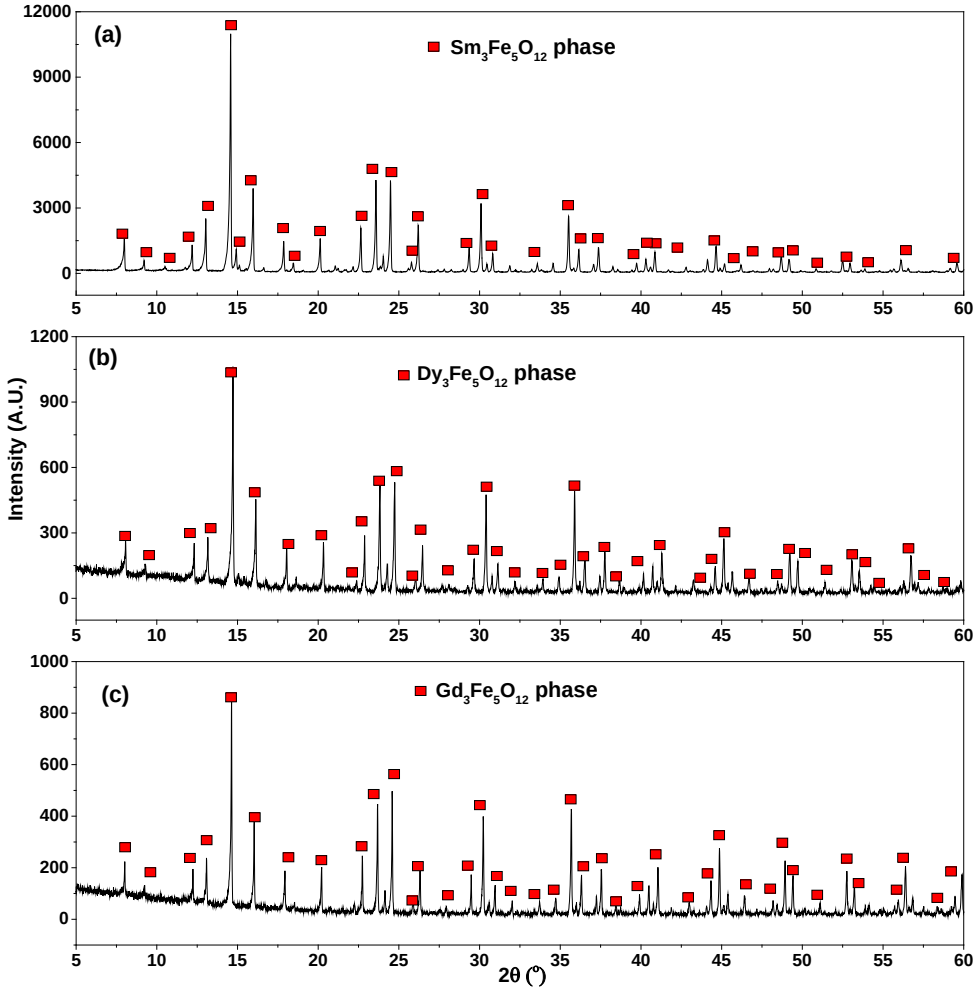

Figure 5.3 x-ray diffractions pattern of the rare earth garnets (a) $Sm_3Fe_5O_{12}$ (b) $Dy_3Fe_5O_{12}$ (c) $Gd_3Fe_5O_{12}$. The peaks corresponding to the respective garnet phases are labelled by red squares. All the diffraction patterns are in 100% agreement with the reference patterns from ICDD.

The spectroscopic analysis results are presented in Table 5.2. The negligible amount of impurities like cobalt (Co), magnesium (Mg), manganese (Mn), chromium (Cr) and copper (Cu) is identified. The Stoichiometry for all the three specimens are turned out to be $Dy_3Fe_5O_{12}$, $Gd_3Fe_5O_{12}$ and $Sm_3Fe_5O_{12}$ respectively. The ICP data consistent with the x-ray diffraction results. The magnetic properties of all the garnets with the magnetometry will be discussed in the next section.

Table 5.2 elemental composition of $Dy_3Fe_5O_{12}$, $Gd_3Fe_5O_{12}$ and $Sm_3Fe_5O_{12}$ garnets is measured by inductive coupled plasma optical emission spectroscopy (ICP-OES). The results of the iron, oxygen and the rare earth elements presented here in weight percentage (weight %). The presence of some impurities like cobalt (Co), magnesium (Mg), manganese (Mn), chromium (Cr) and copper (Cu) also identified.

Specimen	Rare earths (wt. %)	Iron (wt. %)	Oxygen (wt. %)	Impurities (Co, Cu, Mn, Cr, Mg)	Empirical formula
$Dy_3Fe_5O_{12}$	49.1±0.5	29.6±0.3	19.9±0.2	ca.0.02	$Dy_3Fe_5O_{12}$
$Gd_3Fe_5O_{12}$	49.8±0.5	29.0±0.3	19.5±0.2	ca.0.01	$Gd_3Fe_5O_{12}$
$Sm_3Fe_5O_{12}$	48.8±0.5	30.4±0.3	20.74±0.2	ca.0.01	$Sm_3Fe_5O_{12}$

5.5. Magnetic investigation - SQUID results

Magnetic measurements were performed over the temperature range of the 1.7-350 Kelvin with a superconducting quantum interference device (SQUID) magnetometer up to field of 6.5 T magnetic field on rare earth garnets powder ($Dy_3Fe_5O_{12}$, $Gd_3Fe_5O_{12}$ and $Sm_3Fe_5O_{12}$). The measurements are performed tapping powder inside the specially designed quartz tube and the lid of the tube is fixed in such a manner that the powder does not move during measurements. Magnetic hysteresis of the rare earth iron garnets for gadolinium (except at room temperature), samarium and dysprosium are apparently magnetically saturated at moderate fields (~1 to 2 Tesla) at temperatures near 1.7 Kelvin (refer Figure 5.4 (a) to (c)). The compensation points (T_{comp}) obtained by the magnetometer are found to be in good agreement with the previously reported results[124, 130] (refer Figure 5.4 (e) and (f)). General chemical formula for the rare earth garnets is $RE_3Fe_2Fe_3O_{12}$. In these two different types of iron ions contribution, a tetrahedral (T_d) and octahedral (O_h) iron sites antiparallel to each other.

The rare earth ions (RE^{3+}) are weakly anti-ferromagnetic coupled to the iron magnetization. According to Hund's rule each iron magnetic moment should be at around 5 Bohr magneton /atom (3* T_d Fe^{3+}-2* O_h Fe^{3+}) in iron garnets. In order to estimate experimentally the total iron sub-lattice magnetization, the yttrium iron garnets (YIG) can be considered as a good reference, because yttrium is diamagnetic and the total magnetization is just based on the averaged iron sub-lattice magnetization. From the yttrium iron garnet (YIG) magnetization vs temperature curves, the resulting total magnetic moment for iron sub lattice per formula unit is 4.4 Bohr magneton per formula unit (0.88 Bohr magneton /Fe^{3+}ion)[130]. The contribution of the rare

earth ions can be separated from the magnetization vs temperature curves by simple subtraction of the YIG contribution. Figure 5.5 (g) to (l) shows the magnetic moment of the rare earth elements per formula unit.

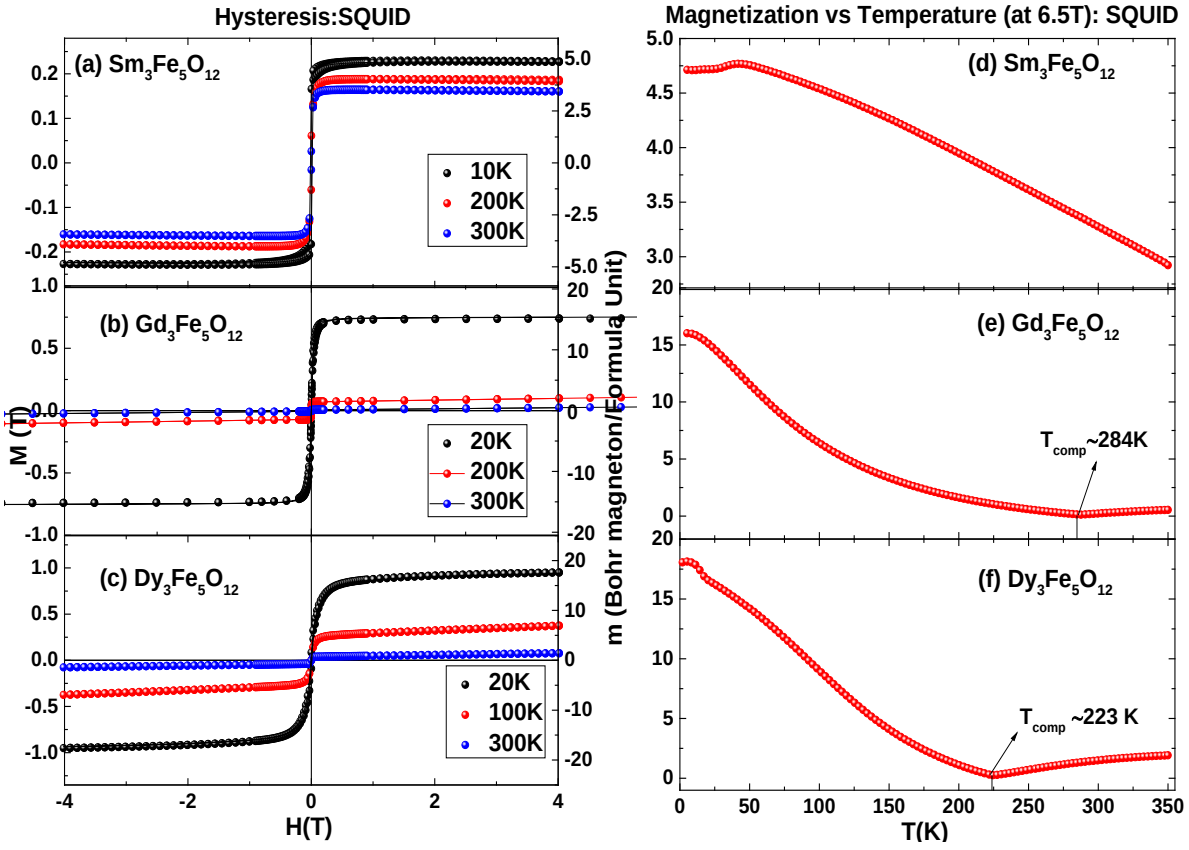

Figure 5.4 SQUID hysteresis loops of (a) $Sm_3Fe_5O_{12}$, (b). $Gd_3Fe_5O_{12}$ and (c) $Dy_3Fe_5O_{12}$ garnets measured at room temperature and low temperatures, Magnetization ($M=\mu_0 J$) vs Temperature curve (temperature range-1.7 Kelvin to 350 Kelvin) of the (d) $Sm_3Fe_5O_{12}$, (e) $Gd_3Fe_5O_{12}$ and (f) $Dy_3Fe_5O_{12}$ garnets at 6.5 T Tesla magnetic field.

The estimation of the rare earth magnetization can be performed via magnetization versus temperature curves in following ways -

(I) At room temperature, Fe^{3+} ions are dominating the total magnetization. In presence of magnetic field, the average Fe^{3+} magnetic moment is aligned parallel and the RE^{3+} moments are antiparallel to the magnetic field (refer figure 5.6). With the decreasing temperature rare earth sub-lattice magnetization is increasing and due to antiferromagnetic coupling with the iron sub lattice total magnetization is decreasing. At a compensation temperature (T_{comp}) (refer figure 5.6 (e) and (f)) the total magnetization vanishes in some of the heavy rare earth garnets. Therefore, for the heavy rare earth elements such as Dy, Tb and completely half- filled shell

Gd which exhibits compensation temperature, at the temperature $T<T_{comp}$ magnetization at the rare earth site can be estimated as follows.

$$M_{RE}=M_{total}\text{ (REIG=SQUID) - }M_{total}\text{l (YIG=reference)}$$

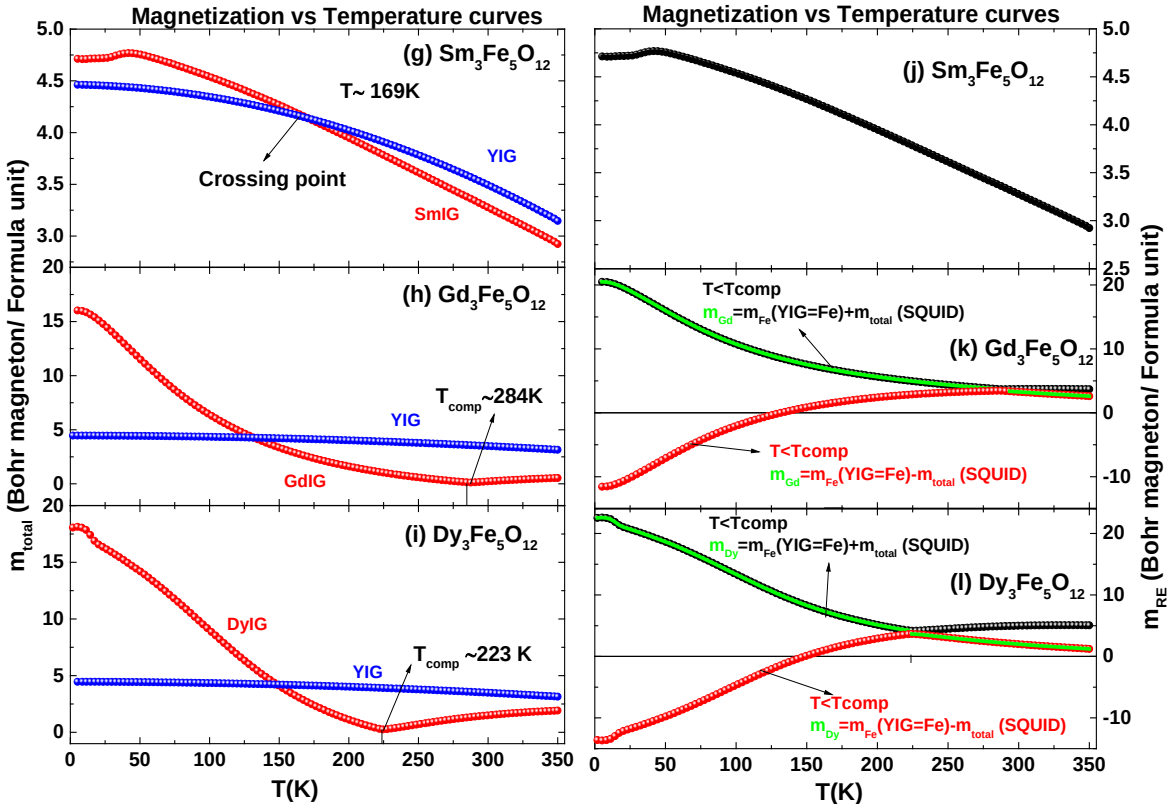

Figure 5.5 magnetic moment of the all the garnets ((g), (j) $Sm_3Fe_5O_{12}$ (h),(k) $Gd_3Fe_5O_{12}$, (i),(l) $Dy_3Fe_5O_{12}$) in Bohr magneton per formula unit vs temperature (in red color). All the curves are overlapped with the YIG magnetization vs temperature curve (in blue color). Estimation of the average magnetic moment of rare earth ions using YIG magnetization verses temperature curve. The flip in the magnetization of the rare earth elements takes place above and below the compensation temperature. Therefore, estimation of the magnetic moment of the rare earth ions needs to be done in different ways above and below the compensation temperature for the dysprosium and gadolinium garnets. The rare earths magnetic moment/formula unit is shown in two different curves (Black-$T<T_{comp}$ and red $T>T_{comp}$) for Dy and Gd. The resultant curve for the Gd and Dy magnetic moment is shown by green curve. This only provides the average contributions of the rare earth magnetic moment so the sign for the rare elements is not considered from here above the compensation temperature. Although Samarium magnetic moment remains negative because the iron moment does not change the sign in case of light rare earth elements, therefore the estimation of samarium magnetic moment cannot be done in similar way by simply subtraction of the YIG total magnetization. The samarium garnet M vs T curve has been presented in the right figure (j).

(II) Below the compensation temperature the flip in the direction of magnetization takes place in the iron and the heavy rare earth ions. The rare earth ion dominates the total

magnetization below the compensation temperature and is parallel to the external magnetic field. While the resulting iron moments are antiparallel (refer figure 5.6). For heavy rare earths such as Dy, Tb and completely half-filled shell Gd $T>T_{comp}$

$$M_{RE} = M_{total}\text{ (YIG= reference) - }M_{total}\text{ (DyIG=SQUID)}$$

(III) Light rare earth elements (Sm, Nd) do not possess any compensation temperature. Therefore

$$M_{total}\text{(REIG=SQUID)- }M_{total}\text{l(YIG=reference)}$$

The resultant curve for the Gd and Dy magnetic moment is shown by green curve in Figure 5.5 (k) and (l). It provides merely the average contributions of the rare earth magnetic moment. Above the compensation temperature, the sign of the magnetization direction for the rare elements is not correct from the Figure 5.5 (k) and (l). The flipping of the magnetization has been observed above and below the compensation temperature in the reported results via XMCD investigation for iron and even for heavy rare earth ions and gadolinium [135, 142]. It is also visible in the M vs T curve and we also discuss these XMCD results in detail in the proceeding sections.

Geller *et al*[129] and Pauthenet[124] reported magnetization versus temperature data on samarium iron garnet (SmIG) and their investigation is in good agreement with our obtained results. Geller has shown that magnetization versus temperature data on polycrystalline samarium iron garnet at fields of 4.8, 9.6, and 14.24 kOe. The M vs T curve behavior is analogous to the reported results [129]. Below 35 kelvin a dip in the magnetization vs temperature curve is due to Sm^{3+} ions [129]. The moment of SmIG is 4.7 Bohr magneton/Formula unit (refer Figure 5.5 (j)) at the temperature of 4 Kelvin implying a contribution of 0.09 bohr magneton / Sm^{3+} ions (refer Figure 5.5 (j)), which is close to the results reported by Geller *et al*[129]. The magnetic moment and the slope of the M vs T curve in case of samarium is larger than the YIG (refer Figure 5.5 (g)). Both the curves are crossing at temperature of 167 Kelvin. The spin (*S*) moment of Sm^{3+} ion is antiparallel to the orbital (*L*) moment, therefore the Sm^{3+} ion magnetization is always antiparallel of the iron sub-lattice magnetization, even at the lower temperatures. Therefore, there is no compensation temperature is observed. Due to this reason, the estimation of the samarium magnetization (in Bohr /formula unit) cannot simply estimated by the subtraction with the YIG total magnetization. As there is no flip in the magnetization in samarium has been observed due to antiparallel coupling of the orbital and spin moment (Hund's rule-Sm^{3+} m_L=5, m_S=5, $m_J = m_L - m_S$=0). Therefore, simply the M vs T curve is presented in the Figure 5.5 (j)

Figure 5.6 schematic representation of coupling between rare earth ions and the ion below and above the compensation temperature (T_{comp}) in heavy rare earth elements.

The gadolinium and dysprosium garnets magnetically saturate between 1.4 and 12 Kelvin at 1.2T [130]. At temperatures above 22 Kelvin the saturation cannot be attained for gadolinium iron garnets (GdIG) and dysprosium iron garnets (DyIG). Gadolinium and dysprosium garnet appears close to the saturation in our experimental results of 16 and 17 Bohr magneton/ formula at 4 Kelvin in presence of 6.5T magnetic field respectively. These obtained results are well matched with the results obtained by Geller [130]. The total magnetic moment estimated for the gadolinium and dysprosium are 20 and 22 Bohr magneton/formula unit (Figure 5.5 (h) and (i)) at the temperature of 4 Kelvin implying a contribution of 6.7 Bohr magneton/Gd^{3+} ions and 7.3 Bohr magneton/Dy^{3+} ions (Figure 5.5 (k) and (l)), which are close to results reported by Geller *et al* by the extrapolation [129] and expected from the Hund's rule (Gd^{3+} m_L=7, m_S =0, m_J = m_L-m_S=7 and Dy^{3+} m_L=5, m_S =5, m_J = m_L-m_S=10). The total spin alignment of the dysprosium garnet should be 10 Bohr magneton / Dy atom (3*5 m Dy-1*5 m Fe), however the SQUID results for the dysprosium garnet are still significantly smaller than the values which are estimated from the Hund's rule [130]. If the dysprosium spin is aligned completely antiparallel to the iron spin without any canting then the spin magnetic moment should be 5 Bohr magneton /atom. This shows the alignment or the orientation of the *J, L* and *S* in case of dysprosium plays a significant role. In order to check the orientation of *J* and *S*, XMCD studies have been performed in this thesis to clarify the situation and to test the new 4*f* sum rules derived here.

5.6. Spectroscopic investigation-XAS and XMCD results

In order to discern the influence of each element in the alloy, XMCD measurements (Refer chapter 2 experimental techniques) have been performed *in-situ* at Fe $L_{2,3}$, Gd $M_{4,5,}$ Sm $M_{4,5}$ and Dy $M_{4,5}$ edges for all the garnets (at room temperature and low temperature–below 30 kelvin) in the presence of 6.5 Tesla magnetic field in powder form and the element specific hysteresis also have been performed at the iron L_3 edge. The disadvantage of using powder form is the charging that occurs at low temperature due to isolating grains. At low temperature the charging of the insulating grains can be prevented by the use of very thin layer of the powdered garnets deposited on colloidal graphite (Aqua dac), used for proper electrical contact. Charging could be futher reduced also by the lowered synchroton light intensities. The iron and rare earth magnetic moment values are corrected for the degree of circular polarizations. All the measured spectra were background subtracted and pre- and postedge normalized. The measurements procedure is similar as reported in reference[135].

5.6.1. XAS and XMCD –Fe $L_{2,3}$ edges:

(i) XAS and XMCD line shape analysis

Figure 5.7 shows the Fe $L_{2,3}$ edges XAS and XMCD spectra at room and low temperatures (below 30 Kelvin) for all the rare earth garnets ((a and d) $Sm_3Fe_5O_{12}$, (b and e) $Gd_3Fe_5O_{12}$ and (c and f) $Dy_3Fe_5O_{12}$. For the specimen $Sm_3Fe_5O_{12}$, no low temperature measurements were performed at iron edge as the iron sub-lattice magnetization is always positive (refer Figure 5.7 (a) ,(d) $Sm_3Fe_5O_{12}$). The shape of the XAS and XMCD spectra at the iron $L_{2,3}$ edges are similar for all the rare earth garnets and are analogous to the iron oxide spectra [99, 145-147]. Above and below the compensation temperature the changes in the iron sub-lattice magnetization is directly visible in case of DyIG and GdIG. At the low temperature, XMCD signal direction changed, refer Figure 5.7 (b), (c), (e) and (f) as it is in agreement with the reported results for the holmium garnet (HOIG) [135]. These systems are very well recognized to have two different types of iron ion contribution, experiencing a tetrahedral (T_d) and octahedral (O_h) coordination environment (Figure 5.1). For the proper shape analysis of the experimental XAS and XMCD spectra of the iron and to discern the features of T_d and O_h site, we have simulated XAS and XMCD spectra for the Fe $L_{2,3}$ edges using the CTM4XAS 5.5 program, which is

based on the crystal field multiplet calculations, including the crystal field parameters (crystal field symmetry and the exchange field) and spin orbit coupling parameters [42]. The simulation parameters used here are analogous to the reference [99].

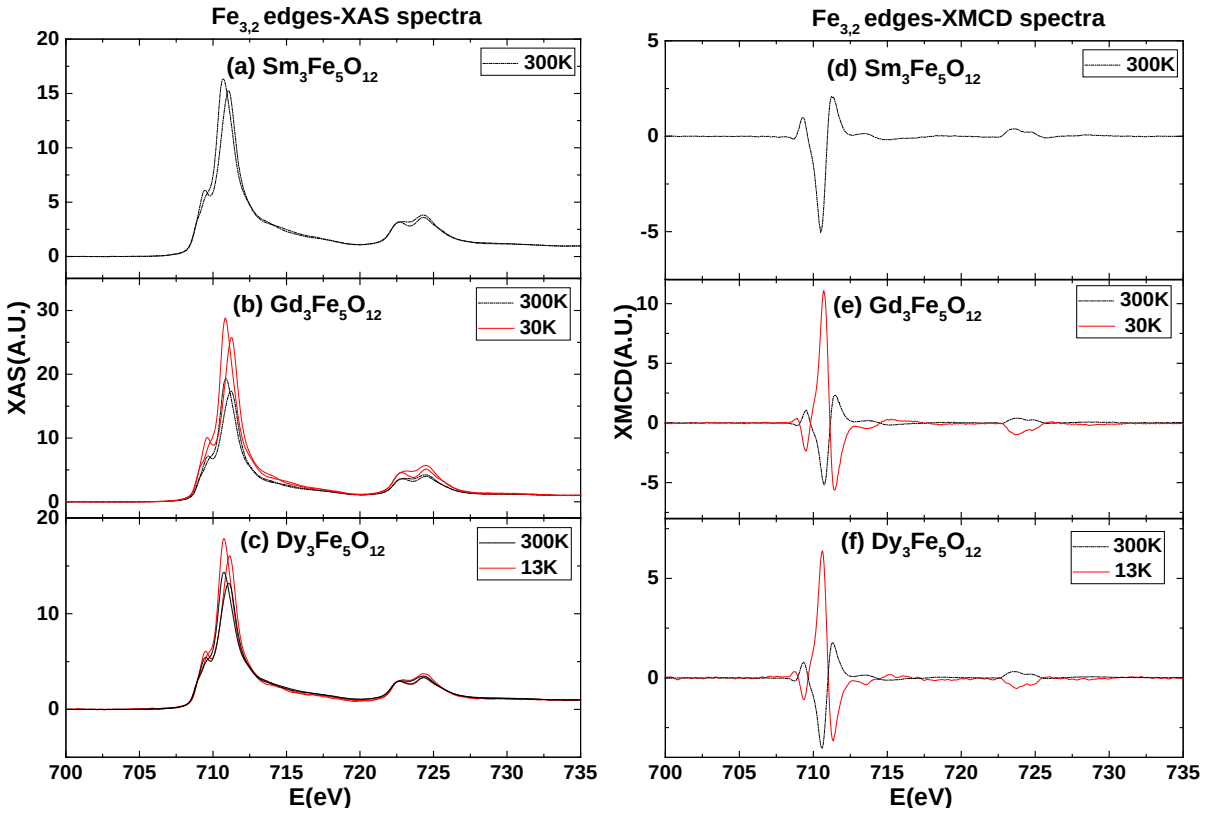

Figure 5.7 edge normalized XAS and XMCD: (difference in left and right polarized XAS spectra) spectra of rare earth's (RE= Gd, Dy, Sm) at Fe $L_{2,3}$ edge for garnets (a and d) $Gd_3Fe_5O_{12}$,(b and e) $Dy_3Fe_5O_{12}$ and (c and f) $Sm_3Fe_5O_{12}$ at 6.5T magnetic field) recorded at low temperature (in red color-solid line) and at room temperature (in black color-dash dot line) are presented here.

For the atomic multiplet calculations, final Slater integrals F_{pd} and G_{pd} of 77% and 74%, respectively were chosen for both the Fe (octahedral-O_h and tetrahedral-T_d) sites[99]. The Slater integral values of F_{dd} for O_h Fe (68%) and T_d Fe (60%) sites are varied. The values used here are all reduced to 80% of the Hartree-Fock values. In the C_4 crystal symmetry, $10D_q$ values of 1.6 and −0.8 eV were used for the O_h and T_d sites respectively [99]. The exchange field for the symmetry breaking for the O_h Fe site (−12 meV) was chosen to be opposite to the T_d Fe sites (18 meV), as the spins of iron ions at T_d sites and O_h sites are antiparallel to each other. All the spectra were further broadened by a Lorentzian half width of 0.2 eV and 0.4 eV. The

instrumental broadening was also accounted for by considering a Gaussian broadening of 0.2 eV. The individual difference is that the contribution of the Fe^{2+} is not considered.

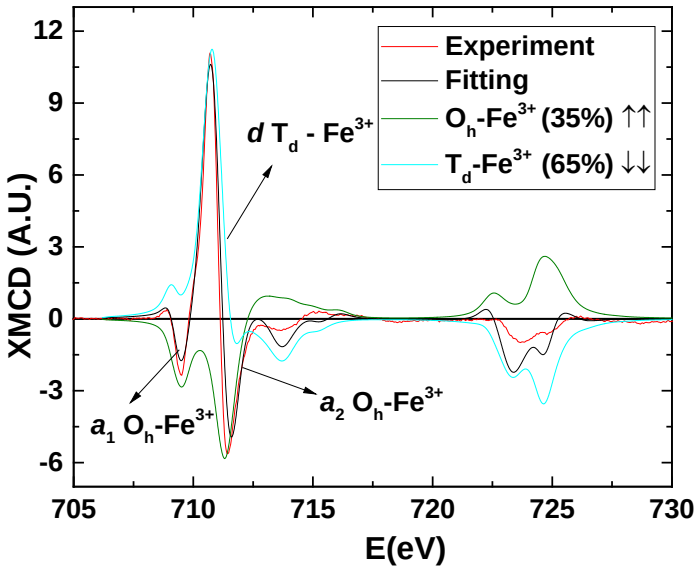

Figure 5.8 simulated XMCD spectra of a_1 and a_2 O_h-Fe^{3+} (in green color), T_d-Fe^{3+} (in cyan color) and their sum (In black color-fitted spectra- O_h 35%*:* T_d 65%) contributions overlapped with the experimental spectra ($Gd_3Fe_5O_{12}$ at Fe $L_{2,3}$ edge measured at 30 Kelvin). Alone one representative XMCD spectra at Fe $L_{2,3}$ edge is shown for fitting because the spectral shape of Fe $L_{2,3}$ edge for other garnets is same, except for the change in XMCD intensity and the relative orientation. The octahedral (O_h-35%) and tetrahedral (T_d-65%) site of Fe^{3+} spectra are antiparallel coupled to each other.

We attempt to reproduce the experimental Fe in order to generate a fit, by mixing the O_h Fe and T_d Fe spectra in an appropriate ratio. As all the iron spectra exhibit similar XMCD shape, merely one spectrum (XMCD of GdIG Fe $L_{2,3}$ at 30 Kelvin Figure 5.7 (e) red curve) is considered for fitting here. The theoretical spectra for the O_h Fe^{3+} and T_d Fe^{3+} are well match to the previous reported simulation results [145, 147]. As observed from the fitting that the L_3 edge of XMCD spectrum of iron is a combination of two negative peaks (labeled as a_1 and a_2 in Figure 5.8) and one large positive peak (labeled as *d* in Figure 5.8). The a_1 and a_2 is caused by the O_h Fe^{3+} contribution and *d* peak is from T_d Fe^{3+} contribution respectively [99, 145]. There is possibility that very small amount of Fe^{2+} is present. But in particular, no strong characteristic features of Fe^{2+} in the octahedral sites (as in Fe_3O_4) are found, such as a shoulder at the onset of the L_3 and L_2 XAS spectra [148, 149]. The spins of O_h Fe^{3+} ions are coupled anti-ferromagnetically with the spins of T_d Fe^{3+} B ions by the super exchange interaction acting via the intervening O^{2-} ions [135, 148]. Spins of O_h Fe^{3+} ions are oriented in a direction parallel to the external magnetic field at low temperatures in garnets and antiparallel to room temperatures (refer Figure 5.8) [135]. As a result of this fitting, at low temperature in these garnets the T_d Fe^{3+}site exhibits the

maximum (65%) contribution in the spectra and the rest (35%) is O_h Fe^{3+} site and vice versa at the room temperature. The fitting at L_2 edge is not very good, however can reproduce all the structures of the experimental spectra very well. The elements specific hysteresis curves are also measured at Fe L_3 edge. The SQUID hysteresis are completely reproduced by the Fe L_3 edge element specific magnetization curves for all the garnets, however not discussed in detail in this chapter.

(ii) XMCD sum rule analysis at Fe $L_{2,3}$ edge

Table 5.3 sum rule analysis results of experimental XMCD spectra of Fe $L_{2,3}$ edge for all garnets. The values of orbital moment ($m_{L)}$), spin moment ($m_{S)}$), total magnetic moment (m_L+m_S), and the orbital to spin ratio (m_L/m_S)) in units of Bohr magneton (μ_B)/atom presented in table.

T (Kelvin)	Orbital (μ_B / atom)	Spin (μ_B / atom)	Total (μ_B / atom)	Ratio
$Gd_3Fe_5O_{12}$ at Fe $L_{2,3}$ edge				
300	0.04±0.01	0.30±0.02	0.34±0.02	0.12±0.02
30	0.04±0.01	-0.46±0.02	-0.42±0.02	-0.09±0.01
$Dy_3Fe_5O_{12}$ at Fe $L_{2,3}$ edge				
300	0.026±0.01	0.30±0.02	0.33±0.02	0.08±0.01
13	0.034±0.01	-0.48±0.02	-0.45±0.02	-0.07±0.01
$Sm_3Fe_5O_{12}$ at Fe $L_{2,3}$ edge				
300	0.084±0.01	0.33±0.02	0.41±0.02	0.25±0.02

Evidence for the flip in the magnetization comes from the sum rule analysis of the iron XMCD spectrum, therefore by using sum rules for $L_{2,3}$ edges [24] quantitative estimation of the spin and orbital sum rule is performed. The number of holes (n_h) is taken 5 for the Fe^{3+} $3d^5$ shell [135]. The values of $<S_Z>$ were determined by assuming that the $<T_Z>$ is negligible because the measured specimens are in the powder form, therefore the average contribution of the $<T_Z>$ is negligible. Figure 5.8 shows the XAS and XMCD spectra of Fe $L_{2,3}$ edges for all garnets at 300 and 80 Kelvin respectively and the corresponding sum rule analysis results are presented in Table 5.3.

The yttrium garnet has been investigated among all the rare earth garnets in the past [99, 130]. The Y^{3+} is diamagnetic, the contribution in the total magnetization is from the iron. Yttrium iron garnet can be considered as a good reference for the iron magnetic moment. The ratio of S_Z moment between room temperature and 80 Kelvin for yttrium iron garnet is (4.7/3.56=) 1.34 as reported [150]. The ratio between low temperature and room temperature S_Z moment values for the $Gd_3Fe_5O_{12}$ and $Dy_3Fe_5O_{12}$ are -1.54±0.2 and -1.6±0.2 respectively, which is close to the YIG value [150] and HoIG [135]. The Fe spin magnetic moment values for all the garnets are almost similar (Table 5.3). For the $Sm_3Fe_5O_{12}$ specimen no low temperature measurements are performed because of the lack of time. The samarium magnetic moment is always negative (does not change the sign) and it does not exhibit any compensation temperature due to antiparallel coupling with spin and orbital moment. It was the least important to perform the measurements and during the measurements, we were struggling with the charging problem also at the low temperature.

A change in the direction of the iron sub-lattice magnetization is observed below compensation temperature (T_{comp}) for GdIG and DyIG (refer Figure 5.8 and 5.7(e) and (f)). The iron sub-lattice magnetization is dominated by the T_d Fe^{3+} (65 % contribution) lattice site (Figure 5.8) as it is visible in the fitting results. At room temperature the total Fe magnetic moment is positive and due to change in direction of the iron sub-lattice magnetization below T_{comp}, the total magnetic moment of iron switches to negative (refer Figure 5.8). The sign of the XMCD signal is a clear indication of the orientation of the iron magnetic moment with respect to the magnetic field. The orbital moment in case of iron is almost negligible. According to Hund's rule the total Fe sub-lattice magnetic moment is around 5 Bohr magneton /F.U. (3* m T_d Fe^{3+}- 2* m O_h Fe^{3+}) for iron and from the YIG magnetization vs temperature curves, the resulting total magnetic moment per formula unit is 4.4 Bohr magneton per formula unit (0.88 Bohr magneton /Fe^{3+}ion) [130]. The YIG results are not the XMCD results, it is estimation from the magnetization vs Temperature curve.

The total magnetic moment of the iron for the $Gd_3Fe_5O_{12}$ (at 30 Kelvin) and $Dy_3Fe_5O_{12}$ (at 13 Kelvin) are -0.42±0.2 and -0.45±0.2 Bohr magneton/atom respectively. The result for iron is half of the reported result from the YIG [99] and 25% increase compared to the reported results on HoIG [135]. It has been considered from sometime that the reduction in the projected magnetic moment of the iron compared to the YIG results can be explained by the Fe^{3+} ions hybridization with oxygen (O^{2-}) ions [135]. This explanation is not the reason for the reduction in the magnetic moment here. The major cause for the reduction in the iron magnetic moment

is that there is a less magnetic iron shell around each grain. The XMCD effect is also almost double in the height in our experimental results at low temperatures compared to the iron XMCD effect reported for the HoIG specimen. The ratio of the spin magnetic moment at low temperature $(m_S)_{LT}$ and room temperature $(m_S)_{RT}$ of iron for garnets ($Gd_3Fe_5O_{12}$, $Dy_3Fe_5O_{12}$) is compared with the reported results of the $Ho_3Fe_5O_{12}$ garnet[135] in Table 5.4. The ratio $(m_S)_{LT}/(m_S)_{RT}$ is close to the $Ho_3Fe_5O_{12}$ garnet[135] in case of $Gd_3Fe_5O_{12}$, however increased 8 % in case of $Dy_3Fe_5O_{12}$ garnet.

Our main purpose is to perform the XMCD investigation at the rare earth sites to check the applicability of the spin rum rule at the $M_{4,5}$ edges. Similar measurements have been performed at the $M_{4,5}$ edges of the rare earth elements. In the consecutive section, the XMCD results will be discussed for rare earth elements.

Table 5.4 spin (m_S) sum rule analysis results of experimental XMCD spectra of Fe $L_{2,3}$ edge for garnets ($Gd_3Fe_5O_{12}$, $Dy_3Fe_5O_{12}$) in units of Bohr magneton (μ_B)/atom at room temperature and low temperature (measured below compensation temperature) presented in table. The ratio of the spin magnetic moment at low temperature $(m_S)_{LT}$ and room temperature $(m_S)_{RT}$ of iron for garnets ($Gd_3Fe_5O_{12}$, $Dy_3Fe_5O_{12}$) is compared with the reported results of the $Ho_3Fe_5O_{12}$ garnet[135].

Specimen	**Spin-room temperature- $(m_S)_{RT}$ (μ_B / atom)**	**Spin-low temperature $(m_S)_{LT}$ (μ_B / atom)**	**Ratio $(m_S)_{LT}/(m_S)_{RT}$**
$Gd_3Fe_5O_{12}$	0.30±0.01	-0.46±0.02	-1.53 ±0.02
$Dy_3Fe_5O_{12}$	0.30±0.01	-0.48±0.02	-1.6±0.02
Literature values[135]			
$Ho_3Fe_5O_{12}$	0.23±0.01	-0.34±0.02	-1.48±0.02

5.6.2. XAS and XMCD –rare earth elements –$M_{4,5}$ edges and sum rule analysis

Figure 5.9 (g to l) shows the rare earth $M_{4,5}$ XAS and XMCD spectra at room temperature and low temperatures (below 30 Kelvin) for all the rare earth garnets ($Gd_3Fe_5O_{12}$ and $Dy_3Fe_5O_{12}$). For the (a) $Sm_3Fe_5O_{12}$ specimen no low temperature measurements have been performed due to charging problem during the measurements. In order to compare with the experimental spectra, the XAS and XMCD spectra at the $M_{4,5}$ edges of the Gd, Sm and Dy have been simulated by atomic multiplet theory calculations (refer chapter 3.4.4). The spectral shape of

the Gd $M_{4,5}$ Sm $M_{4,5}$ and Dy$M_{4,5}$ edge is well match to the theoretical ground state spectrum reported in chapter 3.4.4 and are in good agreement with the previously reported results [33, 37]. The experimental Gd, Sm and Dy $M_{4,5}$ edge XMCD and the nonmagnetic XAS spectra are overlapped with the theoretically simulated Hund's rule ground state spectra of the Gd, Sm and Dy in Figure 5.10 (m to r). As rare earth elements are localized the spectral shape does not vary too much and do not overlap significantly with the oxygen *p* electrons [135]. But here in the case of experimental samarium XMCD and nonmagnetic XAS spectra clear difference has been observed in comparison with the theoretically simulated Hund's rule ground state spectra Figure 5.10 (m and r). In case of dysprosium and gadolinium the difference is not much prominent as compared to samarium.

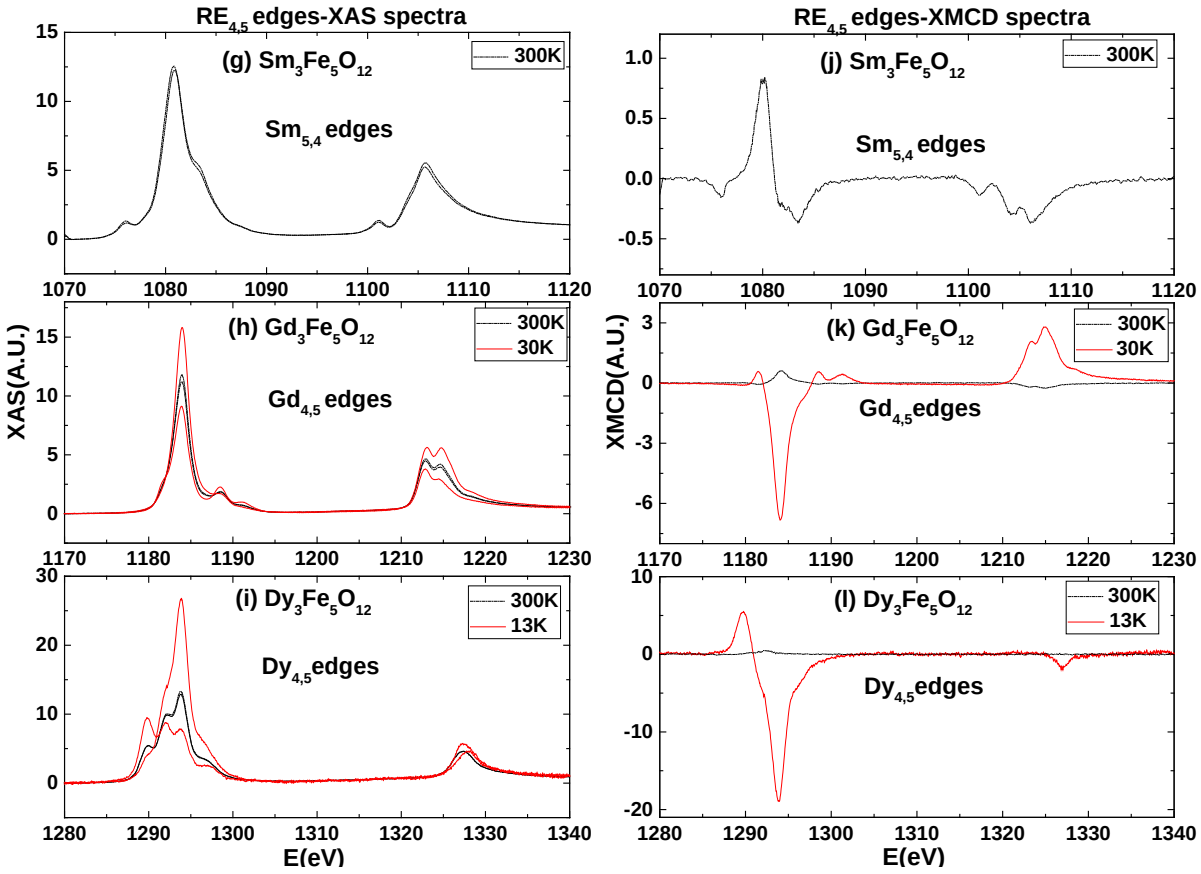

Figure 5.9 edge normalized XAS: left (measured at left and right polarized light) and XMCD: right (difference in left and right polarized XAS spectra) spectra of rare earth's (RE= Gd, Dy, Sm) at $M_{4,5}$ edge for garnets ($Gd_3Fe_5O_{12}$, $Dy_3Fe_5O_{12}$ and $Sm_3Fe_5O_{12}$ at 6.5T magnetic field) recorded at low temperature (red color-solid line) and room temperature (black color-dash dot line).

In case of rare earth element, also flip in the magnetization direction is clearly visible in the XMCD spectra of the gadolinium and heavy rare earth (dysprosium) below compensation temperature (T_{comp}). Similar in case of iron (section 5.5.1 (a)), the sign of the MCD signal is

related to the relative orientation of the magnetic moment of Gd and Dy by simple atomic model for the states [68]. The positive MCD signal at the M_5 edge confirms a residual anti-ferromagnetic coupling between the rare earth ions and the iron. At low temperature, increase in the XMCD signal intensity is clearly visible, is the increase in XMCD is 3 times larger in case of gadolinium and dysprosium compared to their room temperature analogs.

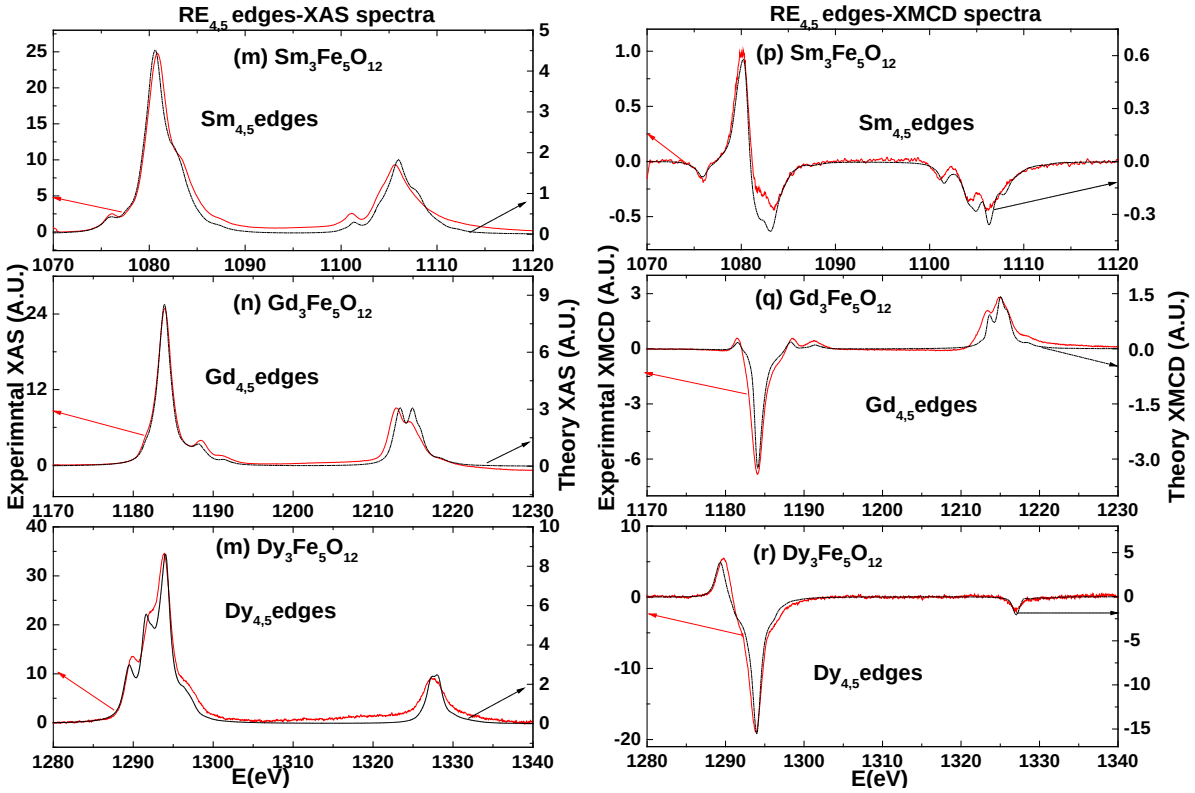

Figure 5.10 edge normalized experimental (red color-solid line) non-magnetic XAS spectra (sum of left and right polarized spectra) of rare earth's (RE= Gd, Dy, Sm) at $M_{4,5}$ edge for garnets ($Gd_3Fe_5O_{12}$, $Dy_3Fe_5O_{12}$ and $Sm_3Fe_5O_{12}$ measured at 6.5T magnetic field) overlapped with the theoretical (black color-dash dot) non-magnetic XAS spectra (sum of zero, left and right polarized spectra) and XMCD spectra of the ground state configuration. The arrow represents the scale of the curves. In order to compare the experimental and the theoretical curves for the experimental spectra scaling is on the left side of the y-axis and for the theoretical spectra in the right side of the y axis. The simulated spectra (black dash dot) of Dy, Sm and Gd are discussed in detail in chapter 3.

The sum rule analysis was performed at the rare earth $M_{4,5}$ edges using all the possible corrections for spin magnetic moment (refer chapter 3) and presented in Table 5.5. Here the number of holes ($n_{h)}$ used for Sm, Gd and Dy are 9, 7 and 5 respectively. The magnetic dipole term (T_Z) used for the sum rule analysis for Sm, Gd and Dy are 0.386, 0.010 and 0.128 respectively (refer chapter 3). The sign of the magnetic dipole term varies according to the direction of the spin. The gadolinium sum rule results at low temperature are not consistent with

the Hund's rule values (m_L=0, and m_S=7) and the sum rule analysis results on simulated spectra (m_L=0.07, m_S=6.49), because we are not in the saturation condition of the magnetization.

Table 5.5 sum rule analysis results of experimental XMCD spectra of rare earth's (RE= Gd, Dy, Sm) at $M_{4,5}$ edge for all garnets presented. The values of orbital moment ($m_{L)}$, spin moment (m_S), total magnetic moment (m_L+m_S), and the orbital to spin ratio (m_L/m_S) in units of Bohr magneton (μ_B)/atom is shown. The sum rule results have been estimated by incorporating all the necessary correction for the spin sum rule presented in chapter 3. The reduction on the experimental spin magnetic moment compared to the theoretical spin magnetic moment is presented in the last column. The sum rule results of the simulated spectra are also presented here. All the simulation details are presented in chapter 3.

T (Kelvin)	**Orbital m_L (μ_B / atom)**	**Spin m_S (μ_B / atom)**	**Total (m_L+m_S) (μ_B / atom)**	**Ratio (m_L/m_S)**	**Reduction in spin compared to theory**
$Gd_3Fe_5O_{12}$ at Gd $M_{4,5}$ edge					
300	-0.02±0.01	-0.46±0.02	-0.45±0.02	0.04±0.01	15.6
30	0.08±0.01	5.06±0.2	5.15±0.2	0.02±0.01	1.4
Simulations (chapter 3)	-0.07	-6.94	-7.01	0.01	-
$Dy_3Fe_5O_{12}$ at Dy $M_{4,5}$ edge					
300	-0.13±0.02	-0.16±0.02	-0.29±0.02	0.81±0.1	29.6
13	2.56±0.2	2.88±0.2	5.44±0.2	0.88±0.1	1.6
Simulations (chapter 3)	-5.11	-4.84	-9.95	1.06	-
$Sm_3Fe_5O_{12}$ at Sm $M_{4,5}$ edge					
300	0.26±0.02	-0.37±0.02	-0.11±0.2	-0.71±0.1	9.8
Simualtions (chapter 3)	4.29	-3.62	0.64	-1.18	-

The saturation in the Gd garnet is around 3 to 4 Kelvin (refer Figure 5.4(e)). Our experimental setup has limitation of measurements up to 10 kelvin. Due to some technical problems we were not able to stabilize the temperature, therefore at 30 kelvin measurements have been performed. In case of dysprosium the orbital and spin moment almost half of the expected values (Hund's rule m_L=5, m_S=5 and the sum rule analysis results Quanty- m_L=5.11, m_S=4.84) even at 15 Kelvin. In case of dysprosium also, it is not at the saturation condition of the dysprosium

moment (1.5 Kelvin). The XMCD results should be compared with the SQUID results, at the temperatures (15K- DyIG and 30K GdIG) where the XMCD measurements have been performed. The comparison of the rare earth magnetic moment obtained using XMCD with the SQUID results at appropriate temperatures will be discussed in the next section.

5.6.3. Comparison of SQUID results with sum rule analysis results

The average magnetic moment contribution of the rare earths (RE= Gd, Dy, Sm) in all the garnets ($Gd_3Fe_5O_{12}$, $Dy_3Fe_5O_{12}$ and $Sm_3Fe_5O_{12}$ measured at 6.5T magnetic field) in Bohr magneton/atom have been estimated from the SQUID results (refer Figure 5.5 (k) and (i)). The qualitative estimation of the magnetic moment of rare earth elements also performed from the M vs T curve (SQUID results). The average contribution of the rare earth element are presented in the Figure 5.11 and the results are compared with the XMCD results in Table 5.6.

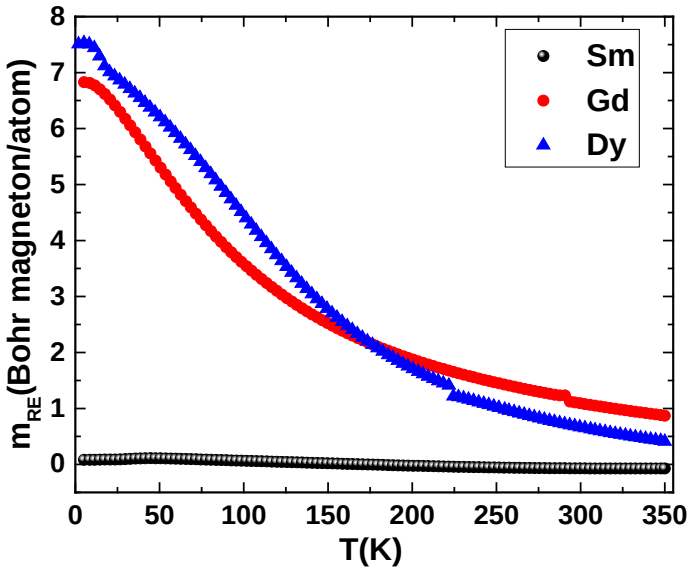

Figure 5.11 average magnetic moment contribution of the rare earths (RE= Gd, Dy, Sm) in all the garnets ($Gd_3Fe_5O_{12}$, $Dy_3Fe_5O_{12}$ and $Sm_3Fe_5O_{12}$ measured at 6.5T magnetic field) in Bohr magneton/atom have been estimated from the SQUID results (M vs T curve- refer Figure 5.5)

In order to compare the XMCD results with the SQUID results, all the values of the total magnetic moment of rare earth elements have been incorporated in the empirical formula m(RE)*3+5*m(Fe). At room temperature, the total magnetic moment from the XMCD sum rule analysis is 0.35 Bohr magneton/formula unit ($Gd_3Fe_5O_{12}$=-0.45*3+0.34*5) and for 30 Kelvin is 13.35 Bohr magneton/formula unit ($Gd_3Fe_5O_{12}$=5.15*3-0.42*5). The results are in good agreement with the SQUID results mentioned in section 5.5. From the SQUID results the total magnetization in Bohr magneton / formula unit is 13.72 (at 30K) in the GdIG (refer Figure

5.4 (e)). The XMCD sum rule analysis results are in good agreement with the SQUID results for the gadolinium garnet. Similarly, the analysis is performed for the dysprosium. The total magnetization in case of DyIG at 15 Kelvin temperature is 16.9 Bohr magneton / formula unit and the XMCD results are 14.07. In case of dysprosium at 15 Kelvin the total magnetic moment is reduced by 18% in the XMCD measurements.

Table 5.6 total magnetic moment of the iron and rare earth elements. As well of the rare earth (RE= Gd, Dy, Sm) present in all the garnets ($Gd_3Fe_5O_{12}$, $Dy_3Fe_5O_{12}$ and $Sm_3Fe_5O_{12}$ measured at 6.5T magnetic field) is compared with the SQUID results in Bohr magneton/ Formula Unit for the room temperature and the low temperature. An estimation for the rare earth elements in Bohr magneton /atom also performed from the SQUID results by subtracting the iron contribution, which is estimated from the YIG M vs T curve (further detail in the section 5.5).

T (Kelvin)	**SQUID (m_{tot}) (μ_B/F.U.)**	**SQUID (m_{RE}) (μ_B/RE atom)**	**XMCD (m_{Fe}) (μ_B/Fe atom)**	**XMCD (m_{RE}) (μ_B/RE atom)**	**XMCD (m_{tot}) (μ_B/ F.U.)**
$Gd_3Fe_5O_{12}$ at 6.5 T					
300	0.3	1.08	0.34±0.02	-0.45±0.02	0.35±0.02
30	13.72	6.18	-0.42±0.02	5.15±0.2	13.35±0.2
$Dy_3Fe_5O_{12}$ at 6.5 T					
300	1.53	0.65	0.33±0.02	-0.29±0.02	0.78±0.02
15	16.9	7.0	-0.45±0.02	5.44±0.2	14.07±0.2
$Sm_3Fe_5O_{12}$ at 6.5 T					
300	3.2	-0.08	0.41±0.02	-0.11±0.2	1.72±0.02

The orbital L_Z to spin S_Z (m_S/2) ratio for the dysprosium is 1.76, which is reduced compared to the Hund's rule (2) and the theoretical simulation results (2.11) refer table 5.7. It shows that in case of dysprosium, that the spin (S) of the dysprosium and iron are coupled in such a way that the dysprosium spin is not oriented along the direction of the magnetic field. The dysprosium spin is canted (with respect to field direction) due to the exchange coupling between iron and dysprosium causing reduction in the orbital to spin ratio. The quantitative estimation of the canting angles beyond the scope of the thesis. Similarly, reduction (1.42) in the orbital to spin ratio has been observed in case of samarium also compared to the Hund's rule (2) and the theoretical simulation results (2.11) refer table 5.7. In case of samarium the reduction in orbital

to spin ratio is almost 30%. It is visible in the XAS and XMCD spectra of the Dy, Sm and Gd that the XAS and XMCD spectral shape is not completely analogous to the ground state simulated spectra (Figure 5.10). Due to the change in the spectral shape from the ground state simulated spectra reflected in the projected orbital to spin ratio. The maximum deviation in the XAS and XMCD spectral shape compared to the simulated ground state spectra is visible in samarium, therefore the largest reduction (30%) in the spin to orbital ratio is observed.

In case of dysprosium the reduction in the orbital to spin ratio compared to the ground state simulation results is 14 %. The sum rule analysis results in the garnets are the clear evidence of the applicability of the XMCD sum rules in case of the rare earth elements at the $M_{4,5}$ edges by incorporating all the necessary corrections. As the contribution of the magnetic dipole term in case of the rare earth garnets in the powdered form is almost negligible because the average contribution of the magnetic dipole term will nullify due to the complete rotation of the grains in the powder. Therefore, the sum rule analysis is more reliable in case of these garnets compared to the other sintered and the thin film specimens.

Table 5.7 the orbital ($L_Z = m_L$) to spin ($m_S = 2*S_Z$) ratio of all the rare earth elements experimental spectra in the garnets are compared with the simulation results in the table.

Elements	Ratio (L_Z/S_Z) Simulations	Ratio (L_Z/S_Z) Experiments
Sm	-2.36	-1.42
Gd	0.02	0.04
Dy	2.11	1.76

5.7. Discussion

The rare earth garnets ferrimagnets are known to exhibit the compensation temperature where the total magnetization of the specimen is zero at the lower temperatures. Due to the relative weak coupling of the RE ions, the RE sub-lattice magnetization has a different temperature dependence, resulting in an increase in the magnetic moment down to lower temperatures. We confirmed the applicability of the XMCD orbital and spin sum rule for the rare earth elements on the experimental spectra measured below the compensation temperature. The contribution

of the magnetic dipole term to the spin moment is negligible in case of powdered samples due to the complete rotation with the grains, therefore the sum rule analysis is more reliable in case of these garnets compared to the other sintered and the thin film specimen.

The XAS and XMCD investigations are performed at the Fe $L_{2,3}$ edges. These systems are very well recognized to have two different types of iron ion contribution, experiencing a tetrahedral (T_d) and octahedral (O_h) coordination environment. For the proper shape analysis of the experimental XAS and XMCD spectra of the iron and to discern the features of T_d and O_h site, we have simulated XAS and XMCD spectra for the Fe $L_{2,3}$ edges and reproduced the experimental spectra by the combination of the 65% Fe^{3+} T_d site and 35% Fe^{3+} O_h site. The iron sub-lattice magnetization is dominated by the T_d Fe^{3+} (65 % contribution) lattice site. The sum rule analysis results for iron is half of the estimated magnetic moment from the YIG magnetization vs temperature curve. The major cause for the reduction in the iron magnetic moment is a less magnetic iron shell around each grain.

From the XMCD sum rule analysis, the reduced magnetic moment and the orbital to spin ratio is observed at the rare earth site (dysprosium and samarium) in these garnets compared to the Hund's rule and theoretical investigation results. It shows that in case of dysprosium, that the spin (S) of the dysprosium and iron are coupled in such a way that the dysprosium spin is not oriented along the direction of the magnetic field. The dysprosium spin is canted (with respect to field direction) due to the exchange coupling between iron and dysprosium causing reduction in the orbital to spin ratio. The difference in the XAS and XMCD spectral shape from the ground state simulated spectra reflected in the projected orbital to spin ratio. Dysprosium and samarium shown 17% and 30% reduction respectively, in the orbital to spin ratio. This is in comparison to the Hund's rule and the simulated spectra sum rule analysis results.

6. XAS and XMCD investigations at Nd $M_{4,5}$ edge in Nd-based permanent magnets

6.1. Introduction

High-performance permanent magnets are one of the essential materials that support modern technologies in which electric energy is transformed to motions, or vice versa, with the possibly highest efficiency. Examples of applications of high-performance permanent magnets include disc drives for information-storage devices, hybrid and electric vehicles (HEV and EV)[151]. In the 1960s, a hexagonal $SmCo_5$ compound with a $CaCu_5$ - type structure appeared as the first rare-earth high-performance magnet [152]. The compound has all the suitable magnetic properties high uniaxial magnetocrystalline anisotropy ($\mu_0 H_a$~200KOe), relatively high magnetization (Js~1.14T) and a high Curie temperature (T_c=720^{o}C) [151, 152]. The main disadvantage of these materials is their comparatively high cost of constituents such as samarium and cobalt, therefore research initiated to focus on trying to find an iron-based magnetic materials, with similar properties. This eventually directed to the development of magnets based on the tetragonal $Nd_2Fe_{14}B$ phase [153]. Croat *et al* [154] prepared using melt-spinning, and Sagawa *et al* [155] using powder metallurgy techniques. The magnetic characteristics of the new $Nd_2Fe_{14}B$ phase were Js = 1.61 T, $\mu_0 H_a$ =73KOe and T_c =312 ^{o}C [153]. Due to their better magnetic properties and low-cost, the Nd–Fe–B magnets had replaced SmCo magnets. [156] In this phase, 3*d* electrons in transition metals with orbital moments that are quenched due to crystal field coexist with the localized rare earth 4*f* electrons of the large orbital moment. However, for the energy-related technologies magnets should operate at the temperatures up to 200 degree Celsius, at this high operating temperature the coercivity of Nd-Fe-B based permanent magnets is decreasing (≤0.5T). Therefore, the current approach involves partial substitution of heavy rare earth (HRE) elements such as dysprosium (Dy) and terbium (Tb) of 4% content within overall rare earth content in order to increase the coercivity and magnetocrystalline anisotropy of the main phase $Nd_2Fe_{14}B$ and to suppress the demagnetization at an operating temperature of ~470 K [2, 157]. For obtaining high heat resistance, a room temperature coercivity of around 2.4 MAm^{-1} (3 Tesla) is needed in Nd–Fe–B sintered magnets. To meet this requirement, addition of a relatively large amount of dysprosium is started in Nd–Fe–B magnets. Though, the magnetic moment of dysprosium is coupled antiparallel to that of iron in $R_2Fe_{14}B$ compounds (*R*-rare earth), which leads to a

decrease in their energy product. In addition, the natural abundance of dysprosium is quite low and dysprosium producing countries are limited. Therefore, the development of dysprosium-free or dysprosium-lean Nd–Fe–B sintered magnets with a high coercivity is in the demand [151, 158].

Since the coercivity and the magnetization of the specimens are related to the microstructure of the system [159]. Ample investigations had been performed to control the microstructure of the Nd-Fe-B based phase [7, 160, 161]. Rare earth permanent magnet (REPM) films can be used as model case for sintered magnets because the microstructure of the films can be more easily controlled than that of sintered magnets. [162, 163] As reported studies by other authors e.g. textured samples could be produced by heating the sapphire substrate upto 895K on sputtering. Especially, the magnetic recording industry is looking for new materials with higher coercivity and crystalline anisotropy perpendicular to the film plane in order to reduce the bit size [164]. The magnetic properties and microstructures of Nd–Fe–B thick films with different neodymium contents were investigated and coercivity of 2.7 T was achieved with the higher neodymium content at room temperature without the addition of heavy rare earth elements [165]. The thin films are also useful for clarifying the fundamental interests, such as coercivity mechanism. Uehara *et al* [166] reported an increase in energy products (364 KJ/m^3) in Nd–Fe–B films. They prepared 200 nm thick multilayers of cobalt-free or cobalt-doped Nd–Fe–B with 10 nm thick tantalum by sputtering on heated glass substrates. The perpendicularly textured $Nd_2Fe_{14}B$ grains evolved in multilayers with sizes nearly controlled by the thickness of the unit layer.

In the last few years, magnetic multilayered films have been the subject of much attention because of their feasibility of showing novel magnetic properties, such as controlled inter-diffusion at the interfaces, giant magnetoresistance, surface anisotropies, exchange interactions between neighboring magnetic layers, etc. Many studies on rare-earth (RE)/transition-metal (TM) multilayers have been performed for reasons of scientific interest, application to magneto-optical recording [167-170]. As it is mentioned earlier the $Nd_2Fe_{14}B$ phase exhibit important magnetic properties that are related to the magneto-crystalline anisotropy and coupling between iron and neodymium. The rare-earth iron multilayers are a representation of the crystalline structure of $Nd_2Fe_{14}B$ permanent magnet which has a layer of neodymium and iron and can be used to understand the origin of this anisotropy as well coupling between the neodymium and iron [169, 171]. Iron neodymium multilayers in the form of thin films can be used as a good reference for understanding the mechanism of these complex neodymium-based permanent magnets. In order to understand the behavior of neodymium in Fe-Nd- B phase and the different

systems like thin film, multilayer and in sintered magnets element specific study will be discussed in the further sections.

6.2. Reported XAS and XMCD studies at Nd edges (*L*, *M*) in Nd-based magnets

The earliest reports of neodymium (Nd) $M_{4,5}$ x-ray absorption spectra dates back in 1931[46]. In 1984, for the first time Kaindl *et al* and coworkers performed the x-ray absorption spectroscopy at the $M_{4,5}$ edges in multivalent rare earth systems [77]. They have shown that the XAS experiment spectra at the Nd $M_{4,5}$ edge in Nd_2O_3 oxide and neodymium XAS spectra have 100 % resemblance with the pure Nd^{3+} spectra. In 1985, Thole *et al.* published experimental and simulated XAS spectra at $M_{4,5}$ for the ground-states of complete rare-earth series including different valences by atomic multiplet theory simulations [37]. In progress, a comprehensive information regarding XAS and XMCD spectra at $M_{4,5}$ edges for the whole rare earth series was given by Goedkoop *et al.* in 1988 [33]. In 1992, for the first time the experimental hard XMCD investigation at Nd L_2 edge have been performed in the temperature range of 77K to 300K on Nd-Fe multilayer system to compare the results with the bulk magnetization results and the magnetization mechanism at the interface of the multilayers also have been addressed [172]. Later the same year, another group [29] have performed the x-ray resonance exchange scattering at Nd $L_{2,3}$ edges and demonstrated the sensitivity of the asymmetry ratio (define by the intensity of the Bragg's reflection for the magnetization parallel and antiparallel to the wave vectors of the incident and the scattered beams) to the magnitude and the direction of the local magnetic moments of the particular site [173].

In the $Nd_2Fe_{14}B$ phase magnet, at higher temperatures, iron, and neodymium magneto-crystalline anisotropies are uniaxial and the magnetization points at the [001] direction (along with the c-axis). However, the magneto-crystalline anisotropy of neodymium moments is more complex. At the lower temperatures, the crystal field at the neodymium sites forces the rotation of the total magnetization (at the spin reorientation temperature T_{SR}=135 kelvin) from the [001] direction to the [110] axis, reaching the tilting angle of about 30.6^o at 4.2 Kelvin [174, 175]. Until 2000, there was no systematic study performed on $Nd_2Fe_{14}B$ phase [176]. Gracia *et al* [177] performed the soft x-ray MCD on the $Nd_2Fe_{14}B$ single crystal at Fe $L_{2,3}$ and Nd $M_{4,5}$ edges as a function of temperature through the spin reorientation transition temperature. They observed the strong instability of the orbital moment at the iron sub-lattice around the spin reorientation temperature (T_{SR}) [178], while there is no anomalous behavior observed at the spin magnetic moment. It is also observed that XMCD spectra at Nd $M_{4,5}$ edges remain constant

over the whole temperature range. However, there is no quantitative estimation of the orbital and spin moment performed at the neodymium site [177].

The Fe-Nd-B system consists of fine crystal grains of the $Nd_2Fe_{14}B$ phase, Nd-rich phases at the triple junction [7, 159-161] and thin intergranular grain boundary phase [6, 160, 161]. This thin intergranular grain boundary phase is considered to play an important role in the exchange coupling between the ferromagnetic $Nd_2Fe_{14}B$ grains. It has been assumed that this grain boundary phase is paramagnetic based on assumption that the composition is similar to the neodymium rich grain boundary phase but very small amount of iron is present in it. But this is until the results presented by the Murakami *et al*, they estimated the magnetism at the grain boundary phase around 1 Tesla using electron holography [179]. Later Nakamura *et al* performed the XMCD investigation on Fe-Nd-B magnets with the composition of $Nd_{14.0}Fe_{79.7}Cu_{0.1}B_{6.2}$ [180]. They have performed quantitative estimation of the temperature dependence of the iron magnetic moments at the grain boundary phase by taking advantage of the surface sensitivity of the soft x-ray XMCD measurements and the sum rule analysis. The temperature dependence curve shows that the Curie temperature (T_C) of the grain boundary phase is lower (less than 250 ^oC) than the main $Nd_2Fe_{14}B$ phase [180]. The same group also performed the effect of annealing on the magnetic properties of iron, neodymium and the grain boundary phases in the sintered magnet ($Nd_{14.0}Fe_{79.7}Cu_{0.1}B_{6.2}$) using XMCD [181]. They have also observed that the neodymium XMCD spectra in the annealed samples is slightly larger than the ones, those are not annealed. It is due to a higher concentration of the neodymium in the grain boundary phase as compare to that in main phase $Nd_2Fe_{14}B$. They also did not perform any quantitative estimation of the magnetic moment at the rare earth (Nd) site. Therefore, in this chapter we will discuss XAS and XMCD investigations of all the neodymium based different systems and perform the quantitative estimation of the orbital and the spin magnetic moment of neodymium.

6.3. Specimen details

In this thesis, the XAS and XMCD investigations are performed on 5 different samples:

1. Soft magnetic reference samples Fe/Nd multilayer (3.6Å Fe/3.6 Å Nd)
2. $Nd_2Fe_{14}B$ single phase specimen
3. $Nd_2Fe_{14}B$ textured film (340 nm).
4. $Fe_{14}(Nd, Dy)_2B$ sintered permanent magnet

We will begin discussion with the structural properties of the specimens and the characterization of the specimens with the basic soft magnetic specimens (multilayer and thin film) and will attempt to describe the complex sintered hard magnets. The magnetic characterization of all the specimens were performed with the SQUID magnetometer via magnetic hysteresis curves and magnetization versus temperature curves. The structural characterization and phase analysis were performed with the x-ray diffraction spectrometry. In order to precisely compare the total sample magnetization with the element specific XMCD results and to find out the contaminations inside the specimens, the chemical compositions of the sintered magnets and textured thick film were analyzed by inductive coupled plasma spectroscopy (ICP-OES) (spectro-ciros).

6.3.1. Fe/Nd multilayer

The Fe/Nd multilayer of 3.6 Å (0.36 nm) thickness of iron (d_{Fe}) and neodymium (d_{Nd}) layers (60 bilayers) prepared on the silica substrate by the ion beam sputtering technique and to prevent the oxidation capping layer of 2 nm is also deposited on the film Figure 6.1 (left). The thickness ratio (d_{Fe} /d_{Nd}≈1) of the rare earth element neodymium and the iron layer is unity and the total film thickness is approximately 432 Å (43.2 nm). Although the layers of the film are very thin, still we attempt to verify the structure of the multilayer by the x-ray diffraction. Figure 6.1 (right) shows the x-ray diffraction pattern of the multilayer. There are no reflections visible in XRD pattern and the film appears amorphous. It is reported that the layer thickness of iron smaller than d_{Fe} <10-15 Å will exhibit amorphous structure [171, 182, 183]. The film thickness smaller than 20 Å exhibits a mesh pattern, in which crystal grains are not visible [171]. The similar type of structure has been observed for the Fe/Gd and Fe/Pr multilayers [171]. As the Fe layer thickness becomes less than about 2 atomic diameters, significant mixing of the neodymium into the iron layer occurs. Thus, a well-defined Nd/Fe interface is lost. In general when the individual layer thickness gets below 15-20 Å, than the resulting structure in the film plane is amorphous and if the iron layer thickness is more than 15-20 Å then the films tends to be crystalline [168].

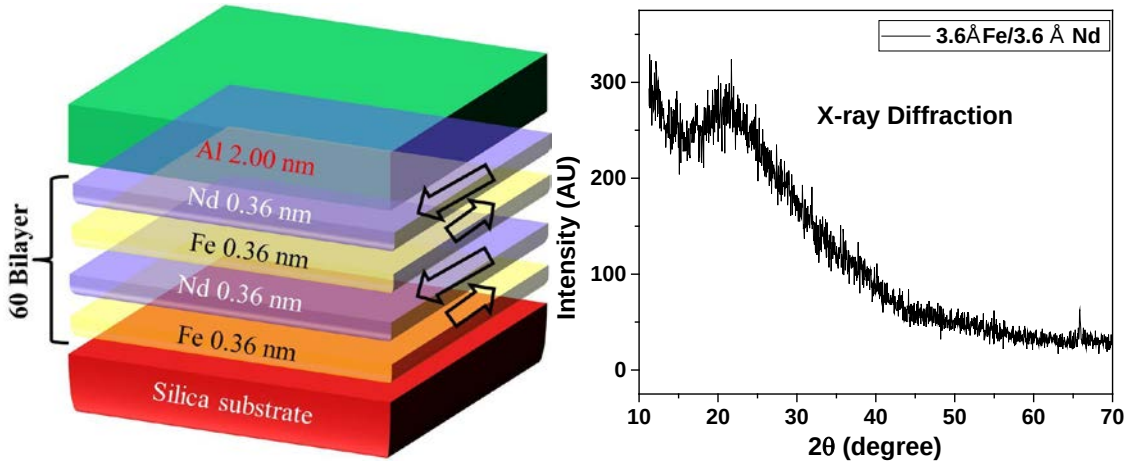

Figure 6.1 schematic representation of the Fe/Nd multilayer film shows the thickness of the layers (3.6Å Fe/3.6Å Nd-60bilayers) and the length of the arrows represent the relative magnitudes of the magnetic moment for respective iron and neodymium layers. Direction of the arrows represents the direction of the spin (parallel or antiparallel) of the respective layer. Right- x-ray diffraction pattern of the Fe (3.6Å)/Nd(3.6 Å) multilayer.

The magnetization versus temperature curve is presented in the Figure 6.2. There is very small contribution imminent from neodymium at room temperature as the total magnetic moment at the room temperature is almost equivalent to the pure iron magnetic moment (2.2 Bohr magneton/atom). At low temperature, the neodymium moments contribution is visible in magnetization vs temperature curves as the total magnetization is twice of the room temperature (refer Figure 6.2).

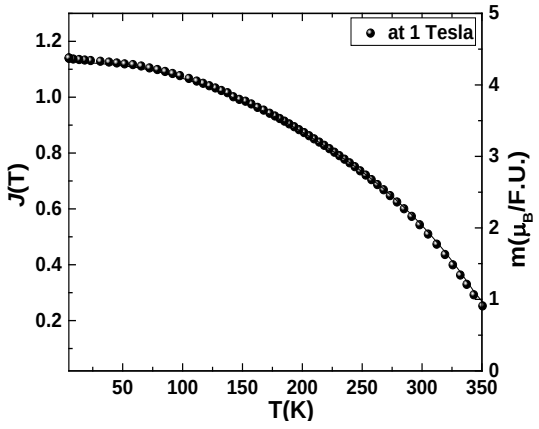

Figure 6.2 magnetization vs temperature (5-350 Kelvin) curve of the Fe (3.6Å)/Nd (3.6 Å) multilayer in presence of 1 Tesla magnetic field.

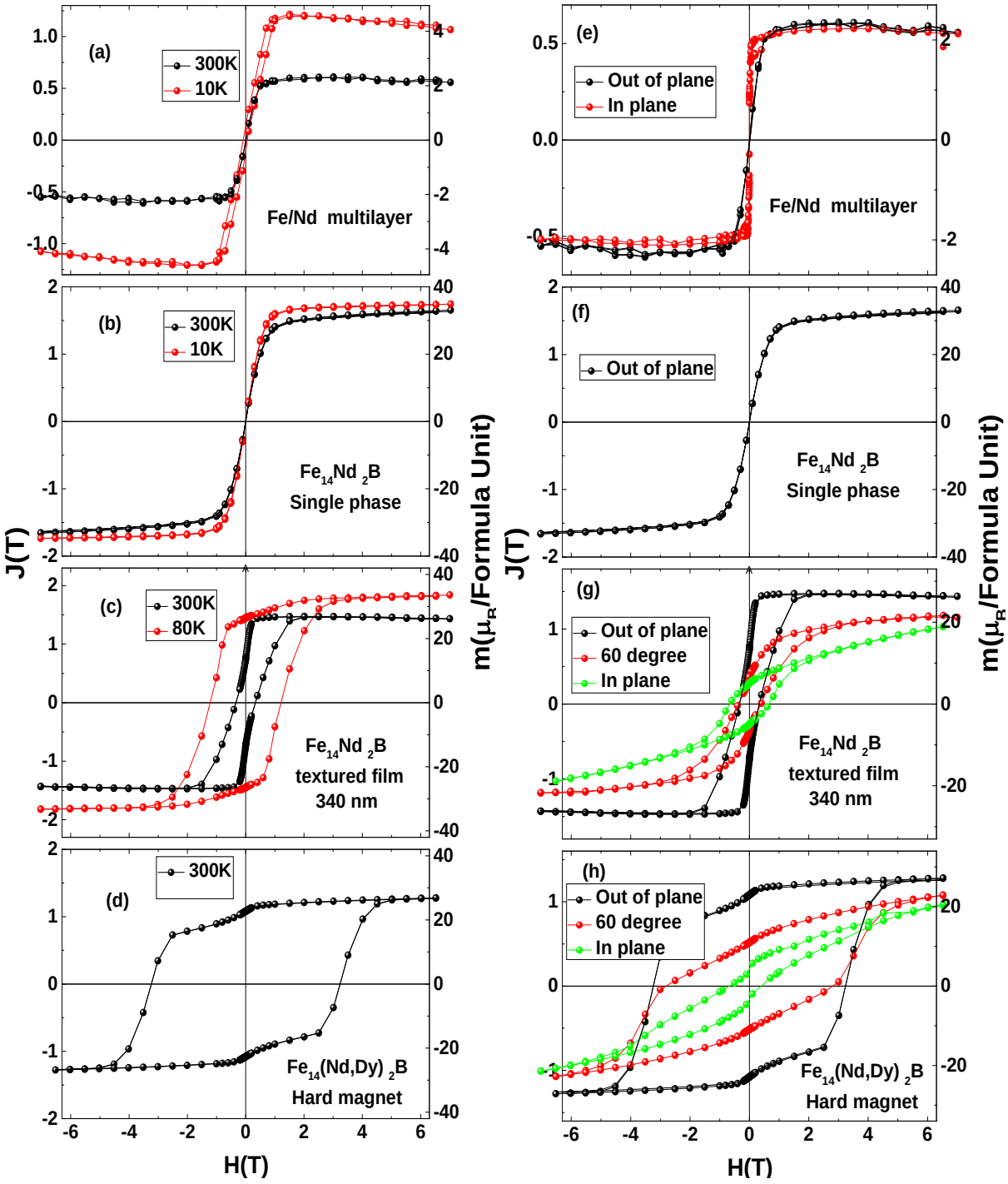

Figure 6.3 magnetic hysteresis curves of (a) Fe/Nd multilayer film, (b) $Fe_{14}Nd_2$ B singles phase (sintered bulk specimen) specimen, (c) $Fe_{14}Nd_2B$ textured thin film and (d) $Fe_{14}(Nd,Dy)_2B$ hard magnet (sintered bulk specimen) at room temperature and low temperature (10 to 80 Kelvin temperature range). Anisotropic (Out of plane, 60 degrees, and in-plane) magnetic hysteresis curves (e) Fe/Nd multilayer film, (f) $Fe_{14}Nd_2$ B singles phase (sintered bulk specimen) specimen, (g) $Fe_{14}Nd_2$ B textured thin film and (h) $Fe_{14}(Nd,Dy)_2B$ hard magnet (sintered bulk specimen) at room temperature.

The magnetization curves of the multilayer are presented in Figure 6.3 (a) and (e) recorded at the room temperature and low temperature. The multilayer possesses the narrow (soft magnetic) hysteresis loops and low values of coercivity and remanence of the order of 100 Oersted. The film appears to be in-plane magnetized (refer Figure 6.3 (e)). The magnetization of the multilayer (single layer of iron and neodymium) at room temperature (10 Kelvin) and in presence of 1 Tesla field is 2.1 Bohr magneton /formula unit: 54 emu/gram (4.3 Bohr magneton /formula unit: 120 emu/gram) (refer Figure 6.3 (a)). It appears that at room temperature the total magnetic moment is close to the bulk iron magnetic moment (2.2 Bohr magneton /atom). The emu/gram to Bohr magneton conversion thickness of the single layer of neodymium and iron is considered. There is possibility that the due to the thickness the conversion in Bohr magneton will have error of maximum 5%. The magnetization results are in good agreement with the previously reported experimental results [168].

This sample is a representative model of coupling between iron and neodymium and hence can be useful in understanding the interaction of rare earth elements and the multifaceted behavior of the neodymium in $Fe_{14}Nd_2B$ magnets. In order to discern the contribution of iron and neodymium then further XAS and XMCD investigations will be discussed to get the complementary and element specific magnetic information.

6.3.2. $Fe_{14}Nd_2B$ single phase

As part of the rare earth lean magnetic materials project [100], our project´s main interest is in neodymium-based permanent magnets, the recognized neodymium-based $Fe_{14}Nd_2B$ hard magnetic tetragonal phase. In order to develop better understanding here we discussed first $Fe_{14}Nd_2B$ single phase specimen. The single phase material has been provided by our collaborators [100]. In order to confirm the phase analysis of the specimen x-ray powder diffraction measurements have been performed using Co-K_α radiation (1.78896 Å). The measurement and analysis procedure via Rietveld refinement is performed in similar manner as discussed in chapter 4. For the analysis $Fe_{14}Nd_2B$ phase is considered, *a* and *c* are the lattice parameters of $Nd_2Fe_{14}B$ as observed in the Rietveld refinement procedure are analogous to the reference [184]. Figure 6.4 shows the x-ray diffraction pattern of the $Fe_{14}Nd_2B$ single phase labeled with the peak position of the $Fe_{14}Nd_2B$ phase. It is visible that, the only phase which is noticeable the expected one ($Fe_{14}Nd_2B$). The x-ray diffraction pattern in Figure 6.4 is in good agreement with the ICDD (International center of diffraction data) patterns. If there are any

other phases drowned in the statistic of the background, there amount is so small that will create problem in their identification.

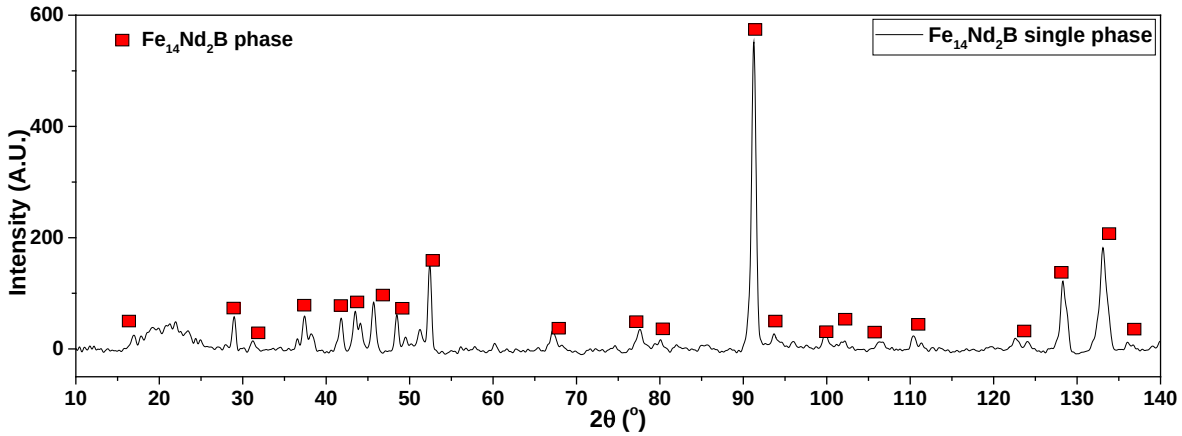

Figure 6.4 x-ray diffraction pattern of the $Fe_{14}Nd_2B$ single phase specimen. The experimental x-ray diffraction pattern is in good agreement with all the peak position of the $Fe_{14}Nd_2B$ phase and is indicated by red squares.

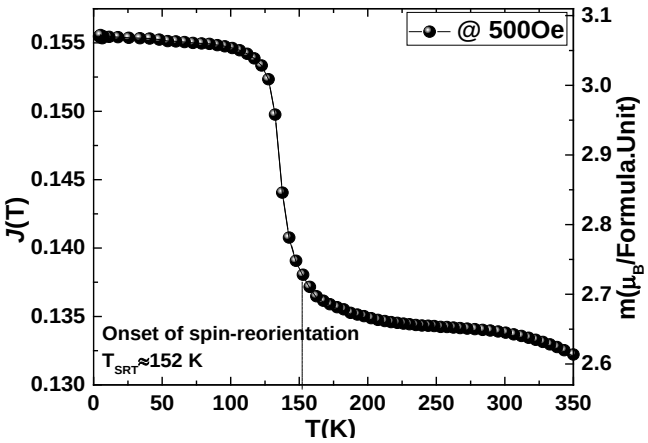

Figure 6.5 magnetization versus temperature (5-350 Kelvin) curves of the $Fe_{14}Nd_2B$ single phase specimen in presence of 500 Oersted magnetic field presented. The onset temperature (152 Kelvin) of the spin reorientation phenomenon is discernable in the figure.

Figure 6.5 shows the magnetization versus temperature curve for the $Fe_{14}Nd_2B$ single phase material at 500 Oersted magnetic field. There is an abrupt increase in magnetization at 152 Kelvin temperature, this indicates the onset of the spin reorientation and the easy direction of magnetization is now canted from the *c* axis (refer section 6.2) [178]. The spin reorientation temperature is in good agreement with the reported results [178]. The magnetization curves of the single-phase specimen is presented in Figure 6.3 (b) and (f) recorded at the room temperature and 10 Kelvin respectively. The sample is isotropic (hysteresis loops are analogous

in the plane and out of plane therefore not presented here) and soft magnetic (coercivity and remanence order of 100Oe). The magnetization of the $Fe_{14}Nd_2B$ single phase specimen at room temperature (10 Kelvin) at 7 Tesla magnetic field is 32 Bohr magneton/formula unit (34 Bohr magneton /formula unit) (refer Figure 6.3 (b)). The total magnetic moment of the specimen is comparable to the literature value (30 Bohr magneton /formula unit) [178]. There is no drastic change (5%) is observed in the magnetization (refer Figure 6.3 (b)) at the low temperature, therefore the element specific studies have been performed only at the room temperature.

6.3.3. $Fe_{14}Nd_2B$ textured thin film (340nm)

As the microstructure of a specimen can be controlled by preparing a film, the $Nd_2Fe_{14}B$ phase film is prepared by using the ion beam sputtering technique. The base pressure is $5 \cdot 10^{-8}$ mbar and sputtering was carried out at an argon gas pressure of 10^{-4} mbar. Sapphire (Al_2O_3) is used as a substrate. The textured samples could be produced by heating the substrate upto ~920K while sputtering [185, 186]. Crystallization takes place during sputtering at the rate of 1.5 Å/s corresponding to a sputtering time of 110 min for a 1 μm film. Chromium (1600 nm) is used as a buffer layer between the substrate and the film. Aluminum is used as a top layer to avoid the oxidation of the main phase film.

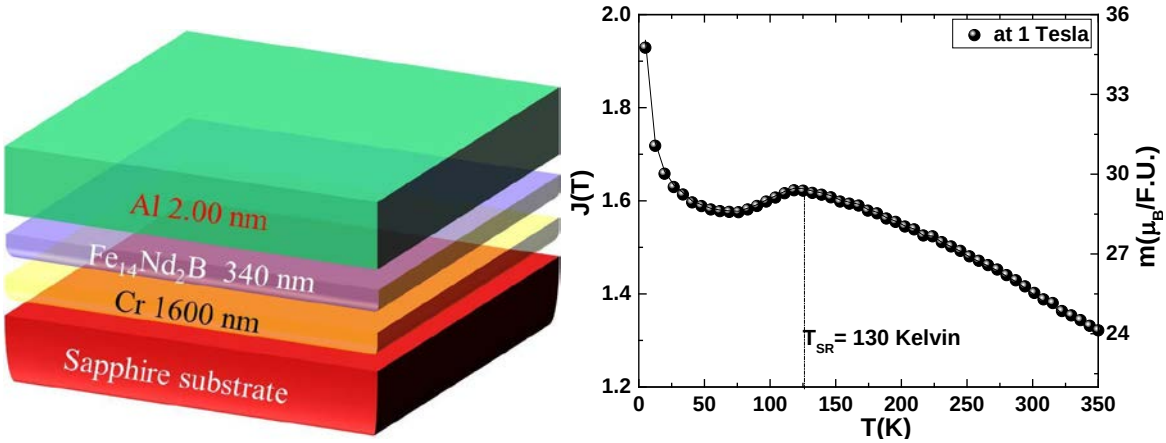

Figure 6.6 schematic representation (left) of the $Fe_{14}Nd_2B$ textured thin film (340nm) (2nm capping layer /main phase /Chromium buffer layer/ sapphire substrate). Magnetization versus temperature (right) (5-350 Kelvin) curves of the $Fe_{14}Nd_2B$ thick film specimen in presence of 1 Tesla magnetic field. The onset temperature (~130 Kelvin) of the spin reorientation phenomenon.

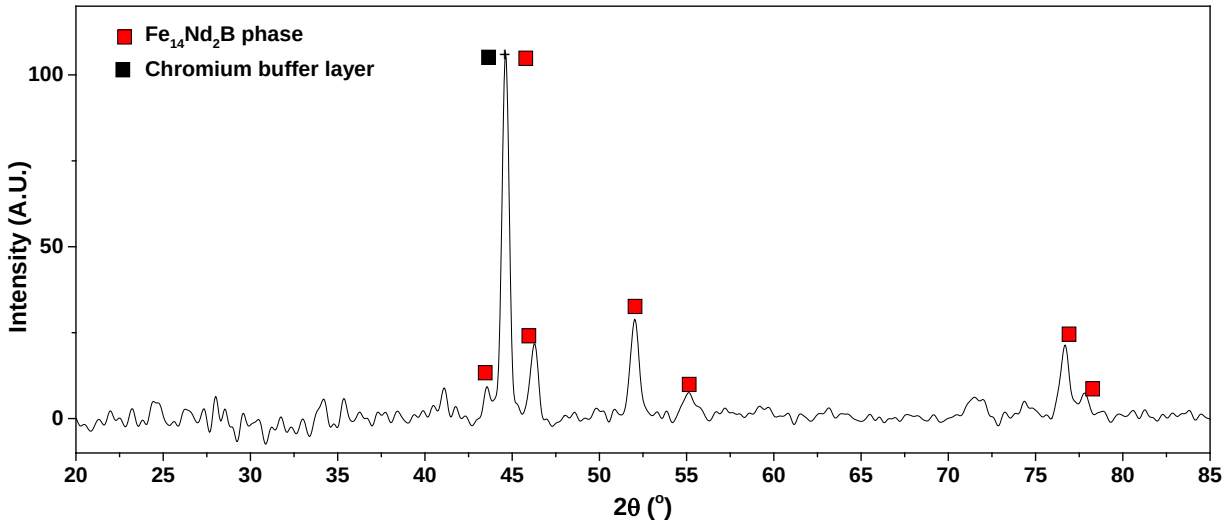

Figure 6.7 x-ray diffraction patterns of the $Nd_2Fe_{15}B$ film in out of plane geometry (with angles $\chi = 0°$ and $\varphi=0°$). The reflections from $Nd_2Fe_{15}B$ phase are labeled by red squares and the reflections from chromium buffer layer (black squares) are also visible.

Schematic representation of the film is shown in Figure 6.6 (left). Without the chromium buffer layer, no good hard magnetic properties and texture could be achieved. The texture of the $Nd_2Fe_{14}B$ films is *c*-axis in presenc of chromium buffer layer [187]. The growth of $Nd_2Fe_{14}B$ films on chromium buffer is rough which acts as pinning sites for the domain wall at the grain boundaries. Roughness is a strong factor in the coercivity enhancement [187]. As the microstructure of the films can be controlled, therefore $Nd_2Fe_{14}B$ film can be useful in better understanding of the complex sintered hard magnets.

In order to confirm the phase analysis of the specimen x-ray diffraction measurements have been performed using cobalt-K_α radiation (1.78896 Å). Figure 6.7 shows the x-ray diffraction pattern for the out of plane geometry of the film. The measurement and Rietveld refinement analysis procedure is performed in similar manner as discussed in chapter 4 section 4.3.2. For the analysis the possible occurrence of the $Fe_{14}Nd_2B$ phase is considered, *a* and *c* are the lattice parameters of $Nd_2Fe_{14}B$ as observed as mentioned in reference [184]. Most of the reflections arise from the $Fe_{14}Nd_2B$ phase (labelled as red squares) and one peak from the chromium buffer layer (labelled as black squares) is also visible at 2θ=45 ° angle. The intensity of the substrate peaks is too low compared to the film intensity, which is 4 orders of magnitude higher (observed from the XRD diffraction pattern). The buffer layer and the film are sufficiently thick, so there is no signal observed from the substrate.

Figure 6.8 shows the pole figure of the $Fe_{14}Nd_2B$ film in 2.5 dimensions ((a) and (b)) and 2 dimensions ((c) and (d)). A pole is a two-dimensional stereographic projection in which the positions and intensities of specific crystallographic orientations are plotted in the relation to specimen geometry in such a manner that the angular relationship between the planes and different directions in the crystal can be easily recited.

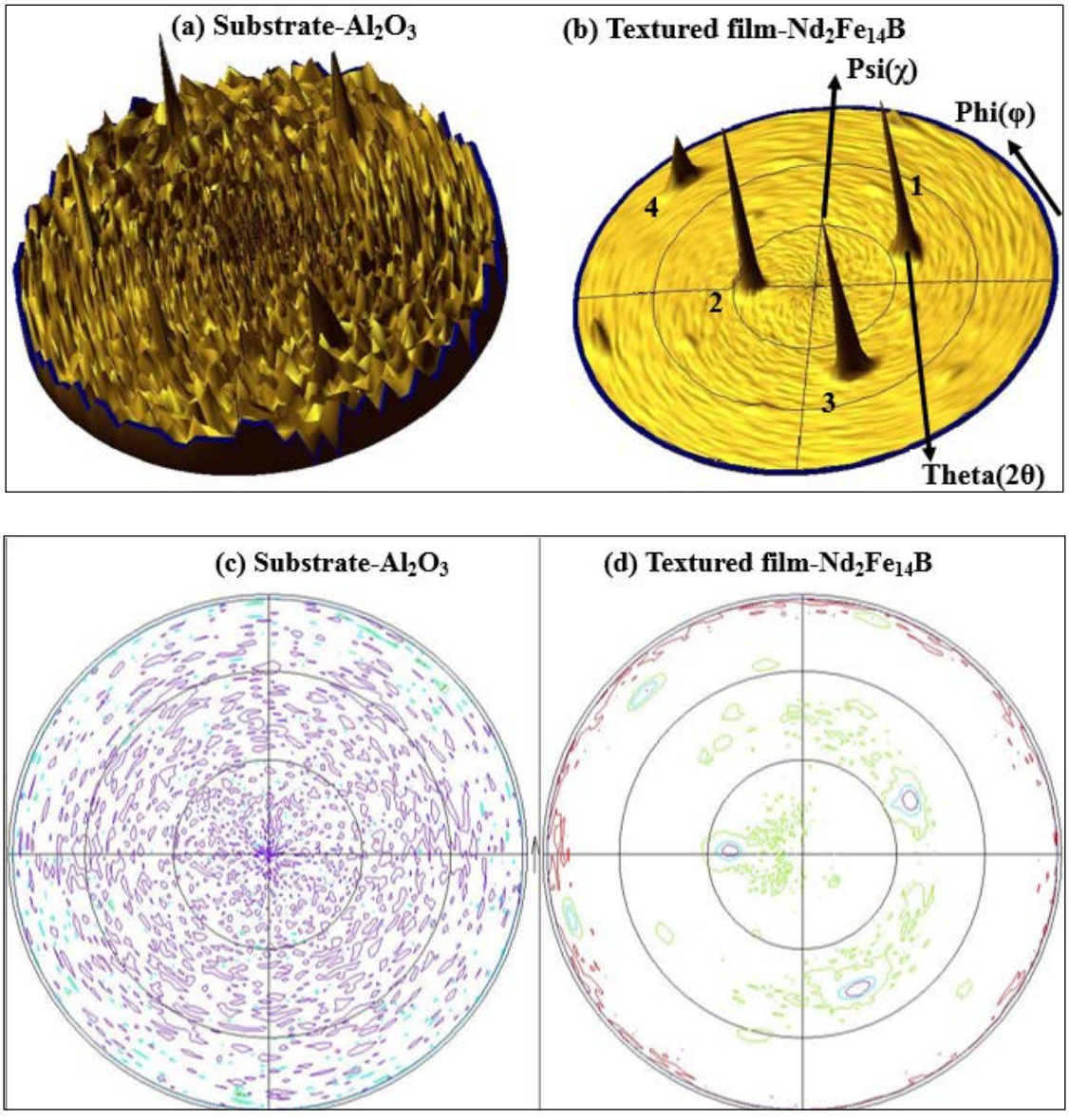

Figure 6.8 pole diagram for the textured thick film in 2.5 dimensions ((a) and (b) top figures) and 2 ((c) and (d) - bottom figures). The pole figure (a) and (c) corresponds to the substrate and (b) and (d) corresponds to the main film thickness. All the poles correspond to reflections from $Fe_{14}Nd_2B$ the main phase film 00*l* plane (2θ=52.1°) are labeled in 2.5 dimension pol figure (b) the pole figure measurements have been performed at 2θ=52.1° ([006] plane) with varying φ=0°-360° (step 3°) and χ=0°-90° (step 1°) using Cobalt-K_α radiation.

The $Fe_{14}Nd_2B$ phase has tetragonal crystal structure and film is supposed to be textured along 00*l* plane on chromium buffer layer. Therefore, the pole figure measurements have been performed at 2θ=52.1° (peak corresponds to one of the 00*l* plane-[006]) with varying φ=0°-360° (step 3°) and χ=0°-90° (step 1°) using cobalt-K_α radiation. All the poles originated here in pole figure is from the 00*l* plane. It is visible that film is highly textured (but not the fiber textured) and exhibits certain orientation of the crystallites along the 00*l* plane. The poles correspond to the main phase layer are labeled (Figure 6.8 (b)). There are only 4 major poles visible. The positions of the corresponding poles are (1) χ=38.3°, φ=26.7°, (2) χ=22.7°, φ=176.3°, (3) χ=46.7°, φ=292.7° and (4) χ=75.7°, φ=134° respectively. So the most of the 00*l* planes are visible at these angles mentioned above. Due to main phase and chromium buffer layer thickness (1600 nm), the substrate (Al_2O_3) shows no contribution in the pole figure.

Figure 6.8 (right curve) shows the magnetization vs temperature (M vs T) curve for the $Fe_{14}Nd_2B$ textured thick film in presence of 1 Tesla magnetic field. There is an increase in magnetization at 130 Kelvin temperature, it is an onset of the spin reorientation (refer section 6.2) [178] and is analogous to the $Fe_{14}Nd_2B$ single phase specimen M vs T curve. The hysteresis curves of the textured film specimen have been also presented in the Figure 6.3 (c) and (g) recorded at the room temperature and 80 Kelvin along the in and out of plane orientation of the film. The thick film is highly anisotropic, indicating strong out of plane texture from the hysteresis loop Figure 6.3 (c). It exhibits a coercivity of 1 Tesla and remanence is 50% of the total magnetization (without elimination of demagnetizing field) along the out of plane orientation. The film is texture along *c*-axis in pole figure and SQUID results show texture along the out of plane orientation, which shows that the SQUID hysteresis results (refer figure 6.3 (c)) are in good agreement with the pole figure results (Figure 6.8). The magnetization of the $Fe_{14}Nd_2B$ single phase specimen at room temperature (80 Kelvin) in presence of 7 Tesla magnetic field is 26.05 Bohr magneton/formula unit 1.45 Tesla (33 Bohr magneton /formula unit: 1.84 Tesla) (Figure 6.3 (c)) along the out of plane orientation. There is a 19% reduction in the total magnetization value of the film compared to the single phase specimen [178] at the room temperature due to the presence of other grain boundary phases, which reduces the total magnetization and acts as decoupling region for higher coercive behavior [165].

In order to precisely compare the total sample magnetization with the element specific XMCD results, the chemical compositions of the sintered magnets have been analyzed by inductive coupled plasma spectroscopy (ICP-OES) (spectro-ciros). The 69.9±3 weight % iron, 29.3±1 weight % neodymium and 1.1±0.2 weight % boron is detected. There is no strong contamination found. The stoichiometry turned out to be $Nd_2Fe_{14}B$ for the specimen.

6.3.4. $Fe_{14}(Nd, Dy)_2B$ hard magnet

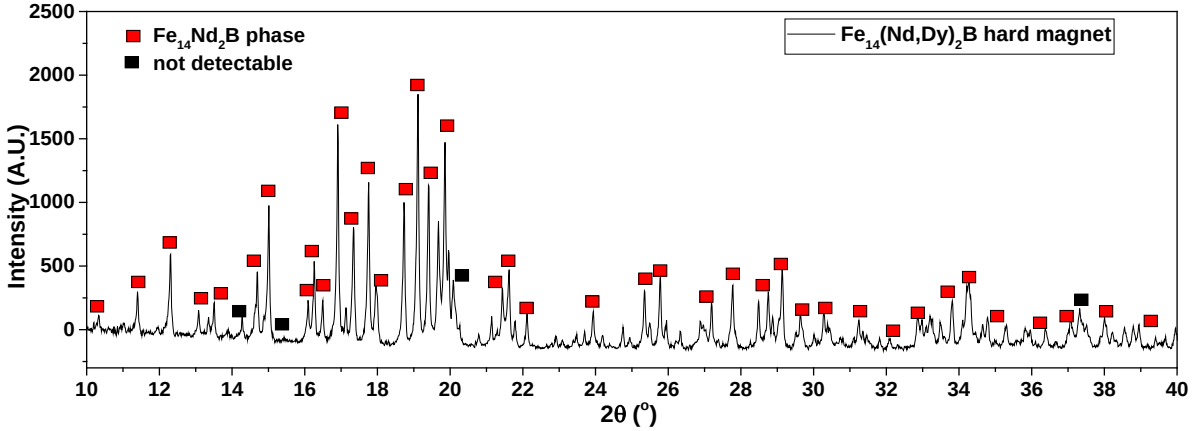

Figure 6.9 x-ray diffraction pattern of the $Fe_{14}(Nd,Dy)_2B$ hard magnetic specimen. The experimental x-ray diffraction pattern in is in good agreement with all the peak position of the $Fe_{14}Nd_2B$ phase. The peaks correspond to $Fe_{14}Nd_2B$ phase are indicated by red squares. There are some impurities also have been present (marked with black squares.

To perform the phase analysis of the specimen x-ray powder diffraction measurements are performed using Co-K_α radiation (1.78896 Å). The measurement and analysis procedure via Rietveld refinement is performed in similar manner as discussed in the chapter 4 (in XRD section 4.3.2). Figure 6.9 shows the x-ray diffraction pattern of the $Fe_{14}(Nd, Dy)_2B$ hard magnet. The possible occurrence of the $Nd_2Fe_{14}B$ tetragonal phase with symmetry *P42/mnm* is considered. The crystallinity of the specimen is not good, there is not much scattering. The corresponding refined lattice parameters are *a*-8.81066 Å, *b*- 8.81066 Å and *c*- 12.2086 Å belong to the space group of *P42/mnm* [184, 188]. The large majority of the Bragg reflections can be explained from the tetragonal $Nd_2Fe_{14}B$ phase. Some of the peaks are still difficult to identify labeled as black squares. If there are any other phases present in the statistic of the background, their amount is so small that creates a general problem in their identification. Some of these undetectable peaks could be a contribution from the dysprosium.

Figure 6.10 shows the magnetization versus temperature curve for the $Fe_{14}(Nd, Dy)_2B$ hard magnetic specimen in presence of 1 Tesla magnetic field. The M vs T curve is analogous to the $Nd_2Fe_{14}B$ textured film curve and previously reported results[189]. The spin reorientation is the fundamental characteristics of the $Nd_2Fe_{14}B$ tetragonal phase and also observed here in the bulk specimen, although here the onset of spin reorientation is lower (100 Kelvin) than the textured film. The magnetization becomes nonlinear below 100 Kelvin. The spin reorientation

and the accompanying enhancement of magnetization of $Nd_2Fe_{14}B$ are presumably due to the interplay between the crystal field interactions and exchange interactions acting on the neodymium ions [189].

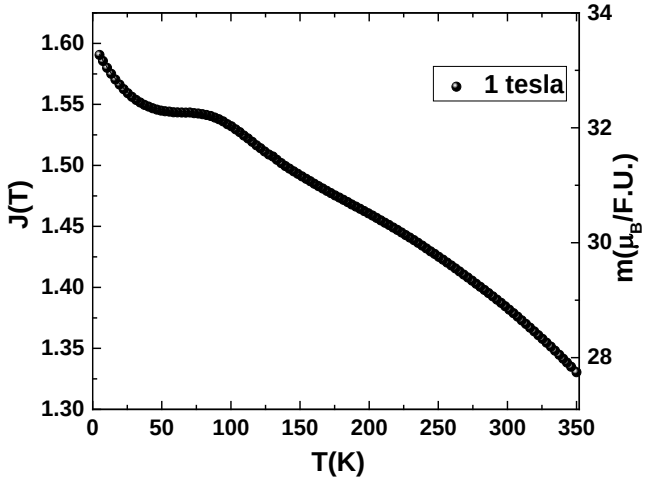

Figure 6.10 magnetization versus temperature (5-350 Kelvin) curves of the $Fe_{14}(Nd, Dy)_2B$ hard magnet specimen in presence of 1 Tesla magnetic field.

The magnetization curves of the $Fe_{14}(Nd, Dy)_2B$ magnetic specimen has been also presented in the Figure 6.3 (d) and (h) recorded at the room temperature (in and out of plane orientation of the sintered magnet). The sintered magnet is highly anisotropic, indicating strong out of plane texture from the hysteresis loop Figure 6.3 (d). It exhibits a coercivity of 3.2 Tesla and remanence is 87% of the total magnetization (without elimination of demagnetizing field). The magnetization of the $Fe_{14}(Nd, Dy)_2B$ specimen at room temperature in presence of 7 Tesla magnetic field is 26.2 Bohr magneton/formula unit 1.35 Tesla ((Figure 6.3 (d)).The magnetization per formula unit is similar to the total magnetization value of the film [178] at the room temperature but the coercivity is high (Figure 6.3 (d)).

In order to see the grains and the grain boundary region transmission electron microscopy was performed on the specimen. The sample preparation is performed by the typical cross section method. Figure 6.11(a to d) shows the transmission electron microscopy (TEM) images of the $Fe_{14}(Nd, Dy)_2B$ hard magnet specimen in different resolutions (). The average grain size is around 500 nm, therefore in the sample preparation for TEM only 3 grains are visible. The sample is inhomogeneous and the grains have different orientations and appear to have dislocations (Figure 6.11(c)). The morphology of the specimen is well match to that of the reported studies [190]. Figure 6.11(d) shows the grain boundary junction of the sintered magnet.

The elemental analysis using electron energy loss spectroscopy (EELS) has been performed in the grain boundary region (a region in red solid line) of Figure 6.11 (d). The results show the presence of Nd_2O_3 phase and dysprosium. The neodymium peak corresponds to the N_4 (120.5 eV) and N_5 (120.5 eV) edge (Figure 6.12). The detection of grain boundary phase needs a very deep analysis. We have performed here a qualitative investigation in order to confirm the similarity of the specimen with the conventional $Nd_2Fe_{14}B$ sintered magnet specimen. The further characterization of the all the specimen has been performed via XAS and XMCD investigation to get the element specific information and will be discussed in the upcoming section.

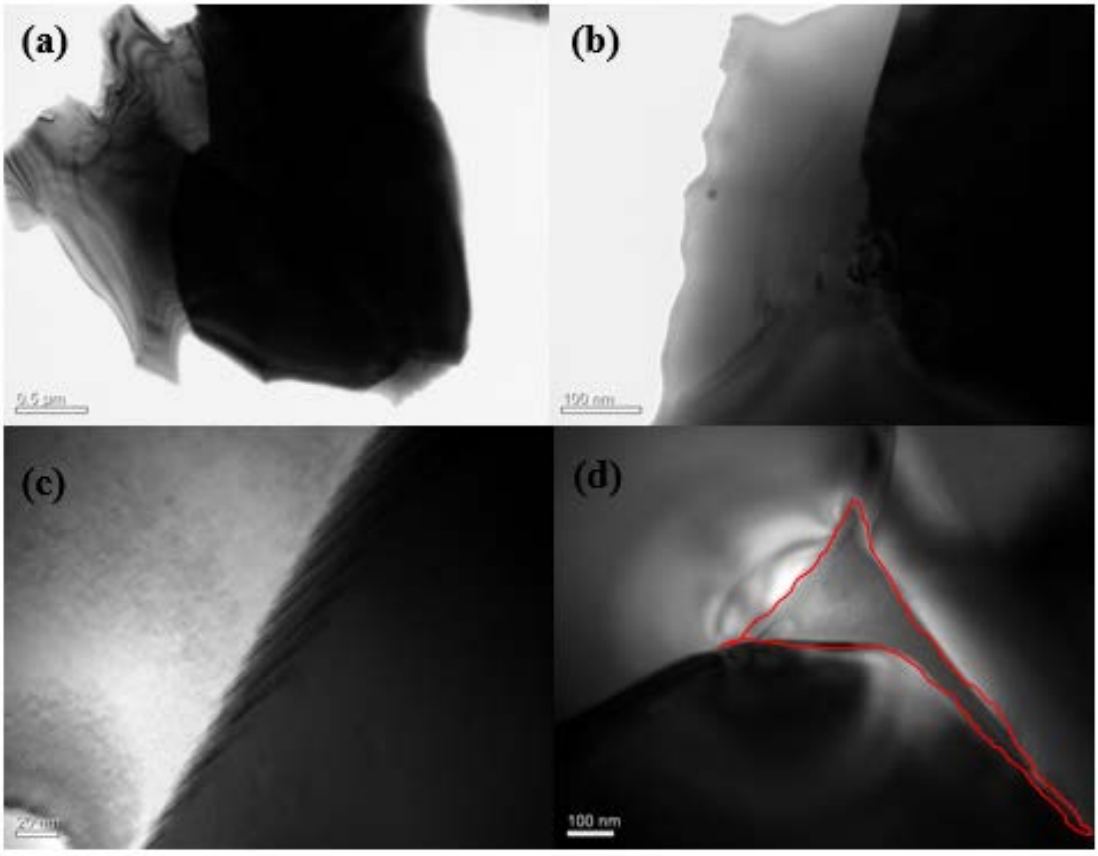

Figure 6.11 transmission electron microscopic images of $Fe_{14}(Nd,Dy)_2B$ sintered hard magnet in different resolutions. Figure (d) shows the grain boundary junction of the sintered magnet (in red solid line). The elemental analysis using electron energy loss spectroscopy (EELS) has been performed in this region and the presence of Nd_2O_3 phase and dysprosium has been observed.

The Fe-Nd-B systems are consists of fine crystal grains of the $Nd_2Fe_{14}B$ phase, Nd-rich phases at the triple junction [7, 159-161] and thin intergranular grain boundary phase [6, 160, 161]. This thin intergranular grain boundary phase is considered to play an important role in the exchange coupling between the ferromagnetic $Nd_2Fe_{14}B$ grains. The morphology of the specimen exhibit the characteristic $Nd_2Fe_{14}B$ sintered magnet microstructure. In order to precisely compare the total sample magnetization with the element specific XMCD results, the chemical compositions of the sintered magnets are analyzed by inductive coupled plasma spectroscopy (ICP-OES) (spectro-ciros). The 62.8±1 weight % iron, 22.1±0.2 weight % neodymium, 8.37±0.02 weight % dysprosium and 0.93±0.2 weight % boron have been detected. The spectroscopic analysis shows the traces of impurities like terbium, cobalt, and copper. The Stoichiometry turned out to be $Fe_{13}DyNd_2B$ for the specimen. There is slightly less iron detected by ICP. Iron contribution is 7% less as it is expected on in average in the specimen.

Figure 6.12 elemental analysis using electron energy loss spectroscopy has been performed in grain boundary junction region and the presence of Nd_2O_3 phase and dysprosium has been observed. The EELS result is presented here. The neodymium peak corresponds to the N_4 (120.5 eV) and N_5 (120.5 eV) edge.

6.4. Spectroscopy results: XAS and XMCD investigation

XMCD measurements (refer chapter 2 experimental techniques) have been performed *in situ* at Fe $L_{2,3}$, and Nd $M_{4,5}$ edges (at 300Kelvin and 80 Kelvin) in the presence of 6.5 Tesla magnetic field in all neodymium-based specimens. The sintered magnets are very sensitive to the

oxidation at the surface, via scrapping oxidation layer can be removed before the measurements. Even inside the ultra-high vacuum chamber, the surface of the sintered specimens (Fe_{14}(Nd, Dy)$_2$B hard magnet and $Fe_{14}Nd_2B$ single phase) have been scrapped [24] and there are no signs of oxidation [106] in all sintered specimens. In case of textured film and multilayer to prevent the oxidation, 2 nm capping layer was deposited on the surface while sputtering the film.

6.4.1. XAS and XMCD spectra of iron $L_{2,3}$ edges

Figure 6.13 (a) and (h) shows the XAS and XMCD spectra of Fe $L_{2,3}$ edges measured at 300 Kelvin and low temperature (15 Kelvin or 80 Kelvin) in the presence of 6.5 Tesla magnetic field along the easy magnetization axis (out of plane orientation) of all the neodymium-based magnets. The line shapes of XAS and XMCD spectra of iron $L_{2,3}$ edges are analogous to the typical metallic iron configuration [24] and is free from oxidation [106]. The iron edge is in good agreement with the previously reported results of the Fe $L_{2,3}$ edges in $Fe_{14}Nd_2B$ single crystal [177].

The orbital and spin sum rules analysis [24] have been performed for the all specimens and results are presented in Table 6.1. The number of 3*d* electrons at iron sites for the $Fe_{14}Nd_2B$ phase is 6.67 (estimated by the ab-initio calculations) [191, 192]. For the reference specimens like Fe/Nd multilayer (d) number of 3*d* electrons in iron are similar to the metallic iron configuration. However, in case of Fe_{14}(Nd, Dy)$_2$B sintered magnet and $Fe_{14}Nd_2B$ thin film, not only main phase ($Fe_{14}Nd_2B$) present but the other phases at the grain boundaries were also reported (morphology of both specimens have been discussed in the section 6.2) [6, 160, 161]. The iron electron occupancy for $Fe_{14}Nd_2B$ phase estimated through the density of states (DOS) calculations varies from 6.5 to 6.6, which is similar to pure metallic configuration [105]. Since XAS and XMCD spectra for Fe_{14}(Nd, Dy)$_2$B sintered magnets and $Fe_{14}Nd_2B$ thin film at Fe $L_{2,3}$ edges are identical to the spectral shape reported by Garcia *et al* [177] on $Fe_{14}Nd_2B$ single crystal. They have used 6.45±0.05, which is close to the DOS results. The number of 3*d* electrons (n_{3d}) used here for the sum rule analysis for all the specimen are also around 6.67. It has been estimated by making the assumption that the n_{3d} are similar for the grain boundary phase and main $Fe_{14}Nd_2B$ phase. The similar assumption has been done by the Nakamura *et al* [180].

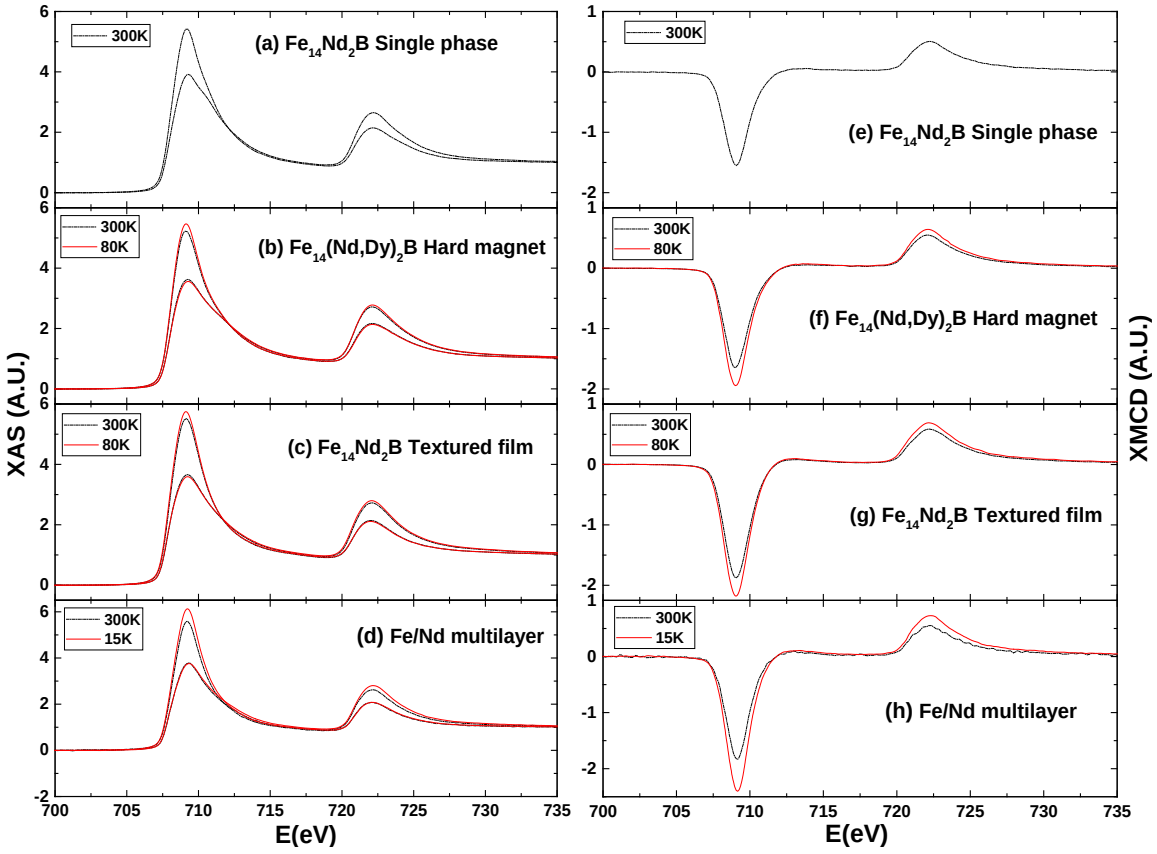

Figure 6.13 edge normalized XAS –left side (average of left and right polarized spectra) and right side -XMCD- (difference of left and right polarized spectra) spectra at Fe $L_{2,3}$ edges of all the neodymium-based specimens (a and e) $Fe_{14}Nd_2B$ single phase, (b and f) $Fe_{14}(Nd,Dy)_2B$ hard magnet, (c and g) $Fe_{14}Nd_2B$ textured thin film and (d and h) Fe/Nd multilayer measured at 300 Kelvin and low temperature are presented here.

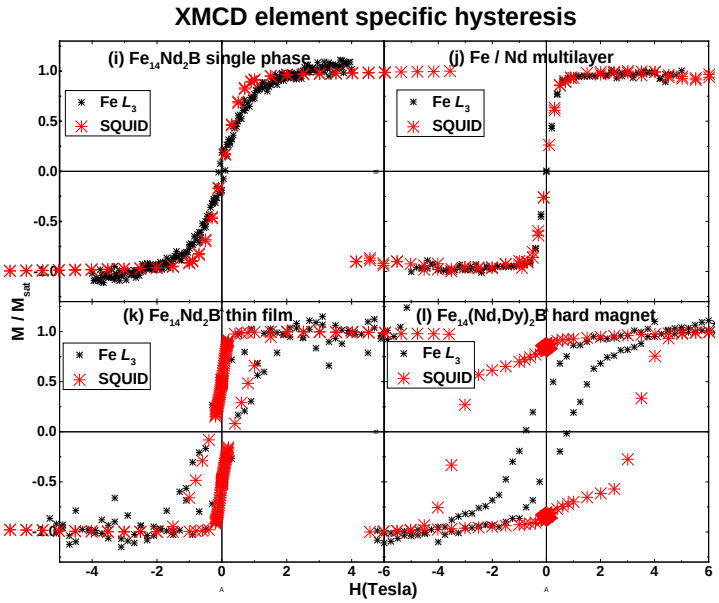

Figure 6.14 element specific hysteresis at Fe L_3 edges have been compared with the SQUID results for all the neodymium-based specimen (i) $Fe_{14}Nd_2B$ single phase (j) $Fe_{14}(Nd, Dy)_2B$ hard magnet (k) $Fe_{14}Nd_2B$ textured thin film and (l) Fe/Nd multilayer.

Table 6.1 values of the orbital magnetic moment m_L, the spin magnetic moment m_S, the total magnetic moment m_{tot}, and the ratio m_L/m_S of Fe 3*d* electrons for all the neodymium-based specimens $Fe_{14}Nd_2B$ single phase, $Fe_{14}(Nd,Dy)_2B$ hard magnet, $Fe_{14}Nd_2B$ textured thin film and Fe/Nd multilayer in units of Bohr magneton /atom, estimated from the sum-rule analysis of the Fe $L_{2,3}$ XMCD results.

T (Kelvin)	**Orbital (m_L) (μ_B / atom)**	**Spin (m_S) (μ_B / atom)**	**Total ($m_S + m_S$) (μ_B / atom)**	**Ratio (m_S / m_S)**
$Fe_{14}Nd_2B$ single phase				
300	0.06±0.01	1.41±0.2	1.47±0.2	0.04±0.01
$Fe_{14}(Nd, Dy)_2B$ hard magnet				
300	0.05±0.01	1.5±0.2	1.55±0.2	0.03±0.01
80	0.06±0.01	1.75±0.2	1.81±0.2	0.03±0.01
$Fe_{14}Nd_2B$ thin film				
300	0.06±0.01	1.68±0.2	1.74±0.2	0.04±0.01
80	0.07±0.01	1.89±0.2	1.96±0.2	0.04±0.01
Fe/Nd multilayer				
300	0.07±0.01	1.67±0.2	1.74±0.2	0.04±0.01
15	0.07±0.01	2.04±0.2	2.11±0.2	0.03±0.01
Pure metallic Fe$L_{2,3}$ edges				
Literature [24]	0.09	1.98	2.07	0.043

The XMCD sum rule analysis total magnetic moment values of the iron for all the specimens does not agrees satisfactorily with the values determined by the other techniques like polarized neutron diffraction (2.20 Bohr magneton/atom) [193], Mössbauer spectroscopy (2.0 Bohr magneton/atom) [194], band structure calculations (2.35 Bohr magneton/atom) [195]. In our results, the iron provides the projected orbital magnetic moment (m_L) of 0.06 to 0.07 Bohr magneton/atom at room temperature and at low temperature in all specimens, which is less than 0.1 Bohr magneton/atom. The total magnetic moment is close to the metallic iron configuration especially in case of multilayer and thin film [24]. It is observed in the SQUID results in case of multilayer system (section 6.3.1 (a)) that at the room temperature very small contribution is visible from neodymium site. The total magnetic moment is originated from iron. At room temperature the iron magnetic moment is 1.74 Bohr magneton /iron atom, which is close to the

metallic iron (2 Bohr magneton/ atom). The XMCD results for the multilayer system are in good agreement with the SQUID results at room temperature (Figure 6.2)).

In the case of sintered magnets (single phase and hard magnet) the total magnetic moment of iron is 30% reduced (refer Table 6.1) than the pure metallic (2 Bohr magneton/ atom). configuration moment [24]. In $Fe_{14}Nd_2B$ phase magnets, especially these sintered magnets consist of fine crystal grains of the $Fe_{14}Nd_2B$ phase, Nd-rich phase [6, 159, 196, 197] and thin intergranular grain boundary phase [6, 197]. The $Fe_{14}Nd_2B$ main-phase grains have the average diameter of about 5 μm. Since we scrap the specimen in-situ to prevent oxidation at the surface, the ferromagnetic grain boundary phase is exposed to the fractured surface. The soft x-ray MCD measurement using a total electron yield (TEY) method is a surface-sensitive magnetic probe which has the probing depth of about 1 nm from the surface. Due to the surface sensitivity of the technique, we are in principle measuring the iron spectrum from the grain boundary phase. Spin scanning electron microscopy results have reported that fractured surface contains the ferromagnetic grain boundary phase in these type of sintered specimen [198]. However, the ferromagnetism is weak in comparison to the main $Fe_{14}Nd_2B$ phase. The estimation of the magnetic moment for the thickness of 3 nm grain boundary phase is approximately 1.4 Bohr magneto/atom, which is too large for paramagnetic phase [180]. In our specimen, it is visible from the TEM image (Figure 6.11 (d)) that the grain boundary is larger than 3 nm. With a varying thickness of grain boundary phase, the magnetic moment is ranging from 1.4 Bohr magneto/atom to 1.6 Bohr magneto/atom[180]. Therefore, the magnetic moment of the Iron is reduced 30% from the total magnetic moment (2 Bohr magneto/atom) of pure metallic Iron.

The element specific hysteresis curves are also recorded by measuring the peak height of the Fe L_3 absorption edges as a function of the applied magnetic field on all the neodymium-based specimen. The magnetic field dependence of the XAS peak at Fe L_3 edge for all specimen at 300 Kelvin along with the SQUID results are shown in Figure 6.14 (i to l) (magnetization curves normalized to unity). The Fe L_3 edge magnetization curve is analogous to the SQUID hysteresis for multilayer (b), single phase specimen (a) and for textured thick film (c) however in case of sintered hard magnet $Fe_{14}(Nd, Dy)_2B$ (d), the hysteresis loops of XMCD and SQUID exhibit the coercivity of 0.7 Tesla and 3 Tesla respectively. The coercivity is reduced in case of the hard magnetic specimen Figure 6.14 (d). The XMCD is surface sensitivity technique and in SQUID the magnetization signal originate from the whole thickness. Therefore the difference in coercivity can be explained by the surface sensitivity of the XMCD measurements.

6.4.2. XAS and XMCD spectra of Neodymium $M_{4,5}$ edges: Line shape analysis

(I) Line shape analysis

Figure 6.15 (a) and (h) shows the XAS and XMCD spectra of Nd $M_{4,5}$ edges ($3d^{10}4f^{n} \rightarrow 3d^{9}4f^{n+1}$ transition) at 300 Kelvin and low temperatures (80 Kelvin and 15 Kelvin) in the presence of 6.5 Tesla magnetic field along the easy magnetization axis (out of plane orientation). In order to compare the experimental spectra with theory, the neodymium XAS and XMCD spectra at the $M_{4,5}$ edges have been simulated by atomic multiplet theory calculations (Further details presented in chapter 3), not only for the ground state configuration but also for the spin-orbit coupled states of the neodymium.

There are no reported results on spin-orbit coupled states of neodymium. The simulation parameters are analogous to the results reported in chapter 3. According to Hund´s rule, neodymium has 3 electrons in *f* shell so the *L* and *S* will be 6 and 3/2. The starting point for the full multiplet calculations at Nd $M_{4,5}$ XAS spectrum is the pure Hund's rule atomic ground state J =9/2 ($^4I_{9/2}$) with a three 4*f* electrons (refer Figure 6.16)). The parallel and antiparallel combination of *L* and *S* could provide 4 different *J* states (9/2, 11/2, 13/2 and 15/2). The ground state is J= 9/2 and next higher energy spin-orbit coupled states are J=11/2, 13/2 and 15/2 [199]. Figure 6.16 (a) and (b) shows the XAS and XMCD simulated spectra respectively.

The line shape of all the neodymium experimental XAS (Figure 6.17 (k) to (h)) and XMCD (Figure 6.17 (o) to (r)) spectra are in good agreement with the earlier reported Nd^{3+} experimental results [33, 37, 180] and analogous to the simulated J= 9/2 ground state configuration spectra (Figure 6.16 (a) and (b)). However the change in the M_5 and M_4 XAS and XMCD intensity ratio is visible in Figure 6.17 compared to the simulated J= 9/2 ground state configuration spectra. Which clearly shows that the different crystal structure, the lattice sites and the nearby environment affecting the shape of the XAS and XMCD spectra. Therefore I order to estimate quantitatively estimation of the spin and orbital moment performed by the XMCD sum rule analysis.

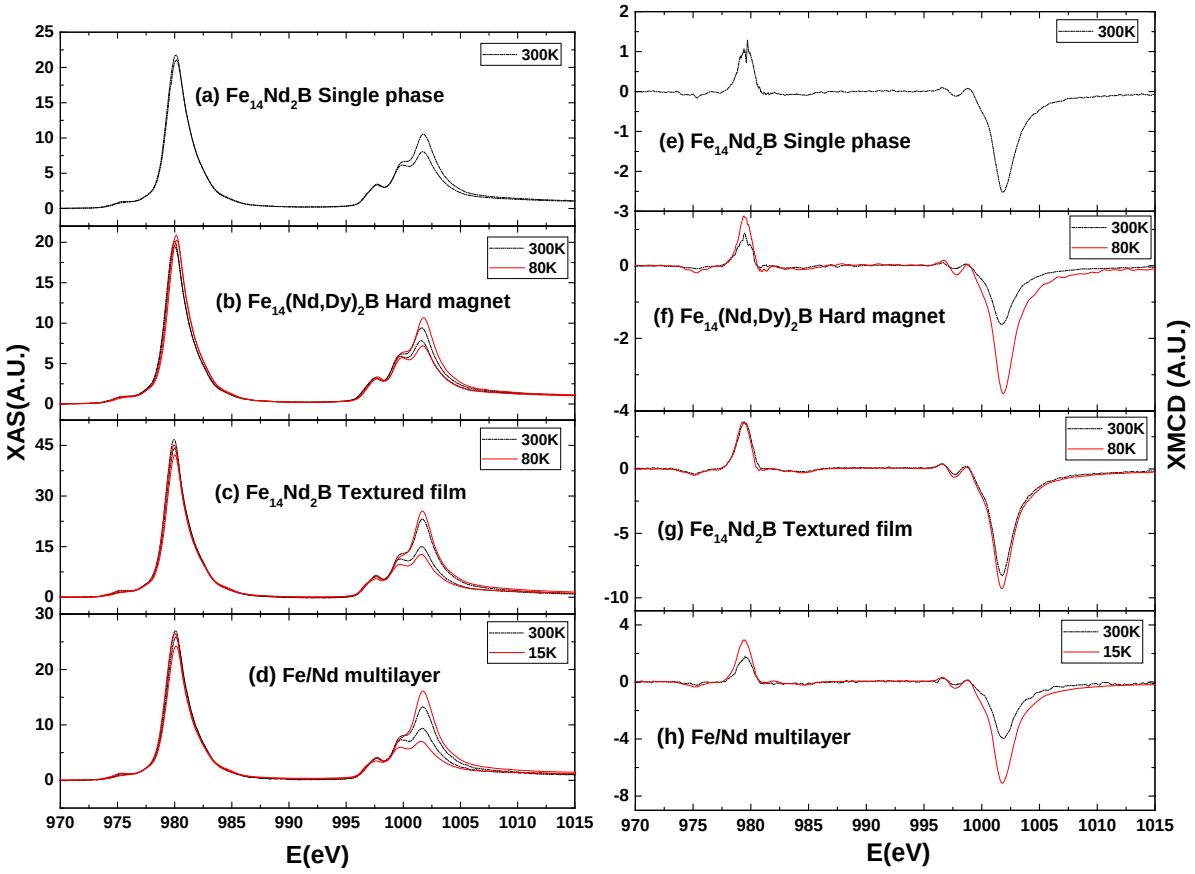

Figure 6.15 edge normalized XAS –left side figures (left and right polarized spectra) and (B) right side figures - XMCD- (the difference of left and right polarized spectra) spectra at Nd $M_{4,5}$ edges of all the neodymium-based specimens (a and e) $Fe_{14}Nd_2B$ single phase, (b and f) $Fe_{14}(Nd,Dy)_2B$ hard magnet, (c and g) $Fe_{14}Nd_2B$ textured thin film and (d and h) Fe/Nd multilayer measured at 300 Kelvin (dot dash black color curve) and low temperature (red solid color curve)

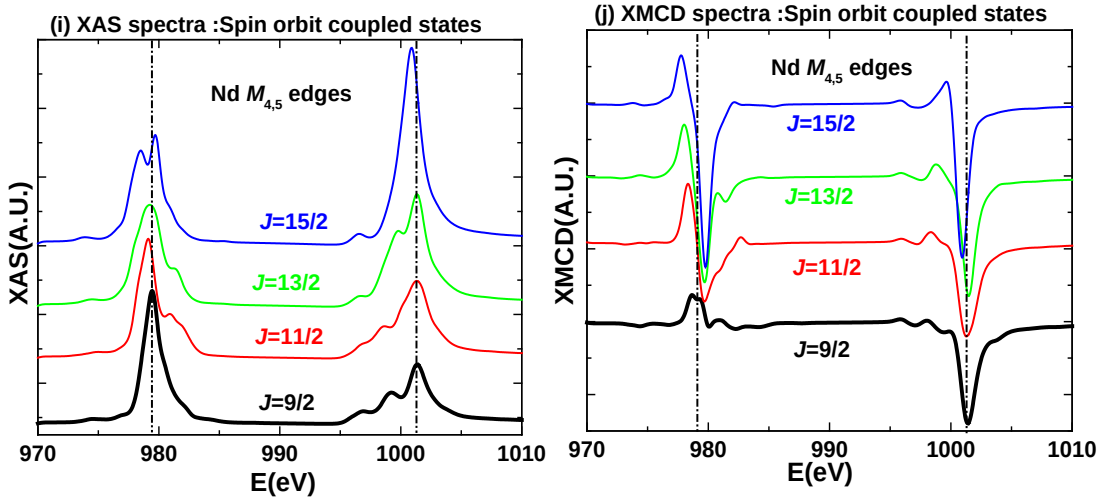

Figure 6.16 Atomic multiplet theory simulated Nd $M_{4,5}$ (i) XAS (average spectra of left, right and linearly polarized spectra) and (j) XMCD: (difference in left and right polarized spectra) spectra for Hund's rule ground state J=9/2: spin and orbital antiparallel coupled (black color) and the subsequent higher energy J=11/2 (red color), J=13/2 (green color) and J=15/2 (blue color). The ground state spectra J=9/2 (black color), which is analogous to the experimental spectra is represented by more darkened in the color.

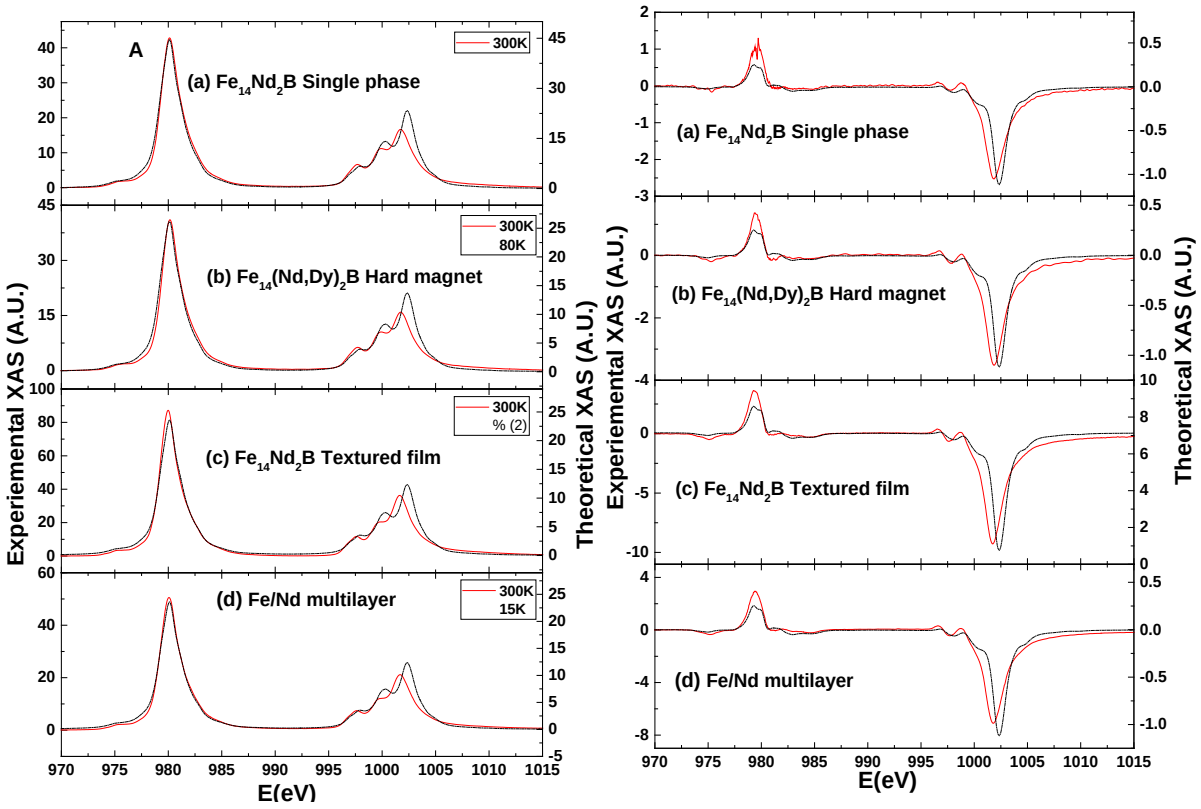

Figure 6.17 edge normalized XAS –left figures (average of left and right polarized spectra) and right figures -XMCD- (the difference of left and right polarized spectra) spectra at Nd $M_{4,5}$ edges of all the neodymium-based specimens (a) $Fe_{14}Nd_2B$ single phase (b) $Fe_{14}(Nd,Dy)_2B$ hard magnet (c) $Fe_{14}Nd_2B$ textured thin film and (d) Fe/Nd multilayer measured at low temperature overlapped with the theoretical ground state (J=9/2) spectra of the neodymium $M_{4,5}$ edges. The left hand side scale is for the experimental spectra and the right hand side scale is for theoretical spectra.

(II) Sum rule analysis

On continuing the discussion from the previous section 6.4.2 that in all neodymium-based specimens' neodymium $M_{4,5}$ edges line shape can be explained by the pure J=9/2 ground state spectrum. Now sum rule analysis [20, 35] have been performed on the integrated XAS and XMCD spectra of J=9/2 theoretical spectra and all the neodymium experimental spectra for all the specimens by using the correction factor and eliminating the magnetic dipole term (T_Z) (As performed in chapter-3 for theoretical spectrum and experimental spectrum). Table 6.2 summarizes the values of m_L, m_S, sum (m_L+m_S) and their ratio (m_L/m_S) of 4f electrons for the Nd $M_{4,5}$ edges at 300 Kelvin and low temperatures along with the theoretical spectra sum rule analysis results. There are 3 electrons present in the 4f shell of neodymium, therefore the number of holes (n_h) used are 11. The neodymium electron occupancy for $Fe_{14}Nd_2B$ phase

through the density of states calculations varies from 3.4 to 3.16, which is close to trivalent neodymium configuration [105].

Table 6.2 orbital magnetic moment m_L, the spin magnetic moment m_S, the total magnetic moment m_{tot}, and the ratio m_L/m_S of Nd 4*f* electrons of all the neodymium-based specimens (a) $Fe_{14}Nd_2B$ single phase (b) $Fe_{14}(Nd,Dy)_2B$ hard magnet (c) $Fe_{14}Nd_2B$ textured thin film and (d) Fe/Nd multilayer in units of Bohr magneton /atom presented and all the magnetic moment values have been estimated from the sum-rule analysis of the Nd $M_{4,5}$ edge XAS and XMCD data.

T (Kelvin)	Orbital (m_L) (μ_B / atom)	Spin (m_S) (μ_B / atom)	Total ($m_S + m_L$) (μ_B / atom)	Ratio (m_L/m_S)	Reduction in m_S from theory
$Fe_{14}Nd_2B$ single phase					
300	0.92±0.1	-0.43±0.1	0.49±0.1	-1.9±0.2	5.67
$Fe_{14}(Nd, Dy)_2B$ hard magnet					
300	0.62±0.1	-0.31±0.1	0.32±0.1	-2.04±0.2	7.89
80	1.39±0.2	-0.63±0.1	0.77±0.1	-2.22±0.2	3.85
$Fe_{14}Nd_2B$ thin film					
300	1.38±0.2	-0.73±0.1	0.65±0.1	-1.89±0.2	3.33
80	2.52±0.2	-1.17±0.2	1.34±0.2	-2.15±0.2	2.07
Fe/Nd multilayer					
300	1.19±0.2	-0.58±0.1	0.62±0.1	-2.07±0.2	4.21
15	2.86±0.2	-1.42±0.2	1.44±0.2	-2.01±0.2	1.71
Nd $M_{4,5}$ edge J=9/2 ground state					
***J*=9/2**	5.71±0.2	-2.42±0.2	3.29±0.2	-2.36±0.2	-

In chapter 3, it has been discussed that there is a large deviation in the spin sum rule in case of light rare earth elements. In order to estimate the spin moment the correction factor for the neodymium (2.019-mentioned in chapter 3) should be used to eliminate $3d_{5/2}$-$3d_{3/2}$ mixing problem [60]. The complete process of correcting effective spin value is explained stepwise in chapter 3 for the experimental spectra. In the similar way the analysis have been performed. The expectation value of the magnetic dipole term used for the J=9/2 ground state is -0.376 [60].

At room temperature, the XMCD sum rule analysis of neodymium spectra provides the projected effective spin of m_S =-0.58±0.1 Bohr magneton/atom and orbital magnetic moment

of m_L (L_z) =1.19±0.2 Bohr magneton/atom for Fe/Nd multilayer. At low temperature (15K) the XMCD spectrum is 2 times larger than room temperature (300K) spectrum and the projected orbital m_L (L_z) =2.86±0.2 Bohr magneton/atom and effective spin is m_S =1.42±0.2 are respectively (refer Table 6.2). The magnetic moment of the neodymium has been reported by the polarized neutron diffraction (2.30 Bohr magneton/atom at 4.2 Kelvin) [193] and Mössbauer spectroscopy (2.3 Bohr magneton/atom) [194]. For multilayer system the highest magentic moment values have been observed compared to other specimens. However the total magnetic moment (at 15 Kelvin -1.44 Bohr magneton/atom) is still 37% reduced than the reported results [193] and 56% than the theoretical simulation results. For other neodymium-based specimens like sintered magnets is much smaller (70%) compared to multilayer and thick film. The XMCD effect is almost 81 % for the neodymium simulated spectra, However it is reduced to 44% for multilayer, 36% for textured thick film, 21% for hard magnet and 10% for single phase specimen respectively. The reduction in the neodymium magnetic moment is consistent as the coercivity increases in the specimen, only single phase specimen is the exception and the coercivity is correlated with grain boundary phase. The reduction in the XMCD effect at the neodymium edge has strong correlation with the grain boundary phases.

At low temperature, in all the specimens (multilayer, textured film and hard magnets) a trend is observed that the total magnetic moment is twice of the room temperature magnetic moment. The M versus T curves for all the specimens (Figure 6.2, 6.5, 6.6 and 6.10) also show that at low temperature increase in the magnetic moment is almost twice of that at the room temperature. The increase of magnetic moment at a lower temperature in neodymium signifies that the neodymium and iron are not very well coupled with each other in all transition metal–neodymium-based magnets studied here and the neodymium magnetic moments are not saturated. At room temperature, the orbital magnetic moment is almost quenched in case of sintered magnets ($Fe_{14}Nd_2B$ single phase and $Fe_{14}(Nd, Dy)_2B$ hard magnet) and the spin magnetic moment is 5 to 7 times reduced in the sintered magnets (refer Table 6.2) compared to the simulation results. Due to slight change in the spectral shape of the neodymium spectra (refer Figure 6.17) in all the neodymium specimens compared to the J=9/2 pure ground state spectra, the change in the spin to orbital ratio also observed (refer Table 6.2).

There is very weak ferromagnetism observed at the neodymium edge. It could be that the surface and the bulk of the specimen behaves different and can cause the reduction in the magnetic moment. In order to explain this, the XMCD sum rule analysis results with the SQUID results comparison need to perform. Although the XAS and XMCD spectral shape is not varying significantly but the neodymium behaves different in all the specimen. The crystalline

environment of the solid and the grain boundary phase is noticeably affecting the magnetic properties and the orientation of the spin alignment of the neodymium 4*f* electrons.

(III) Comparison of sum rule analysis results with SQUID results

Table 6.3 total magnetic moment of the Fe-3*d* electrons and Nd-4*f* electrons of all the neodymium-based specimens (a) $Fe_{14}Nd_2B$ single phase (b) $Fe_{14}(Nd, Dy)_2B$ hard magnet (c) $Fe_{14}Nd_2B$ textured thick film and (d) Fe/Nd multilayer in units of Bohr magneton /atom and from the empirical formula of the specimens converted in to Bohr magneton /formula unit presented. The XMCD sum rule analysis has been compared with the SQUID results in terms of Bohr magneton /formula unit to confirm the similarity between bulk and the surface behavior.

T (Kelvin)	Empirical formula	SQUID (m_{tot}) (μ_B/F.U.)	XMCD (m_{Fe}) (μ_B/Fe atom)	XMCD(m_{RE}) (μ_B/RE atom)	XMCD (m_{tot}) (μ_B/ F.U.)
$Fe_{14}Nd_2B$ single phase					
300	**$Fe_{14}Nd_2B$**	31±2	1.47±0.2	0.49±0.1	21.56±2
$Fe_{14}(Nd, Dy)_2B$ hard magnet					
300	**$Fe_{13}DyNd_2B$**	26.72±2	1.55±0.2	0.32±0.1	20.76±2
80	**$Fe_{13}DyNd_2B$**	-	1.81±0.2	0.77±0.1	-
$Fe_{14}Nd_2B$ thin film					
300	**$Fe_{14}Nd_2B$**	26.0±2	1.74±0.2	0.65±0.1	25.66±2
80	**$Fe_{14}Nd_2B$**	33±2	1.96±0.2	1.31±0.1	30.06±2
Fe/Nd multilayer					
300	**Fe/Nd**	2.1±0.2	1.74±0.2	0.62±0.1	2.36±0.2
15	**Fe/Nd**	4.0±0.2	2.11±0.2	1.44±0.1	3.55±0.2

As XMCD is surface sensitive technique, we observed the reduction in the iron and neodymium magnetic moment in sintered magnets. The elements specific sum rule analysis for iron and neodymium arte compared with the SQUID magnetic moment in Bohr magneton / formula unit. The total magnetic moment evaluated from the sum rule analysis by the elimination of magnetic dipole term T_Z and by correcting the mixing problem is in good agreement with the SQUID magnetization result in case of Fe/Nd multilayer and textured thick film. The conversion of SQUID results from emu/gram to Bohr magneton include the density and the thickness of the film so the 2 to 5% difference in the SQUID and XMCD results in case of multilayer could be related to the error in estimation of exact thickness of the film. On the other hand, the total

magnetic moments of the sintered magnet is 25 to 30% compare to the bulk magnetization from the SQUID results. In case of multilayer and thick film surface and the bulk have similar behavior but it is different in case of sintered magnets. There are several possible reasons due to which reduction in the magnetic moment of the neodymium is taking place are as follows:

1. Unsaturated magnetic moments
2. The neodymium is paramagnetic.
3. Grain boundary phase is less ferromagnetic.
4. Crystal field effects
5. Surface sensitivity of the total electron yield measurements.

All possible reasons could be the cause of the reduction in the magnetic moment and it will be explained in the upcoming sections in more detail.

6.4.3. Explanation for reduction in neodymium magnetic moment

(I) Unsaturated moments

As it is well known for the rare earth elements that the ordering tempertaures are very low [16]. There is possibility that the neodymium moments are not completely aligned along the field direction or canted, due to which the projection of the neodymium magentic moment is smaller and even on 7 Tesla magnetic field is not enough to saturate the neodymium magnetic moment and the linear increase at the lower temperature also shows that the there is possibility that the neodymium magentic moment is paramagnetic at room temperature in these specimens.

(II) Grain boundary phase

In $Fe_{14}Nd_2B$ phase magnets, especially these sintered magnets consist of fine crystal grains of the $Fe_{14}Nd_2B$ phase, neodymium rich phase [6, 159, 196, 197] and thin intergranular grain boundary phase [6, 197]. As discussed earlier in case of iron (section 5.4.1) that we scrap the sintered specimen in-situ to prevent oxidation at the surface, the ferromagnetic grain boundary phase is exposed to the fractured surface. Due to the surface sensitivity of the technique, we are in principle measuring the spectrum, where the signal also originating from this grain boundary phase. These grain boundary phases also contain the neodymium rich phase [6, 159, 196, 197], there is Nd-O rich phase also observed in hard magnetic specimen in the grain boundary via EELS investigation (refer Figure 6.13).

Figure 6.18 (a) the oblate-shaped 4*f* orbitals of a neodymium ion sitting in an aspherical distribution of valence electrons which has larger density along the principal axis of symmetry of the $Nd_2Fe_{14}B$ lattice. (b) Schematic representation at an interface with a sub-phase containing oxygen in which the neodymium valence electrons moved toward the oxygen atom for bonding.

The local environments around the rare earth ions at the interfaces can be strongly affected by the nearest neighbor atomic arrangements at the interface. The neodymium exhibits the oblate shaped spin distribution. This aspherical distribution of the valance electrons, which has the density concentrated along the principle axis of the symmetry of the $Fe_{14}Nd_2B$ lattice. The hypothetical situation of an interface with a sub-phase containing oxygen in which the neodymium valence electrons moved toward the oxygen atom for the bonding is shown in the Figure 6.18 (a) and (b). This situation can provide the reduced average neodymium magnetic moment at the neodymium site in the sintered magnets.

In principle, the grain boundary paramagnetic phase is responsible for the reduction in the average magnetic moment of the neodymium and this grain boundary phase is causing the misalignment of the spin moments. Due to this the spin moments are not oriented completely in the direction of the magnetic field.

(III) Crystal field multiplet model

Full multiplet calculation under consideration of the crystal field allows the quantitative clarification of the ground state. The Hund's rule ground state of the 4*f* electron in Nd^{3+} ion is characterized by J=9/2. For the simplification the cubic symmetry (C_4) is considered for the simulations. The crystal field calculations have been performed by changing the crystal field

strength ($10D_q$) from 0 to 100 meV with quanty software. The simulation parameters like Slater integrals, spin-orbit parameters are identical as mentioned in chapter 3 section 3.4.4. There is no change in the XMCD spectral shape observed while changing the crystal field. The XMCD effect has been reduced from 80% to 43% on the application of the 0 to 100 meV crystal filed energy. The XMCD effects in case of experimental spectra at room temperature is 17%, so even on incorporating the crystal field of 100 meV, XMCD effect is 43%. The crystal field is responsible for the reduction in the XMCD effect at Nd M4,5 edge without change in the spectral shape however the reduction in the sintered magnets cannot completely explained by the crystal field effects. The crystal field is playing role but in practical it will not be more than 25 meV in case of neodymium. The further model need to be searched

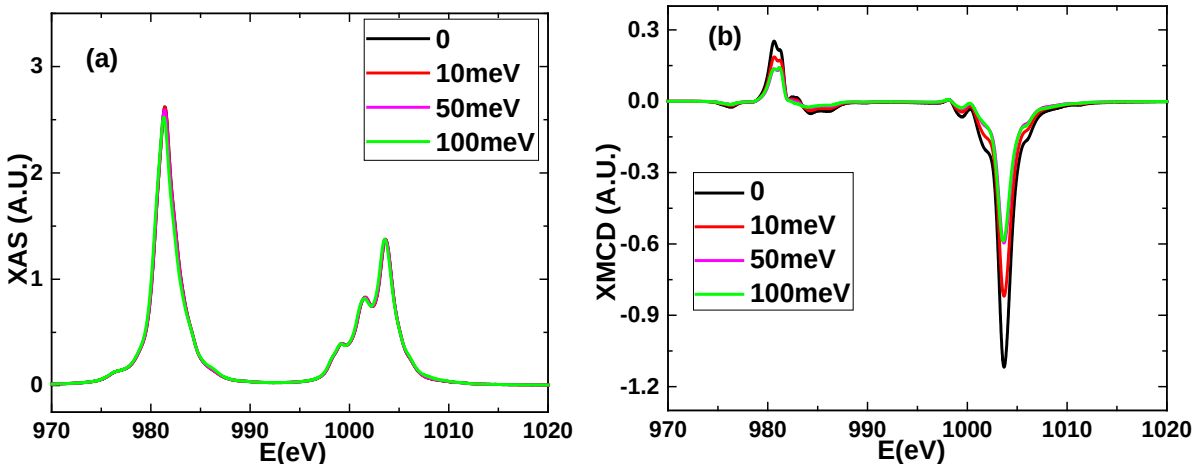

Figure 6.19 simulations of (a) XAS and (b) XMCD spectra of cubic crystal field effects for Nd^{3+} ion via Quanty software. The variations in the spectra with increasing 10Dq parameter from 0 (no crystal field) to 100 meV are shown.

(IV) $Fe_{14}Nd_2B$ film – XAS and XMCD investigation in transmission yield (TMY)

The soft XMCD measurement using a total electron yield (TEY) method is a surface-sensitive magnetic probe which has the probing depth of about 1 nm from the surface. It can be possible that the surface and the bulk properties are different in these sintered magnets. In order to confirm the surface sensitivity, attempts were made to produce hard magnetic layers of smallest possible thickness to perform the XMCD measurements in the transmission mode along with the total electron yield at the same time. For this purpose, $Fe_{14}Nd_2B$ thin film of thickness 30nm layer was deposited on 75 nm silica membrane with the hole of ~ 2-3 micron using the

sputtering technique. The preparation technique is presented with details in reference [200]. Figure 6.20 (b) shows the corresponding hysteresis curves at room temperature with the 7.5 tesla applied magnetic field perpendicular and parallel orientation to the substrate surface. The film is soft magnetic and in-plane magnetized. In general, with the small thickness, it is difficult to get the hard magnetic properties. The Al_2O_3 (sapphire) deposited samples with the 100 nm thickness shows better hard magnetic properties than deposited on silica membranes [200].

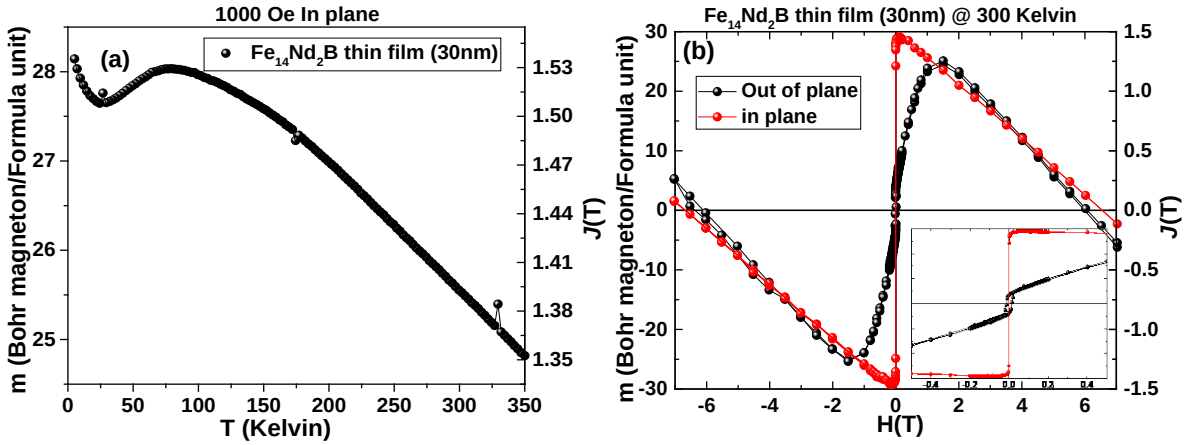

Figure 6.20 (a) magnetization versus temperature curve $Fe_{14}Nd_2B$ film 30 nm thickness deposited on silica membrane in presence of 1000 Oe magnetic field. (b) SQUID Hysteresis loops of $Fe_{14}Nd_2B$ film 30 nm (red) and out of plane (black) orientation in presence of 6.5 T magnetic field at room temperature. AT higher magnetic fields, the diamagnetic contribution from the substrate is visible. Therefore the magnetization curve at the lower field is presented in the figure (b) on the right side.

Our objective is to perform the transmission and electron yield measurements at the same time to check the surface sensitivity of the XMCD signal for iron and neodymium, therefore 30 nm thickness of $Fe_{14}Nd_2B$ phase on silica membrane is the appropriate choice. Figure 6.18 (a) shows the magnetization vs temperature curve for the film at 1000 Oersted along the in-plane orientation. The magnetization vs temperature curve shows the typical $Fe_{14}Nd_2B$ phase linear behavior up to spin reorientation temperature (around 110 Kelvin) for this film. The curve is analogous to the previously reported $Fe_{14}Nd_2B$ specimen results in section 6.3.2 and 6.3.3. The total magnetic moment of the film along the in-plane direction and out of plane direction is 29.57 Bohr magneton/formula unit (1.46 T) and 24.62 Bohr magneton/formula unit (1.24 T) respectively without eliminating the diamagnetic background from the substrate. The total

magnetization in-plane orientation is close to the pure $Fe_{14}Nd_2B$ phase magnetization (32 Bohr magneton/formula unit) reported in the literature[178, 200].

In order to precisely compare the total sample magnetization with the element specific XMCD results, the chemical compositions of the sintered magnets are analyzed by inductive coupled plasma spectroscopy (ICP-OES) (spectro-ciros). The 73 ±1 weight % iron, 25.0±1 weight % neodymium and 2±0.2 weight % boron have been detected. The spectroscopic analysis shows the traces of impurities like titanium and manganese. The stoichiometry turned out to be $Nd_2Fe_{14}B$ for the specimen.

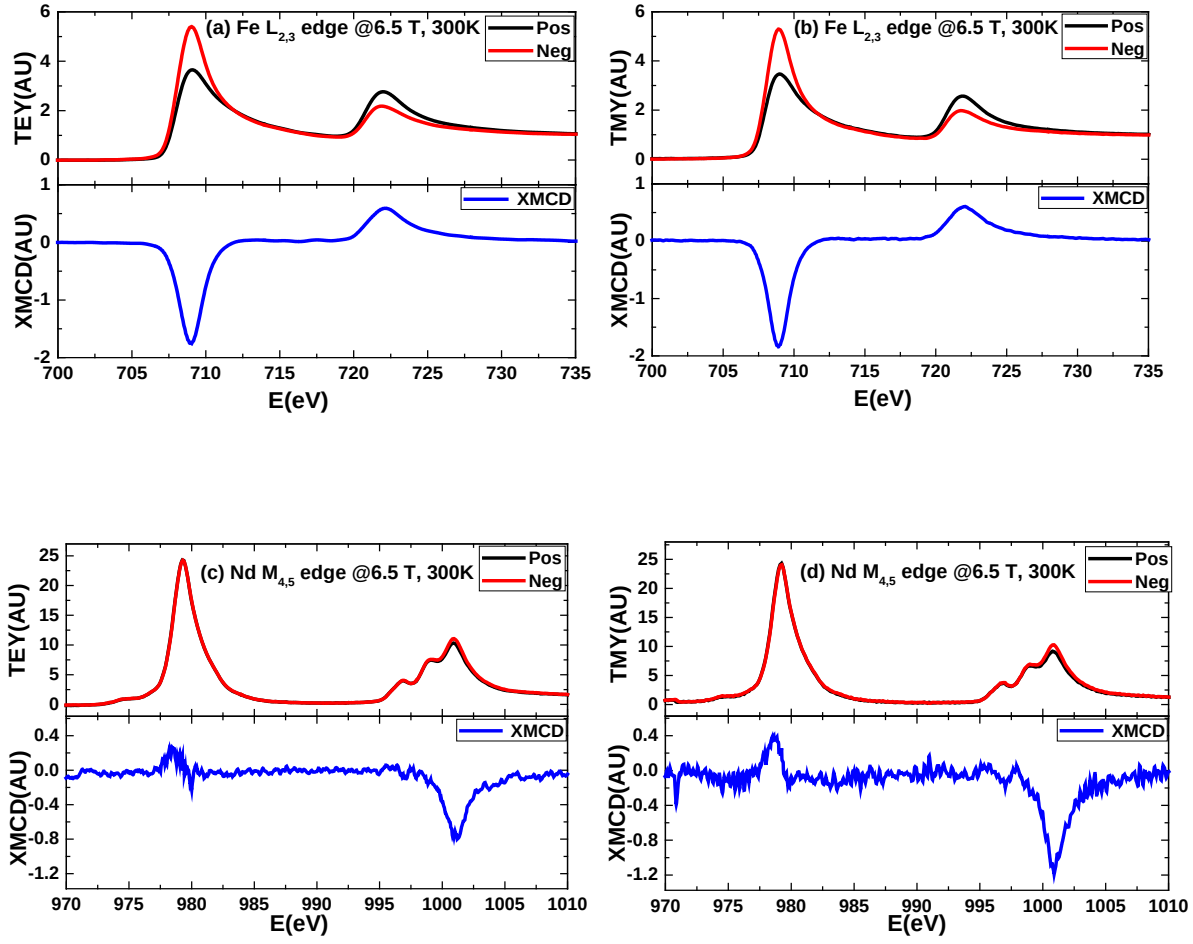

Figure 6.21 edge normalized XAS –top panel (measured left and right polarized spectra) and XMCD- bottom panel (the difference of left and right polarized spectra) spectra measured at Fe $L_{2,3}$ (a and b) and Nd $M_{4,5}$ (c and d) edges in total electron yield (a and c) and transmission yield (b and d) for the $Fe_{14}Nd_2B$ thin film 30 nm thickness deposited on silica 75 nm silica membrane (at 300 Kelvin and in presence of 6.5 Tesla magnetic field) are presented.

Due to the technical limitations we can perform the measurements only along the out of plane orientation, therefore the XAS and XMCD investigation have been performed at Fe $L_{2,3}$ and Nd $M_{4,5}$ edges in presence of 6.5 T magnetic field along the out of plane orientation in total electron yield (TEY) and the transmission yield (TMY) and presented in Figure 6.21. The analysis procedure and number of holes are similar for both iron and neodymium edges as presented in section 6.4.1 and 6.4.2. The shape of XAS and XMCD spectra of iron $L_{2,3}$ edges is analogous to the typical metallic iron configuration [24] and for neodymium also line shape is analogous to the pure Nd^{3+} configuration [37] and the atomic multiplet theory simulated Nd^{3+} spectra.

Table 6.4 orbital magnetic moment m_L, the spin magnetic moment m_S, the total magnetic moment m_{tot}, and the ratio m_L/m_S of Nd 4*f* electrons of $Fe_{14}Nd_2B$ 30nm film in units of Bohr magneton/atom along the out of plane orientation presented in total electron yield and transmission yield mode.

T (Kelvin)	**Orbital (m_L) (μ_B / atom)**	**Spin (m_S) (μ_B / atom)**	**Total ($m_S + m_L$) (μ_B / atom)**	**Ratio (m_S / m_L)**	**Reduction in m_S from theory**
Fe $L_{2,3}$ edge					
TEY	0.06±0.01	1.57±0.2	1.64±0.2	0.04±0.01	-
TMY	0.03±0.01	-1.72±0.2	1.75±0.2	0.02±0.01	-
Nd $M_{4,5}$ edge					
TEY	0.32±0.1	-0.10±0.02	0.22±0.02	-3.06±0.2	23
TMY	0.34±0.1	-0.16±0.02	0.18±0.02	-2.15±0.2	15.08

The sum rule analysis results for iron and neodymium are presented in Table 6.4. There is no prominent difference visible in electron yield and transmission yield measured XMCD line shape intensity at the iron $L_{2,3}$ edge in Figure 6.21 (a) and (b). However, there is still 6% increase in the total magnetic moment of the iron is observed in transmission yield results compared to electron yield results (refer Table 6.4). In case of neodymium, the XMCD line shape intensity at M_4 edge is twice of the total electron yield results in transmission signal (Figure 6.21 (c) and (d)). There is 7% XMCD effects in TEY mode and 13% XMCD effect in TMY mode are recorded at Neodymium $M_{4,5}$ edge. There is a clear increase in XMCD effect is observed in transmission signal at neodymium edge.

The $Fe_{14}Nd_2B$ thin film exhibit 24.62 Bohr magneton/formula unit from the SQUID measurements results. From the XMCD sum rule analysis, the total magnetic moment per formula unit in total electron yield is 23.4 Bohr magneton/formula unit ($Fe_{14}Nd_2B$ =1.64*14+0.22*2) and in transmission yield measurements 24.5 Bohr magneton/formula unit ($Fe_{14}Nd_2B$ =1.75*14+0.22*0.18). The sum rule analysis in case of transmission is surprisingly in excellent agreement with the SQUID results. The inclusive difference in the total magnetic moment is 5% in TEY and TMY measurements in case of film, which clearly shows that the surface effects plays important role in these systems. The sum rule analysis results show that the surface in case of thin film is different than bulk, there is resilient difference in the magnetic moment of the transmission and electron yield has been observed.

6.5. Discussion

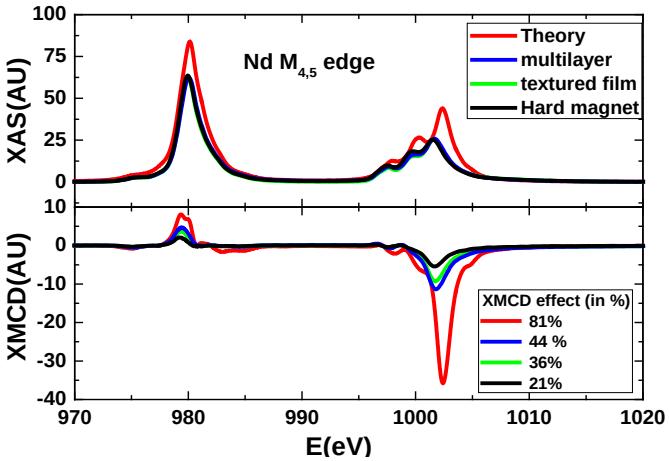

Figure 6.22 comparison of neodymium $M_{4,5}$ edges XAS- sum of the left and right polarized spectra (top panel) and XMCD-difference between left and right polarized spectra (bottom panel) spectra of the specimens– multilayer (blue color), textured thick film (green color) and hard magnet (black color) with the theoretically simulated J=9/2 ground state spectrum. All the spectra are scaled for the comparison.

The XAS and XMCD investigation were performed at the Fe $L_{2,3}$ and the Nd $M_{4,5}$ edges in serval neodymium based specimens like sintered magnets ($Fe_{14}Nd_2B$ single phase and $Fe_{14}(Nd, Dy)_2B$ hard magnet) , Fe/ Nd multilayer and $Fe_{14}Nd_2B$ 340nm textured thick film. The XAS and XMCD line shape of the neodymium $M_{4,5}$ edges can be explained by the J=9/2 ground state configuration, however change in the M_4 and M_5 edges XMCD intensity has been

observed. Although the XAS and XMCD spectral shape is not varying significantly but the neodymium behaves different in all the specimen. The crystalline environment of the solid and the grain boundary phase is noticeably affecting the magnetic properties and the orientation of the spin alignment of the neodymium 4*f* electrons. Which is causing the severe reduction (refer Figure 6.22) in the magnetic moment of the Nd in the sintered magnets compared to the thin film and the multilayer.

The total magnetic moment at room temperature is originating from the iron magnetic moment and the contribution of the neodymium magnetic moment at room temperature is very small. The 34 % discrepancy between the total magnetic moment in total electron yield XMCD results and the SQUID results in case of $Fe_{14}Nd_2B$ single phase and $Fe_{14}(Nd, Dy)_2B$ hard magnet are originating due to reduction in the total iron magnetic moment and the surface sensitivity of the total electron yield measurements. It is the presence of weak ferromagnetic iron and neodymium based intergranular grain boundary phase in sintered magnets. This intergranular boundary phase acts as pinning site or the decoupling site between the large grains of the $Fe_{14}Nd_2B$ main phase, which increases the coercivity of the specimen and the hard magnetic properties. It is also correlated with the coercivity of the specimen that the specimen with the higher coercivity shows the large reduction in the magnetic moment of the neodymium although the $Fe_{14}Nd_2B$ single phase specimen is exception in this case. The XMCD effect is only 10 % which shows that the neodymium moments are almost paramagnetic at room temperature in the $Fe_{14}Nd_2B$ single phase specimen.

In order to confirm the surface sensitivity the measurements have been performed in transmission and electron yield at the same time on 30nm $Fe_{14}Nd_2B$ thin film. The excellent agreement between SQUID and XMCD transmission yield results shows that the surface in these magnets behaves different than the bulk of the specimen. As the difference in total electron yield and the transmission yield results is 5 to 10% in case of 30nm $Fe_{14}Nd_2B$ thin film, but it can be enormous in sintered magnets, which is responsible for the reduction in the neodymium magnetic moment.

7. Reference

1. K. J. Strnat, *Modern Permanent Magnets for Applications in Electro-Technology*.
2. J.M.D. Coey, *Rare- earth Permanent Magnets*. "Rare-earth Permanent Magnets", Clarendon Press Oxford New York 1996.
3. J. Fidler, D. Suess, T. Schrefl, *Rare-earth Intermetallics for Permanent Magnet Applications*, in *Handbook of Magnetism and Advanced Magnetic Materials*. 2007, John Wiley & Sons, Ltd.
4. H. Sepehri-Amin, T. Ohkubo, K. Hono,, *The mechanism of coercivity enhancement by the grain boundary diffusion process of Nd–Fe–B sintered magnets*. Acta Materialia, 2013. **61**(6): p. 1982-1990.
5. H. Sepehri-Amin, T. Ohkubo,T. Shima,K. Hono, , *Grain boundary and interface chemistry of an Nd–Fe–B-based sintered magnet*. Acta Materialia, 2012. **60**(3): p. 819-830.
6. Y. Shinba, T. J. Konno, K. Ishikawa, K. Hiraga,M. Sagawa,, *Transmission electron microscopy study on Nd-rich phase and grain boundary structure of Nd–Fe–B sintered magnets*. Journal of Applied Physics, 2005. **97**(5): p. -.
7. J. Fidler, K. G. Knoch,, *Electron microscopy of Nd-Fe-B based magnets*. Journal of Magnetism and Magnetic Materials, 1989. **80**(1): p. 48-56.
8. Thomas Schrefl Josef Fidler *Micromagnetic modelling—the current state of the art*. 2000.
9. Josef Fidler and Dieter suss Thomas Schreß, *Micromagnetic Modelling of Nanocomposite Magnets*.
10. H. Kronmüller, *General Micromagnetic Theory*, in *Handbook of Magnetism and Advanced Magnetic Materials*. 2007, John Wiley & Sons, Ltd.
11. H. Ebert, *Magneto-optical effects in transition metal systems*. Reports on Progress in Physics, 1996. **59**(12): p. 1665.
12. J. L. Erskine, E. A.Stern *Calculation of the $M_{2,3}$ magneto-optical absorption spectrum of ferromagnetic nickel*. Physical Review B, 1975. **12**(11): p. 5016-5024.
13. G. Schütz, W. Wagner, W. Wilhelm, P. Kienle, R. Zeller, R. Frahm, G. Materlik, , *Absorption of circularly polarized x rays in iron*. Physical Review Letters, 1987. **58**(7): p. 737-740.
14. S.J. Blundell, *Magnetism in condensed Matter*. Oxford Master series in Condensed matter physics, Oxford university press, 2010.
15. H. Haken, H. C. Wolf, *The Physics of atoms and Quanta*. Springer verlag Berlin, 2001.
16. J. Stöhr, *Magnetism from fundamentals to nanoscale dynamics*. 2006.
17. F. de Groot, *Multiplet effects in X-ray spectroscopy*. Coordination Chemistry Reviews, 2005. **249**(1–2): p. 31-63.
18. C. M. Praetorius, *Ce $M_{4,5}$ XAS and XMCD as Local Probes for Kondo and Heavy Fermion Materials-A Study of $CePt_5$/Pt(111) Surface Intermetallics*. Thesis, 1990.

19. R. D. Cowan, *The Theory of Atomic structure and spectra*. Univeristy of California press Berkeley and Los angeles , California, 1981.
20. B. T. Thole, P.Carra, F. Sette, G. van der Laan, *X-ray circular dichroism as a probe of orbital magnetization*. Physical Review Letters, 1992. **68**: p. 1943-1946.
21. B. T. Thole, G. van der Laan, G. A. Sawatzky, *Strong Magnetic Dichroism Predicted in the $M_{4,5}$ X-Ray Absorption Spectra of Magnetic Rare-Earth Materials*. Physical Review Letters, 1985. **55**: p. 2086-2088.
22. T. H. Tietze, *magentism of unconventional nanoscale materials: An x-ray circular dichrosim and muon spin rotation study*. Thesis, 2014.
23. T. Funk, A. Deb, S. J George, H. Wang, S. P.Cramer,, *X-ray magnetic circular dichroism—a high energy probe of magnetic properties*. Coordination Chemistry Reviews, 2005. **249**(1–2): p. 3-30.
24. C. T. Chen, Y. U. Idzerda, H. J. Lin, N. V. Smith, G. Meigs, E. Chaban, G. H. Ho, E.Pellegrin, F. Sette, , *Experimental Confirmation of the X-Ray Magnetic Circular Dichroism Sum Rules for Iron and Cobalt*. Physical Review Letters, 1995. **75**: p. 152-155.
25. C. T. Chen, Y. U. Idzerda, H. J. Lin, G. Meigs, A. Chaiken , G. A. Prinz, G. H. Ho *Element-specific magnetic hysteresis as a means for studying heteromagnetic multilayers*. Physical Review B, 1993. **48**: p. 642-645.
26. *Diamond Light Source is the UK's national synchrotron science facility website*.
27. E. Goering, *Habiltationsscrift, Max-Planck-Institut für metallforschung*. 2006.
28. S. Schüppler, P. Nagel, M. Merz, *Guidelines for user experiments at WERA beamline*. 2013. **Version 0.2**.
29. E. Goering, S. Gold, A. Bayer, G. Schütz, *Non-symmetric influences in total electron yield X-ray magentic circular dichroism signal in applied magentic fields*. Journal of Synchrotron Radiation, 2001. **8**: p. 434-436.
30. M. Weissbluth, *Atoms and Molecules;* . Plenum Press: New York, , (1978).
31. W. A. Caliebe, C. C. Kao, J. B. Hastings, M. Taguchi, A. Kotani, T. Uozumi, F. M. F. de Groot,, *1s2p resonant inelastic x-ray scattering in $\alpha-Fe_2O_3$*. Physical Review B, 1998. **58**(20): p. 13452-13458.
32. F. M. F. de Groot, *X-ray absorption and dichroism of transition metals and their compounds*. Journal of Electron Spectroscopy and Related Phenomena, 1994. **67**(4): p. 529-622.
33. J. B. Goedkoop, B. T. Thole, G. van der Laan, G. A. Sawatzky, F. M. F. de Groot, J. C. Fuggle,, *Calculations of magnetic x-ray dichroism in the 3d absorption spectra of rare-earth compounds*. Physical Review B, 1988. **37**(4): p. 2086-2093.
34. F.M. de Groot, *High-Resolution X-ray Emission and X-ray Absorption Spectroscopy*. Chemical Reviews, 2001. **101**(6): p. 1779-1808.

35. B. T. Thole, G. van der Laan, *Sum rules for magnetic dichroism in rare earth 4f photoemission*. Physical Review Letters, 1993. **70**: p. 2499-2502.
36. K. C. Williams, *The M IV,V spectra of 63 Eu*. Proceedings of the Physical Society, 1966. **87**(4): p. 983.
37. B. T. Thole, G. van der Laan, J. C. Fuggle, G. A. Sawatzky, R. C Karnatak, J. M. Esteva, , *3d x-ray-absorption lines and the $3d^9 4f^{n+1}$ multiplets of the lanthanides*. Physical Review B, 1985. **32**: p. 5107-5118.
38. P.H. Butler, *Point Group Symmetry, Applications, Methods and Tables*. Plenum, New York, 1981.
39. F. M. F. de Groot, J. C. Fuggle, B. T. Thole, G. A. Sawatzky, *$L_{2,3}$ x-ray-absorption edges of d^0 compounds: K^+, Ca^{2+}, Sc^{3+} and Ti^{4+} in O_h (octahedral) symmetry*. Physical Review B, 1990. **41**(2): p. 928-937.
40. G. van der Laan, *$M_{2,3}$ absorption spectroscopy of 3d transition-metal compounds*. Journal of Physics: Condensed Matter, 1991. **3**(38): p. 7443.
41. H. Ogasawara, A. Kotani, K. Okada, B.T. Thole, , *title-not availaible-cited by*. Phys. Rev. B 1991a. **43**: p. 854–859.
42. E. Stavitski, F. M. de Groot, *The CTM4XAS program for EELS and XAS spectral shape analysis of transition metal L edges*. Micron, 2010. **41**(7): p. 687-694.
43. J. Sugar., *cited by Goedkoop in Phd thesis* Physical Review A. **6**(1972): p. 1764.
44. J. B. Goedkoop, *XMCD on RE elements*
45. G. van der Laan, *Angular momentum sum rules for x-ray absorption*. Physical Review B, 1998. **57**(1): p. 112-115.
46. E. Lindberg, *The title is unknown to the author. Cited after Thole et al., Phys. Rev. B 1985.32:p. 5107*. Nova Acta Reg. Soc. Sci. Upsaliensis 7, 1931. **7**
47. G. Schütz, *Magnetic Absorption of Hard X-rays: New Aspects*.
48. G. van der Laan, B. T. Thole, *X-ray-absorption sum rules in jj-coupled operators and ground-state moments of actinide ions*. Physical Review B, 1996. **53**(21): p. 14458-14469.
49. O. Gunnarsson, K. Schönhammer *Photoemission From Ce Compounds , Exact Model Calculation In the Limit of Large Degeneracy*. Physical Review Letters **50** (1983): p. 604
50. O. Gunnarsson, K. Schönhammer *Electron Spectroscopies For Ce Compounds :In the Impurity Model,* . Physical Review B **28** (1983): p. 4315
51. C. Bonnelle, R. C. Karnatak, J. Sugar, *Photoabsorption in the vicinity of 3d absorption edges of La, La_2O_3, Ce, and CeO_2*. Physical Review A, 1974. **9**(5): p. 1920-1923.
52. G. Kaindl, G. Kalkowski, W. D. Brewer, E. V. Sampathkumaran, F. Holtzberg, A. Schach, *4f occupation and hybridization from M-shell excitations in Rare-Earth materials*. Journal of Magnetism and Magnetic Materials, 1985. **47-48**: p. 181-189.

53. T. Jo, I. Shin, *Circular dichroism in the 3d-and 4d-core photoabsorption for ferromagnetic mixed valent Ce compounds*. Physica Scripta, 1990. **41**: p. 560-564.
54. R. D. Cowan, *Theoretical Calculation of Atomic Spectra Using Digital Computers**. J. Opt. Soc. Am., 1968. **58**(6): p. 808-818.
55. several authors, *See the "Theo Thole Memorial Issue"*. J. Electron Spectrosc. Relat. Phenom., 1997. **86**: p. 1
56. C. T. Chen, F. Ma. Sette, S. Modesti, *Soft-x-ray magnetic circular dichroism at the $L_{2,3}$ edges of nickel*. Physical Review B, 1990. **42**: p. 7262-7265.
57. T. Jo, S. Imada *Circular Dichroism in the 3d and 4d Core Photoabsorption for Ferromagnetic Ce Compounds -Interplay of Hybridization, Spin Orbit Interaction and Crystal Field*. Journal of the Physical Society of Japan, 1990. **59**(4): p. 1421-1429.
58. S. Imada, T. Jo, *Magnetic Circular Dichroism in Core X-Ray Absorption Spectra of Rare-Earths*. Journal of the Physical Society of Japan, 1990. **59**(9): p. 3358-3373.
59. G. van der Laan, *Spin-orbit branching ratio and magnetic X-ray dichroism*. Physica Scripta, 1990. **41**(4): p. 574.
60. Y. Teramura, A. Tanaka, B. T. Thole, T. Jo, *Effect of Coulomb Interaction on the X-Ray Magnetic Circular Dichroism Spin Sum Rule in Rare Earths*. Journal of the Physical Society of Japan, 1996. **65**(9): p. 3056-3059.
61. T. Jo, *The 3d-4f exchange interaction, X-ray second-order optical processes and the magnetic circular dichroism (MCD) spin sum rule in rare earths*. Journal of Electron Spectroscopy and Related Phenomena, 1997. **86**(1): p. 73-82.
62. T. Tolinski, J. C. Cezar, H. Wende, A. Kowalczyk, K. Baberschke, *X-Ray Magnetic Circular Dichroism Studies on $CeNi_4B$*. Acta Phys. Pol. A 2009. **115**: p. 129
63. T.Takeda Okane, Y.Yamagami, H.Fujimori, A.Matsumoto, Y.Kimura, N.Komatsubara, T.Aoki, H., *Magnetic behavior near the boundary of 4f delocalization in ferromagnetic $CeRu_2Ge_2$ and paramagnetic $CeRu_2Si_2$ observed by Ce $M_{4,5}$ XAS and XMCD*. Physical Review B, 2012. **86**: p. 125138.
64. P. Carra, H. König, B. T. Thole, M. Altarelli, *Magnetic X-ray dichroism: General features of dipolar and quadrupolar spectra*. Physica B: Condensed Matter, 1993. **192**(1): p. 182-190.
65. Y. Lu, M. Höppner, O. Gunnarsson, M. W. Haverkort, *Efficient real-frequency solver for dynamical mean-field theory*. Physical Review B, 2014. **90**(8): p. 085102.
66. M. W. Haverkort, M. Zwierzycki, O. K. Andersen, *Multiplet ligand-field theory using Wannier orbitals*. Physical Review B, 2012. **85**(16): p. 165113.
67. M. W. Haverkort, G. Sangiovanni, P. Hansmann, A. Toschi, Y. Lu, S. Macke, *Bands, resonances, edge singularities and excitons in core level spectroscopy investigated within the dynamical mean-field theory*. Euro. Phys. Lett., 2014. **108,** : p. 57004
68. J. B. Goedkoop, *X-ray dichroism of rare earth materials*. Thesis, (1989).

69. G. van der Laan, *Theory of simple spectra*. Journal of Electron Spectroscopy and Related Phenomena, 1997. **86**(1): p. 41-47.
70. G. Schütz, E. Goering, H. Stoll,, *Synchrotron Radiation Techniques Based on X-ray Magnetic Circular Dichroism*, in *Handbook of Magnetism and Advanced Magnetic Materials*. 2007, John Wiley & Sons, Ltd.
71. R. Skomski, *Simple Models of Magnetism*. Oxford university press.
72. S. D. Jiang, W. B. Wang, S. Gao, *Advances in Lanthanide Single-Ion Magnets*, in *Molecular Nanomagnets and Related Phenomena*, Song Gao, Editor. 2015, Springer Berlin Heidelberg: Berlin, Heidelberg. p. 111-141.
73. R. Nakajima, J. Stöhr, Y. U. Idzerda, *Electron-yield saturation effects in L-edge x-ray magnetic circular dichroism spectra of Fe, Co, and Ni*. Physical Review B, 1999. **59**(9): p. 6421-6429.
74. C. Sorg, *Magnetic Properties of 3d and 4f Ferromagnets Studied by X-Ray Absorption Spectroscopy*. im Fachbereich Physik der Freien Universit¨at Berlineingereichte Dissertation, 2005.
75. D. Ottewell, E. A. Stewardson, J. E. Wilson *The $M_{4,5}$ spectrum of ^{58}Ce and the γ-α phase transition* J. Phys. B: At., Mol. Opt. Phys., 1973: p. 62184.
76. J. C. Fuggle, F. U. Hillebrecht, J. M. Esteva, R. C. Karnatak, O. Gunnarsson, K. Schönhammer, *f-count effects in x-ray-absorption spectra of the 3d levels in Ce and its intermetallic compounds*. Physical Review B, 1983. **27**: p. 4637-4643.
77. G. Kaindl, G. Kalkowski, W. D. Brewer, B. Perscheid, F. Holtzberg, *M-edge x-ray absorption spectroscopy of 4f instabilities in rare-earth systems (invited)*. Journal of Applied Physics, 1984. **55**(6): p. 1910-1915.
78. C. Dallera, M. Grioni, A. Palenzona, M. Taguchi, E. Annese, G. Ghiringhelli, A. Tagliaferri, N.B. Brookes, Th Neisius, L. Braicovich, L., *α-γ transition in metallic Ce studied by resonant x-ray spectroscopies*. Physical Review B, 2004. **70**(8): p. 085112.
79. B. T. Thole G. van der Laan , G. A. Sawatzky, J. C. Fuggle,R. Karnatak, *Identification of the relative population of spin-orbit split states in the ground state of a solid*. Journal of Physics C: Solid State Physics, 1986. **19**: p. 817-827.
80. J. P. Schillé, F. Bertran, M. Finazzi, Ch. Brouder, J. P. Kappler, G. Krill, *4f orbital and spin magnetism in cerium intermetallic compounds studied by magnetic circular x-ray dichroism.* Physical Review B, 1994. **50**(5): p. 2985-2989.
81. M. Finazzi, F. M. F. de Groot, *Direct Evidence of the Role of Hybridization in the X-Ray Magnetic Circular Dichroism of a-Ce*. Physical Review Letters, 1995. **75**: p. 4654-4657.
82. P. Hansmann, A. Severing, Z. Hu, M. W. Haverkort, C. F. Chang, S. Klein, A. Tanaka, H. H. Hsieh, H. J. Lin, C. T. Chen, B. Fåk, P. Lejay, L. H.Tjeng, *Determining the Crystal-Field Ground State in Rare Earth Heavy Fermion Materials Using Soft-X-Ray Absorption Spectroscopy*. Physical Review Letters, 2008. **100**: p. 066405.

83. C. Praetorius, M. Zinner,P. Hansmann, M. W. Haverkort, K. Fauth, *Exploring small energy scales with x-ray absorption and dichroism*. Physical Review B, 2016. **93**(16): p. 165107.
84. T. Jo, A. Kotani, *Effect of valence mixing on multiplet structure in core photoabsorption spectra for Ce compounds*. Physical Review B, 1988. **38**(1): p. 830-833.
85. D. Goll, R. Loeffler, J. Herbst, R. Karimi, G. Schneider, *High-throughput search for new permanent magnet materials*. Journal of Physics: Condensed Matter, 2014. **26**(6): p. 064208.
86. O. Isnard, S. Miraglia, M. Guillot, D. Fruchart, *Hydrogen effects on the magnetic properties of $RFe_{11}Ti$ compounds*. Journal of Alloys and Compounds, 1998. **275**: p. 637-641.
87. D. B. De Mooij, K. H. J. Buschow, *Some novel ternary $ThMn_{12}$-type compounds*. Journal of the Less Common Metals, 1988. **136**(2): p. 207-215.
88. M. Akayama, H. Fujii, K. Yamamoto, K. Tatami, *Physical properties of nitrogenated $RFe_{11}Ti$ intermetallic compounds (R=Ce, Pr and Nd) with $ThMn_{12}$-type structure*. Journal of Magnetism and Magnetic Materials, 1994. **130**: p. 99-107.
89. J. L. Soubeyroux, D. Fruchart, O. Isnard, S. Miraglia, E. Tomey, *Role of the (H,C,N) interstitial elements on the magnetic properties of iron-rare earth permanent magnet alloys*. Journal of Alloys and Compounds, 1995. **219**: p. 16-24.
90. F. E. Pinkerton, C. D. Fuerst, J. F. Herbst, *Nitriding of melt-spun Nd-Fe-Mo alloys*. Journal of Applied Physics, 1994. **75**: p. 6015-6017.
91. C. Zhou, M. Tessema, M. S. Meyer, F. E. Pinkerton, *Synthesis of $CeFe_{10.5}Mo_{1.5}$ with $ThMn_{12}$-type structure by melt spinning*. Journal of Magnetism and Magnetic Materials, 2013. **336**: p. 26-28.
92. A. Delin, B. Johansson, *Valence degeneracy in cerium systems*. Journal of Magnetism and Magnetic Materials, 1998. **177–181, Part 1**(0): p. 373-374.
93. C. Zhou, F. E. Pinkerton, J. F. Herbst, , *Magnetic properties of $CeFe_{11-x}Co_xTi$ with $ThMn_{12}$ structure*. Journal of Applied Physics, 2014. **115**: p. 17C7161-3.
94. D. Loeffler Goll, R. Stein, R. Pflanz, U. Goeb, S. Karimi, R. Schneider, G. , *Temperature dependent magnetic properties and application potential of intermetallic $Fe_{11-x}Co_x$ TiCe*. physica status solidi (RRL), 2014. **8**: p. 862-865.
95. H. Kotani Ogasawara, A. Potze, R. Sawatzky, G. A. Thole, B. T., *Praseodymium 3d- and 4d-core photoemission spectra of Pr_20_3*. Physical Review B, 1991. **44**: p. 5465-5469.
96. S. J. Kennedy, B. R. Coles, *The magnetic phases of pseudobinary $Ce(Fe_{1-x} M_x)_2$ intermetallic compounds; M=Al, Co, Ru*. Journal of Physics: Condensed Matter, 1990. **2**: p. 1213.
97. J. Chaboy, A. Marcelli, L. Bozukov, F. Baudelet, E. Dartyge, A. Fontaine, S. Pizzini, *Effect of hydrogen absorption on the cerium electronic state in $CeFe_{11}Ti$: An x-ray-absorption and circular-magnetic-dichroism investigation*. Physical Review B, 1995. **51**: p. 9005-9014.
98. M. Finazzi, F. M. De Groot, A. M. Dias, J. P. Kappler, O. Schulte, W. Felsch, G. Krill, *Influence of hybridization in the Magnetic Circular X-ray Dichroism at the Ce-$M_{4,5}$ absorption edges of*

Ce-Fe systems. Journal of Electron Spectroscopy and Related Phenomena, 1996. **78**: p. 221-224.

99. H. B. Vasili, B. Casals, R. Cichelero, F. Macià, J. Geshev, P.,G. Herranz Gargiani, *Direct observation of multivalent states and 4f→3d charge transfer in Ce-doped yttrium iron garnet thin films*. Physical Review B, 2017. **96**: p. 014433.
100. L. Bommer, *Bosch- Releamag*. 2013. **Project number-03X4626D**.
101. W. Körner, G. Krugel, C. Elsässer, *Theoretical screening of intermetallic $ThMn_{12}$-type phases for new hard-magnetic compounds with low rare earth content*. Scientific Reports, 2016. **6**: p. 24686.
102. *$CeFe_{11}Ti$ Crystal Structure: Datasheet from "PAULING FILE Multinaries Edition – 2012" in SpringerMaterials* Pierre Cenzual Villars, Karin, Editor., Springer-Verlag Berlin Heidelberg & Material Phases Data System (MPDS), Switzerland & National Institute for Materials Science (NIMS), Japan.
103. J. Chaboy, M. A. Laguna-Marco, M. C. Sánchez, H. Maruyama, N. Kawamura, M. Suzuki, *Rare-earth orbital contribution to the Fe K-edge x-ray magnetic circular dichroism in rare-earth transition-metal intermetallic compounds*. Physical Review B, 2004. **69**(13): p. 134421.
104. K. H. J. Buschow, J. S. van Wieringen, *Crystal structure and magnetic properties of cerium-iron compounds*. physica status solidi (b), 1970. **42**(1): p. 231-239.
105. B. I. Min, J. S. Kang, J. H. Hong, J. I. Jeong, Y. P. Lee, S. D.,W. Y. Lee Choi, C. J. Yang, C. G. Olson, *Electronic and magnetic structures of the rare-earth permanent magnet $Nd_2Fe_{14}B$*. Physical Review B, 1993. **48**: p. 6217-6224.
106. B. Gilbert, J. E. Katz, J. D. Denlinger, Y. Yin, R. Falcone, ,G. A. Waychunas, *Soft X-ray Spectroscopy Study of the Electronic Structure of Oxidized and Partially Oxidized Magnetite Nanoparticles*. The Journal of Physical Chemistry C, 2010. **114**(50): p. 21994-22001.
107. Eli Stavitski, F. M. de Groot, *The CTM4XAS program for EELS and XAS spectral shape analysis of transition metal L edges*. Micron, 2010. **41**: p. 687-694.
108. T. Willers, Z. Hu, N. Hollmann, A. Severing, *Crystal-field and Kondo-scale investigations of $CeMIn_5$ (M=Co, Ir, and Rh): A combined x-ray absorption and inelastic neutron scattering study*. Physical Review B, 2010. **81**(19): p. 195114.
109. E. M. Collins, N. Kioussis, S. P. Lim, B. R. Cooper, *Competition of exchange and crystal field interactions in cerium monopnictides and monochalcogenides*. Journal of Applied Physics, 2000. **87**(9): p. 5143-5145.
110. F. M. De Groot, A. Kotani, *Introduction*, in *Core Level Spectroscopy of Solids*. 2008, CRC Press. p. 1-9.
111. M. FANCIULLI, *Spin-Orbit and Crystal Field Excitations in Cerium Compounds probed by Resonant Inelastic X-ray Scattering*. Master Thesis, 2013.
112. F. M. De Groot, A. Kotani, *Core level spectroscopy of solids*.

113. E. Wuilloud, B. Delley, W. D. Schneider, Y. Baer, *Spectroscopic Evidence for Localized and Extended f -symmetry States in CeO_2*. Physical Review Letters, 1984. **53**(2): p. 202-205.
114. S. M. Butorin, D. C. Mancini, J. H. Guo, N. Wassdahl, D. K. Shuh, *Resonant X-Ray Fluorescence Spectroscopy of Correlated Systems: A Probe of Charge-Transfer Excitations*. Physical Review Letters, 1996. **77**(3): p. 574-577.
115. F. Sayetat, *Huge magnetostriction in $Tb_3Fe_5O_{12}$, $Dy_3Fe_5O_{12}$, $Ho_3Fe_5O_{12}$, $Er_3Fe_5O_{12}$ garnets*. Journal of Magnetism and Magnetic Materials, 1986. **58**(3–4): p. 334-346.
116. K. Uchida, J. Xiao, E. Saitoh, *Spin Seebeck insulator*. Nature Materials, 2010. **9**: p. 894.
117. Michael Schreier, T. Chiba, R. Gross,, *Current-induced spin torque resonance of a magnetic insulator*. Physical Review B, 2015. **92**(14): p. 144411.
118. W. A. Crossley, R. W. Cooper, J. L. Page, R. P. van Stapele, *Faraday Rotation in Rare-Earth Iron Garnets*. Journal of Applied Physics, 1969. **40**(3): p. 1497-1498.
119. Ryan Nakamoto, X.Changsong L. Hu Bellaiche, *Properties of rare-earth iron garnets from first principles*. Physical Review B, 2017. **95**(2): p. 024434.
120. H. Lassri, E. K. Hlil, S. Prasad, R. Krishnan,, *Magnetic and electronic properties of nanocrystalline $Gd_3Fe_5O_{12}$ garnet*. Journal of Solid State Chemistry, 2011. **184**(12): p. 3216-3220.
121. M. A. Gilleo, *Chapter 1 Ferromagnetic insulators: Garnets*, in *Handbook of Ferromagnetic Materials*. 1980, Elsevier. p. 1-53.
122. C. Kittel, *Introduction to Solid State Physics*. 2004: Wiley.
123. L. Néel, Ann. de Phys. , 1948 **3** p. 137.
124. R. Pauthenet, Ann. Phys. (Paris) 1958. **3**: p. 424.
125. M.A. Belyanchikova K.P. Belov, R.Z. Levitin and S.A. Nikitin, Redkozemel'nye ferro-i antiferro magnetiki (Nauka, Moscow) 1965.
126. Arthur E. Clark, Earl Callen, *Néel Ferrimagnets in Large Magnetic Fields*. Journal of Applied Physics, 1968. **39**(13): p. 5972-5982.
127. K.P. F Belov, errity v sil'nykh magnitnykh polyakh (Nauka, Moscow) 1972: p. 173.
128. M.A. Gilleo, *in: Ferromagnetic Materials ed.* E.P. Wohlfarth (North-Holland, Amsterdam 1981. **vol. 2**: p. 7.
129. S. Geller, H. J. Williams, G. P. Espinosa, *Magnetic Study of the Lighter Rare-Earth Ions in the Iron Garnets*. Physical Review, 1963. **131**(3): p. 1080-1082.
130. S. Geller, J. P. Remeika, G. P. Espinosa, *Magnetic Study of the Heavier Rare-Earth Iron Garnets*. Physical Review, 1965. **137**(3A): p. A1034-A1038.
131. S. Hosseini Vajargah, H. R. Madaah Hosseini, ,Z. A. Nemati, *Preparation and characterization of yttrium iron garnet (YIG) nanocrystalline powders by auto-combustion of nitrate-citrate gel*. Journal of Alloys and Compounds, 2007. **430**(1–2): p. 339-343.
132. S. Blundell, *Magnetism in condensed matter*. (2001).

133. H. Maruyama, N. Kawamura, *XMCD study of electronic states in rare-earth iron garnet*. Journal of Electron Spectroscopy and Related Phenomena, 2004. **136**(1–2): p. 135-141.

134. P. Rudolf, F. Sette, L. H. Tjeng, G. Meigs, C. T. Chen *Magnetic moments in a gadolinium iron garnet studied by soft-X-ray magnetic circular dichroism*. Journal of Magnetism and Magnetic Materials, 1992. **109**(1): p. 109-112.

135. E. Goering, S. Gold, G. Schutz, *Ho-Fe-Garnet soft XMCD measurements below and above the compensation temperature*. Journal of Synchrotron Radiation, 2001. **8**(2): p. 422-424.

136. P. Novák, *4.1.2.1.1 Saturation magnetization and Curie temperature: Datasheet from Landolt-Börnstein - Group III Condensed Matter · Volume 27E: "Garnets"* H. P. J. Wijn, Editor., Springer-Verlag Berlin Heidelberg.

137. D. L. Huber, *A. Yttrium and rare earth iron garnets: Datasheet from Landolt-Börnstein - Group III Condensed Matter · Volume 4A: "Part A"* K. H. Hellwege, A. M. Hellwege, Editor., Springer-Verlag Berlin Heidelberg.

138. P. Novák, *4.1.2.1.3 Magnetic moments of the rare earth ions: Datasheet from Landolt-Börnstein - Group III Condensed Matter · Volume 27E: "Garnets"*, H. P. J. Wijn, Editor., Springer-Verlag Berlin Heidelberg.

139. H. Maruyama, I. Harada, K. Kobayashi, H. Yamazaki,, *Magnetic circular X-ray dichroism at Fe K-edge in ferrimagnetic Fe-oxides*. Physica B: Condensed Matter, 1995. **208-209**: p. 760-762.

140. P. Fischer, G. Schütz, S. Scherle, M. Knülle, S. Stähler, G. Wiesinger, *Experimental study of the circular magnetic X-ray dichroism in Ho-metal, $Ho_3Fe_5O_{12}$, Ho_6F_{e23} and Ho_2Co_{17}*. Solid State Communications, 1992. **82**(11): p. 857-861.

141. H. Maruyama,N. Kawamura, *XMCD study of electronic states in rare-earth iron garnet*. Journal of Electron Spectroscopy and Related Phenomena, 2004. **136**(1): p. 135-141.

142. P. Rudolf, F. Sette, L. H. Tjeng, G. Meigs,C. T. Chen, *Magnetic moments in a gadolinium iron garnet studied by soft-X-ray magnetic circular dichroism*. Journal of Magnetism and Magnetic Materials, 1992. **109**(1): p. 109-112.

143. G. van der Laan, B.T. Thole, G. A. Sawatzky, J. B.Goedkoop, J. C. Fuggle, J. M. Esteva,,H. A. Dabkowska R. Karnatak, *Experimental proof of magnetic x-ray dichroism*. Physical Review B, 1986. **34**(9): p. 6529-6531.

144. G. P. Espinosa, *Crystal Chemical Study of the Rare-Earth Iron Garnets*. The Journal of Chemical Physics, 1962. **37**(10): p. 2344-2347.

145. C. Klewe, M. Meinert ,A. Boehnke, K. Kuepper, E. Arenholz, A. Gupta, J.-M. Schmalhorst, T. Kuschel, G. Reiss, *Physical characteristics and cation distribution of $NiFe_2O_4$ thin films with high resistivity prepared by reactive co-sputtering*. Journal of Applied Physics, 2014. **115**(12): p. 123903.

146. B. Liu, C. Piamonteze, M. U. Delgado-Jaime, F.Nolting, F. M. F. de Groot, , *Sum rule distortions in fluorescence-yield x-ray magnetic circular dichroism*. Physical Review B, 2017. **96**(5): p. 054446.

147. E. Pellegrain, M. Hagelstein,N. B. Brookes, *Characterization of Nanocrystalline γ-Fe_2O_3 with Synchrotron Radiation Techniques*. physica status solidi (b), 1999. **215**(1): p. 797-801.

148. S.. M. A. Arrio Brice-Profeta, Ph. Sainctavit, *Magnetic order in γ-Fe_2O_3 nanoparticles: a XMCD study*. Journal of Magnetism and Magnetic Materials, 2005. **288**: p. 354-365.

149. pattrick Richard A.D., gerrit Vanderlaan ,C. Michale B. Henderson, David J. vaughan, *Cation site occupancy in spinel ferrites studied by X-ray magnetic circular dichroism: developing a method for mineralogists*. Eur. J. Mineral., 2002. **14**: p. 1095–1102.

150. L. et al. Neel, Prog.low. temp.phys., 1964 **4** p. 344 - 383.

151. S. Sugimoto, *Current status and recent topics of rare-earth permanent magnets*. Journal of Physics D: Applied Physics, 2011. **44**(6): p. 064001.

152. K. Strnat, G. Hoffer, J. Olson, W. Ostertag, J. J. Becker, *A Family of New Cobalt-Base Permanent Magnet Materials*. Journal of Applied Physics, 1967. **38**(3): p. 1001-1002.

153. J. F. Herbst, *$R_2Fe_{14}B$ materials: Intrinsic properties and technological aspects*. Reviews of Modern Physics, 1991. **63**(4): p. 819-898.

154. J.J. Croat, J. F. Herbst, R. W. Lee, F. E. Pinkerton, *Pr-Fe and Nd-Fe-based materials: A new class of high-performance permanent magnets (invited)*. Journal of Applied Physics, 1984. **55**(6): p. 2078-2082.

155. M. Sagawa, S. Fujimura, N. Togawa, H. Yamamoto, Y. Matsuura, *New material for permanent magnets on a base of Nd and Fe (invited)*. Journal of Applied Physics, 1984. **55**(6): p. 2083-2087.

156. E. Eurzo, H.R. Kirchmayr, *Handbook on the Physics and Chemistry of Rare Earth*. Handbook on the Physics and Chemistry of Rare Earth, edited by K. A. Gchneidner and L.Eying _Elsevier Science, Amsterdam, 1989. **12**.

157. W. F. Li, H. Sepehri-Amin, T. Ohkubo, N. Hase, K. Hono, *Distribution of Dy in high-coercivity (Nd,Dy)–Fe–B sintered magnet*. Acta Materialia, 2011. **59**(8): p. 3061-3069.

158. H. Satoshi, N. Masamichi, M. Seiji, *Perspectives for high-performance permanent magnets: applications, coercivity, and new materials*. Advances in Natural Sciences: Nanoscience and Nanotechnology, 2017. **8**(1): p. 013002.

159. M. Sagawa, S. Hirosawa, H. Yamamoto, S. Fujimura , Y. Matsuura *Nd–Fe–B Permanent Magnet Materials*. Japanese Journal of Applied Pysics 1987 **26**: p. 785.

160. F. Vial, F. Joly, E. Nevalainen, M. Sagawa, K. Hiraga, K. T. Park, *Improvement of coercivity of sintered NdFeB permanent magnets by heat treatment*. Journal of Magnetism and Magnetic Materials, 2002. **242-245**: p. 1329-1334.

161. W. F. Li, T. Ohkubo, K. Hono, *Effect of post-sinter annealing on the coercivity and microstructure of Nd–Fe–B permanent magnets*. Acta Materialia, 2009. **57**(5): p. 1337-1346.

162. W. B.. Y.K. Takahashi Cui, K. Hono, *Microstructure optimization to achieve high coercivity in anisotropic Nd–Fe–B thin films*. Acta Materialia, 2011. **59**(20): p. 7768-7775.

163. A. Melsheimer, H. Kronmüller, *Magnetization processes in isotropic and textured $Nd_2Fe_{14}B$-films*. Physica B: Condensed Matter, 2001. **299**(3–4): p. 251-259.

164. L.R.White, Journal of Magnetism and Magnetic Materials, 2000. **1**.

165. N. M. Dempsey, T. G. Woodcock, H. Sepehri-Amin, Y.,H. Kennedy Zhang, D. Givord, K. Hono, O. Gutfleisch, *High-coercivity Nd-Fe-B thick films without heavy rare earth additions*. Acta Materialia, 2013. **61**(13): p. 4920-4927.

166. M. Uehara, N. Gennai, M. Fujiwara, T. Tanaka, *Improved perpendicular anisotropy and permanent magnet properties in Co-doped Nd-Fe-B films multilayered with Ta*. IEEE Transactions on Magnetics, 2005. **41**(10): p. 3838-3843.

167. S. Honda, M. Nawate,I. Sakamoto, *Magnetic structure and perpendicular magnetic anisotropy of rare-earth (Nd,Pr,Gd)/Fe multilayers*. Journal of Applied Physics, 1996. **79**(1): p. 365-372.

168. D. J. Sellmyer, Z. R. Zhao, Z. S. Shan, S. Nafis, *Magnetic properties of Fe/Nd multilayer films*. Journal of Applied Physics, 1987. **61**(8): p. 4323-4325.

169. Z. S. Shan, S. Nafis,K.D. Aylesworth, D. J. Sellmyer, *Magnetic properties, anisotropy, and microstructure of sputtered rare-earth iron multilayers*. Journal of Applied Physics, 1988. **63**(8): p. 3218-3220.

170. J. Tejada, F. Badia, B. Martinez, J. M. Ruiz, *Magnetic properties of compositionally modulated thin films of rare earth and transition metal*. Journal of Magnetism and Magnetic Materials, 1991. **101**(1–3): p. 181-186.

171. S. Honda, M. Nawate, I. Sakamoto, *Magnetic structure and perpendicular magnetic anisotropy of rare-earth (Nd,Pr,Gd)/Fe multilayers*. Journal of Applied Physics, 1996. **79**(1): p. 365-372.

172. F. Baudelet, E. Dartyge, A. Fontaine, C. Brouder, G. Krill, ,M. Piecuch J. P. Kappler, *Magnetic properties of the neodymium atoms in Nd-Fe multilayers studied by the magnetic circular dichroism on Nd L_2 and Fe K edges*. Physical Review B, 1991. **43**(7): p. 5857-5866.

173. A. Koizumi, K. Namikawa, H. Maruyama, K. Mori and H. Yamazaki *X-ray Resonance Exchange Scattering Study of $Nd_2Fe_{14}B$*.

174. D. Givord, H. S. Li,, *Magnetic properties of $Y_2Fe_{14}B$ and $Nd_2Fe_{14}B$ single crystals*. Solid State Communications, 1984. **51**(11): p. 857-860.

175. K. Tokuhara, Y. Ohtsu, F. Ono, O. Yamada, M. Sagawa, Y. Matsuura, *Magnetization and torque measurements on $Nd_2Fe_{14}B$ single crystals*. Solid State Communications, 1985. **56**(4): p. 333-336.

176. J. F. Herbst, J. J. Croat, F. E. Pinkerton, W. B. Yelon, *Relationships between crystal structure and magnetic properties in $Fe_{14}Nd_2B$*. Physical Review B, 1984. **29**(7): p. 4176-4178.

177. L. M. Garcia, J. Chaboy, F. Bartolome, J. B. Goedkoop, *Orbital magnetic moment instability at the spin reorientation transition of $Nd_2Fe_{14}B$.* Phys Rev Lett, 2000. **85**(2): p. 429-32.

178. C. Abache, H. Oesterreicher, *Magnetic properties of compounds $R_2Fe_{14}B$.* Journal of Applied Physics, 1985. **57**(8): p. 4112-4114.

179. Y. Murakami, T. Tanigaki, T. T.Sasaki, Y. Takeno,,T. Matsuda H. S. Park, T. Ohkubo, K. Hono, D. Shindo, *Magnetism of ultrathin intergranular boundary regions in Nd–Fe–B permanent magnets*. Acta Materialia, 2014. **71**(0): p. 370-379.

180. T. Nakamura, A. Yasui, S. Hirosawa et al, *Direct observation of ferromagnetism in grain boundary phase of Nd-Fe-B sintered magnet using soft x-ray magnetic circular dichroism*. Applied Physics Letters, 2014. **105**(20): p. 202404.

181. A. Yasui, T. Nakamura, T., Kotani, F. Yoshinori,N. Tomoki , H. Takeshi, *Temperature dependence of post-sintered annealing on magnetic properties of intergranular phase in Nd-Fe-B permanent magnet*. Journal of Applied Physics, 2015. **117**(17): p. 17B313.

182. K.. N. Hosoito Mibu, T. Shinjo, *Magnetic properties of Fe/Nd artificial superstructure films*. Hyperfine Interact, 1990. **54**(1-4): p. 831-838.

183. D. J. Sellmyer, Z. R. Zhao, Z. S. Shan, S. Nafis, *Magnetic properties of Fe/Nd multilayer*. J. Appl. Phys., , 1987. **61**.

184. S. Obbade, P. Wolfers, D. Fruchart,,J. Muller R. Argoud, E. Palacios, *A precise crystal structure determination. Part II: an X-ray four-circle study of $Nd_2Fe_{14}B$ at 20 and 290 K.* Journal of Alloys and Compounds, 1996. **242**(1): p. 80-84.

185. K. D. Z.R. Zhao Aylesworth, G.C. Hadjipanayis, , *Growth and control of the microstructure and magnetic properties of sputtered $Nd_2Fe_{14}B$ films and multilayers*. Journal of Magnetism and Magnetic Materials, 1989. **82**

186. H. Sun, T.Tomida, S. Hirosawa, *Magnetic properties and microstructure studies of Nd-Fe-B thin films*. Journal of Magnetism and Magnetic Materials 1996. **18**

187. U. Hannemann, S. Fähler,S. Oswald, *Effect of Cr and Ta buffers on hard magnetic $Nd_2Fe_{14}B$ films*. Journal of Magnetism and Magnetic Materials, 2002. **242–245, Part 2**(0): p. 1294-1296.

188. *$Fe_{14}Nd_2B$ ($Nd_2Fe_{14}B$) Crystal Structure: Datasheet from "PAULING FILE Multinaries Edition – 2012" in SpringerMaterials* Pierre Villars and Karin Cenzual, Editors. 2012, Springer-Verlag Berlin Heidelberg & Material Phases Data System (MPDS), Switzerland & National Institute for Materials Science (NIMS), Japan.

189. M. Sagawa, S. Fujimura, H. Yamamoto, Y. Matsuura,S. Hirosawa, *Magnetic properties of rare-earth-iron-boron permanent magnet materials*. Journal of Applied Physics, 1985. **57**(8): p. 4094-4096.

190. J. Fidler, T. Schrefl, *The Role of Intergranular Regions in Sintered Nd-Fe-B Magnets with $(B.H)max > 420\ kJ/m^3$ (52.5 MGOe).*

191. T. Ozaki, *Variationally optimized atomic orbitals for large-scale electronic structures*. Physical Review B, 2003. **67**(15): p. 155108.

192. Z. Torbatian, O. Taisuke, T. Shinji, G. Yoshihiro, *Strain effects on the magnetic anisotropy of $Y_2Fe_{14}B$ examined by first-principles calculations*. Applied Physics Letters, 2014. **104**(24): p. 242403.

193. D. Li Givord, H. S. Tasset, *Polarized neutron study of the compounds $Y_2Fe_{14}B$ and $Nd_2Fe_{14}B$* Journal of Applied Physics, 1985. **57**(8): p. 4100-4102.

194. H. Onodera, H. Yamauchi, S. Hirosawa, *Mössbauer study of the intermetallic compound $Nd_2Fe_{14}B$. II. Temperature dependence and spin reorientation*. Journal of Magnetism and Magnetic Materials, 1987. **68**(1): p. 15-27.

195. B. Szpunar, W. E. Wallace, J. Szpunar, *Local spin and orbital moment in $Nd_2Fe_{14}B$ and Y_2Fe_{17}*. Physical Review B, 1987. **36**(7): p. 3782-3790.

196. J. Fidler,K. G. Knoch, *Electron microscopy of Nd-Fe-B based magnets*. Journal of Magnetism and Magnetic Materials, 1989. **80**(1): p. 48-56.

197. F. Vial, F. Joly, E. Nevalainen, M. Sagawa, K. Hiraga,K. T. Park, *Improvement of coercivity of sintered NdFeB permanent magnets by heat treatment*. Journal of Magnetism and Magnetic Materials, 2002. **242-245**(Part 2): p. 1329-1334.

198. T. Kohashi, K. Motai, T. Nishiuchi, S. Hirosawa, *Magnetism in grain-boundary phase of a NdFeB sintered magnet studied by spin-polarized scanning electron microscopy*. Applied Physics Letters, 2014. **104**(23): p. 232408.

199. V. A. G. Rivera, F.A. Ferri, E. Marega Jr., *Localized Surface Plasmon Resonances: Noble Metal Nanoparticle Interaction with Rare-Earth Ions*, in *Plasmonics - Principles and Applications*, Ki Young Kim, Editor. 2012, InTech: Rijeka. p. Ch. 11.

200. L. bommer, *Thesis-Magnetische und strukturelle Eigenschaften von NdFeB und Co Nanostrukturen auf unterschiedli-chen Zeitskalen*. 2011.

8. CURRICULUM VITAE

Personal Details

Family Name: Tripathi

Given Name: Sapana

Gender: Female

Date and Place of Birth: 15 February 1988, Indore (INDIA)

Nationality: Indian

Address for Correspondence

Max Planck Institute für Intelligente Systeme -+49 711 689 1811

Heisenbergstr. 3, D-70569 Stuttgart, Germany E-mail: tripathi@is.mpg.de

Education Qualifications

Since 08.February 2012: *Doctorate student* at Max Planck Institute for intelligent Systems in the department of Modern magnetic systems under supervision of Prof. Dr. Gisela Schütz and PD Dr. Eberhard Goering.

2011-2012 As a *research student (intern)* at L'Istituto Nazionale di Ricerca Metrologica (INRIM) Strada delle Cacce 91 10135 Torino, ITALY under supervision of Dr. Franco Vinai , Prof. Dr. Marcello Baricco and Dr.Marco Coisson.

2008-2010 -*Master of Science in physics (MSc)* School of physics department, Devi Ahilya University, Indore (M.P.), India under Supervision of Dr. S. N. Kane

2005-2008-*Bachelor of Science in Physics, Chemistry and Mathematics (BSc)* Girls Degree College, Devi Ahilya University, Indore (M.P.), India.

Publications

Published

1. S. N. Kane, S. Tripathi, M. Coisson, E. S. Olivetti, P. Tiberto, F. Vinai, M. Baricco, G. Fiore, A. Apolinário, C. T. Sousa, J. P. Araujo,L. K. Varga, *Microstructure and magnetic properties of* $(Fe_{100-x}Co_x)_{84.5}Nb_5B_{8.5}P_2$ *alloys*. Journal of Alloys and Compounds, 2012. **536**: p. S337-S341

2. S. M. Jain, S. Tripathi, S. Tripathi, G. Spoto, T. Edvinsson, *Acid-catalyzed oligomerization via activated proton transfer to aromatic and unsaturated monomers in Nafion membranes: a step forward in the in situ synthesis of conjugated composite membranes*. RSC Advances, 2016. **6**(106): p. 104782-104792

In process of submission

1. S. Tripathi, Y.C Chen, K. Son, S. Schuppler, P. Nagel, M. Merz, F. de. Groot, G. Schütz and E. Goering, *X-ray absorption (XAS) and x-ray magnetic circular dichroism (XMCD) investigation of* $CeFe_{11}Ti$ *magnets* in process of submission in Physical Review B.

9. Erklärung

Hiermit erkläre ich, Sapana Tripathi, dass ich, abgesehen von den ausdrücklich bezeichneten Hilfsmitteln, die Dissertation selbst verfasst habe.

Stuttgart, den 19.07.2018
Sapana Tripathi